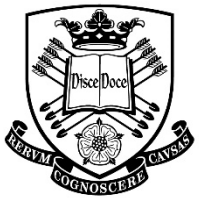

The
University
Of
Sheffield.

Thesis

The University Of Sheffield.

APPLICATION OF NON-LINEAR SYSTEM IDENTIFICATION APPROACHES TO MODELLING, ANALYSIS AND CONTROL OF FLUID FLOWS

José de Jesús Solis Cordova

A thesis submitted for the degree of
Doctor of Philosophy

The University of Sheffield

Faculty of Engineering

Department of Automatic Control & Systems Engineering

February 2017

To my wife, Daniela,
and my son, José Alberto.

Abstract

Flow control has become a topic of great importance for several applications, ranging from commercial aircraft, to intercontinental pipes and skyscrapers. In these applications, and many more, the interaction with a fluid flow can have a significant influence on the performance of the system. In many cases the fluids encountered are turbulent and detrimental to the latter.

Several attempts have been made to solve this problem. However, due to the non-linearity and infinite dimensionality of fluid flows and their governing equations, a complete understanding of turbulent behaviour and a feasible control approach has not been obtained.

In this thesis, model reduction approaches that exploit non-linear system identification are applied using data obtained from numerical simulations of turbulent three-dimensional channel flow, and two-dimensional flow over the backward facing step. A multiple-input multiple-output model, consisting of 27 sub-structures, is obtained for the fluctuations of the velocity components of the channel flow. A single-input single-output model for fluctuations of the pressure coefficient, and two multiple-input single-output models for fluctuations of the velocity magnitude are obtained in flow over the BFS.

A non-linear model predictive control strategy is designed using identified one- and multi-step ahead predictors, with the inclusion of integral action for robustness. The proposed control approach incorporates a non-linear model without the need for expensive non-linear optimizations.

Finally, a frequency domain analysis of unmanipulated turbulent flow is perfumed using five systems. Higher order generalized frequency response functions (GFRF) are computed to study the non-linear energy transfer phenomena. A more detailed investigation is performed using the output FRF (OFRF), which can elucidate the contribution of the n-th order frequency response to the output frequency response.

Acknowledgement

I would, first and foremost, like to express my sincere thanks and gratitude to my supervisor, Professor Daniel Coca. The guidance and support provided has been vital for the development of my doctoral research work, and the writing of this Thesis. I benefited greatly from our discussions, and his insight on the different subjects that I worked with, without it I would not have managed to accomplish all here presented.

I appreciate the help and support of the members of ACSE staff, past and present, who in one way or another have contributed to the work carried out, as well as my personal development over these years.

Additionally, I am grateful to many colleagues from the University, and all around Sheffield, especially those who I proudly consider my friends Nora, Francisco, Carlos, Yuri, Matei, Victor, Erik, and many others. My stay in this country was made so much more enjoyable thanks to all the experiences shared, in addition to our cheerful work-related and personal conversations. I gratefully acknowledge all my past teachers, mentors and friends who believed in me, and have helped set me on my path.

I am indebted of course, to my parents Beatriz and José, and my little sister Jacqueline. You have always worked hard and helped me throughout my life, so that I could get to where I am. Thank you for your support and guidance in all these years.

Finally, I am eternally thankful with my cherished wife Daniela, and my son José Alberto. You have been at my side throughout the difficult moments, and been my source of inspiration these past four years. I am certain that without your love, patience and support I would never have succeeded, and I am grateful for all the blessings we have received in our time in England.

I am grateful with the National Council for Science and Technology (CONACyT) of Mexico, and the ACSE Department for the joint funding of this research work.

Contents

List of Figures

List of Tables

CHAPTER 1

Introduction

1.1. Background and Motivation

Flow control has been investigated for nearly a century (Braslow, 1999; Tuttle & Bushnell, 1979). Since the proposition by Prandtl of the boundary layer (Prandtl, 1905), researchers have sought ways to improve the performance of machinery that interacts with fluid flows. Several applications have been reported prior to, and during the first and second world-wars (Braslow, 1999; Tuttle & Maddalon, 1982), when interest regarding aircraft and marine applications peaked. Most approaches at the time were passive, and involved the optimization of the geometries of air foils and marine vessels, some uses of suction have also been reported (Braslow, 1999; Tuttle & Bushnell, 1979; Tuttle & Maddalon, 1982).

After the wars, interest waivered mainly due to low oil prices and the limited amount of applications where flow control could achieve a significant improvement, of performance or reduction of fuel consumption (Braslow, 1999; Tuttle & Bushnell, 1979; Tuttle & Maddalon, 1982). Between 1960-70 there was almost no progress in this area.

However, the increase of fuel costs, coupled with insecure sources of petroleum, for example, in addition to the desire of reducing aircraft noise and lower pollution, meant that this research field became active once again. In recent years, similar economic and environmental demands have maintained the focus on flow control. In particular, the reduction of fuel costs and pollution, as well as the significant increase in computation power which enables the real-time implementation of computationally demanding algorithms, have given this topic an urgent and implementable tone (Åkervik, Hœpffner, Ehrenstein, & Henningson, 2007; Bewley, 2001; Kim, 2003; Kim & Bewley, 2007; Lumley & Blossey, 1998; Scott Collis, Joslin, Seifert, & Theofilis, 2004).

The performance of many engineering systems, especially transport and power generation, buildings, and structures, is greatly degraded as a consequence of their interactions with fluids (Bewley, 2001; Kim, 2003; Scott Collis et al., 2004). In the modern world, it is therefore of paramount importance to be able manipulate/control a fluid flow. Further, the technologies required for the implementation of such control methods, are readily available in the form of sensors and actuators (Ho & Tai, 1998; Lofdahl & Gad-el-Hak, 1999; Varadan & Varadan, 2000).

Fluids in motion are governed by the Navier-Stokes equations and can be classified as being laminar or turbulent (Bradshaw, 1994; Davidson, Kaneda, & Sreenivasan, 2013; Frank, 2011), those encountered in numerous applications are of the latter kind.

Turbulent flows are characterised as being chaotic and stochastic and the determination of their behaviour remains one of the unsolved problems of classic physics (Bradshaw, 1994; Davidson et al., 2013; P. George, 2003; Li, 2013). For this reason, turbulence has even been said to have been "*invented by the Devil, on the seventh day of Creation*" (Bradshaw, 1994).

In some cases turbulence is beneficial and even pursued, to improve heat transfer in (heat) exchangers or heighten mixing within combustion engines or chemicals in pharmaceutical plants (Bewley, 2001; Bewley, Moin, & Temam, 2001). However, in many others, there is a great drive to diminish it (Kim & Bewley, 2007; Kubo, Modi, Kotsubo,

Hayashida, & Kato, 1996; Ricco, Ottonelli, Hasegawa, & Quadrio, 2012). Turbulent boundary layers over aircraft or ships for example, induce higher skin-friction drag than that of laminar flow (Davidson et al., 2013; Frank, 2011; Scott Collis et al., 2004). In turn, this decreases the overall performance of the vehicle, while increasing fuel consumption (Bewley, 2001; Kim & Bewley, 2007; Scott Collis et al., 2004). It is estimated that skin-friction drag makes up 45% of the total drag of a commercial aircraft, while 50-80% of a large marine vessel (Heins, 2015; IPCC, 2014). Therefore, one of the sectors most benefitted by the implementation of a flow control strategy, is transport.

It has been estimated that a control strategy which generates a drag reduction, leading to a one-percent saving of world fuel-consumption, is worth over $1.25M (£1.01M) per day (Scott Collis et al., 2004). This figure shows how millions of dollars could be saved in transportation, as well as many other fuel consuming applications by achieving a relatively small flow alteration.

In terms of ecological benefits, the decrease of fuel consumption alone is a great achievement, for it would help to preserve earth's resources. More importantly, it would mean the lessening of CO_2 emission as well as other greenhouse gases and pollutants due to the increased performance (Quadrio, Ricco, & Viotti, 2009; Scott Collis et al., 2004). Although the extent of these outcomes is difficult to quantify, it would certainly be evident. Considering that international shipping accounted for 2.2% of CO_2 and 2.1% of green-house gas emissions[1] in 2012, while the aviation industry was estimated to contribute 2.5% of the world's CO_2 emissions (IPCC, 2014), a way to reduce this ecological foot-print is urgently needed.

Other just as important effects can be obtained with the reduction of vibrations. For example, those caused by wind and ocean effects, on civil engineering structures. This can lead to a decrease in material and construction costs (Kubo et al., 1996). Increased efficiency in the intercontinental transportation of oil and natural gas in pipes, wind turbine effectiveness, and many other examples of areas of opportunity and potential benefits can be given (Kim, 2003; Kim & Bewley, 2007).

[1] This is quantified in a carbon dioxide equivalent (CO_2e) basis (IPCC, 2014)

The behaviour of wall bounded fluids has been studied in the past through several canonical scenarios, such as: Couette flow, pipe flow, boundary layer flow and plane channel flow, as well as flow over a backward facing step (Bewley, 2001; Choi, Moin, & Kim, 1994; Dean & Bhushan, 2012; Gad-el-Hak, 1989; Gibson, Halcrow, & CvitanoviĆ, 2008; Heenan & Morrison, 1998; Huang & Kim, 2008; Kim, 2003; Le, Moin, & Kim, 1997; Neumann & Wengle, 2003; Scott Collis et al., 2004; Uruba, Jonáš, & Mazur, 2007). In this work, the channel flow and flow over the backward facing step scenarios will be studied, and used in conjunction with methods oriented towards the development of a flow control scheme and the increase of the understanding of turbulent flow behaviour.

The topic of flow between two infinite parallel plates has been used as a test-bed, or stepping stone, towards more complex applications, however, much can still be learned from transition and fully turbulent flows in this geometry (Bewley, 2001; Heins, Jones, & Sharma, 2016; Kim, 2003). Plane channel flow is that found in a rectangular domain, with periodic boundary conditions for the stream- and span-wise directions, and zero-velocity at the walls in the wall-normal direction (Frank, 2011; Gibson et al., 2008; Kim, 2003; Nakayama, 1999). The flow over a backward facing step is similar, with the addition of a sudden expansion in the streamwise direction, which creates the step characteristic of this scenario (Frank, 2011; Le et al., 1997).

One way in which approaches to control flow have been classified is whether the scheme obtained is passive or active (Perlin, Dowling, & Ceccio, 2016; Scott Collis et al., 2004). The former often resulting of a modification of the wall or geometry such as riblets and grooves (Heenan & Morrison, 1998; Neumann & Wengle, 2003; Perlin et al., 2016; Pollard, 1998). The latter being a dynamic closed- or open-loop modification of flow-structures using methods that include an external energy input, and in the case of closed-loop methods, require the sensing of the systems' state (Choi, Moin, & Kim, 1993; Choi et al., 1994; Perlin et al., 2016; Scott Collis et al., 2004). Examples of active control strategies include adaptive neural networks (Bewley, 2001; C. Lee, Kim, Babcock, & Goodman, 1997), schemes based purely on the understanding of

dominant physics (Hervé, Sipp, Schmid, & Samuelides, 2012; Kim, 2003), and model-based classic and modern control schemes (Allgower, Findeisen, & Nagy, 2004; Bewley et al., 2001; Choi et al., 1994; Heins et al., 2016; Huang & Kim, 2008; Jones, Heins, Kerrigan, Morrison, & Sharma, 2015; Joshi, Speyer, & Kim, 1997; Kim & Bewley, 2007; C. Lee, Kim, & Choi, 1998), among others.

The systems analysed are, in terms of control theory, of a high complexity; non-linear and infinite-dimensional, even when the flow being studied is considered as basic in other disciplines such as fluid mechanics or computational fluid dynamics (CFD) (Baramov, Tutty, & Rogers, 2001; Hervé et al., 2012; Joshi et al., 1997; Kim & Bewley, 2007). Thus, several of the present attempts of fluid control have often been based on physical intuition, experience, and in some cases even sheer luck (Kim, 2003; K. H. Lee, Cortelezzi, Kim, & Speyer, 2001; Scott Collis et al., 2004). Many more require information that is extremely hard at bests to obtain in reality, and so, turn out to be close to impossible to implement outside of simulations without the use of linearized equations and other assumptions (Kim, 2003; C. Lee et al., 1997; K. H. Lee et al., 2001). Therefore, as far as it was observed a need for the development of an accurate reduced-order model and active closed-loop controller, which is both robust and realistic so that it is feasible for implementation, is found within the literature (Bewley et al., 2001).

The control approach implemented in this work is the family of model-based predictive control. These are methods which rely on an explicit model of the plant to generate future predictions, and optimize a control sequence that drives the system to the desired state using a receding horizon (Camacho & Bordons-Alba, 2003; Clarke, Mohtadi, & Tuffs, 1987a; García, Prett, & Morari, 1989).

A non-linear variant of the generalized predictive control algorithm is implemented. The latter is defined to be used with finite control and prediction horizons, in addition to the inclusion of constraints during the control law design stage (Bai & Coca, 2011; Camacho & Bordons-Alba, 2003; Clarke & Mohtadi, 1989; Clarke et al., 1987a; Rossiter, 2003).

The explicit constraint handling is the most attractive feature of several MPC methods, considering that real systems are subject to

limitations set by the plant, sensors and actuators (Camacho & Bordons-Alba, 2003; Clarke & Mohtadi, 1989; Clarke et al., 1987a). Additional distinguishing features of interest for the current project are firstly, the ability to use models of any form, including non-linear multivariable NARMAX models identified from input/output data (Bai & Coca, 2011; Camacho & Bordons-Alba, 2003; Clarke et al., 1987a; García et al., 1989). Secondly, the use of a receding horizon which, coupled to the use of integral action in the model, provide robustness to the strategy, which in the case of infinite control and prediction horizons, yields nominal stability (Bai & Coca, 2011; Camacho & Bordons-Alba, 2003; Clarke et al., 1987a; García et al., 1989; Rossiter, 2003).

The analysis of non-linear systems in the frequency domain is possible thanks to the development of methods such as the generalized frequency response functions and output frequency response functions (D. A. George, 1959; Lang & Billings, 1997, 2004; Peyton Jones & Choudhary, 2012; Yue, Billings, & Lang, 2005). Prior to the development of these theories, this kind of analysis was limited due to the difficulty of identifying models from data, in addition to the complexity that they themselves represent, many attempts were made using Volterra series representation of the systems (Billings, 2013; Billings & Lang, 2002; Billings & Tsang, 1989a; Jing, Lang, & Billings, 2010; Lang & Billings, 1997).

Frequency-domain representations of many time-domain models are unique, which allows for the study of the invariant dynamics of the system to be identified (Billings & Lang, 2002; Jing et al., 2010; Lang & Billings, 2004). In addition to this, the study of this kind of models is of importance since most, if not all, real processes encountered are non-linear. Considering that systems are subject to tighter constraints in addition to increasing complexity, the use of simplified models can no longer be justified in many applications (Billings, 2013; Lang & Billings, 2004). A more comprehensive understanding of non-linear systems, in addition to the possibility of design of controllers that exploit phenomena only attainable through this kind of models has also been identified (Bai & Coca, 2011; Bewley, 2001; Billings & Lang, 2002; Henson, 1998).

1.2. Aims and objectives

The current research looks towards working within the gap found in the existing literature and take advantage of existing theories from the disciplines that intersect in this area of study, mainly fluid mechanics, control and optimization theory, and mathematics (Kim & Bewley, 2007).

The aim of the current research project is to develop model-based active flow control strategies in addition to an analysis of turbulent flows in the frequency domain, likewise based on reduced-order models. The objectives can therefore be summarized as follows:

- Obtain accurate and representative data of flow in the selected geometries through simulations using specialized computational fluid dynamics (CFD) packages. For the case of channel flow, highly accurate but computationally demanding direct numerical simulation (DNS) are performed using the ChannelFlow package (Gibson, 2012; M. Lee & Moser, 2015) due to the simple geometry. On the other hand, large-eddy simulation (LES) using Fluent is used to simulate the flow over the backward facing step (Le et al., 1997; Neumann & Wengle, 2003). Such simulations are based on successfully implemented experimental and simulation configurations to ensure the validity of the data obtained (Driver & Jovic, 1994; Le et al., 1997).
- Develop model reduction approaches that exploit nonlinear system identification, based on the NARMAX model and associated methodology. Data obtained from actuated simulations of both scenarios is used to perform the identification of one-step ahead (OSA), in the case of channel flow, and multi-step ahead (MSA) predictors (Bai & Coca, 2011) in the case of flow over the BFS. The identification procedure is tailored to ensure that the resulting flow over the BFS models facilitate fast implementation of control algorithms.
- Formulate and implement non-linear model predictive control (NMPC) strategies for fluid flows (Bewley et al., 2001;

Camacho & Bordons-Alba, 2003; Clarke, Mohtadi, & Tuffs, 1987b), based on the reduced-order models, capable of taking the fluid state to a desired trajectory. NMPC strategies using localized sensing and actuation are proposed for the flow over the backward facing step where a single-input single-output approach is given to control the fluctuations of the pressure coefficient on the step wall, additionally a multiple-input single-output (MISO) case is taken for the manipulation of the velocity magnitude within the recirculation zone.

- Perform an analysis of energy transfer and investigate the influence of the upstream (of the step) flow on downstream behaviour. This is achieved by identifying one-step ahead non-linear models, relating the velocity magnitude at points upstream of the step, to locations downstream. The models are mapped into the frequency domain to obtain the generalized and output frequency response functions (GFRF and OFRF) (Billings & Lang, 2002; D. A. George, 1959; Lang & Billings, 1997).
- Carry out an analysis of the generalized frequency response functions. The multivariable nature of the GFRF's make this analysis complicated for quadratic or higher order systems (Billings & Lang, 2002; Lang & Billings, 1997; Peyton Jones & Choudhary, 2012; Yue et al., 2005). However, they can provide a unique visualisation of the physical underlying behaviour of the system, which can be hidden in the time-domain model. They can elucidate the impact of individual model terms on the response of the system (Billings & Lang, 2002; Billings & Tsang, 1989a, 1989b; Lang & Billings, 1997; Peyton Jones & Choudhary, 2012; Yue et al., 2005).
- Analytically define the way in which the output frequency response, and specific output frequencies of interest, are generated using the output frequency response functions. The OFRF's are one dimensional functions of frequency, which are easier to visualize and interpret than the GFRF's, and can establish the contribution of the different order non-

linearities to the whole output frequency response or of individual elements (Billings & Lang, 2002; Lang & Billings, 1996, 1997, 2004; Lang, Billings, Yue, & Li, 2007; Peyton Jones & Choudhary, 2012; Yue et al., 2005).

1.3. Thesis outline

The current thesis presents the results obtained during this PhD research program. This work can be split into three sections, which are made up of the seven chapters included, as:

- Fluid flow simulation and analysis (*Chapter 2* and *3*)
- System identification of reduced-order models (*Chapter 4*)
- Development of applications of the identified models, in the form of control schemes and analysis of the system in the frequency domain. (*Chapter 5*, *6* and *7*)

The remaining chapters are organized as follows:

- *Chapter 2* presents a brief introduction to fluid mechanics and a more detailed description of fluid dynamics, where the latter deals with fluids in motion. The derivation of the governing equations is given, in addition to the definitions of relevant concepts required for an understanding of fluid flows. The numerical methods employed by the CFD packages used are discussed.

- *Chapter 3* introduces the two cases of wall bounded flows studied in the remainder of the work, mainly the channel flow and flow over the backward facing step. The definition and reasoning for the selected parameters is given. The chapter also includes an analysis of natural flow and Fourier analysis of the extracted data to generate a persistently exciting input for system identification purposes.

- *Chapter 4* gives an overview of system identification using the NARMAX methodology, in addition to discussing the importance of deriving dynamical models from experimental data. The implementation of these algorithms for the identification of SISO and MISO models from the CFD data is detailed, and results presented. A discussion on the accuracy of the identified models, in addition to challenges faced in the identification on non-linear systems, particularly of fluid flows, is also given.

- *Chapter 5* presents a review of the theoretical and practical flow control approaches in the literature, with a focus on those applied on wall-bounded flows of the active and passive type. A detailed presentation of active open- and closed-loop methods is given, where the latter are the most relevant to the current work. Existing actuator and sensing technologies are briefly reported.

- *Chapter 6* introduces linear and non-linear model predictive control, in addition to the modifications made to the generalized predictive control algorithm to obtain compatibility with the current problem, and the identified OSA and MSA predictors. Simulations of the implemented MPC strategy are given for both the control of the pressure coefficient fluctuations, C_p, using a SISO approach and the MISO control of the velocity magnitude fluctuations, $|V|$. The simulations of both systems are performed through a noise-free, measurement noise, and measurement noise with load disturbance case.

- *Chapter 7* introduces the frequency properties of non-linear systems, in addition to the concept and methods to compute the GFRF's and OFRF's. An analysis of four different systems relating velocity magnitude from two upstream points with two downstream locations, in addition to the interaction of the two upstream nodes is performed using these tools. The GFRF's are used to see the contribution that the different model orders have on the output frequency spectrum. The OFRF's provide a more

detailed insight into the contribution of individual frequencies on the output response.

- *Chapter 8* draws the general conclusions of the current thesis in addition to a discussion of issues encountered within the disciplines involved in this work. In addition, possible areas for improvement are presented with recommendations for future work.

CHAPTER 2

Overview of the theory of fluids and computational fluid dynamics

2.1 Introduction

In order to control the behaviour of a fluid using a model-based control approach, it is of the upmost importance to obtain an accurate, reliable and robust model of the different phenomena which constitute a flowing fluid (Kim, 2003; Scott Collis, Joslin, Seifert, & Theofilis, 2004). Since it is very difficult, and in some cases impossible, to carry out repeatable experiments to obtain data or validate schemes, simulations of the scenarios of interest are often performed to enable understanding of what goes on within the flow (John, 1995).

Nowadays, it is possible to carry out such simulations with great accuracy thanks to hundreds of years of studying flows (John, 1995), and the developments which have been made in this field (Canuto, Hussaini, Quarteroni, & Zang, 1988; John, 1995; Temam, 1977).

The study of fluid flows and the forces which act upon them, also known as fluid mechanics, is one of the oldest branches of physics and is nowadays considered a sub-branch of continuum mechanics (Frank, 2011; Nakayama, 1999). In turn, fluid mechanics is divided into hydrostatics and fluid dynamics, in which the former studies fluids at rest and the latter is focused on the forces of fluids in motion (Davidson, Kaneda, & Sreenivasan, 2013; Frank, 2011; Nakayama, 1999).

Since the equations that govern the flow of fluids are non-linear and highly complex, there are no general solutions and often even case specific ones are prohibitively expensive to derive and solve. It is because of this that techniques to obtain approximations to the solutions have been created. This practice has evolved into a branch of fluid dynamics, namely Computational Fluid Dynamics or CFD (Bewley, 2001; Canuto, Hussaini, Quarteroni, & Zang, 1988; John, 1995).

This project has been especially concerned with the dynamical study of the flow, where the forces acting upon the particles of the fluid, as well as the effects they have on the flow are considered. Furthermore, the impact of the fluid on its surroundings, and vice versa, is considered, to have a full picture of the motion of the flow inside of the studied domain.

A clear understanding of this theory was necessary to obtain the tools needed, in turn, to derive an accurate data-based model of the flow using simulations.

The chapter is divided as follows, Section 2.2 presents the general theory of fluid flows, with a description of the main concepts that are needed to derive the governing equations, and understand the behaviour of flows. Section 2.2.1 contains details of the derivation of the continuity equation and 2.2.3 shows the approach used to obtain the momentum equation.

Section §2.3 goes on to describe computational fluid dynamics, with an emphasis on the methods employed by the specialized packages used to obtain the simulations of flows in the two studied geometries of this project. Section 2.3.1 explains DNS and the ChannelFlow package, whereas Section 2.3.2 presents the LES method and Ansys-Fluent.

Section 2.4 contains a brief discussion on the presented theory and simulation approaches.

2.2 General theory of fluid mechanics and dynamics

A fluid is a state of matter which can be defined as being a substance that, in the presence of a shearing or tangential force, will deform continuously regardless of the magnitude of such a force and cannot return to its original state at any time (Frank, 2011; Nakayama, 1999).

In order to truly study the flow of a fluid, it would be necessary to describe the motion of all the particles that make it up. This is, of course, impossible to achieve, thus some considerations are made to simplify the analysis. The first is that the intermolecular cohesive forces are strong[1] and the second states that the molecular mean free path[2] must be less than one per-cent of some characteristic length in the flow (Frank, 2011; Nakayama, 1999).. Where the latter is a property of the domain in which the flow is found. If both of these conditions are met then the fluid can be considered as behaving as one continuous mass, such a model is referred to as a continuum (Frank, 2011; Nakayama, 1999).

A further simplification made to the analysis, is that it is carried out on an infinitesimal control volume in a fixed position in space (x, y, z), as seen in Figure 2.1. The fundamental physical properties are then applied to the fluid, and relationships between the different variables are sought at this position and within the control volume. This method is referred to as the Eulerian approach (Frank, 2011; Nakayama, 1999), and it results in the governing equations to be represented in conservation form[3], with a partial differential equation (PDE) structure.

[1] This is true for a number of gases and almost any liquid.

[2] Term that refers to the statistical average distance that molecules travel between collisions.

[3] Term commonly used in CFD literature to describe an equation derived when studying a fixed control volume, it is closely related to the numerical method that is used to discretize and solve the equation. This form is said to have a more apparent physical meaning and certain computational advantages for CFD applications when compared against the integral or non-conservational forms.

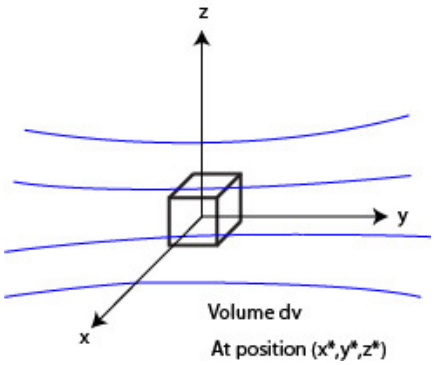

Figure 2.1 Schematic of an infinitesimal element of fluid in a fixed position (x, y, z) within the flow[4]

Following are definitions of fluid properties whose understanding is necessary for the derivation of the governing equations, also presented are concepts related to turbulence.

Additional and more detailed definitions of other useful concepts can be found in Appendix A.1 (Frank, 2011; Nakayama, 1999).

- Dynamic viscosity (μ): The result of the intermolecular forces which occur when a layer, or particles of fluid, slide by one another. This is partially responsible for the boundary layer and the no-slip condition.
- Velocity ($\boldsymbol{U}$): This is the rate of change of position of the particles within the control volume, often referred to as the vector $\boldsymbol{U}$ for three-dimensional Cartesian coordinates (x, y, z).
- Reynolds number (Re): Dimensionless ratio of inertial and viscous forces found within a fluid, often used to define whether a flow is laminar or turbulent. The most common way of calculating this value is using $R_e = \frac{\rho v L}{\mu}$.
- No-slip condition: Boundary condition which states that the velocity **U** of all fluid particles at the interface with a solid, is equal to the velocity V of such solid, that is $\mathbf{U} = \mathrm{V}$ and can be seen in Figure 2.2a for the case of stationary and moving walls.

[4] Image adapted from (Kim, 2003)

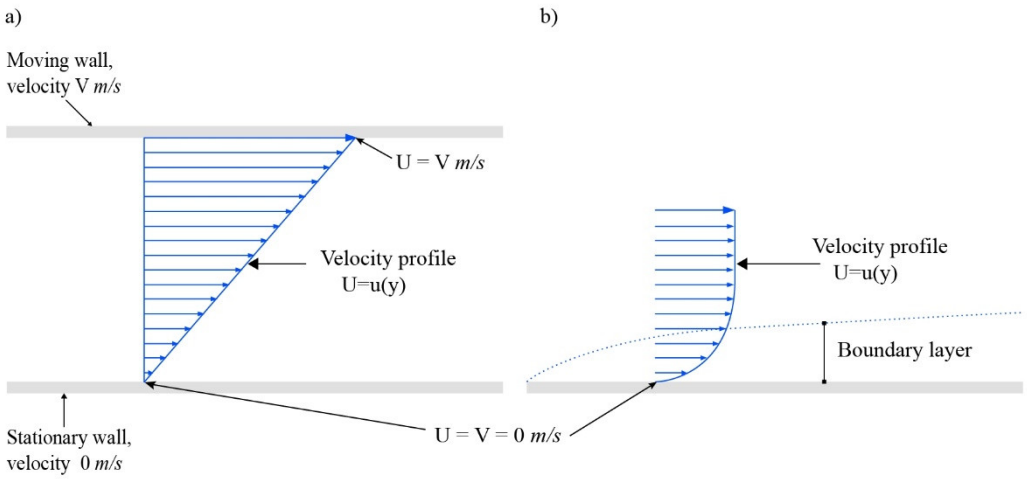

Figure 2.2 a) Schematic of the no-slip condition between a flow velocity profile and stationary/moving walls.[5] b) Schematic of the boundary layer with a corresponding velocity profile over a flat plate.

- Boundary layer: Small region near the vicinity of a fluid-solid interface where the viscosity effects are dominant or at least of the same magnitude as the inertial forces. This concept introduced by Prandtl in 1904 (Prandtl, 1905), states that due to the adhesion of the fluid to the surface of the solid, a no-slip condition is present and a thin layer is created. There exists a high velocity gradient going from stationary flow, to approximately 99% of the velocity magnitude given by the free stream or outer flow. Figure 2.2b is a simplified representation of the velocity profile of a boundary layer of a flow over a flat plate.
- Laminar flow: Regime characterized by parallel flow in which there is no mixing between adjacent layers (Frank, 2011; Nakayama, 1999). This regime is usually found in flows at low speeds and disturbances tend to decay over time.
- Turbulent flow: Is a flow regime characterized by chaotic changes in its state, with velocity and pressure fluctuations in space and time (Davidson et al., 2013; Frank, 2011; George, 2003). It presents rotational and irregular interaction of a wide range of temporal and spatial scales and is not fully understood to this day (George, 2003).
- Flow separation and reattachment: occurs when a flow over a surface encounters an adverse pressure gradient, which makes

[5] Image adapted from (Lee, K. H., Cortelezzi, Kim, & Speyer, 2001)

the boundary layer decelerate until the flow is reversed and is said to be detached or separated (Frank, 2011; Nakayama, 1999). It can also happen when an expansion of the geometry is present, resulting in a free shear layer which separates a recirculation zone from the free flow (Gautier & Aider, 2013; Huang & Kim, 2008; Le, Moin, & Kim, 1997). The point at which the free shear layer or line of zero velocity touches the wall again is the reattachment point (Gautier & Aider, 2013; Hervé, Sipp, Schmid, & Samuelides, 2012; Le, Moin, & Kim, 1997; Pouryoussefi, Mirzaei, & Hajipour, 2015). The latter is defined as being the point where the reversed and free flow meet, additionally, it is the location that the streamwise wall shear stress will change sign. These phenomena are depicted in Figure 2.3

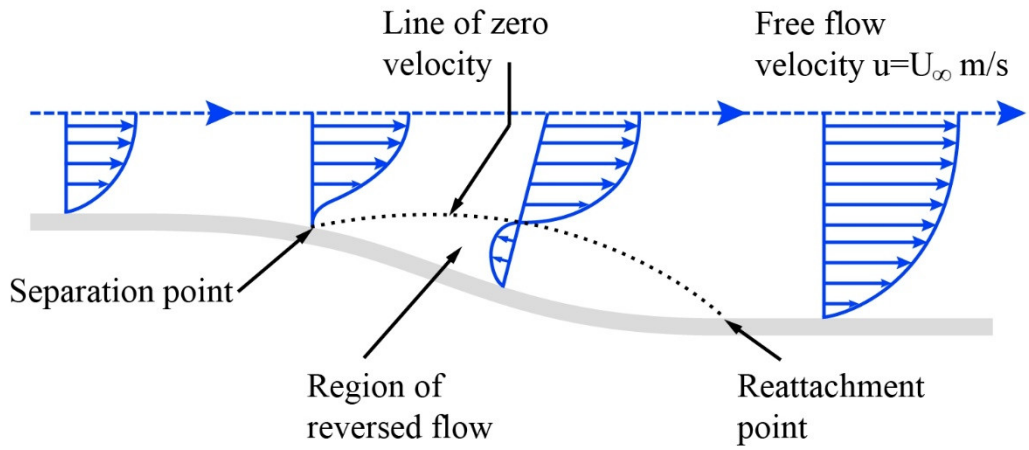

Figure 2.3 Schematic of flow velocity profiles with separation and reattachment over curved surface.

The complete description of a three-dimensional fluid flow depends on six variables u, v, w, P, ρ and temperature (Frank, 2011; Nakayama, 1999). However, during this project, the fluid considered is viscous, incompressible, and isothermal. These considerations mean that the density, ρ, and temperature, T, will be held constant, therefore only the four remaining variables will be used. A further effect of this simplification is that the energy equation is decoupled from the system of governing equations, and is not therefore required to solve for the remaining variables. Thus, only details for the continuity and momentum equations will be addressed.

2.2.1 Continuity equation

The continuity equation arises from the law of conservation of mass, which states that mass cannot be created nor destroyed (Frank, 2011; Nakayama, 1999). As shown in Figure 2.4 considering an infinitesimal volume, $\Delta\sigma$, within a surface, S that encloses a volume of fluid, σ, then, having an element of mass $m = \rho\Delta\sigma$, the following must hold:

$$\frac{D}{Dt}(\rho\Delta\sigma) = 0 \tag{2.1}$$

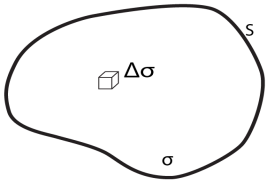

Figure 2.4. Schematic of a control volume σ, within surface S and infinitesimal volume element Δσ.[6]

If the entire mass enclosed in S is considered, equation (2.1) becomes:

$$\lim_{\Delta\sigma\to 0}\sum\left[\frac{1}{\rho}\frac{(\mathrm{D}\rho)}{\mathrm{D}t}\Delta\sigma + \frac{\mathrm{D}(\Delta\sigma)}{\mathrm{D}t}\right] = 0 \tag{2.2}$$

Equation (2.2) shows that an increase in density leads to a decrease in volume and vice versa. After some manipulations, which are beyond the scope of this description and can be found in books regarding fluid mechanics such as (Frank, 2011; Nakayama, 1999), each term in the brackets of equation (2.2) becomes respectively,

$$\iiint \frac{1}{\rho}\left[\frac{\delta\rho}{\delta t} + \boldsymbol{U}\cdot\nabla\rho\right]d\sigma \qquad \text{and} \qquad \iiint \nabla\cdot\boldsymbol{U}\,d\sigma$$

combining these two terms,

$$\iiint \frac{1}{\rho}\left[\frac{\delta\rho}{\delta t} + \nabla\cdot\rho\boldsymbol{U}\right]\mathrm{d}\sigma = 0$$

from which the equation of continuity can be obtained, namely:

$$\frac{\delta\rho}{\delta t} + \nabla\cdot(\rho\boldsymbol{U}) = 0 \tag{2.3}$$

This is the most general form of the continuity equation for fluids. As mentioned before, this project will deal with incompressible fluids, in which the density, ρ, is a constant, therefore with this consideration equation (2.3) reduces to:

$$\nabla\cdot\boldsymbol{U} = 0 \tag{2.4}$$

[6] Image adapted from (Lee, K. H., Cortelezzi, Kim, & Speyer, 2001)

Equation (2.4), also known as the continuity constraint, states that an incompressible flow must be divergence free. Which means that the time rate of change of the volume of an element in a fluid in motion, per unit volume, is equal to cero. That is, an element within an incompressible fluid cannot be deformed or vary in volume from one instant to the next with respect to its original volume.

2.2.2 Momentum equations

For the derivation of these equations a slightly different approach is taken, where the analysis will be done on an infinitesimal volume, $\Delta\sigma$, that is moving with the flow. In this way, the derivation of the equations is slightly clearer and faster (Frank, 2011; Nakayama, 1999).

The physical principle that is enforced to obtain this equation is that of Newton's second law, which states that the summation of forces acting upon a body must be equal to the mass times the acceleration of said body, or $\boldsymbol{F} = m\boldsymbol{a}$.

Since Newton's second law states a vector relation, it can be split into three scalar parts, therefore the remainder of the analysis will be carried out on the streamwise, or 'x' component only to illustrate the procedure and an identical approach can be used to derive the relations along the remaining directions.

The element under consideration will have two main types of forces acting upon it, mainly body and surface forces (Frank, 2011; Nakayama, 1999). The former are those which act on the volumetric mass of the element and at a distance such as gravitational, magnetic, or electric forces. The latter type, act as the name denotes, directly on the surface of the element, and are due to the pressure distribution by the rest of the fluid on the element or viscous effects that create stress distributions, of the shear and normal kind.

The body force per unit mass $\boldsymbol{f}$ will have a x direction component, $f_{b,x}$, acting on the fluid element, hence if the volume of the element is $dv = (dx\ dy\ dz)$, the body force will be denoted by:

$$f_{b,x} = \rho f_x (dx\ dy\ dz) \tag{2.5}$$

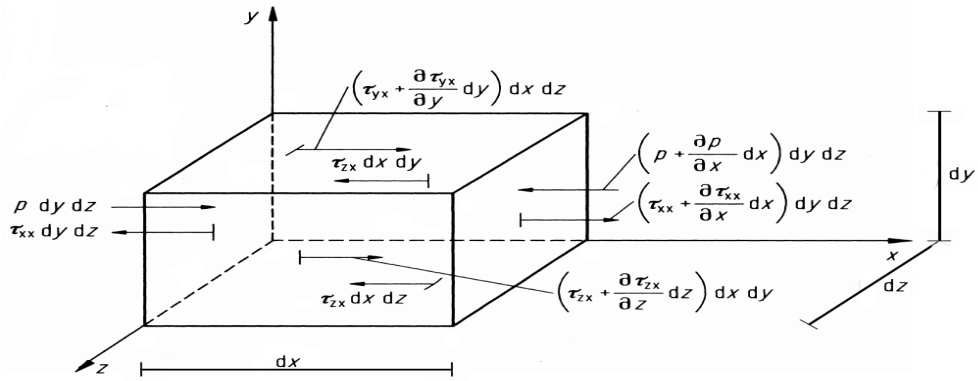

Figure 2.5. Schematic of an infinitesimal moving fluid element with the x direction surface forces and pressure components.[7]

Considering the fluid element in Figure 2.5, the surface forces in the x direction are shear stress, such as τ_{xy}, normal stress, as τ_{xx} and the pressure effects. The signs of the forces are given by existing conventions relating to the velocity components which cause the stresses, and the fact that pressure always points into the element upon which it acts.
Taking all the forces shown in the diagram and equation (2.5), the total force in the x direction F_x is

$$F_x = \left[-\frac{\delta p}{\delta x} + \frac{\delta \tau_{xx}}{\delta x} + \frac{\delta \tau_{yx}}{\delta y} + \frac{\delta \tau_{zx}}{\delta z}\right] dx\, dy\, dz + \rho f_x (dx\, dy\, dz) \tag{2.6}$$

The mass, m, of the element of volume dv is given by

$$m = \rho\, dv = \rho\, dx\, dy\, dz \tag{2.7}$$

The acceleration is then defined as the rate of change of u by the substantial derivative[8] as

$$a_x = \frac{Du}{Dt} \tag{2.8}$$

Therefore, substituting equation (2.6) through to (2.8) into Newton's second law we obtain

$$\left[-\frac{\delta p}{\delta x} + \frac{\delta \tau_{xx}}{\delta x} + \frac{\delta \tau_{yx}}{\delta y} + \frac{\delta \tau_{zx}}{\delta z}\right] dx\, dy\, dz + \rho f_x (dx\, dy\, dz) = (\rho\, dx\, dy\, dz)\frac{Du}{Dt} \tag{2.9}$$

Simplifying equation (2.9) the x component of the momentum equation is obtained. Following a similar approach it is possible to get the

[7] Image adapted from (Lee, C., Kim, Babcock, & Goodman, 1997)
[8] Defined as the time rate of change of velocity of the fluid element as it moves through space. In calculus it is known as the total differential.

remaining components to obtain the Navier-Stokes equations in non-conservation form, given by

$$\rho\frac{Du}{Dt}=\left[-\frac{\delta p}{\delta x}+\frac{\delta\tau_{xx}}{\delta x}+\frac{\delta\tau_{yx}}{\delta y}+\frac{\delta\tau_{zx}}{\delta z}\right]+\rho f_x$$
$$\rho\frac{Dv}{Dt}=\left[-\frac{\delta p}{\delta y}+\frac{\delta\tau_{xy}}{\delta x}+\frac{\delta\tau_{yy}}{\delta y}+\frac{\delta\tau_{zy}}{\delta z}\right]+\rho f_y$$
$$\rho\frac{Dw}{Dt}=\left[-\frac{\delta p}{\delta z}+\frac{\delta\tau_{xz}}{\delta x}+\frac{\delta\tau_{yz}}{\delta y}+\frac{\delta\tau_{zz}}{\delta z}\right]+\rho f_z$$

This set of equations has to be transformed into the conservation form in order for them to be able to be used in an easier way in numerical simulations. The details are omitted in this work but the interested reader may use (Frank, 2011; John, 1995; Nakayama, 1999).

$$\frac{\delta(\rho u)}{\delta t}+\nabla\cdot(\rho u\boldsymbol{U})=\left[-\frac{\delta \mathrm{p}}{\delta \mathrm{x}}+\frac{\delta\tau_{xx}}{\delta \mathrm{x}}+\frac{\delta\tau_{yx}}{\delta \mathrm{y}}+\frac{\delta\tau_{zx}}{\delta \mathrm{z}}\right]+\rho f_x$$
$$\frac{\delta(\rho v)}{\delta t}+\nabla\cdot(\rho v\boldsymbol{U})=\left[-\frac{\delta \mathrm{p}}{\delta \mathrm{y}}+\frac{\delta\tau_{xy}}{\delta \mathrm{x}}+\frac{\delta\tau_{yy}}{\delta \mathrm{y}}+\frac{\delta\tau_{zy}}{\delta \mathrm{z}}\right]+\rho f_y$$
$$\frac{\delta(\rho w)}{\delta t}+\nabla\cdot(\rho w\boldsymbol{U})=\left[-\frac{\delta \mathrm{p}}{\delta \mathrm{z}}+\frac{\delta\tau_{xz}}{\delta \mathrm{x}}+\frac{\delta\tau_{yz}}{\delta \mathrm{y}}+\frac{\delta\tau_{zz}}{\delta \mathrm{z}}\right]+\rho f_z \qquad (2.10)$$

The set of equations (2.10) needs to be further modified, since for Newtonian fluids there is a relationship between the time rate of strain or the velocity gradients and the shear stress in the fluid, these relationships are stated below

$$\tau_{xx}=\lambda(\nabla\cdot\boldsymbol{U})+2\mu\frac{\delta u}{\delta x},\qquad \tau_{yy}=\lambda(\nabla\cdot\boldsymbol{U})+2\mu\frac{\delta v}{\delta y},$$
$$\tau_{zz}=\lambda(\nabla\cdot\boldsymbol{U})+2\mu\frac{\delta w}{\delta z}$$
$$\tau_{xy}=\tau_{yx}=\mu\left[\frac{\delta v}{\delta x}+\frac{\delta u}{\delta y}\right],\qquad \tau_{xz}=\tau_{zx}=\mu\left[\frac{\delta u}{\delta z}+\frac{\delta w}{\delta x}\right],$$
$$\tau_{yz}=\tau_{zy}=\mu\left[\frac{\delta w}{\delta y}+\frac{\delta v}{\delta z}\right] \qquad (2.11)$$

Where μ is the molecular viscosity coefficient and λ is the second viscosity coefficient that, according to a hypothesis by Stokes, is given by $\lambda=-\frac{2}{3}\mu$ (Frank, 2011; Nakayama, 1999).

Therefore substituting the stresses from equation (2.11) into equation (2.10) and applying the incompressible flow assumption, together with the continuity constraint, equation (2.3), makes the complete incompressible Navier-Stokes equations in conservation form.

This is a closed set of equations which can be solved numerically for the velocity and pressure components (Frank, 2011; Nakayama, 1999).

$$\rho\left(\frac{\delta u}{\delta t}+u\frac{\delta u}{\delta x}+v\frac{\delta u}{\delta y}+w\frac{\delta u}{\delta z}\right)=-\frac{\delta \mathrm{p}}{\delta \mathrm{x}}+\mu\left(\frac{\delta^2 u}{\delta x^2}+v\frac{\delta^2 u}{\delta y^2}+w\frac{\delta^2 u}{\delta z^2}\right)+\rho f_x$$

$$\rho\left(\frac{\delta v}{\delta t}+u\frac{\delta v}{\delta x}+v\frac{\delta v}{\delta y}+w\frac{\delta v}{\delta z}\right)=-\frac{\delta \mathrm{p}}{\delta \mathrm{y}}+\mu\left(\frac{\delta^2 v}{\delta x^2}+v\frac{\delta^2 v}{\delta y^2}+w\frac{\delta^2 v}{\delta z^2}\right)+\rho f_y$$

$$\rho\left(\frac{\delta w}{\delta t}+u\frac{\delta w}{\delta x}+v\frac{\delta w}{\delta y}+w\frac{\delta w}{\delta z}\right)=-\frac{\delta \mathrm{p}}{\delta \mathrm{z}}+\mu\left(\frac{\delta^2 w}{\delta x^2}+v\frac{\delta^2 w}{\delta y^2}+w\frac{\delta^2 w}{\delta z^2}\right)+\rho f_z$$

These equations in vector notation can be written as

$$\rho\left(\frac{\delta \mathbf{U}}{\delta \mathrm{t}}+\boldsymbol{U}\cdot\nabla\boldsymbol{U}\right)=-\nabla\boldsymbol{p}+\mu\nabla^2\boldsymbol{U}+\rho\boldsymbol{f} \tag{2.12}$$

Where variables in bold are vector valued and the operator ∇^2 is the Laplacian of the velocity, defined as $\nabla^2 := \mathrm{i}\frac{\delta^2}{\delta \mathrm{x}^2}+\mathrm{j}\frac{\delta^2}{\delta \mathrm{y}^2}+\mathrm{k}\frac{\delta^2}{\delta \mathrm{z}^2}$.

These equations describe both the compressible and incompressible flow and together with the appropriate continuity constrain are a coupled system of non-linear equations that to this day, do not have a closed-form solution; in the case of the incompressible flow, they are a self-contained set of PDE's (Temam, 1977).

2.3 Computational fluid dynamics

This section provides an overview of the methods employed by the CFD packages, to solve the governing equations for the cases studied. This is known as computational fluid dynamics (CFD), and is defined as a technique which uses numerical methods together with computational tools to solve problems from fluid mechanics and dynamics, since they cannot be readily solved analytically (Frank, 2011; John, 1995).

There are several CFD methods, each with strong points and weaknesses. The desired application defines the elements that the CFD method should include. That is depending on the accuracy required, or memory limitations for example, one has to choose an appropriate way to simulate the flow.

Even though there are several schemes, most of them have the following stages (Canuto, Hussaini, Quarteroni, & Zang, 1988; John, 1995):

- Pre-processing: stage where the type of flow, PDE model to be used, domain and other characteristics or requirements of the problem to be solved are established.
- Discretization: stage where the physical and temporal domain of the simulations are transformed into discrete meshes, over which the numerical methods are applied to solve the equations. Methods for this include Finite Volume (FVM), Finite Element (FEM) or Spectral Element (SEM) for spatial discretization and Finite Differencing (FDM) for temporal discretization.
- Iterative solver: stage where the calculations take place and requires the most time and computational resources. The time to obtain a solution depends on the accuracy required, the convergence criteria, size of the problem, as well as the methods chosen during the previous stages.
- Post-processing: stage that involves performing final manipulations on the computed flow to extract the required information, in many cases it includes visualizing the data and validation with benchmark cases or experimental results.

For the development of this project dedicated CFD packages were used to simulate flow in two scenarios, as described in detail in Chapter 3. In the current chapter the discussion will be limited to an overview of the scenario studied using each package and a description of the algorithms employed in solving the relevant equations.

2.3.1 The ChannelFlow package and channel flow

The first case that has been studied is that of channel flow. This is rectangular flow in a wall bounded domain, driven by the movement of the boundaries or the presence of a pressure gradient (Heins, Jones, & Sharma, 2016; Kim, Moin, & Moser, 1987; Moser, Kim, & Mansour, 1999).

The simulations regarding this case were obtained using direct numerical simulation (DNS) (John, 1995) of the full non-linear incompressible Navier-Stokes equations in a CFD package named ChannelFlow (Gibson, 2012). DNS methods resolve all the time and

length scales of the Navier-Stokes equations (John, 1995), and for practical applications are usually too computationally expensive. However, in this particular case given the periodicity of the domain and simple geometry it can be readily applied (Choi, Moin, & Kim, 1993; Gibson, Halcrow, & Cvitanović, 2008).

This package integrates the Navier-Stokes equations within a domain that is periodic in spanwise and streamwise directions, and follows the algorithm set by Canuto (Canuto, Hussaini, Quarteroni, & Zang, 1988) to solve the equations. The software uses spectral discretization in spatial directions and finite differencing in time, considering primitive variables which are velocity and pressure.

ChannelFlow is designed to be a series of classes that handle a different part of the mathematical algorithm in a separate manner, such as carrying out Fourier and Chebyshev transforms to discretize the domain, time marching the equations, and solving them throughout the simulation domain.

Defining a rectangular domain Ω, as $\Omega \triangleq L_x\mathbb{M} \times [a, b] \times L_z\mathbb{M}$ where $\mathbb{M}$ is the unit interval in the periodic directions and L_x, [a, b], L_z indicate the size of the domain in the streamwise, wall-normal and spanwise direction respectively and N_x, N_y, N_z represent the number of grid-points in each direction as shown in Figure 2.6.

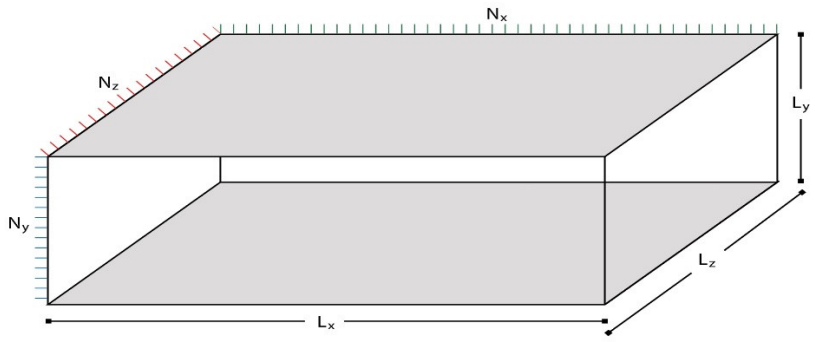

Figure 2.6. Schematic of physical domain Ω used in ChannelFlow, with dimensions and discretized grid-point labels.

There are rigid walls at y = a and y = b where no-slip boundary conditions give $\boldsymbol{u}_{Tot} = 0$[9], and periodic boundary conditions are considered in the x and z direction, so that:

$$\boldsymbol{u}_{\mathrm{Tot}}(x + L_x, y, z, t) = \boldsymbol{u}_{\mathrm{Tot}}(L_x, y, z, t),$$

$$\boldsymbol{u}_{\mathrm{Tot}}(x, y, z + L_z, t) = \boldsymbol{u}_{\mathrm{Tot}}(x, y, z + L_z, t)$$

The flow in Ω is governed by the incompressible Navier-Stokes equations, repeated here for convenience

$$\frac{\partial \boldsymbol{u}_{\mathrm{Tot}}}{\partial \mathrm{t}} + \boldsymbol{u}_{\mathrm{Tot}} \cdot \nabla \boldsymbol{u}_{\mathrm{Tot}} = -\nabla p_{\mathrm{Tot}} + \nu \nabla^2 \boldsymbol{u}_{\mathrm{Tot}}$$

$$\nabla \cdot \boldsymbol{u}_{\mathrm{Tot}} = 0 \tag{2.13}$$

Here the body forces are neglected and the coefficient ν is the kinematic viscosity defined as $\nu = \frac{\mu}{\rho}$, however note that the density has been considered as unit.

The total velocity and pressure terms are broken into a constant and a fluctuating element as:

$$\mathbf{u_{Tot}}(\boldsymbol{x}, t) = \boldsymbol{U}(y) e_x + \boldsymbol{u}(\boldsymbol{x}, t) \tag{2.14}$$

$$p_{\mathrm{Tot}}(\boldsymbol{x}, t) = \prod\nolimits_x (t)\, x + p(\boldsymbol{x}, t) \tag{2.15}$$

$$\nabla p_{\mathrm{Tot}}(\boldsymbol{x}, t) = \prod\nolimits_x \boldsymbol{e}_x + \nabla p\,(\boldsymbol{x}, t) \tag{2.16}$$

In equation (2.14), the first term on the right-hand side is the base velocity and the second term the fluctuating velocity. Similarly the total pressure is decomposed into a linear-in-x term and a periodic fluctuating pressure. The gradient of equation (2.15) is the division of a spatially constant base pressure gradient and a fluctuating pressure gradient.

Applying equation (2.14) and (2.16) into the momentum equation (2.13) gives

$$\frac{\partial \boldsymbol{u}}{\partial t} + \nabla p = \nu \nabla^2 \boldsymbol{u} - \boldsymbol{u}_{\mathrm{Tot}} \cdot \nabla \boldsymbol{u}_{\mathrm{Tot}} + \left[\nu \frac{\delta^2 \mathbf{U}}{\delta \mathrm{y}^2} - \prod\nolimits_x \right] \boldsymbol{e}_x \tag{2.17}$$

[9] Where $\boldsymbol{u}_{\mathrm{Tot}} = \boldsymbol{U} = u + v + w$ represents the total velocity, the notation has been changed to make clear the derivation of further details.

The non-linear term $\boldsymbol{u}_{\mathrm{Tot}} \cdot \nabla \boldsymbol{u}_{\mathrm{Tot}}$ is then expanded and equation (2.17) becomes

$$\frac{\partial \boldsymbol{u}}{\partial t} + \nabla\left[\mathrm{p} + \frac{1}{2}\boldsymbol{u}\cdot\boldsymbol{u}\right] = \nu\nabla^2\boldsymbol{u} - [(\nabla\times\boldsymbol{u})\times\boldsymbol{u} + \boldsymbol{U}\frac{\delta\boldsymbol{u}}{\delta x} + v\frac{\delta \boldsymbol{U}}{\delta y}\mathbf{e}_{\mathrm{x}}] + \left[\nu\frac{\delta^2\boldsymbol{U}}{\delta y^2} - \prod_x\right]\boldsymbol{e}_x \tag{2.18}$$

Defining the linear and non-linear term as

$$\boldsymbol{Lu} = \nu\nabla^2\boldsymbol{u} \text{ and } \boldsymbol{N}(\boldsymbol{u}) = (\nabla\times\boldsymbol{u})\times\boldsymbol{u} + \mathbf{U}\frac{\delta\boldsymbol{u}}{\delta x} + \mathrm{v}\frac{\delta\boldsymbol{U}}{\delta y}\mathbf{e}_x,$$

and introducing

$$q = p + \tfrac{1}{2}\boldsymbol{u}\cdot\boldsymbol{u} \text{ and } \boldsymbol{C} = \left[\nu\tfrac{\delta^2\boldsymbol{U}}{\delta y^2} - \prod_x\right]\boldsymbol{e}_x,$$

equation (2.18) becomes

$$\frac{\partial\boldsymbol{u}}{\partial t} + \nabla q = \boldsymbol{Lu} - \boldsymbol{N}(\boldsymbol{u}) + \boldsymbol{C} \tag{2.19}$$

This equation is then Fourier transformed and a truncation is done at a later stage. The definition of the continuous transform for a function $f(x,z) = u_0(x,z)$ of two variables, is as follows:

$$\tilde{f}_{k_x,k_z} = \frac{1}{L_xL_z}\int_0^{L_x}\int_0^{L_z} f(x,z)e^{-2\pi i\left(\frac{k_xx}{L_x}+\frac{k_zz}{L_z}\right)}\,dx\,dz$$

The Fourier transform for the operators in equation (2.19) such as the gradient, Laplacian and $\boldsymbol{L}$ operator, are defined as:

$$\widetilde{\nabla}_{k_x,k_z} := 2\pi i\frac{k_x}{L_x}\boldsymbol{e}_x + \frac{\delta}{\delta y}\boldsymbol{e}_y + 2\pi i\frac{k_z}{L_z}\boldsymbol{e}_z$$

$$\widetilde{\nabla}^2_{k_x,k_z} := \frac{\delta^2}{\delta^2 y} - 4\pi^2\left(\frac{k_x^2}{L_x^2} + \frac{k_z^2}{L_z^2}\right)$$

$$\tilde{L}_{k_x,k_z} := \nu\widetilde{\nabla}^2_{k_x,k_z}$$

Therefore $\widetilde{\nabla q} = \widetilde{\nabla}\tilde{q}$ and $\widetilde{\boldsymbol{Lu}} = \tilde{\boldsymbol{L}}\tilde{\boldsymbol{u}}$ [10], note also that since $\boldsymbol{C}$ is spatially constant $\widetilde{\boldsymbol{C}} = \boldsymbol{C}\delta_{k_x0}\delta_{k_z0}$ and equation (2.19) becomes

$$\frac{\partial\tilde{\mathbf{u}}}{\partial t} + \widetilde{\nabla}\tilde{q} = \tilde{\boldsymbol{L}}\tilde{\boldsymbol{u}} - \widetilde{\boldsymbol{N}(\boldsymbol{u})} + \widetilde{\boldsymbol{C}} \tag{2.20}$$

ChannelFlow includes several time-stepping algorithms that allow for equation (2.20) to be integrated in time. The method which has been used

[10] Narrow tildes are used for continuous transforms and wide ones are for discrete transforms.

for the simulations considered in the project, is a third order Runge-Kutta scheme. This procedure treats the linear term implicitly and the non-linear term explicitly.

Details for this and the equations solving schemes shall not be further developed since they are methods that have been well established in their disciplines, for both the time marching and solution of PDE's. It is important to mention that the techniques for such methods are outlined in the Temporal Discretization chapter, section §4.3, and §7.3, of (Canuto, Hussaini, Quarteroni, & Zang, 1988).

In broad terms, a pressure correction and tau method is used to decompose the coupled equations that arise with the time-marching methods, into an array of one-dimensional Helmholtz equations. Following, an influence-matrix method is used to solve them for each time-step resulting in the values of the velocity components and the dependant pressure. The procedure is then repeated at each time step.

A final set of equations that are necessary to mention in this section, is that of the relation between the coordinates of grid-points $x_{n_x}, y_{n_y}, z_{n_z}$ and the grid-point indices n_x, n_y, n_z, to ensure that a clear way to obtain the precise source of data analysed is established.

Considering the total amount of N_x, N_y, N_z grid-points and the index of the grid-point being studied, these relations are:

$$x_{n_x} = \frac{n_x L_x}{N_x}, \qquad 0 \leq n_x < N_x \tag{2.21}$$

$$y_{n_y} = \frac{b+a}{2} + \frac{b-a}{2}\cos\left(\frac{n_y \pi}{N_y - 1}\right), \qquad 0 \leq n_y < N_y \tag{2.22}$$

$$x_{n_z} = \frac{n_z L_z}{N_z}, \qquad 0 \leq n_z < N_z \tag{2.23}$$

2.3.2 Ansys-Fluent and flow over a backward facing step

The case of flow over a backward facing step (BFS) is one that has also been studied in the past since the geometry remains simple to a degree (Driver & Jovic, 1994; Gautier & Aider, 2013; Hervé, Sipp, Schmid, & Samuelides, 2012; Le, Moin, & Kim, 1997; Neumann & Wengle, 2003). However, additional phenomena are present in comparison to a channel flow (Neumann & Wengle, 2003; Ruisi, Zare-Behtash, Kontis, & Erfani, 2016).

The presence of a sudden expansion, mainly the step, causes these new structures and events. The most important are the separation of the flow and boundary layer and their posterior reattachment (Driver & Jovic, 1994; Gautier & Aider, 2013; Neumann & Wengle, 2003).

A more detailed description can be found in Chapter 3. Simulations for this case were performed using the commercial software Ansys-Fluent (ANSYS Inc, 2016).

Briefly, the domain consists of an inlet of dimension $L_i = 15H$, which ends with a step where the flow expansion takes place of height H and an outlet of length $L_o = 30H$, it can be seen in Figure 2.7. In this case the lower wall is assumed rigid, therefore the no slip condition is present. The upper wall is sufficiently far away for the effects of the flow interacting with it can be neglected. This upper boundary is placed at a height $D_y = 6H$.

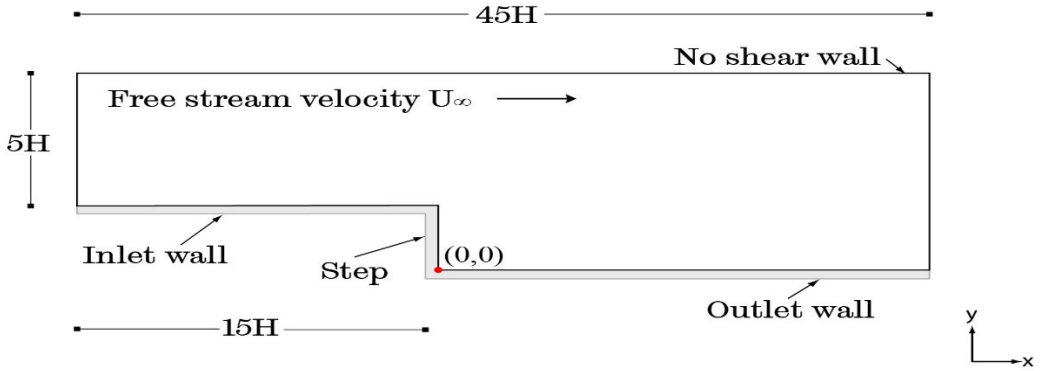

Figure 2.7 Schematic of flow over a BFS physical domain, with dimensions.

As it was mentioned previously, for more complicated flows or geometries, DNS methods cannot be used due to their computational burden, and so alternative methods have been created (Zheng, Zhang, &

Zhang, 2011). Of these, each has advantages and disadvantages and care must be taken when selecting a model and solution methods.

Since in the case being studied, there is an inhomogeneous domain in the wall normal direction, spectral discretization cannot be applied and so the mesh requirements to carry out a DNS become prohibitively expensive for the project. Considering that the computational burden of the DNS arises from the need to solve all the time and length scales of the flow, which include the highly complex turbulence phenomenon entirely, alternative methods often propose the use of averaging, filtering or linearizing the Navier-Stokes equations to lessen it (John, 1995). There are several algorithms which have been developed using these techniques to help decrease the difficulty associated with simulating flows in different domains, such as the famous Unsteady Reynolds averaged Navier-Stokes method (URANS) (Reynolds, 1894).

The use of methods such as URANS, which are the least computationally expensive would not provide accurate results due to the high adverse pressure gradient found after the expansion (Le, Moin, & Kim, 1997; Neumann & Wengle, 2003; Zheng, Zhang, & Zhang, 2011). Therefore, to ensure accurate and correct results the Large Eddy Simulation or LES method has been used. Where this is an expensive algorithm in terms of CPU and memory requirements but far less than DNS, and at the same time is capable of resolving the expansion with better accuracy than many other methods.

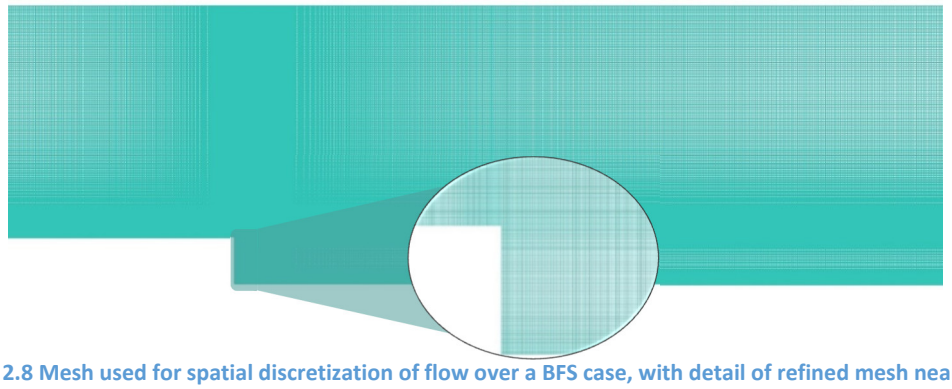

Figure 2.8 Mesh used for spatial discretization of flow over a BFS case, with detail of refined mesh near the step and lower wall.

However, a small time-step and high grid resolution is required, especially near the lower wall and step to ensure all relevant structures are properly resolved, as seen in

Figure 2.8. The reader is directed to (Canuto, Hussaini, Quarteroni, & Zang, 1988; Davidson, Kaneda, & Sreenivasan, 2013; John, 1995) for more details of alternative procedures.

The principle of the LES method, is to filter the Navier-Stokes equations either in Fourier or physical space, eliminating the need for any information whose time- or length-scale is smaller than the filter width (Smagorinsky, 1963). Thus, reducing the mesh and time-step requirements to carry out an accurate and numerically stable simulation.

A filtered variable as defined within Fluent is:

$$\overline{\phi}(x) = \int_D \phi(x')G(x,x')\,dx'$$

Where D is the fluid domain and G is the filter function that determines the cut-off time and/or length (ANSYS FLUENT, 2016).

Applying the definition for a filtered variable to the set of Navier-Stokes equations in the form of (2.3) and (2.12), one obtains:

$$\frac{\partial}{\partial t}(\rho\overline{u_i}) + \frac{\partial}{\partial x_j}(\rho\overline{u_i u_j}) = \frac{\partial}{\partial x_j}(\sigma_{ij}) - \frac{\partial \overline{p}}{\partial x_i} - \frac{\partial \tau_{ij}}{\partial x_j} \tag{2.24}$$

$$\frac{\partial \rho}{\partial t} + \frac{\partial}{\partial x_i}(\rho\overline{u_i}) = 0 \tag{2.25}$$

Where σ_{ij} is the stress tensor due to molecular viscosity and τ_{ij} is the subgrid-scale stress, defined by

$$\sigma_{ij} = \mu\left(\frac{\partial \overline{u_i}}{\partial x_j} + \frac{\partial \overline{u_j}}{\partial x_i}\right) - \frac{2}{3}\mu\frac{\partial \overline{u_l}}{\partial x_l}\delta_{ij}$$

and

$$\tau_{ij} = \rho\overline{u_i u_j} - \rho\overline{u_i}\,\overline{u_j}$$

The filtering operation which is applied in Fluent is performed by the discretization method itself, that is, finite volume method (FVM).

The finite volume method consists of splitting the domain into control volumes or cells, these can be rectangular, non-orthogonal and even unstructured grids, which is one of the main advantages of this method. The transport equations are then integrated over each of the control volumes, and as this is applying a set of conservation principles

over each of the small volumes, then a global conservation is also ensured.

The filter function $G(x, x')$ is then defined as:

$$G(x, x') = \begin{cases} \frac{1}{V}, & x' \in v \\ 0, & otherwise \end{cases}$$

And the filtered variable is then:

$$\overline{\phi}(x) = \frac{1}{V} \int_V \phi(x')\, dx', \quad x' \in v$$

Where V is the volume of the computational cell.

The settings chosen to carry out the simulations were, a pressure-based segregated solver, which decouples and solves the governing equations iteratively to obtain the solution variables $(u, v, w, p, k, \epsilon)$ at each time step, this method also employs a pressure-correction algorithm as the ChannelFlow package.

A second-order upwind scheme was used for the spatial discretization, and a second order implicit transient formulation for the temporal one.

The pressure-velocity coupling method used is the SIMPLE (Semi-Implicit Method for Pressure-Linked Equations). Although this method is best suited for simple or laminar flows, it has been used in this study since the LES formulation is being used with a small time step and fine mesh resolution. This helps to improve accuracy to avoid a greatly increased computational burden, resulting from other methods such as PISO (Pressure Implicit with Split Operator). Details for each of these methods are not presented here since they have been well stablished and the reader is directed to (ANSYS FLUENT, 2016) for further information of the implementation in FLUENT.

The boundary conditions defined for these simulations are as follows:

- In the streamwise direction velocity inlet and outflow conditions are imposed, where the former is used to set the flow velocity along the boundary, in addition to the scalar properties of the flow, and the latter define a zero-diffusion flux for flow variables with an overall mass balance correction.

- The lower inlet walls and step are given no-slip conditions, as in the case of the channel flow and the upper wall of the entire domain is defined with zero-shear-stress and $\boldsymbol{u} = \boldsymbol{U}_{\infty}$ to simulate an open channel as in (Driver & Jovic, 1994; Le, Moin, & Kim, 1997).

2.4 Discussion

This chapter has presented the relevant concepts of fluid dynamics required to understand the basic behaviour of fluid flows. Additionally, an overview of the way in which the Navier-Stokes equations are obtained was given, with details of the derivation of the continuity and momentum equations.

Further it briefly introduced the two scenarios that have been studied to generate data to perform the system identification, and posterior design of control schemes. These being the channel flow and flow over the backward facing step.

A more detailed description is given in the following chapter, together with the definition of the corresponding variables and parameters which define the simulations that were run using the methods presented here.

Additionally, the numerical methods which are selected to perform the simulations of the flows, in addition to other settings and boundary conditions are stated for each of the cases with some detail on the specific considerations taken by each of the CFD packages.

CHAPTER 3

Simulation and analysis of natural and actuated channel flow and flow over a backward facing step

3.1. Introduction

The ability of manipulating fluid flows to achieve a desired behaviour is key to improving the performance of many engineering systems (Kim, J. & Bewley, 2007; Kubo, Modi, Kotsubo, Hayashida, & Kato, 1996). The development of flow control strategies requires mathematical models that can accurately predict the behaviour of fluid flows in different geometrical configurations (Billings, 2013; Scott Collis, Joslin, Seifert, & Theofilis, 2004).

System identification strategies to obtain these models are based on data of the variables of interest, in the presence of a persistently exciting inputs (Billings, 2013; Coca & Billings, 2002a).

Given the difficulty and expense of carrying out experiments to be able to generate such data, this work has been based on numerical simulations of the governing equations. These simulations have been obtained from the full non-linear Navier-Stokes equations using advanced CFD packages to generate accurate and realistic simulations.

This chapter introduces the numerical simulations for two geometrical configurations commonly used to evaluate active flow control strategies, namely the three-dimensional channel flow and two-dimensional flow over the backward facing step (Bewley, 2001; Choi, H., Moin, & Kim, 1994; Huang & Kim, 2008; Kim, J., 2003).

The Chapter is organized as follows. Section 3.2.1 and 3.3.1 present a description of the channel flow, and flow over the BFS case, respectively. The reasoning behind the most important parameters and specifications needed to characterise the simulations is given, in addition to an analysis of the natural flow in both geometries in the time and frequency domain.

Using the study performed on the data of the natural flows, the procedure to design a persistently exciting input signal to be used for system identification techniques is specified in Section 3.2.2 and 3.3.2.

Finally, Section 3.4 contains a brief discussion on the properties of these simulations and some comments on their validity, accuracy, and bases for their use.

3.2. The channel flow

In the past, many scenarios of fluid flows have been studied, where experiments and simulations have often been designed as simplified forms of natural or man-made systems or applications of interest. Such as the introduction of symmetry planes and periodic boundary conditions, when studying flows that appear to have repeating behaviours (De Brederode & Bradshaw, 1978; Gibson, Halcrow, & Cvitanović, 2008). As it has been observed within the literature, the canonical scenario used to test from new CFD methods to the field of flow control is that of the channel flow (Lee & Moser, 2015; Ricco, Ottonelli, Hasegawa, & Quadrio, 2012).

Channel flow is characterized as being flow enclosed within a pipe or rectangular channel, where the length of such domain is much larger than the height and width (Lee & Moser, 2015; Mito & Kasagi, 1998; Moser, Kim, & Mansour, 1999; Ricco & Quadrio, 2008). This property allows for several simplifications to be done, as will be discussed later, while carrying out the simulations and analysis of the flow. The flow can be driven either by a pressure gradient along the domain, or the movement of one, or both enclosing walls. The particular geometry used in this work is sometimes referred to as *plane* channel flow, throughout the rest of the thesis, it will be referred to simply as the channel flow. Given the large number of flow control publications that feature it, (Biserni, Fichera, Guglielmino, Lorenzini, & Pagano, 2006; Kim, K., Beskok, & Jayasuriya, 2005), this geometrical configuration was one of two used to test the proposed strategy to develop, be means of system identification, non-linear reduced-order models for fluid-flow control applications.

3.2.1. Model definition and analysis of natural flow

The channel flow case represents a wall-bounded flow found between infinite parallel plates, where the width and length of the domain are larger than the height (Kim, J., 2003; Lee & Moser, 2015). This is important to define the computational boundary conditions, set as a no-slip condition on the lower and upper wall, and periodic boundaries for the streamwise and spanwise directions as detailed in Chapter 2.

The previous consideration is possible since, as stated, the domain is greatly larger in the stream- and span-wise directions than in the wall-normal one. Therefore, the flow will be able to become fully developed in the streamwise direction and be affected by local behaviour. The domain is also assumed to be large enough to accommodate all scales of the flow dynamics, which are also affected by the mesh resolution. This condition is ensured by the dimensions given to the domain prior to the discretization (Moser, Kim, & Mansour, 1999; Rozhdestvensky & Priymak, 1982).

This scenario has been studied due to the basic nature of the geometry as seen in Figure 3.1, which makes it simple, to a certain degree,

for disciplines such as fluid mechanics itself and to generate CFD simulations. In terms of control theory, however, it is still of a high complexity, being a system that distributed, non-linear and infinite-dimensional (Joshi, Speyer, & Kim, 1997; Kim, J., 2003; Kim, J. & Bewley, 2007).

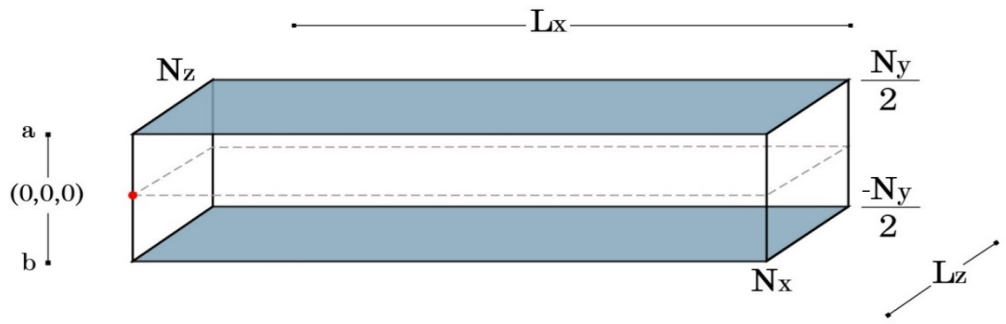

Figure 3.1. Schematic showing the channel flow domain, its physical dimensions and node positioning.

Due to the focus of this work and the simplicity of the geometry, it is possible to focus at this stage on the overall fluid flow properties and phenomena. Rather than being concerned with the generation of computational meshes capable of resolving the smallest time and length scales, or running high numbers of iterations per time-step to ensure the residuals are below highly demanding thresholds. While later chapters focus on how to alter and control them. Having said this, it should be noted that it has been fundamental to ensure that the simulations provide realistic flow data to carry out a feasible system identification and posterior control design and implementation.

As mentioned in §2.3, the first stages of the CFD method are the pre-processing and definition of the scenario, the posterior selection of the discretization methods and finally the implementation of the iterative solver. Since the ChannelFlow package has been developed specifically to study flow in this configuration, it was only necessary to define the geometrical and simulation parameters.

The full non-linear Navier-Stokes equations (2.13) are solved in the domain Ω, defined previously and shown in Figure 2.6, using spectral discretization for spatial dimensions and finite differencing for temporal ones. The way in which the equations are solved was chosen to be the 'rotational form' as mentioned in §2.3.1. Detailed descriptions on the time marching algorithms as well as other issues regarding the way

in which this is carried out can be found in section §4.3, and §7.3, of (Canuto, Hussaini, Quarteroni, & Zang, 1988).

Several simulations to test the performance, limitations, and capabilities of the ChannelFlow package were carried out. In these, variables such as Reynolds numbers, sampling times and grid resolution were tested in the ranges of 350 – 2500, 0.1 – 0.005 seconds and 80,000 – 1,250,000 nodes, respectively.

Once these tests were completed and the data analysed, parameters were chosen to generate adequate simulations which optimize performance and facilitate the posterior analysis of the data.

The final values employed in the CFD code to simulate the channel flow scenario were given the values shown in Table 3.1.

Table 3.1. Domain and fluid parameter definition for channel flow simulations.

Variable	Meaning	Value
N_x	Number of grid-points in x-direction	180 ($\Delta_x = 0.06$)
N_y	Number of grid-points in y direction	141 ($\Delta_y = 2.5\times10^{-4}$)
N_z	Number of grid-points in z direction	150 ($\Delta_z = 0.04$)
l_x	Domain size in x direction $L_x = 2 \cdot \pi \cdot l_x$	2
l_z	Domain size in z direction $L_z = 2 \cdot \pi \cdot l_z$	1.5
a	Upper wall height	1
b	Lower wall height	-1
Re_τ	Reynolds number	450
dt	Time-step size	0.01

These values represent the dimensions of the physical and computational domain, as well as the characteristics of the flow. They were chosen to provide a large enough amount of data to ensure accurate simulations, at the same time of maintaining a reasonable computational load.

The dimensionless size of the physical domain $L_y = a - b = 2$, $L_x = 1.5, L_z = 1.2$, is the minimum size of domain to sustain the scales of laminar and turbulent flow (Gibson, Halcrow, & Cvitanović, 2008). In addition, the number of nodes in this domain is again chosen to ensure the appearance of all the dynamics of interest which make up the flow. This is set to be at least the number of nodes necessary to solve the NS equations accurately according to (Canuto, Hussaini, Quarteroni, & Zang, 1988; Gibson, Halcrow, & Cvitanović, 2008).

It should be noted that the number of nodes may appear to be small in comparison with other CFD simulations, this is due to the method used for the spatial discretization. Spectral transforms provide exponential accuracy with a reduced number of nodes (Åkervik, Hœpffner, Ehrenstein, & Henningson, 2007; Canuto, Hussaini, Quarteroni, & Zang, 1988; Choi, H., Moin, & Kim, 1994; Choi, K. S., Debisschop, & Clayton, 1998).

Scripts were developed to extract and arrange the data from the generated binary files to a format which could be used in Matlab. As can be seen, the bulk of this project deals with the last of the CFD stages, mainly the post-processing and analysis of the data obtained.

Once a simulation that was considered suitable had been obtained, a detailed analysis of the velocity fluctuations was carried out in addition to Fourier analysis. The study in the time domain was performed to determine a suitable data sampling time for system identification. Fourier analysis was used to investigate the response spectrum of the system to determine the frequency range required to persistently excite the system.

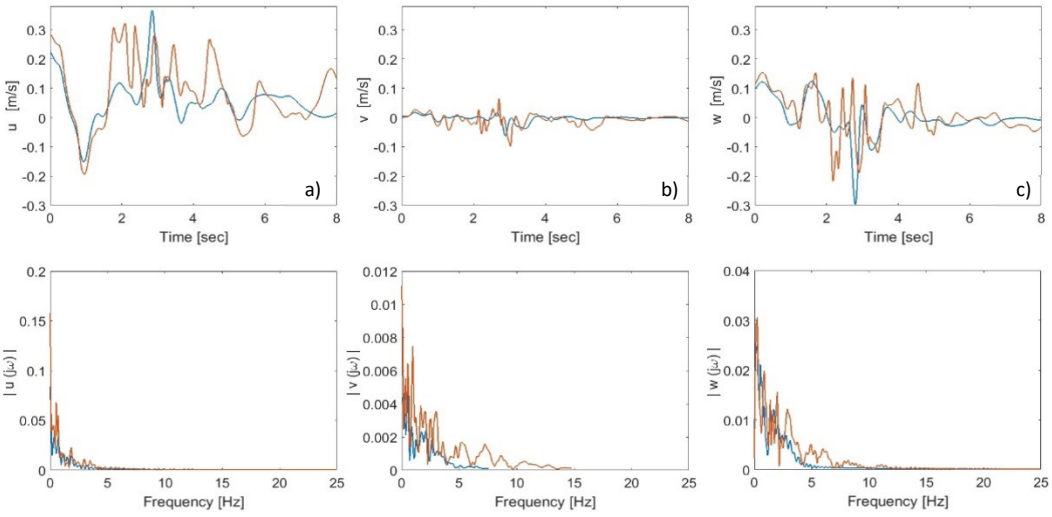

Figure 3.2. Fluctuation of velocity components and corresponding spectrum for Re=450 in blue and Re=1100 in blue at node [5, 4, 5]. a) Streamwise velocity b) Wall-normal velocity c) Spanwise velocity.

This analysis was performed over a subset of nodes to compare the frequency content of these measurements at different spatial locations, as fluid flows are highly time and space dependant (Canuto, Hussaini, Quarteroni, & Zang, 1988; Davidson, Kaneda, & Sreenivasan, 2013; Frank, 2011).

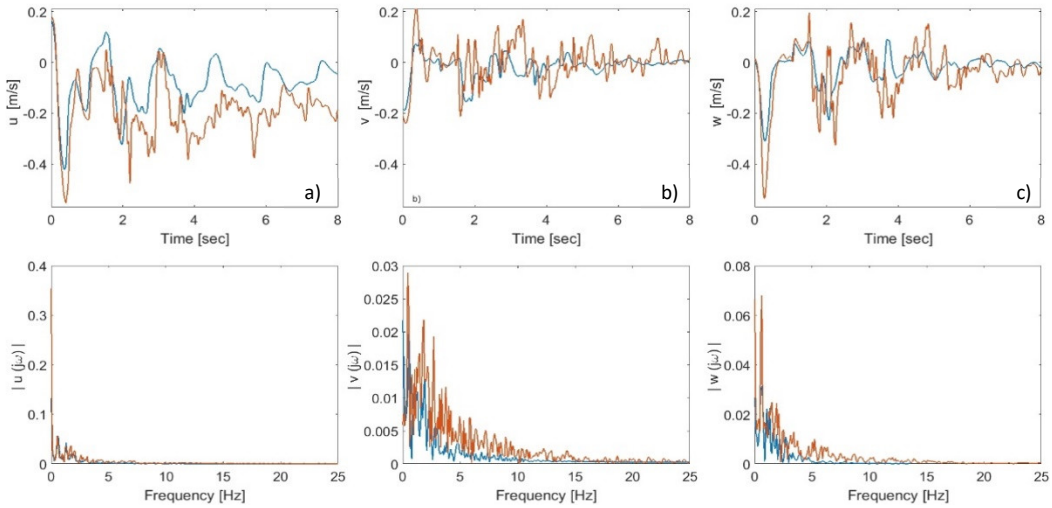

Figure 3.3. Fluctuation of velocity components and corresponding spectrum for Re=450 in blue and Re=1100 in blue at node [15, 14, 12]. a) Streamwise velocity b) Wall-normal velocity c) Spanwise velocity.

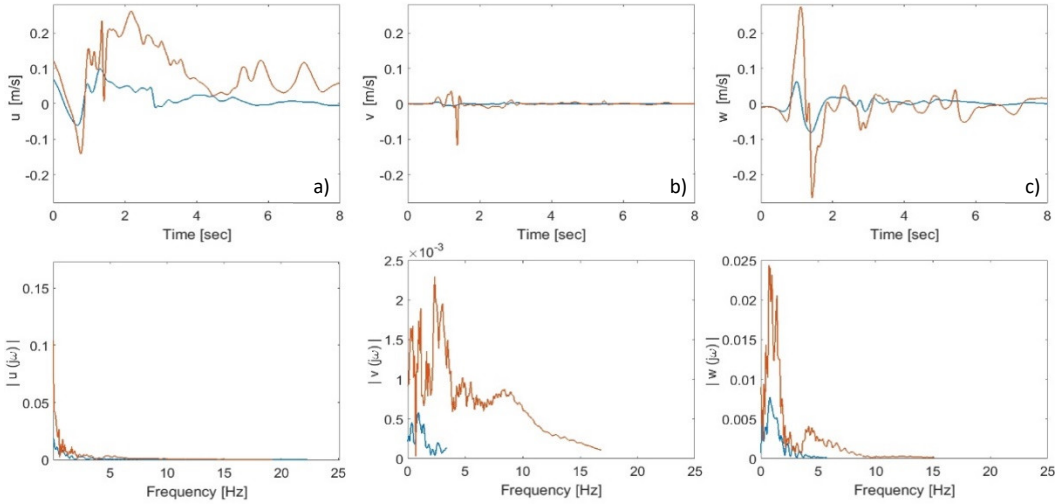

Figure 3.4. Fluctuation of velocity components and corresponding spectrum for Re=450 in blue and Re=1100 in blue at node [25, 25, 20]. a) Streamwise velocity b) Wall-normal velocity c) Spanwise velocity.

In Figure 3.2, Figure 3.3 and Figure 3.4, the time-series and spectrum of the three components of the flow velocity can be seen for different locations in the domain. Additional locations were analysed, however, only these are given to show that a similar pattern is visible across the entire domain. The spectrum has significant peaks at low frequencies, and behaves like a low-pass filter, with a cut-off frequency observable at around 5-10Hz, depending on the location.

Tests under different Reynolds numbers were then performed to see the effect that this fluid property has on the spectrum of the system. A similar analysis was carried out and as it can be seen in Figure 3.2 – Figure 3.4, the spectrum indeed varies with the Re number of the flow.

However, the differences are relatively small with an increase of around 5Hz of the cut-off frequency when comparing flow at double the Reynolds number.

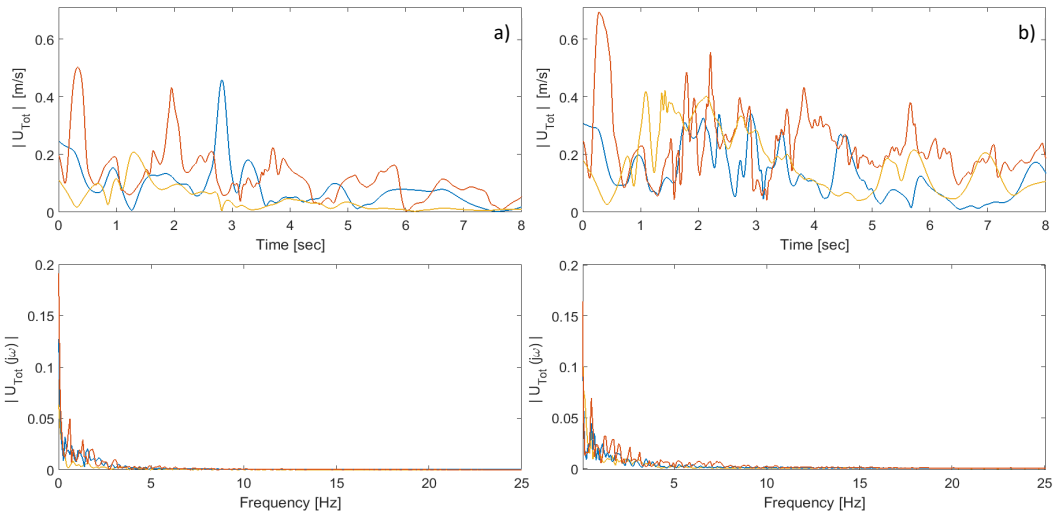

Figure 3.5. Fluctuation of velocity magnitude and corresponding spectrum at node [5, 4, 5] in blue, [15, 14, 12] in red and [25, 25, 20] in yellow. a) Re=450 b) Re=1100

The magnitude of the flow velocity was analysed in addition to the components, Figure 3.5 shows that the spectrum at these two Reynolds numbers is nearly identical.

Therefore, to ensure that the analysis and models identified in the next chapter remain valid over a larger operating range, the cut-off frequency for the persistently exciting input will be considered as 15Hz, which is considerably larger than that obtained in the tests under $Re = 450$.

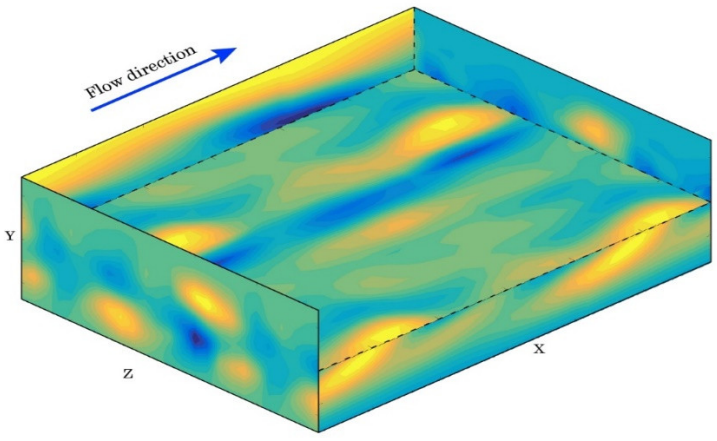

Figure 3.6. Snapshot of instantaneous velocity field showing the streamwise component of the velocity on the boundary planes. The upper half of the inner flow has been removed to allow for the visualization of the $y = 0$ plane.

To finalize the analysis of the un-manipulated flow, visualisations of the instantaneous velocity fields were obtained. A snapshot of an

instantaneous velocity field is shown in Figure 3.6. Here the streamwise component is shown on the inlet and outlet planes, in addition to the upper half of the $z = L_z$ plane and the lower half of the $z = 0$ plane. This was so that the same streamwise component of the $y = 0$ plane could be shown as well.

3.2.2. Design of persistently exciting input

The objective of analysing this system is to obtain a finite dimensional model, which can later be used for control design. Therefore, it was necessary to create a simulation which showed the behaviour of the flow before a known and carefully designed input signal (Billings, 2013; Coca, 2003; Coca & Billings, 2002).

This was possible once the analysis of the natural flow had been carried out, since enough knowledge of the system was obtained to create a tailored actuation signal. The generated signal could then be applied onto the flow to generate data suited for system identification schemes, so that the reduced-order-model, of the data fitting type, could be identified (Scott Collis, Joslin, Seifert, & Theofilis, 2004).

The actuation which is to be applied in the simulation is in the form of boundary suction and blowing, known as transpiration, and is implemented on the flow through a modified version of the ChannelFlow package (Heins, 2012).

This modified code allows for a non-zero wall-normal velocity to be imposed and modified versions of the discretization and solver methods are implemented, particularly on the homogeneous Dirichlet and Neumann boundary conditions which represent the no-slip condition at the walls.

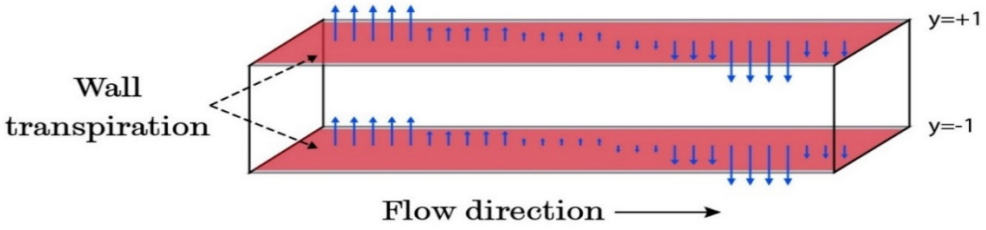

Figure 3.7. Schematic showing wall transpiration on channel flow domain.

A new flow field composed of the base flow and a velocity field with the same dimensions and resolution of the former, except in the wall normal direction is generated. In this direction, two sets grid-points are created on the top and bottom boundaries, essentially creating two planes at $ny = a$ and $ny = b$ as represented in Figure 3.7.

The code then advances the new flow field according to the modified algorithm, so that the output in each time-step is the base flow with an artificial blowing/suction action on the walls.

The designed signal is required to be persistently exciting in both frequency and magnitude content. To account for the former, a white noise signal was created and filtered to cover the system bandwidth. This signal had a higher cut-off frequency than that of the systems', to ensure that the validity of the models is maintained even with slight changes in the system.

In regards to the magnitude, a series of actuated simulations were performed with varying amplitudes. During these, it was noted that the ChannelFlow package has a limitation on the magnitude of the signal which can be applied as actuation. The numerical stability of the simulations was compromised when this limit was surpassed. This is likely to be because the original time-stepping algorithms, as well as the solvers and other operations, were not specifically chosen for this particular case and may not be the best suited.

After several tests, it was noted that per the mesh resolution and flow properties used in this study, the actuation signal should remain within the range of amplitude $\mathrm{M} = \pm 0.95$. Therefore, to avoid numerical issues during the simulations, the actuation has been truncated at the value $M = \pm 0.90$.

Considering this limitation, a new signal was generated and the spectrum analysed to ensure that it was adequate for the excitation of this system, and indeed persistently exciting to the configuration of channel flow. These requirements exist to ensure that all of the system dynamics are triggered, and at the same time, energy in the form of the actuation signal is only applied over the operating bandwidth (Billings, Chen, & Korenberg, 1989; Coca & Billings, 2002b).

Several attempts of the system identification of a single model to represent the entire system were made. It was noted that this approach would not provide positive results due to the large range of different dynamics that occur at different locations. Considering that a single degree of freedom would likely be insufficient to successfully manipulate the flow, it was decided that a higher number of inputs were needed to allow for a successful control to be designed and implemented. Therefore, simulations with six actuators applied at the walls were carried out using different signals designed following the procedure stated above.

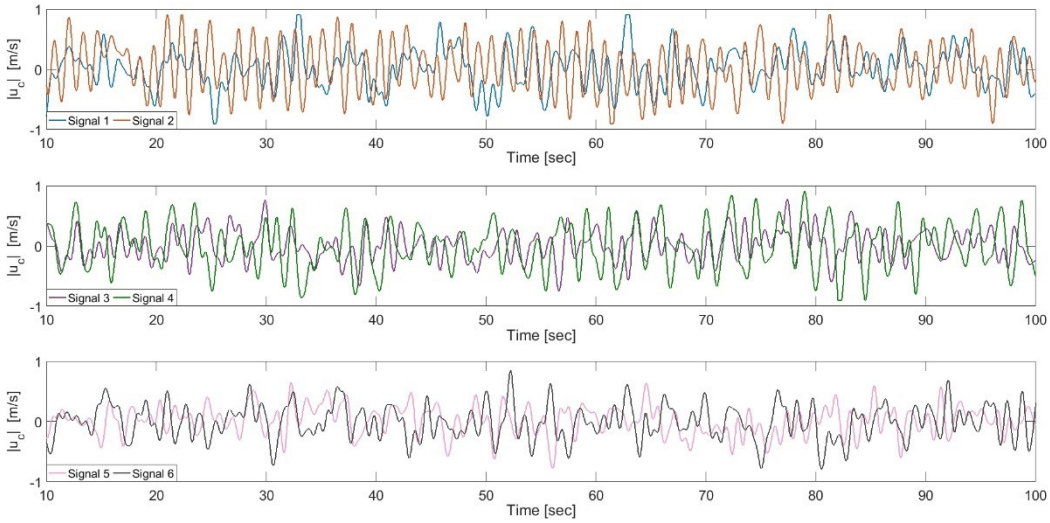

Figure 3.8. Tailored signals designed and implemented on the actuated channel flow simulations used for system identification.

The signals which were ultimately used with the system identification techniques can be seen in Figure 3.8. As mentioned, more details regarding the reasoning behind the additional actuators, specifically the spatial arrangement, are given in Chapter 4.

3.3. Flow over a backward facing step

The case of flow over a Backward Facing Step (BFS), is a variation of the geometry of channel flow as shown in Figure 3.9. Once again, the domain is wall bounded and considered to be of much greater length in the streamwise and spanwise directions, in comparison to the distance between the upper and lower boundaries. The variation of the geometry

however, is the addition of an expansion of the channel, giving way to a backward facing step of height (H).

This second scenario was chosen since it has gained attention in recent years; firstly, due to the geometry being simple enough to test new ideas in the presence of a flow with more complex phenomena. Secondly, to the development of new actuator and sensor technologies (Hervé, Sipp, Schmid, & Samuelides, 2012; Koide, Sasaki, Kameya, & Motosuke, 2015; Uruba, Jonáš, & Mazur, 2007; Xu et al., 2015). The latter will be discussed in Chapter 5.

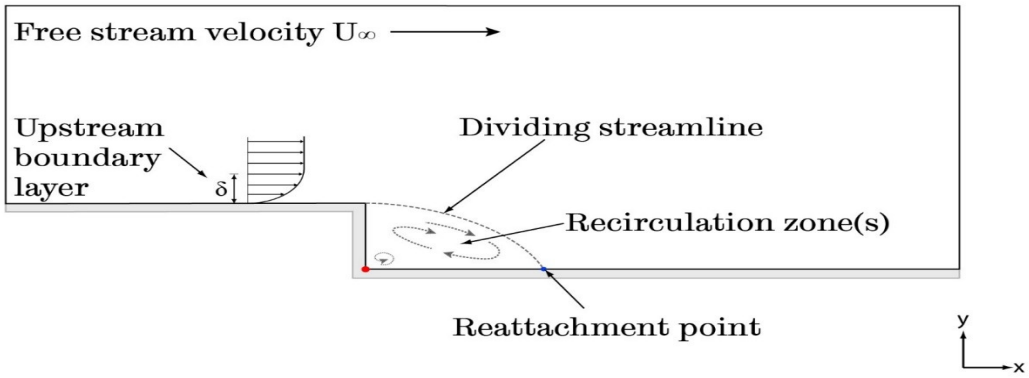

Figure 3.9 Schematic of the flow over a backward facing step, showing developed boundary layer upstream and recirculation/reattachment zone downstream of the step.

As explained in Chapter 2, there is a separation of the flow at the top corner of the step due to the adverse pressure gradient generated downstream. This leads to a recirculation *bubble* or *zone* immediately behind the step, and later a reattachment of the flow to the outlet wall as shown in Figure 3.9 (Driver & Jovic, 1994; Le, Moin, & Kim, 1997; Okada, Miyaji, Fujii *et al.*, 2010). It has to be noted that depending on the length of the domain downstream of the step as well as the Reynolds number, there may be more than one recirculation- and, in turn, reattachment-zones (Driver & Jovic, 1994; Le, Moin, & Kim, 1997). However, in this study only the *main* recirculation zone after the step will be considered.

This case has also been used as a benchmark to derive and test control schemes, usually focused on manipulating the reattachment of the flow. However, a feasible application of non-linear reduced order models, and active feedback control laws to predict and alter this position has not been found (Henning & King, 2007; Kim, J., Moin, &

Moser, 1987; Okada, Miyaji, Fujii *et al.*, 2010; Uruba, Jonáš, & Mazur, 2007). Details of the existing applications are given in Chapter 5.

3.3.1. Model definition and analysis of natural flow

Like the channel flow scenario, the backward facing step flow case was chosen due to the simplicity of the geometry and availability of literature. Considering that there is a richer content of dynamics in this configuration, and the fact that it can be considered as a simplified version of flows which present similar phenomena, such as flow over air-foils, the study of this is of interest for both system identification and control design and implementation purposes (Uruba, Jonáš, & Mazur, 2007; Xu, Gao, Ming *et al.*, 2015).

To achieve the latter objective, accurate and reliable models are needed. A similar procedure to that carried out when performing the channel flow simulations was followed. The first step is to generate adequate data, to analyse the natural flow and generate a persistently exciting input.

As mentioned in Chapter 2, the model which was used to simulate the governing equations was LES. This model requires a small time-step and fine mesh resolution to provide accurate results. The domain size and flow properties were defined according to that used in (Driver & Jovic, 1994; Le, Moin, & Kim, 1997). Le et al. presents data obtained from a DNS simulation, which was also validated using an experimental set-up with almost identical characteristics by Driver and Jovic.

Table 3.2 Dimensions of physical and computational domain

Location	Value [m]	Number of nodes	Minimum distance [m] ($\Delta_i \;\; i = x, y, z$)
Step (height - y)	0.0098	180	5.7×10^{-5}
Inlet wall (length - x)	0.1470	400	4.4×10^{-5}
Inlet (height - y)	0.0490	200	5.8×10^{-5}
Outlet wall (length - x)	0.2940	1275	3.6×10^{-5}
Domain width (length - z)	.0588	400	5.8×10^{-5}

The values used from their work in addition with the remainder of the parameters used in Fluent for the initial simulations are presented in

Table 3.2 and Table 3.3. All dimensions stated here are labelled according to Figure 2.7.

Table 3.3. Additional simulation parameters for un-manipulated flow over the BFS

Variable	Description	Value (Range tested)
T_s	Fixed sample time of simulations	$0.005\ sec$
U_∞	Free stream velocity.	$7.7\ [m/s]$
ρ	Fluid density.	$1.2039\ [kg/m\text{^}3\ ]$
μ	Dynamic viscosity	$1.5131\times10^{-5}\left[\frac{kg}{m\cdot sec}\right]$
Re	Reynolds number.	5000
Iterations	Minimum number of iterations per time-step.	40

Such values were set to be able to capture a large range of time and length scales while keeping in mind the time the simulations took to finish and amount of data generated, since this increases massively with mesh resolution.

Given that these simulations were carried out to identify a reduced order model and later design and implement a controller scheme, it was decided to make a simplification on the geometry. The geometry would be considered as two-dimensional, to focus on the design of a single SISO/MISO controller, and thus remove the issue of determining three-dimensional spatial positioning of the actuator. This two-dimensional flow assumption is possible since, as given in (De Brederode & Bradshaw, 1978), a flow maintains two-dimensionality regardless of the boundary layer thickness, as long as the aspect ratio between the step height and domain width is over 10. They showed experimentally that with this consideration, the side wall effects can be neglected.

However, since the LES method is designed to be applied on 3D scenario, additional considerations were made during the pre-processing stage to ensure that the simulation was as accurate as possible in this reduced configuration. Such considerations were related to the mesh resolution and initial conditions. Regarding the former, the element sizes were carefully selected to ensure that the most relevant structures could be resolved. Simulations using incremental refinement in certain areas were carried out to ensure that mesh dependency was eliminated.

On the topic of the initial conditions (IC's), it is well known that CFD simulations using most algorithms are sensitive to the imposed IC's, especially for time varying flows (Le, Moin, & Kim, 1997). Therefore, the following procedure was followed to ensure that the IC's used in this work were representative of a turbulent flow.

Firstly, a LES simulation of three-dimensional channel flow, with the same mesh resolution and dimensions as the inlet of the flow over the BFS was generated. This simulation was given no-slip wall boundary conditions in the wall-normal directions and velocity inlet / outflow in the streamwise directions. A symmetry boundary was imposed for the spanwise direction. The simulation was run using the time-step in Table 3.2 and allowed to run for 5000 time-steps to ensure that the flow was developed.

The velocity and pressure data obtained were used as inlet conditions for a simulation of three-dimensional flow over the BFS, again with the parameters stated in Table 3.2 and boundary conditions described in Chapter 2. This simulation was allowed to run for a further 5000 time-steps to allow for the flow to develop once again.

An instantaneous profile of all relevant variables was taken from the mid-plane, in the spanwise direction, of this three-dimensional domain. This was used as the initial condition for the two-dimensional simulations.

Finally, the 2D simulations was run for 10,000 time-steps to allow for the flow to recover and develop. This last instant was considered as the initial condition for later simulations. The case of natural flow was started from these conditions and flow statistics and data was extracted after 2000 time-steps. The time and frequency domain analysis of this flow was performed on this last data set.

This method was done to avoid the over-simplified scheme of generating a velocity field with random fluctuations, given that this option results in an excess of small-scale motions. The latter are unreal and deteriorate the performance of the LES methods (Kim, J., Moin, & Moser, 1987; Moser, Kim, & Mansour, 1999).

This procedure requires a set of computationally expensive simulations to obtain the initial conditions for the two-dimensional un-

manipulated flow. Therefore, tests with varying Reynolds were not carried out during this work. For the remainder of the analysis, all data has been obtained from simulations set to $Re = 5000$, to match the simulations and experiments of (Driver and Jovic 1994, Le, Moin et al. 1997).

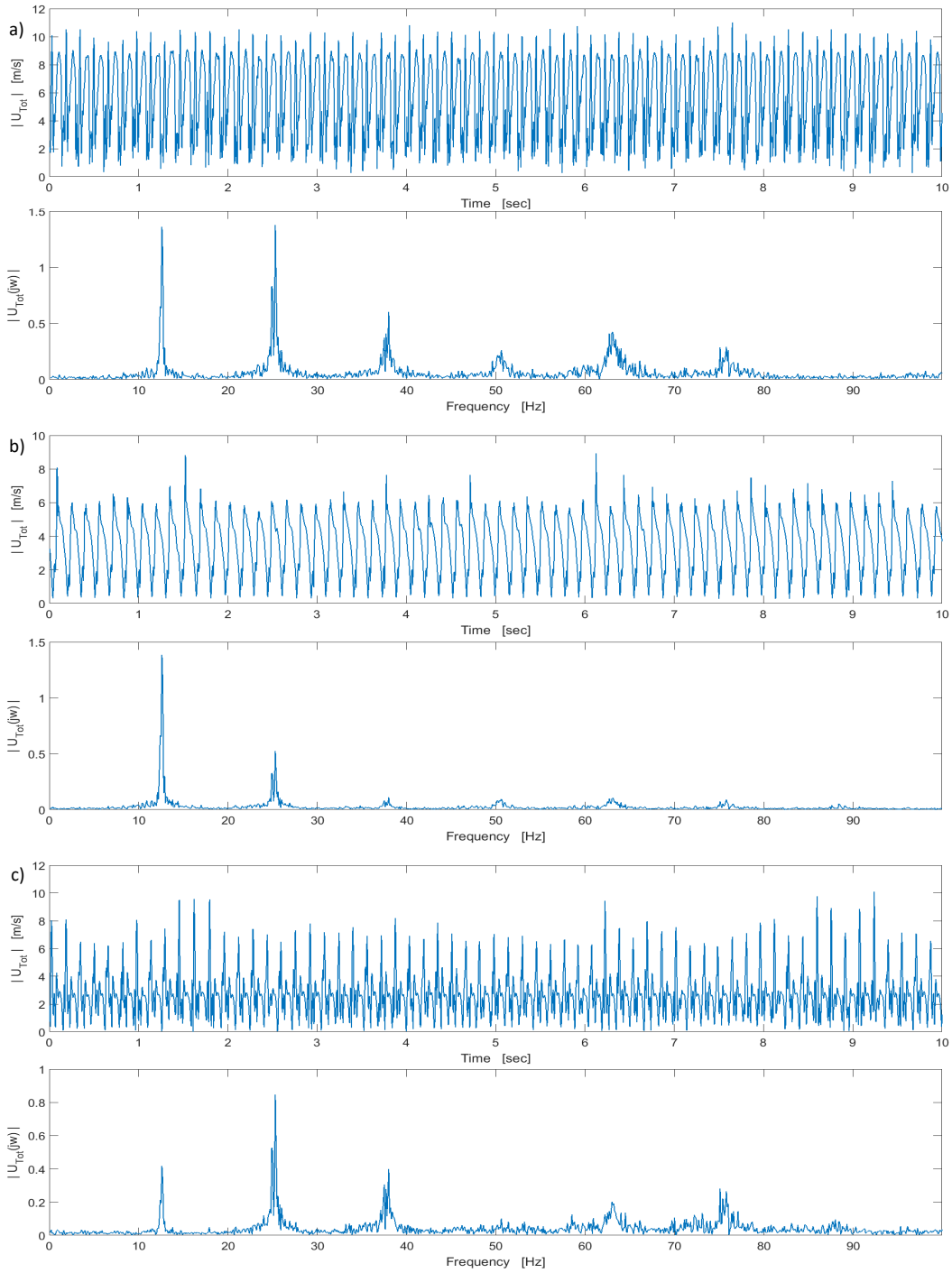

For caption please see next page

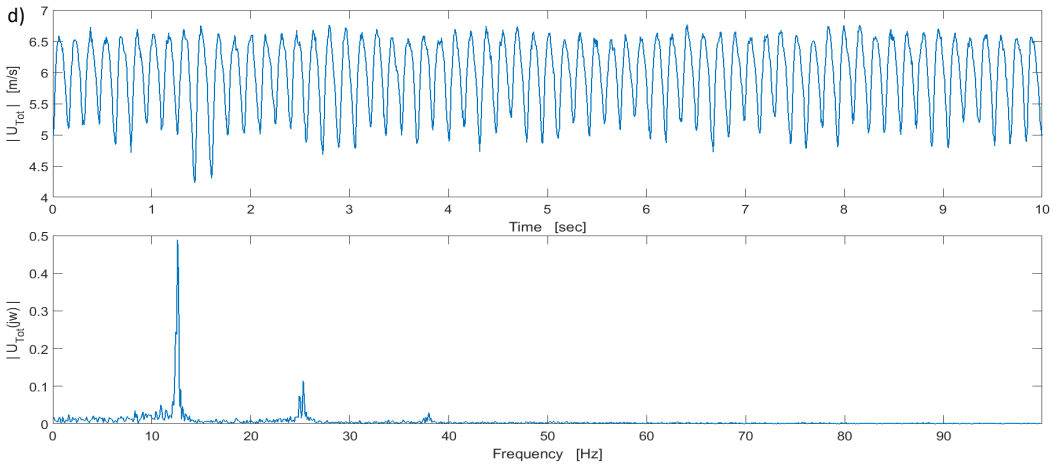

Figure 3.10. Time series and spectrum for velocity magnitude fluctuations at different spatial locations. a) Node at (H, 0.1H) b) Node at (4H, 0.1H) c) Node at (18H, 0.1H) and d) Node at (-1H, 0.1H)

Like with the channel flow data, an analysis of the velocity fluctuations at several points down- and up-stream of the step was carried out. Fourier analysis was performed on this data once more to determine the frequency range needed for inputs to be persistently exciting for this set-up.

Figure 3.10a), b), and c) show the time fluctuations and spectrum of the velocity magnitude at three spatial coordinates downstream of the step and Figure 3.10 d) at a single location upstream of the flow.

As it can be seen, the flow behaves like the channel flow case, where there are significant peaks in the lower frequencies such as 12, 25 Hz but are attenuated towards higher values.

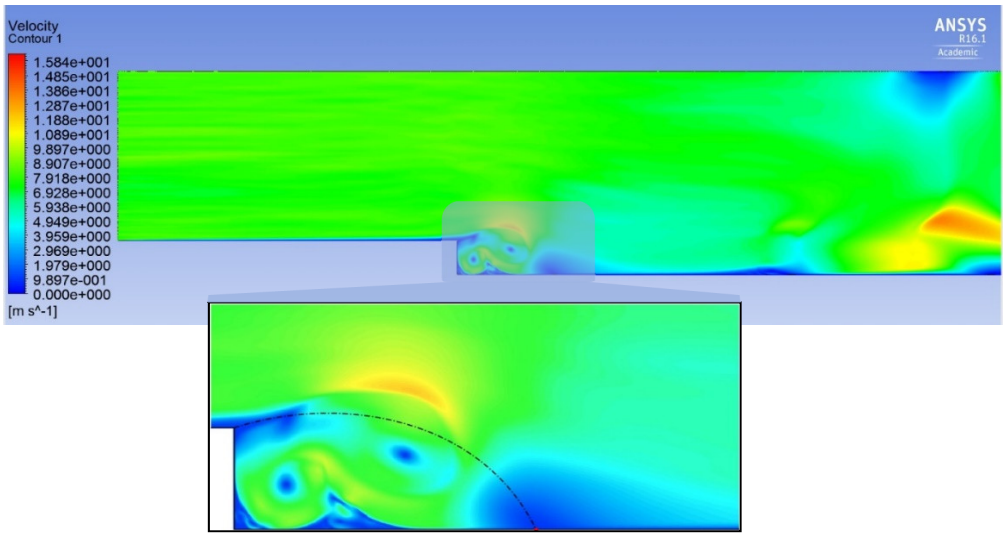

Figure 3.11. Snapshot of instantaneous velocity magnitude field of flow over the BFS. The recirculation zone is enclosed in the dotted line and the red dot is the location of the instantaneous reattachment point.

To conclude with the analysis of the un-manipulated flow a snapshot of the velocity field of the flow over the BFS domain is shown in Figure 3.11 with a close-up of the step area. The recirculation and approximate instantaneous reattachment point have been superimposed on the image. The latter is identified by analysing the streamwise component of the wall-shear stress at the outlet wall, and is the point where this stress changes sign, or the point of zero velocity. In the figure, it is the darkest point downstream of the recirculation zone.

3.3.2. Design of persistently exciting input and analysis of actuated flow

Using the results obtained from the frequency analysis, once more, a signal which is persistently exciting for the flow over the BFS was created. The process was the same as with the channel flow case, where a white-noise sequence was generated and filtered to have the required bandwidth to match that of the system.

As for the amplitude, the signal was applied onto the system with increasing magnitudes until a value at which the simulations become unstable was reached. This was determined to be when the solution became divergent, or if the residuals converged to a value greater than the tolerance of a solution considered correct after a few time-steps with 40 iterations per time-step (ANSYS FLUENT, 2016). The magnitude of the actuation signal was then adapted to be at the most $M = 30$ which is less than the limit identified, and thus ensures that the simulations are still accurate and reliable.

To apply the signals, a modified version of the mesh was used. This mesh had the inlet and step wall divided into several sections, which can be switched between a velocity inlet and a no-slip wall boundary condition. The relevant nodes were then prescribed to be equal to the generated signals at each time-step. Using this configuration three cases have been studied, a single actuator at the top of the step, and two / four actuators on the step wall.

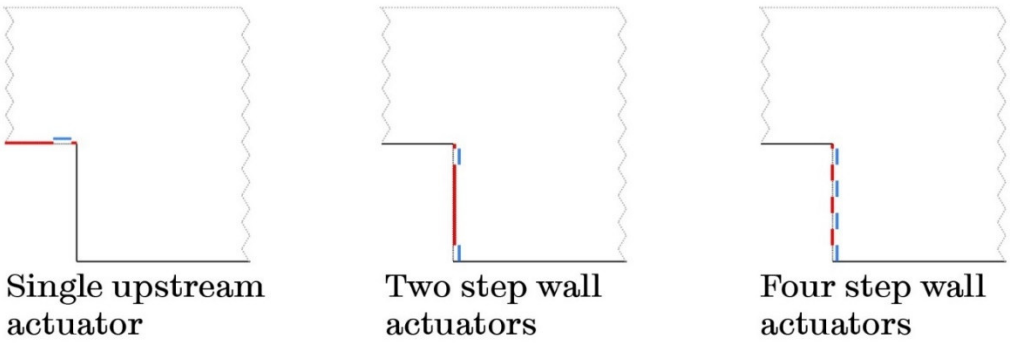

Figure 3.12. Actuator layouts for the three studied cases of manipulated flow over a BFS

This implementation can be seen in Figure 3.12 where the boundary zones given the velocity inlet boundary conditions are shown in blue and the sections which remain as no-slip walls are shown in red. The dimensions for the actuator sections were set to be in the range of previous experimental applications, where (Okada, Miyaji, Fujii *et al.*, 2010; Uruba, Jonáš, & Mazur, 2007; Xu, Gao, Ming *et al.*, 2015) have considered actuators which are between 3% and 15% of the step height. Hence, the actuator size has been set as 10% of H, that is, 9.8×10^{-4}m. More details on previous studies of the manipulated flow over the BFS will be given in Chapter 5.

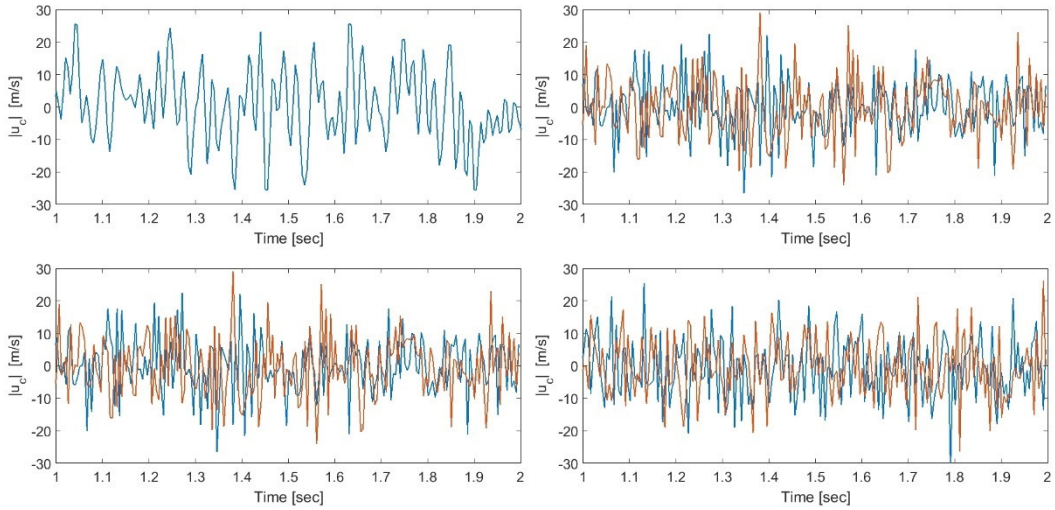

Figure 3.13. Tailored signals designed and implemented on the actuated flow over the BFS simulations used for system identification. Top left: One actuator upstream of the step. Top right: Two step wall actuators Bottom: Four step wall actuators, two per plot.

A portion of the signals created for each of the three actuation cases is shown in Figure 3.13.

Simulations were run with the signals and the parameters shown in Table 3.3 and the data extracted at predefined locations, as will be detailed in the next chapter.

3.4. Discussion

This chapter has presented the definition of the physical and computational domains used in the flow over the backward facing step and channel flow scenarios.

For the case of the channel flow, a simulation of natural flow was generated and the velocity fluctuations across several spatial positions analysed in the time and frequency domain. The spectrum of each of the components, and the magnitude of the velocity were studied in order to define the bandwidth of the system, to create a persistently exciting signal tailored for this case (Billings, 2013). To define the limits of the actuation signal it is necessary to define the device which will be used. In the current work, this was done by using the maximum magnitude possible considering the numerical limitations of the CFD package. Tests using signals of increasing magnitudes were carried out until a limit value at which the simulations remained stable was determined. The final actuation signal designed was therefore tailored to excite the full range of frequencies and magnitudes possible of this system.

A similar procedure was undertaken for the flow over a BFS, where again, all relevant parameters and settings for Fluent were defined and a simulation of the natural flow was obtained. Given that the simulations using the LES method require a high mesh resolution and small time-steps, it was decided to simplify the three-dimensional domain to a two-dimensional case (De Brederode & Bradshaw, 1978; Le, Moin, & Kim, 1997). Here some further considerations were made and a procedure followed to create accurate initial and inlet conditions in order to help reduce the effect of this simplification (Le, Moin, & Kim, 1997).

An analysis of the time velocity fluctuations and their spectrum was carried out to define the bandwidth of this flow. A signal was then generated which covers the relevant frequencies and applied with increasing magnitudes on a modified mesh. Three cases were studied,

using one, two and four actuators. Simulations were run until the solution became unstable due to the control action. Using this limit on magnitude, a final actuation signal was generated that is persistently exciting for this scenario and implemented into the simulations.

Regarding the accuracy and validity of the simulations, as with the use of any model or approximation, there exists a trade-off between accuracy and computational requirements. In the case of CFD the latter can grow massively with an increase in mesh resolution or a decrease of time-step. On the other hand, the gain in accuracy of the simulations is not as large, except when comparing very different methods such as DNS with RANS (John, 1995).

The values defined in this chapter, such as time-step and mesh resolution, are therefore chosen to provide data which is accurate and representative of the case being studied, but at the same time do not require as many computational resources with the selected numerical methods.

In order to verify this, several simulations were carried out to test for dependency on certain parameters such as the mesh resolution, until a value was found that ensured the convergence, to a certain threshold, of the variables of interest (John, 1995). For other parameters, however, a value had to be 'arbitrarily' chosen, to allow for a sufficient amount of dynamics to be captured but ensuring that these were still relevant.

An example of this is the simulation time-step, where it is possible to select decreasing values almost indefinitely, and a richer dynamic content will always be captured. However, many of the effects that will be seen with smaller values of T_s, are too fast for any real implementation of a controller, or may be impossible to measure in real flows with current and perhaps even future technology (Ho & Tai, 1998; Lofdahl & Gad-El-Hak, 1999a).

Therefore, it is necessary to stablish a limit where the data sampled is sufficient, in this work this was simplified since the purpose of the data generation was the use of system identification schemes. The latter require that consecutive data-points be correlated, something that may not be ensured with large time-steps, but with a degree of difference

between them, hence the sampling rate cannot be such that successive values are very similar (Billings, 2013; Lofdahl & Gad-El-Hak, 1999b).

Finally, the analysis and measurements used for the system identification and posterior control design were of the velocity fluctuations from the entire domain in the channel flow case, and of certain nodes in the flow over the BFS. This is something that would be hard to accomplish (Ho & Tai, 1998; Lofdahl & Gad-El-Hak, 1999a). However, as the objective of the current work is to study the flows and the capability that the schemes have in this application, it was decided to use these variables as they enhanced the performance. For a practical application, both the models and controllers obtained, will need to be modified to overcome this issue.

Variables such as the wall-shear stress would be better suited to be the controlled variables, since it can be readily measured using current technologies (Lofdahl & Gad-El-Hak, 1999a). As for the control input, the limitations in frequency and magnitude of the implemented microelectromechanical system (MEMS), to be used as the actuators, would need to be enforced in the control design stage (Ho & Tai, 1998; Lofdahl & Gad-El-Hak, 1999b; Varadan & Varadan, 2000).

CHAPTER 4

System identification of non-linear reduced-order models of channel flow and flow over the backward facing step

4.1 Introduction

The use of mathematical models arises from the desire to understand, control and enhance systems which we encounter every day in our lives (Coca & Billings, 2002b; Scott Collis, Joslin, Seifert, & Theofilis, 2004). Since it is often impossible to experiment freely with existing systems, a tool that would allow for a simplified representation or simulation of such systems was needed (Coca & Billings, 2002b; John, 1995). Through mathematical expressions, it is possible to capture the dynamics and express the relationships of different variables of existing natural, and man-made systems. And so, after centuries of development, mathematical models that describe and predict accurately the evolution of complex dynamical processes can be routinely derived, analysed and

simulated, providing the foundation for modern system design (Billings, Chen, & Korenberg, 1989; Coca & Billings, 2002b; Kerschen, Worden, Vakakis, & Golinval, 2006; Ljung, 2010).

Mathematical models of dynamical systems characterize the relationship between the inputs, state variables and outputs (Billings, 2013; Hong, Mitchell, Chen *et al.*, 2008). The complexity and accuracy of a model of a dynamical system may vary significantly, according to the application and its purpose. In some cases, linear models involving one or two variables are sufficient, whilst in other cases, non-linear integro-differential equations are needed (Chen & Billings, 1989; Coca & Billings, 2002b; Kerschen et al., 2006).

In the modern day, the use of mathematical models to represent and simulate complex systems play a central role in a wide spectrum of applications ranging from the animation of hair in a movie-clip (Wu & Kanai, 2016), to the design of control laws for jet engines.

In Chapter 3, computationally expensive mathematical models of incompressible flows, namely the Navier-Stokes equations, were used to simulate fluid flows in different scenarios. In this Chapter, the NARMAX system identification approach is used to identify reduced-order models of the system, based on data generated by numerical simulations. The identified models describe the flow dynamics with a desired level of accuracy, and can predict an actuated flow with an incredibly reduced computational and time cost. Both of which are essential to design an effective and feasible controller for such an application (Huang & Kim, 2008; Scott Collis, Joslin, Seifert, & Theofilis, 2004).

According to the *a priori* knowledge about a system of interest, mathematical models can be classified into three categories: white box, grey box, and black box models (Hong, Mitchell, Chen *et al.*, 2008; Ljung, 2004, 2010; Scott Collis, Joslin, Seifert, & Theofilis, 2004).

White box models are those which are built entirely from fundamental principles, such as the physical laws which describe the process (Ljung, 2004, 2010).

This type requires a thorough knowledge of the system to define the relations between all the variables involved, something that is often extremely difficult or impossible to achieve due to the complexity of

most real-world problems (Billings, 2013; Coca & Billings, 2002b; Hong et al., 2008; Ljung, 2010).

Black box models are those for which there is no available knowledge of the structure or parameters of the model, and so both have to be determined (Ljung, 2004, 2010). When this is done using available observations of the input-stimuli and measured outputs it is known as system identification (Billings, 2013; Ljung, 2010). This work is focused on the identification of black box models.

Grey box models incorporate some knowledge of the system but not enough to define the model in its entirety (Ljung, 2004, 2010). The model is built such that it exploits all *a priori* information about the system, such as model equations, and appropriate algorithms are used to estimate the unknown model parameters, for example (Hong, Mitchell, Chen *et al.*, 2008; Ljung, 2010).

The remainder of this chapter is organized as follows. Section 4.2 presents the NARMAX system identification methodology and associated algorithms. Considerations needed during the experiment design are given in Section 4.2.1, the structure detection algorithm used in 4.2.2 and Section 4.2.3 presents dynamical and statistical model validation methods.

Section 4.3 and 4.4 present the identification of reduced-order models of the 3D channel flow and the flow over a backward facing step, respectively. Finally, Section 4.5 presents a discussion on the accuracy of the identified models as well as the challenges faced by the system identification of non-linear systems, and their application to the analysis of fluid flows.

4.2 Review of non-linear system identification – the NARMAX methodology

System identification techniques have been developed and tested in the past to derive grey and black box models (Ljung, 2004, 2010). Within this discipline there are two important challenges (Billings, 2013; Hong, Mitchell, Chen *et al.*, 2008). The first is the detection of an appropriate model structure that captures the systems' dynamics, and the second is

the estimation of the correct model parameters (Billings, 2013; Billings et al., 1989; Coca & Billings, 2002b; Ljung, 2010; Sjöberg et al., 1995).

The former is of great importance since it is the procedure which defines the functions that will make up the model and ultimately the relations between all variables (Billings, 2013; Ljung, 2010; Sjöberg, Zhang, Ljung *et al.*, 1995). Meanwhile, the latter is also of importance since the parameters will dictate if the overall model is biased, a good fit to a particular data-set or an adequate representation of the underlying dynamics of the system (Billings, 2013; Chen & Billings, 1989; Coca & Billings, 2002b; Hong et al., 2008; Ljung, 2010; Sjöberg et al., 1995).

In the past, linear model identification and analysis has been the main object of focus and is a topic which has been studied extensively (Billings, 2013; Hong et al., 2008; Lang & Billings, 2004). The use of such models has been known to be carried out even when the systems under study were highly complex or known to be non-linear (Billings, 2013; Chen & Billings, 1989; Ljung, 2010; Wei, Liu, & Billings, 2003). It is known that the dynamics which can be represented through linear expressions are not sufficient to simulate a wide number of real systems (Billings, 2013; Lang & Billings, 2004).

Over the past 30 years, powerful tools to identify and analyse the nonlinear systems, have become available (Billings, 2013; Billings et al., 1989; Coca & Billings, 2002a; Lang & Billings, 2004).

The NARMAX methodology encompasses a set of methods and algorithms for identifying a Non-linear Auto Regressive Moving Average with eXogenous inputs – NARMAX – model (Billings, 2013; Billings, Chen, & Korenberg, 1989; Boaghe, Billings, Li, Fleming, & Liu, 2002; Chen & Billings, 1989; Coca & Billings, 2002; Leontaritis & Billings, 1985a, 1985b; Wei, Liu, & Billings, 2003).

The general NARMAX model with s inputs, r outputs; n_u, n_y and n_e maximum lags[1] for inputs, outputs and error, respectively, in addition to a zero mean noise sequence, is given in equation (4.1) (Billings, 2013;

[1] For simplicity in the remainder of this work, the values for n_y, n_u, and n_e are set as constant for all the respective input, output, and error signals of the system. However, the methodology allows for each of the signals to have a different value, resulting in n_{yi}, n_{uj}, with $i = 1 \dots s$ and $j = 1 \dots r$.

Billings et al., 1989; Chen & Billings, 1989; Coca & Billings, 2002a, 2002b, Leontaritis & Billings, 1985, 1987; Wei et al., 2003).

$$\boldsymbol{y}(k) = \boldsymbol{F}\Big(\boldsymbol{y}(k-1), \dots, \boldsymbol{y}\big(k-n_y\big), \boldsymbol{u}(k-1), \dots, \boldsymbol{u}(k-n_u), \boldsymbol{e}(k-1), \dots, \boldsymbol{e}(k-n_e)\Big) + \boldsymbol{e}(k) \tag{4.1}$$

Where bold denotes a vector or matrix value, $\boldsymbol{F}(\cdot) = [\mathrm{f}_1(\cdot), \dots, \mathrm{f}_\mathrm{r}(\cdot)]^\mathrm{T}$ yields a vector-valued non-linear mapping function, and

$$\boldsymbol{y}(k) = \begin{bmatrix} y_1(k) \\ \vdots \\ y_r(k) \end{bmatrix}, \ \boldsymbol{u}(t) = \begin{bmatrix} u_1(k) \\ \vdots \\ u_s(k) \end{bmatrix} \text{ and } \boldsymbol{e}(t) = \begin{bmatrix} e_1(k) \\ \vdots \\ e_r(k) \end{bmatrix}$$

It is important to note that both the inputs $\boldsymbol{u}(t-1), \dots, \boldsymbol{u}(t-n_u)$ and the outputs $\boldsymbol{y}(t-1), \dots, \boldsymbol{y}\big(t-n_y\big)$ are the measurements obtained at the defined sampling time T_s. The notation $\boldsymbol{y}(t-\alpha)$ stands for $\boldsymbol{y}(t-\alpha \cdot T_s)$.

In equation (4.1) the function $\boldsymbol{F}(\cdot)$ or any information relating to it is usually not known *a priori*, and has to be identified using structure selection methods and the parameters identified posteriorly using the measured input-output data.

The NARMAX model is capable of representing a wide class of non-linear systems under very mild assumptions (Billings, Chen, & Korenberg, 1989; Leontaritis & Billings, 1985a, 1985b). To deal with measurement and process noise, this methodology implements noise modelling procedures that ensure that the estimates of the model parameter are unbiased (Billings, 2013; Chen & Billings, 1989; Leontaritis & Billings, 1985a, 1985b).

Most system identification algorithms include four stages or steps for an adequate model to be derived (**i.** – **iv.**) the NARMAX methods expand on these to also include a posterior analysis of the model for a better understanding of the system (**v.**, **vi.**) in the time and frequency domain (Billings, 2013; Hong, Mitchell, Chen *et al.*, 2008; Ljung, 2010).

i. Experiment design and pre-conditioning of data
ii. Model structure selection
iii. Parameter estimation
iv. Model validation
v. Simulating the evolution of the systems
vi. Analysis of the systems' dynamics

The NARMAX methodology is able to produce models which are both parsimonious and faithful to the dynamics of the initial system (Billings, 2013; Chen & Billings, 1989). The simplicity of the models allows for a break-down of complex behaviours, giving way to a better analysis and understanding of the process, which is something that cannot be done when using fuzzy models, or neural networks are employed (Billings, 2013; Boynton, Balikhin, Billings, Sharma, & Amariutei, 2011; Ljung, 2010).

A further advantage is that it can be mapped directly into the frequency domain (Billings, 2013; Billings & Lang, 2002; Billings & Tsang, 1989; Lang & Billings, 1996, 1997, 2004; Lang, Billings, Yue, & Li, 2007; Yue, Billings, & Lang, 2005). This allows for the computation of the Generalized (GFRF) and Output Frequency Response Functions (OFRF) of the original system in a straight forward manner (Billings, 2013). Both allow for the effects of individual terms and parameters of the time domain model to be analysed in the frequency domain, and provide a greater insight to the properties of the system and dynamics which would otherwise be hard to identify and interpret (Billings, 2013; Hong, Mitchell, Chen *et al.*, 2008; Jing, Lang, & Billings, 2008; Lang, Billings, Yue, & Li, 2007; Liu, 2002; Ljung, 2010).

4.2.1 Experiment design

The initial stage of any system identification procedure is the generation and collection of input/output data (Billings & Zhu, 1994; Haynes & Billings, 1994; Leontaritis & Billings, 1987). The input design for non-linear models is not as straightforward as with linear models, where only the mean, variance and bandwidth need to be selected (Billings, 2013; Billings & Zhu, 1994; Haynes & Billings, 1994; Leontaritis & Billings, 1987; Ljung, 2004).

In the case of a nonlinear system, one of the requirements which contributes to the effectiveness of the system identification procedure, is the input applied. Where the latter, should be persistently exciting to the system of interest (Billings, 2013; Billings, Chen, & Korenberg, 1989; Billings & Zhu, 1994; Leontaritis & Billings, 1987; Ljung, 2004). That is,

the input used to generate identification data needs to cover the expected operating range both in frequency and amplitude, to ensure that the identified model captures in full, the underlying dynamics (Billings, 2013; Hong, Mitchell, Chen *et al.*, 2008; Ljung, 2010). For non-linear models, signals such as the pseudo-random binary sequence PRBS are not persistently exciting (Haynes & Billings, 1994).

The importance of the amplitude range is that, unless all magnitudes are covered, the resulting output may be difficult to distinguish from measurement uncertainties and other error sources, further it may not trigger all relevant dynamics which is the reason for an external pre-designed input to be applied (Billings & Zhu, 1994; Leontaritis & Billings, 1987; Ljung, 2004).

The study of the frequency content is of importance to identify the bandwidth of the system and only apply energy where truly required, since going over the system's cut-off frequency has little use (Billings & Zhu, 1994; Hong, Mitchell, Chen *et al.*, 2008; Leontaritis & Billings, 1987). A margin, however, can be beneficial to account for slight changes in the operating region. In (Leontaritis & Billings, 1987) it is suggested that for an unknown system, the input signal be a filtered Gaussian sequence when dealing with power constraints and a uniformly distributed one for amplitude constraints. Taking into consideration the limits of the physical or simulation limits.

Finally, the sampling time also has an important effect on the structure and parameters estimates generated, therefore a study such as that proposed by (Billings & Zhu, 1994) is of use to define the best suited conditions. Smaller sampling values favour accurate parameter estimation but can deter structure selection whereas the opposite occurs for longer sampling times (Bai, 2010; Billings & Zhu, 1994).

4.2.2 Structure selection & parameter estimation

The functions $\boldsymbol{F_i}(\cdot), i = 1, \dots, r$ from equation (4.1) can be expanded in several ways. To choose a particular form, it is necessary to analyse the ease of use, performance, and other factors according to the application

being studied. Possible representations include polynomial, rational, radial basis functions as well as wavelets (Chen & Billings, 1989).

In this work, only polynomial NARMAX models were considered. The main reasons are that the polynomial model structure is particularly suitable both for design of control laws as well as for analytical derivation of the Generalized Frequency Response Functions associated with the identified models (Billings, 2013; Chen & Billings, 1989; Jing, Lang, & Billings, 2008; Lang, Billings, Yue, & Li, 2007). The polynomial expansion with a non-linearity of degree l of the ith output is represented by

$$y_i(t) = \theta_0 + \sum_{i_1=1}^{n} \theta_{i_1} x_{i_1}(t) + \sum_{i_1=1}^{n} \sum_{i_2=i_1}^{n} \theta_{i_1,i_2} x_{i_1}(t) x_{i_2}(t) + \cdots + \sum_{i_1=1}^{n} \cdots \sum_{i_l=i_{l-1}}^{n} \theta_{i_1,\ldots,i_l} x_{i_1}(t) \cdots x_{i_l}(t) + e_i(t) \tag{4.2}$$

Where in equation (4.2), $x_{i_{(\cdot)}}(t)$ represent lagged terms in y, u or e, $n = r \cdot n_y + s \cdot n_u + r \cdot n_e$ and $\theta_{i_{(\cdot)}}$ are the unknown parameters to be approximated. As can be seen, this expansion is linear in the parameters which allows for the general output of the NARMAX model, equation (4.2), to be represented as a linear regression equation. For the remainder of the chapter, a SISO system will be considered to ease the derivation. Equation (4.2) becomes:

$$y(t) = \sum_{j=1}^{M} \theta_j p_j(t) + \xi(t) \ , \qquad t = 1, \ldots, N \tag{4.3}$$

In equation (4.3) , N is the number of observations of the input/output/error, p_j are the regressors or predictors, which are monomials of $x_1(t)$ to $x_n(t)$ up to degree l, M is the total number of predictors, θ_j are the unknown coefficients and $\xi(t) = e(t) + e_m(t)$ with $e(t)$ being noise and $e_m(t)$ the modelling error.

In matrix form this becomes

$$\boldsymbol{y} = \boldsymbol{P\theta} + \boldsymbol{\xi}$$

with

$$\boldsymbol{y} = \begin{bmatrix} y_1 \\ \vdots \\ y_N \end{bmatrix}, = \begin{bmatrix} \theta_1 \\ \vdots \\ \theta_M \end{bmatrix}, \boldsymbol{\xi} = \begin{bmatrix} \xi_1 \\ \vdots \\ \xi_N \end{bmatrix}, \quad \boldsymbol{P} = [\boldsymbol{p}_1 \dots \boldsymbol{p}_M] \quad \text{and} \quad \boldsymbol{p}_i = \begin{bmatrix} p_1 \\ \vdots \\ p_N \end{bmatrix}$$

$$\text{for } i = 1 \dots M.$$

Here M is defined:

$$M = \sum_{i=1}^{l} n_i + 1$$

and

$$n_i = \frac{n_{i-1}(n_y + n_u + n_e + i - 1)}{i}, \qquad n_0 = 1.$$

The structure selection now consists of choosing a subset $\boldsymbol{P}_m$ from $m \ll M$ elements belonging to $\boldsymbol{P}$, which represents the full model set to a certain accuracy or tolerance ε. Then finding the estimates of the parameters $\hat{\theta}_m$ by solving the quasi-linear least squares (LS) problem (Billings, 2013), given by

$$\widehat{\boldsymbol{\theta}}_m = \min_{\theta_m} \|\boldsymbol{y} - \boldsymbol{P}_m \boldsymbol{\theta}_m\|_2^2.$$

The number of selected model terms/regressors is crucial. Selecting too few model terms means that the model will not capture in full the underlying dynamics (Billings, 2013; Chen, Billings, & Luo, 1989). Selecting too many model terms leads to overfitting, that is, the model will fit the data including the noise but fail to capture the underlying dynamics (Billings, 2013; Chen, Billings, & Luo, 1989).

There are several methods such as optimal multiple-selection methods or stepwise regression to determine the relevant regressors (Hong, Mitchell, Chen *et al.*, 2008), but most of these become highly computationally expensive or extremely difficult to use even with systems that are of a low complexity (Hong, Mitchell, Chen *et al.*, 2008; Ljung, 2010).

The most effective approach to model structure selection is the Orthogonal Forward Regression (OFR) method proposed by Chen et al. (Chen, Billings, & Luo, 1989). The OFR is an improvement on the well-known orthogonal least squares (OLS), a method that assigns an error reduction ratio (ERR) to each candidate regressor and chooses the most significant until a termination criterion is reached (Chen, Billings, & Luo, 1989). The OLS method was impaired by the fact that the ERR

depended on the orthogonalisation path, which meant that the terms were not always correctly graded (Billings, 2013). The OFR used in this project is based on the modified Gram-Schmidt (MGS) algorithm, which is one of the more stable and well-conditioned orthogonalisation procedures (Billings, 2013; Billings, Chen, & Korenberg, 1989).

The structure selection is split into two stages, firstly a non-linear average model with exogenous inputs (NARX) is identified by omitting the error terms for all regressors, and then an iterative scheme is performed to model the residuals which exist between the measured and predicted output, until the residuals are un-correlated with all past measurements (Billings, 2013).

The regression matrix is partitioned into process and noise terms, $\boldsymbol{P}_p$ and $\boldsymbol{P}_n$ respectively, where $\boldsymbol{P} = [\boldsymbol{P}_p|\boldsymbol{P}_n]$ and $M_p + M_n = M$. The regression equation of the NARX model is $\boldsymbol{y} = \boldsymbol{P}_p\boldsymbol{\theta}_p + \boldsymbol{\xi}$.

Assuming $\boldsymbol{P}_p$ is of full rank, the orthogonal decomposition is $\boldsymbol{P}_p = \boldsymbol{WA}$, with $\boldsymbol{A}$ defined as:

$$\boldsymbol{A} = \begin{bmatrix} 1 & \alpha_{12} & \alpha_{13} & \cdots & \alpha_{1M} \\ 0 & 1 & \alpha_{23} & \cdots & \alpha_{2M} \\ 0 & 0 & 1 & \cdots & \vdots \\ \vdots & \vdots & \vdots & \vdots & \alpha_{M-1M} \\ 0 & \cdots & \cdots & \cdots & 1 \end{bmatrix}$$

and $\boldsymbol{W}$ is defined such that $\boldsymbol{W^T W} = \boldsymbol{D}$ where $\boldsymbol{D}$ is a positive diagonal matrix.

Considering $\boldsymbol{W} = \boldsymbol{PA}^{-1}$, the NARX model can be rewritten $\boldsymbol{y} = (\boldsymbol{PA}^{-1})(\boldsymbol{A\theta}_p) + \boldsymbol{\xi} = \boldsymbol{Wg} + \boldsymbol{\xi}$, by defining $\boldsymbol{g} = (\boldsymbol{A\theta}_p)$.

Since the auxiliary regressors, $\boldsymbol{w}_i$, are uncoupled, the resulting parameters $\boldsymbol{g}_i$ are uncoupled as well, so that the contribution of each regressor can be evaluated independently and so:

$$\boldsymbol{g} = \boldsymbol{D}^{-1}\boldsymbol{W}^T\boldsymbol{y}$$

or

$$\boldsymbol{g}_i = \frac{\boldsymbol{w}_i^T\boldsymbol{y}}{\boldsymbol{w}_i^T\boldsymbol{w}_i}, \quad 1 \le i \le \boldsymbol{M}$$

The sum of the squares of the output variable $\boldsymbol{y}$ is

$$\boldsymbol{y}^T\boldsymbol{y} = \sum_{j=1}^{M} g_j^2 w_j^T w_j + \boldsymbol{\xi}^T\boldsymbol{\xi}$$

Therefore, the ERR of w_k is defined as:

$$[ERR]_k = \frac{g_k^2 w_k^T w_k}{\boldsymbol{y}^T \boldsymbol{y}}.$$

The ERR is the proportion of the output variance explained by the term in question (Billings, 2013).

To estimate the process model using the MGS algorithm, the A matrix is filled one row at a time with the following steps:

Denote $P^0 = P$ where P has been transformed into $P^{(k-1)} = [w_1 \dots w_{k-1}\ p_k^{(k-1)} \dots p_M^{(k-1)}]$ and y into $y^{(k-1)}$.

(i) Then, for $k \le j \le M_p$, compute:

$$g_k^{(j)} = \frac{\left(p_j^{(k-1)}\right)^T y^{(k-1)}}{\left(p_j^{(k-1)}\right)^T p_j^{(k-1)}}$$

$$[ERR]_k = \frac{\left(g_k^{(j)}\right)^2 \left(p_j^{(k-1)}\right)^T p_j^{(k-1)}}{\boldsymbol{y}^T \boldsymbol{y}}$$

(ii) Find $[ERR]_k = [ERR]_k^{(j_k)} = \max\left\{[ERR]_k^{(j)}, k \le j \le M_p\right\}$

Then the j_kth column of $P^{(k-1)}$ is changed with the kth column of $P^{(k-1)}$ and the j_kth column of A in interchanged up to the $(k-1)$th row with the kth column of A.

(iii) Calculate the kth row of A, transform $P^{(k-1)}$ and $y^{(k-1)}$ into $P^{(k)}$ and $y^{(k)}$, respectively, then calculate

$$\begin{cases} w_k = p_k^{(k-1)}, \\ a_{k,j} = \dfrac{w_k^T \boldsymbol{y}^{(k-1)}}{w_k^T w_k}, \qquad k+1 \le j \le M_p, \\ p_j^k = p_j^{(k-1)} - a_{k,j} w_k, \quad k+1 \le j \le M_p. \end{cases}$$

$$\begin{cases} g_k = \dfrac{w_k^T \boldsymbol{y}^{(k-1)}}{w_k^T w_k}, \\ \boldsymbol{y}^{(k)} = \boldsymbol{y}^{(k-1)} - g_k w_k. \end{cases}$$

The selection is terminated at the M_sth stage when the tolerance is reached[2] by

$$1 - \sum_{k=1}^{M_s} [ERR]_k < \varepsilon$$

[2] An alternative termination criterion is to define the maximum number of terms allowed in P_p.

Where the model now has M_s significant terms and the parameter selection can now be carried out by

$$A_s\theta_s = g_s$$

The intermediate steps and a more thorough description of these algorithms, as well as the iterative procedure needed to include the identification of the noise model can be found in (Billings, 2013; Billings, Chen, & Korenberg, 1989; Chen, Billings, & Luo, 1989; Wei, Liu, & Billings, 2003). In this work, noise-free data used in identification is generated through numerical simulations of Navier-Stokes equations and so the identified models are in fact NARX-type models that do not include noise terms. However, for the remainder of the thesis they will be addressed as NARMAX models to emphasise the method used to identify them and the fact that the noise model can easily be incorporated.

4.2.3 Model validation methods

Model validation is the last of the base steps of system identification, prior to the analysis of the identified model (Billings & Voon, 1983, 1986; Billings & Zhu, 1994; Haynes & Billings, 1994; Zhu & Billings, 1997). In this stage, the model is analysed to ensure that it is a representation of the system and its dynamics and not simply a good fit to the training data. Methods of statistical and qualitative nature exist (Billings & Voon, 1983; Billings & Zhu, 1994; Haynes & Billings, 1994; Ljung, 2004; Zheng & Billings, 1999).

The main statistical validation methods developed for linear models consist in calculating correlation functions of the residuals and system inputs, then performing several tests and check that they are within defined confidence intervals (Billings & Voon, 1986; Billings & Zhu, 1994; Zhu & Billings, 1997). This is satisfied when the residuals are truly, or close to, a white random sequence, and therefore do not contain unmodeled dynamics. These tests can be applied to whatever form of model is used to represent the input/output map.

Linear SISO methods have existed since the 1970's, however, it has been shown that they are not sufficient to detect unmodeled non-linear terms (Mao & Billings, 2000). Methods to overcome this have been

proposed by (Billings & Voon, 1986; Billings & Zhu, 1994) where the output signals have also been included in the tests, and are successful for most cases. However, it was determined that for the small value problem, they can also provide incorrect results, therefore multidirectional tests were proposed (Billings & Zhu, 1994; Mao & Billings, 2000; Zhu & Billings, 1997). The MIMO case has also been studied (Billings & Zhu, 1995).

The full set of tests to ensure that there the residuals are unpredictable are

- Linear tests: $\begin{cases} \phi_{\xi\xi}(\tau) = \delta(\tau) & \forall\, \tau \\ \phi_{u\xi}(\tau) = 0 & \forall\, \tau \end{cases}$
- Non-linear tests: $\begin{cases} \phi_{(u^2)'\xi}(\tau) = 0 & \forall\, \tau \\ \phi_{(u^2)'\xi^2}(\tau) = 0 & \forall\, \tau \\ \phi_{\xi(\xi u)}(\tau) = 0 & \tau \geq 1 \end{cases}$

Where $\delta(\tau)$ is the Kronecker delta, $\xi(k)$ are the residuals, and the dash denotes that the mean level has been removed from the respective signal.

- Tests using output signal: $\begin{cases} \phi_{(\xi^2)'(y\xi)'} = \kappa\delta(\tau) & \forall\, \tau \\ \phi_{(u^2)'(y\xi)'} = 0 & \forall\, \tau \end{cases}$

where $0 < \kappa < 1$.

Multi-directional tests (1): $\begin{cases} \phi_{\xi_\gamma\xi_\gamma}(\tau) = \delta(\tau) & \forall\, \tau \\ \phi_{u_\gamma\xi_\gamma}(\tau) = 0 & \forall\, \tau \\ \phi_{(u_\gamma^2)'\xi_\gamma}(\tau) = 0 & \forall\, \tau \\ \phi_{(u_\gamma^2)'\xi_\gamma^2}(\tau) = 0 & \forall\, \tau \\ \phi_{\xi_\gamma(\xi_\gamma u_\gamma)}(\tau) = 0 & \tau \geq 1 \end{cases}$

- Multi-directional tests (2): $\begin{cases} \phi_{(\xi_\gamma^2)(y_\gamma\xi_\gamma)'}(\tau) = \kappa\delta(\tau) & \forall\, \tau \\ \phi_{(u_\gamma^2)'(y_\gamma\xi_\gamma)'}(\tau) = 0 & \forall\, \tau \end{cases}$

Where $0 < \kappa < 1$ and the tests have to be valid for all γ, for the definition of this variable and further details, the reader is directed to (Mao & Billings, 2000). Given that these correlation tests provide only statistical information, the discrepancies between the modelled and real dynamics may not always be shown.

Dynamical validation therefore complements the previous statistical tests to ensure that the model exhibits the appropriate behaviour (Zheng & Billings, 1999). These approaches often compare the

dynamical invariants of the model to those of the real system (Zheng & Billings, 1999). These include the equilibrium points, Lyapunov exponents, bifurcation diagrams, among others. In practice this is often not realizable since there is usually not enough knowledge of the system to obtain these, and the methods to compute them from data are complicated at best (Zheng & Billings, 1999). Therefore, the model predicted output (MPO) and the one-step ahead predictions of the model are studied (Condrea, 2014).

The OSA predictions are computed entirely using past measured input/output data according to equation (4.1). The procedure is repeated for the whole sequence that is to be studied. It can be noticed that the modelling error introduced is minimal since it is corrected for at each time-step when new measured data is used, and it shows how well the model approximates output measurements (Condrea, 2014).

On the other hand, the MPO is an iterative procedure, where for the first time-step, the OSA prediction is obtained using measured data. For the following calculations, the last estimated output is used to compute the future value. The equivalent expression for equation (4.1) in this case is

$$\widehat{\boldsymbol{y}}_{\boldsymbol{MPO}}(k) = \boldsymbol{F}\big(\widehat{\boldsymbol{y}}_{\boldsymbol{MPO}}\,(k-1), \dots, \widehat{\boldsymbol{y}}_{\boldsymbol{MPO}}\big(k-n_y\big), \boldsymbol{u}(k-1), \dots, \boldsymbol{u}(k-n_u), \dots, \boldsymbol{e}(k-1), \dots, \boldsymbol{e}(k-n_e)\big) + \boldsymbol{e}(k)$$

Where the accent is added to emphasise that it is the previous prediction which is used. In this case the prediction error builds up at each iteration, hence the MPO is a far clearer indicator to assess the quality of the model.

Once the MPO has been calculated, the error can be defined as $\xi(t) = y(t) - \hat{y}(t)$ and several measures of error exist to evaluate the model (De Gooijer & Hyndman, 2006; Hyndman & Koehler, 2006). These will be discussed later. When analysing the MPO, care has to be taken while defining the *goodness* of the model, since it is not always necessary for the model to have great performance tens or hundreds of steps-ahead, and so, the evaluation should be done according to the application (Billings, 2013).

A further test which can be performed using the OSA and MPO is that of using the model on *unseen* data (Billings, 2013). The process consists

of using a subset of the data set for training and the remainder for validation. To analyse the performance on the new set of the OSA and MPO using the selected error measure. This can be further enhanced using methods such as k-fold cross-validation, random subsampling and bootstrap techniques (Ayala Solares & Wei, 2015; Condrea, 2014).

The choice of test used for validation depends on the form of the model in addition to the availability of data or possibility of running several tests (Billings, 2013; Billings & Voon, 1986; Hong, Mitchell, Chen *et al.*, 2008; Ljung, 2010).

4.3 System identification of channel flow

Numerical simulation of the Navier-Stokes equations are computationally expensive (John, 1995). This even when the geometry and the flow are simple in nature, and is made more so when the Reynolds number is in the transition or turbulent regime (Bewley, 2001; John, 1995). Further, many model reduction approaches provide results which are not always suitable for real-time control applications due to the over-simplification of the system or still unfeasible computational requirements (Bewley, 2001; Pollard, 1998; Scott Collis, Joslin, Seifert, & Theofilis, 2004). In this case, reduced order models of flow dynamics, which are sufficiently accurate for analysis or control purposes, are needed.

4.3.1 Experiment design

Simulations have been carried out of the channel flow in a wall bounded domain. The domain was defined to have dimensions $L_x = 4\pi$, $Ly = 2$, and $Lz = 3\pi$ for the streamwise, wall-normal and spanwise directions, respectively. An appropriate mesh and sampling time, $T_s = 0.01$ seconds, were defined to sufficiently resolve the scales for the simulation to be representative of the flow.

The data was subsampled spatially, to avoid subsequent measurements to be overly similar and reduce the length of the data-

series. The data which was finally used for the system identification was from a sub-mesh M_s of $N_{x2} = 30$, $N_{y2} = 29$, and $N_{z2} = 25$ grid-points.

Since the mesh M_s had a fewer number of nodes, but still over 20,000, it was decided that the entire time series of each node would be used for training the model, and then validated on the remaining models of the same type and the best performing chosen. Figure 4.1 shows the data used for a single node, where plotted are the three velocity components of the velocity v_x, v_y, v_z.

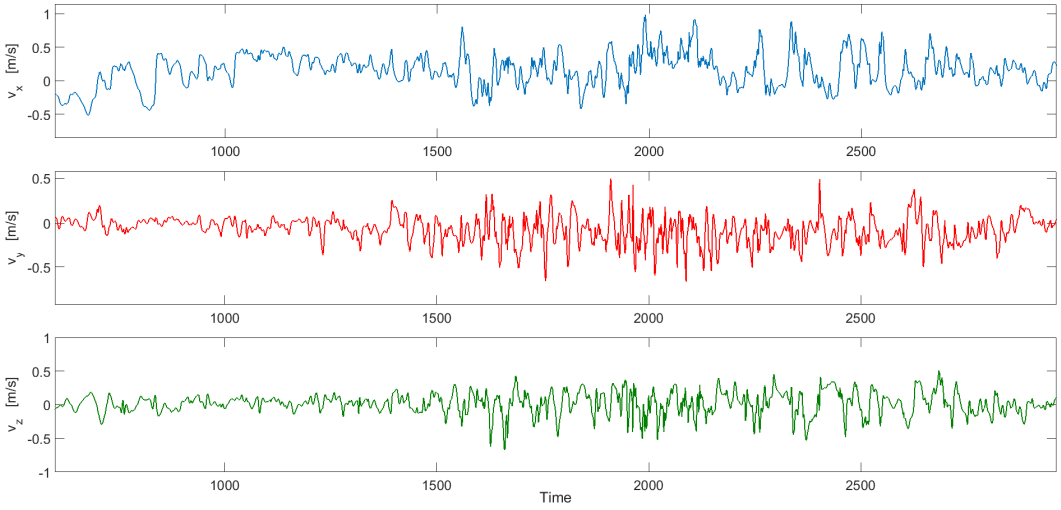

Figure 4.1. Components of velocity fluctuations over time from node [15,20,12] of mesh M_s, v_x in blue, v_y in red, and v_z in green.

As it was mentioned in Chapter 3, data from several simulations under different initial conditions, and with varying Reynolds numbers were used to study the frequency content variation of the output signals, to design an appropriately exciting input. The generated signal was then applied to the system using a modified version of the ChannelFlow package and data extracted from the new sub-mesh as mentioned above.

Due to conflicting notation from the fluid flows and control disciplines, from this chapter onwards, the input/actuations signals will be referred to as u. The components of the velocity and magnitude will be labelled as (v_x, v_y, v_z) and $|V|$, respectively, where $|V| = \sqrt{v_x^2 + v_y^2 + v_z^2}$.

4.3.2 Structure selection & parameter estimation

Multiple-input multiple-output models have been sought, using the flow velocity components v_x, v_y, v_z as the variable to be modelled. Each of

these were considered as outputs (y_{v_x}, y_{v_y}, y_{v_z}) and the velocity components of the surrounding nodes were selected as the inputs ($u_{v_x ij}$, $u_{v_y ij}$, $u_{v_z ij}$), therefore, the terms of equation (4.1) are given by:

$$\boldsymbol{y}_{v_{(\cdot)}}(k) = \begin{bmatrix} y_{\mathrm{v_x}}(k-1) \\ \vdots \\ y_{\mathrm{v_x}}(k-n_y) \\ y_{\mathrm{v_y}}(k-1) \\ \vdots \\ y_{\mathrm{v_y}}(k-n_y) \\ y_{\mathrm{v_z}}(k-1) \\ \vdots \\ y_{\mathrm{v_z}}(k-n_y) \end{bmatrix}, \quad \boldsymbol{u}(t) = \begin{bmatrix} u_{\mathrm{v_x} ij}(k-1) \\ \vdots \\ u_{\mathrm{v_x} ij}(k-n_u) \\ u_{\mathrm{v_y} ij}(k-1) \\ \vdots \\ u_{\mathrm{v_y} ij}(k-n_u) \\ u_{\mathrm{v_z} ij}(k-1) \\ \vdots \\ u_{\mathrm{v_z} ij}(k-n_u) \\ \vdots \end{bmatrix}$$

Where the index ij is used to identify the surrounding nodes to the one being analysed and $y_{v_{(\cdot)}}(k)$ is considered for each of the three components $y_{v_x}(k)$, $y_{v_y}(k)$, $y_{v_z}(k)$.

After several initial tests, where a single model was sought for the entire domain, it became evident that this would not be adequate. Even with varying values for the model order and input/output lags. This was of course to be expected since it is a highly spatial and time varying system (Bewley, 2001).

Therefore, an approach was undertaken where different structures would be used across spatial locations. Further, to enhance the performance of the model of a particular node, data from the surrounding ones would be considered as inputs, in addition to the external actuation.

a) **b)**

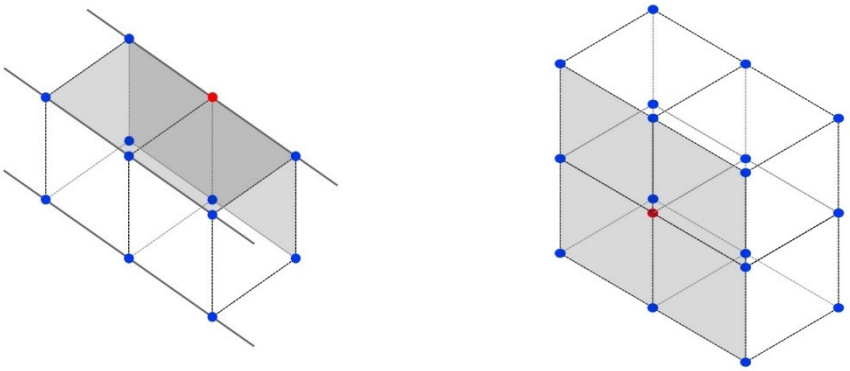

For caption, see next page

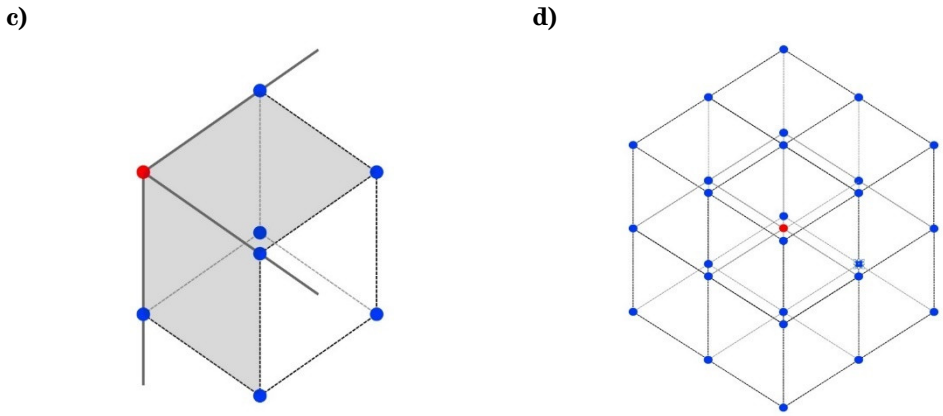

Figure 4.2. Schematic of the four node classes for the identification of the model at the red node. Input data obtained from blue nodes and the output data from the current (red) node. a) Edge node b) Wall node c) Vertex node d) Inner flow.

Since not all the nodes have neighbours in every direction, as is the case of the boundary nodes, the structure could not be equal at every location. Therefore, 4 different node *classes* with several sub-types were defined. Figure 4.2 shows schematics of the different node types, where the blue and red dots represent the nodes being used as inputs and outputs, respectively, during the system identification procedure.

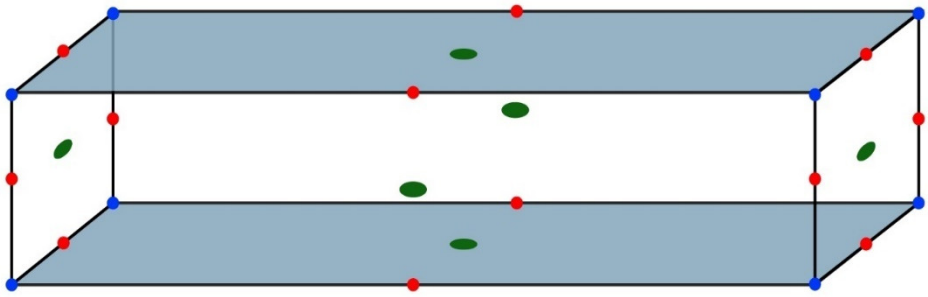

Figure 4.3. Schematic of node types of entire domain, showing location and number of each sub-type. Wall nodes in green, edge nodes in red, and vertex node in blue. Inner flow nodes are those which do not belong to the previous types.

In turn, Figure 4.3 again shows the node classes including their corresponding sub-types. Wall nodes in green with 6 sub-types, edge in red with 12 sub-types, vertex in blue with 8 sub-types, and inner flow not shown to avoid confusion. Each of the sub-types could have a different structure.

Table 4.1. Range of variables used in the MIMO system identification of the velocity fluctuations.

Variable	Meaning	Value
n	Order of non-linearity	$2, 3$
P_p	Process terms	$2, \dots, 30$
n_y	Output lag	$2, 3, 4$
n_u	Input lag	$2, \dots, 7$

In order to find the best combination for model degree and input/output lags, these two variables were varied in the ranges shown in Table 4.1 and models identified and analysed for each combination.

The values shown in Table 4.1 were chosen for several reasons. Linear, quadratic, and cubic models were tested, however, for the case of the latter, the increase in accuracy did not warrant the increased complexity and computational burden during the computation and simulation of the model. Additionally, since the Navier-Stokes are quadratic then a model of this order should be able to capture the relevant dynamics and represent the system faithfully (Billings, 2013; Davidson, Kaneda, & Sreenivasan, 2013).

The limits for input and output lags were chosen since it is well-known that past conditions greatly affect the evolution of the flow (Davidson, Kaneda, & Sreenivasan, 2013; John, 1995), and so large values would be needed. However, due to the high number of inputs being tested for some of the structures as well as the model orders, the limit for this value could not be larger without making the computational burden overly costly.

The identification procedure was applied with all the combinations of the variables defined in Table 4.1, the termination criteria was set to be an increasing limit number of terms. At each iteration of the procedure, the model predicted output was computed by providing initial conditions and the input training signal. The evolution of the Normalized Root Mean Squared Error (NRMSE) (Boynton, Balikhin, Billings, Sharma, & Amariutei, 2011) as defined in equation (4.4) was monitored and used to choose the best performing model.

$$NRMSE = \frac{\sqrt{\frac{\sum_{i=1}^{N}(y_i - \hat{y}_i)^2}{N}}}{\sigma_y} \tag{4.4}$$

Where y_i is the ith measured signal, $\hat{y}_i$ the ith prediction from the identified model and σ_y the standard deviation of the measured signal.

After a series of tests, it was noted that adding data from beyond a lag of $n_y = 6$ time-steps did not contribute to a great increase the model accuracy. A slightly longer lag was still allowed to account for any future

changes in the operating region. Many models however did not require this amount as can be seen in the final structures.

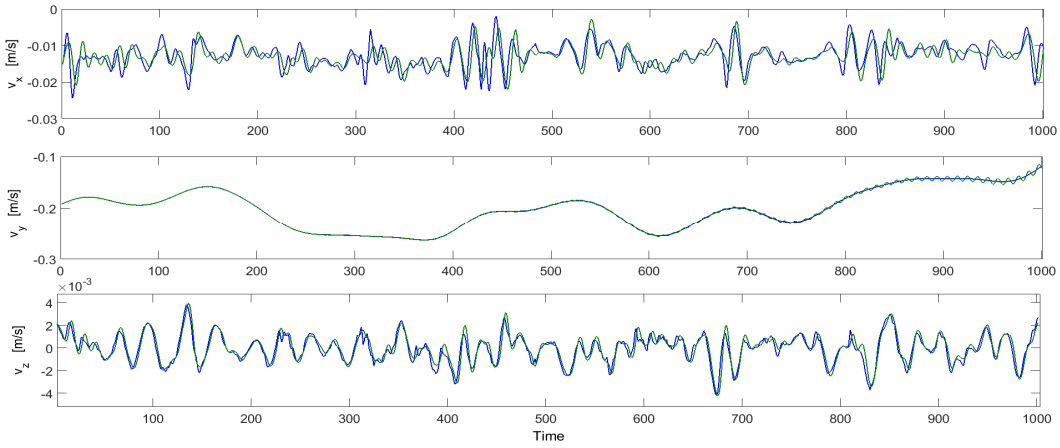

Figure 4.4. Model predicted output (in blue) and measured signal (in green) for each of the velocity components at node [1,9,1] for the best performing edge vertex on training data. Top: v_x with $NRMSE = 35.6\%$. Middle: v_y with $NRMSE = 2.42\%$. Bottom: v_z with $NRMSE = 19.24\%$.

Table 4.2. Model structure for each of the velocity components at node [1,9,1].

Structure v_x		Structure v_y		Structure v_z	
$y_{16}(k-1)$	1	$y_7(k-1)$	1	$y_{18}(k-1)$	1
$y_7(k-1)$	$u_1(k-1)$	$y_7(k-2)$	1	$y_{18}(k-2)$	1
$y_1(k-4)$	$u_1(k-2)$	$y_7(k-3)$	1	$y_{18}(k-3)$	1
$y_{16}(k-2)$	1	$y_7(k-4)$	1	$y_3(k-4)$	1
$y_7(k-2)$	$u_1(k-2)$	$y_{17}(k-1)$	1	$y_8(k-5)$	1
$y_7(k-3)$	$u_1(k-2)$	$y_{14}(k-5)$	$y_{16}(k-1)$	$y_8(k-2)$	$y_2(k-4)$
$y_{16}(k-3)$	1	$y_{17}(k-2)$	1	$y_8(k-1)$	1
$y_7(k-4)$	$u_1(k-2)$	$y_7(k-5)$	1	$y_8(k-2)$	1
$y_6(k-7)$	$u_1(k-2)$	$y_7(k-6)$	$y_1(k-5)$	$y_8(k-3)$	1
$y_6(k-1)$	$y_2(k-3)$	$y_7(k-6)$	$y_1(k-5)$	$y_8(k-4)$	1
$y_6(k-2)$	$y_2(k-3)$			$y_{10}(k-7)$	$y_2(k-5)$
$y_{14}(k-7)$	$y_1(k-4)$			$y_{13}(k-4)$	$y_4(k-1)$
$y_6(k-1)$	$y_1(k-1)$			$y_{14}(k-7)$	$y_{11}(k-2)$
$y_6(k-2)$	$y_1(k-6)$			$y_8(k-6)$	1
$y_{14}(k-2)$	$y_2(k-2)$			$y_3(k-3)$	1
$y_{15}(k-5)$	$y_{15}(k-1)$			$y_5(k-7)$	$y_{17}(k-2)$
$y_{12}(k-6)$	$y_{10}(k-7)$			$y_8(k-1)$	$y_{17}(k-2)$
$y_9(k-5)$	$y_7(k-2)$			$y_8(k-1)$	$y_{17}(k-2)$
$y_{14}(k-3)$	1				
$y_{14}(k-3)$	1				

Figure 4.4 shows the performance of a model identified at node [1,9,1] and Table 4.1 presents the corresponding model structure. The parameters are not shown since these were calculated at each node independently. In these structures, only the actuation is shown as an input, the data from the surrounding nodes has been identified as

$y_i(t-k)$ for $i = 4, \dots, 18$ and the $(y_{v_x}, y_{v_y}, y_{v_z})$ outputs for the current node are $y_i(t-k)$ for $i = 1, 2, 3$. This was done to clarify that the surrounding nodes are outputs of the full model, even if at individual nodes they are used as input data.

After some analysis, it was noted that should the model be used for control purposes in later work, the single actuation signal would not be enough to manipulate the system in the desired form. According to the literature, it has been found that variations of actuators or actuating signals along the spanwise directions, while applying wall normal actuation, can cause a faster modification of the flow (Klumpp, Meinke, & Schröder, 2010; Quadrio & Ricco, 2004; Quadrio, Ricco, & Viotti, 2009; Zare, Lieu, & Jovanovic, 2012). This even with a reduced amount of input energy.

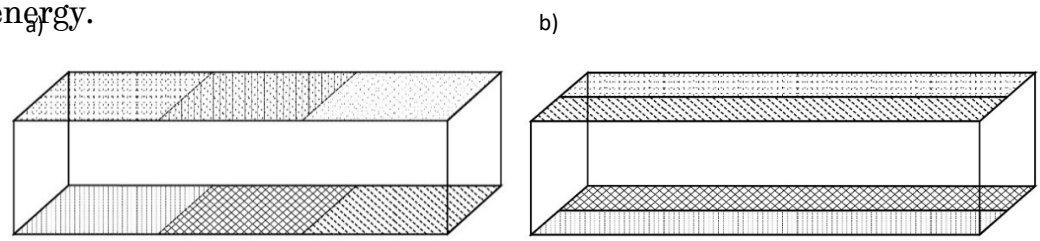

Figure 4.5. Schematic of multi-actuation arrays over channel flow domain. a) Three different streamwise actuation signals per wall b) Two different spanwise actuations per wall.

Therefore, new simulations with an array of actuators were performed, here tests were done to ensure that in the current geometry, the hypothesis of spanwise variations were indeed better at modifying the flow. For this purpose, the configurations shown in Figure 4.5 were tested. Each of the bands represents a different actuation signal applied at all nodes included in that area. In Figure 4.5 a) the streamwise varying actuations are depicted while b) shows the spanwise varying set-up. Cases with two and three different actuations at each wall were tested. After analysing the results from these simulations, it was clear that the spanwise varying case has the largest effect in the least time when the same signals are applied.

New simulations using three actuations at each wall were performed and the system identification was carried out once again following the same procedure explained. Models were obtained using the training data and tested on the remainder nodes of the same sub-type, until a suitable model which performed adequately was found.

For the inner flow, it was found that a single structure was suitable to represent the entire zone. However, depending on the application it is likely that more structures would help to improve the predictions, and to account for changes in conditions such as the Reynold number.

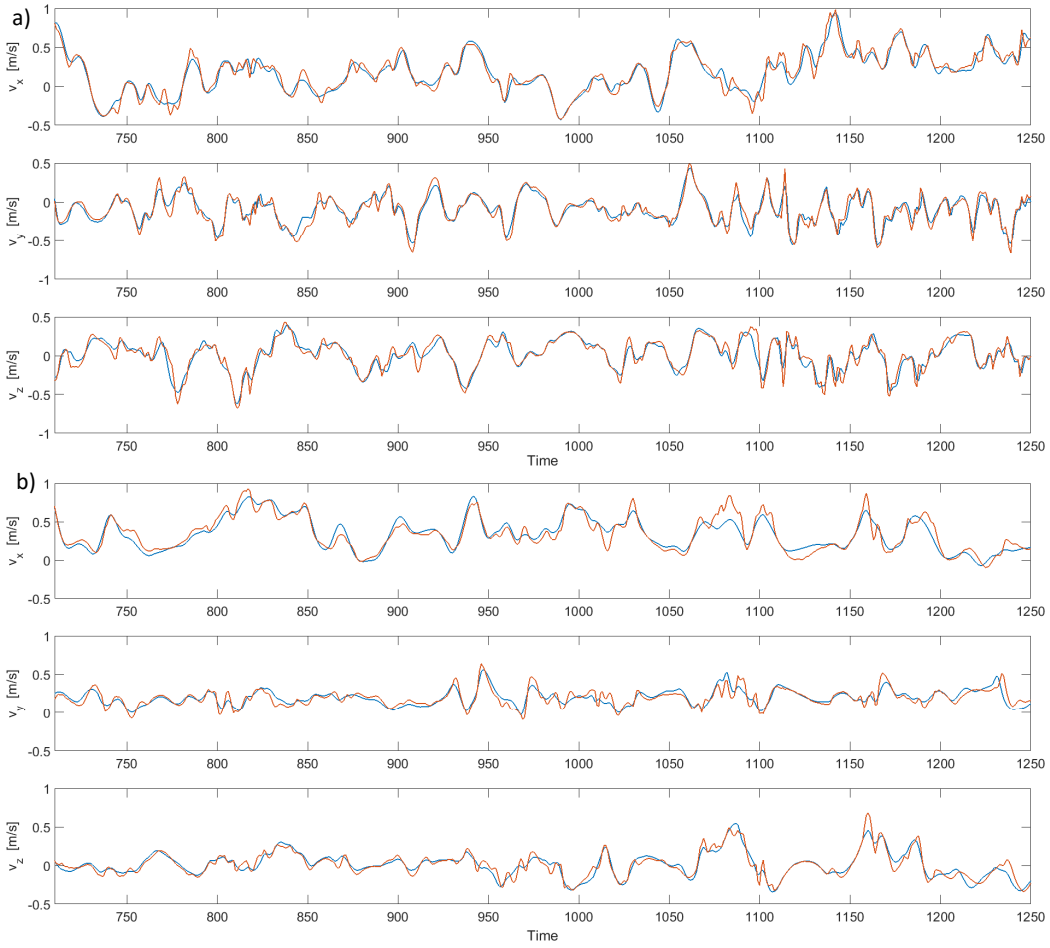

Figure 4.6. Model predicted output (in blue) and measured signal (in red) for training data of the velocity components for the best performing a) Inner flow node at [15,20,12]. Top: v_x with $NRMSE = 15.12\%$. Middle: v_y with $NRMSE = 19.73\%$. Bottom: v_z with $NRMSE = 20.17\%$. b) Edge node at [30,7,25]. Top: v_x with $NRMSE = 21.85\%$. Middle: v_y with $NRMSE = 31.67\%$. Bottom: v_z with $NRMSE = 19.65\%$.

The performance of models identified for two locations can be seen in Figure 4.6. The model structures for these two locations are also shown in Table 4.3 and Table 4.4. Again, the parameters are not shown since they have been calculated per node.

Table 4.3. Model structure for each of the velocity components at node [15,20,12].

Structure v_x		Structure v_y		Structure v_z	
$y_1(k-1)$	1	$y_2(k-1)$	1	$y_3(k-1)$	1
$u_7(k-1)$	1	$u_{53}(k-1)$	1	$u_{24}(k-1)$	1
$u_{37}(k-1)$	$u_{27}(k-1)$	$u_{35}(k-1)$	1	$u_{15}(k-1)$	1
$u_{49}(k-1)$	$u_{31}(k-1)$	$u_{14}(k-1)$	1	$u_{20}(k-1)$	1

$u_{45}(k-1)$	1	$u_{24}(k-1)$	$u_{23}(k-1)$	$u_{33}(k-1)$	$u_{31}(k-1)$
$u_{15}(k-1)$	1	$u_{54}(k-1)$	$u_{53}(k-1)$	$u_{31}(k-1)$	$u_{15}(k-1)$
		$u_{17}(k-1)$	1	$u_{47}(k-1)$	$u_{35}(k-1)$
				$u_{10}(k-1)$	$u_{10}(k-1)$
				$u_{25}(k-1)$	$u_{19}(k-1)$
				$u_{25}(k-1)$	$u_{13}(k-1)$
				$u_{16}(k-1)$	$u_{12}(k-1)$

Table 4.4. Model structure for each of the velocity components at node [30,7,25].

Structure v_x		Structure v_y		Structure v_z	
$y_1(k-1)$	1	$y_2(k-1)$	1	$y_3(k-1)$	1
$u_7(k-1)$	$u_6(k-1)$	$u_{26}(k-1)$	1	$u_{27}(k-1)$	$u_{27}(k-1)$
$u_{10}(k-1)$	1	$u_{68}(k-1)$	1	$u_{72}(k-1)$	1
		$u_{58}(k-1)$	$u_8(k-1)$		
		$u_{23}(k-1)$	1		

Finally, to improve the performance of the identified structures across the entire domain, the parameters at each of the nodes were recalculated using data from the corresponding training set, so that an additional tuning of the model was obtained prior to the validation.

4.3.3 Model validation

Once suitable models had been identified for each location, the model validation procedure was performed. The model selected for each node sub-type was tested on the remainder alike nodes for validation.

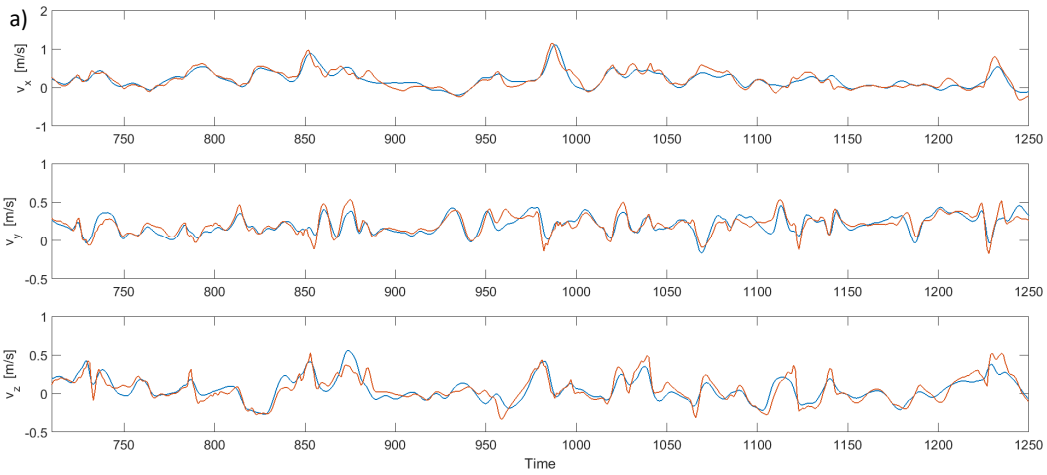

For caption, see next page

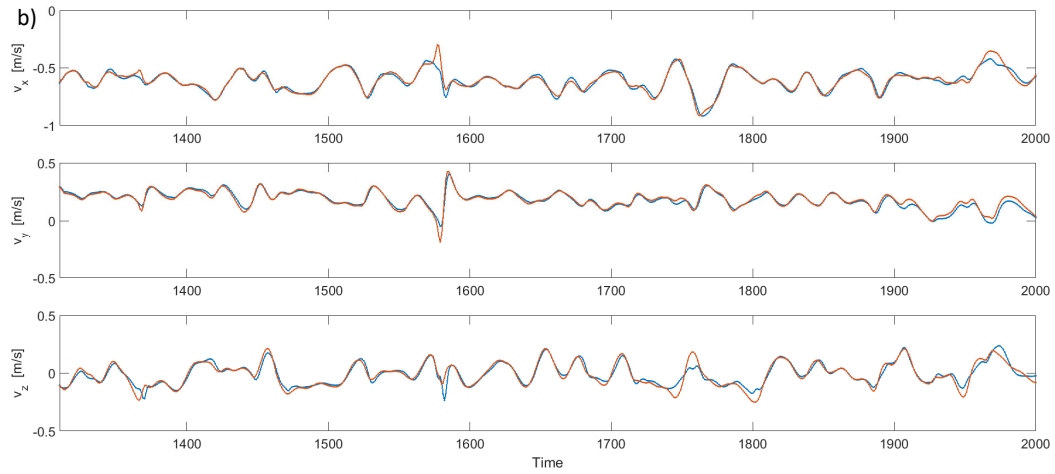

Figure 4.7. Model predicted output (in blue) and measured signal (in red) for validation data of the velocity components for the best performing a) Inner flow node at [20,8,21]. Top: v_x with $NRMSE = 25.59\%$. Middle: v_y with $NRMSE = 32.55\%$. Bottom: v_z with $NRMSE = 28.29\%$. b) Edge node at [30,19,25]. Top: v_x with $NRMSE = 15.96\%$. Middle: v_y with $NRMSE = 16.03\%$. Bottom: v_z with $NRMSE = 18.4\%$.

Figure 4.7 shows performance of the models obtained for the locations shown before. For most of the node sub-types, the models selected per the NMRSE on the training data had a good performance while predicting the evolution of the flow with the validation data. However, there were some which were inadequate, and so the process was repeated until a suitable model which performed well on all the alike nodes, was obtained. The entire set of model structures can be found in Appendix B.1.

The NRMSE was computed for all the nodes of M_S. Since there are $30\times29\times25 = 21{,}750$ nodes and three velocity components for each node, the visualization of the performance of the entire model is difficult. Therefore, the NRMSE for every node was computed and a probability density function (PDF) fitted to the values. The values of NRMSE were grouped according to the velocity components, i.e. three PDF's have been fitted, one for each component over the entire domain. The PDF's can be seen in Appendix B.2.

4.4 System identification of backward facing step flow

The backward facing step is another example of a flow in a relatively simple geometry, which can be used to model and understand the behaviour of turbulence (Heenan & Morrison, 1998; Le, Moin, & Kim, 1997). Additionally, this case contains new phenomena such as detached flow and a reattachment point (Driver & Jovic, 1994; Le, Moin, & Kim,

1997). These are of interest in many applications, as discussed in Chapter 3.

Here once again, a reduced order model which can replicate the evolution of the flow, and help to predict the reattachment point for example, is of great interest for control applications.

The simulation method of the Fluent package is described in Chapter 2. The LES method simulates a simplified version of the Navier-Stokes equations, where the discretization methods act as a filter so that only the eddies, which have larger scales in time and space than T_s and mesh size, respectively, are solved whereas the smaller ones are modelled (Ansys, 2016).

This package and method of generating data was used since it is considered to be the second most accurate, after DNS methods (John, 1995).

4.4.1 Experiment design

Simulations were run using the Ansys-Fluent CFD package. To simulate flow over the backward facing step, a refined mesh was created in the specialized ICEM meshing program. This mesh was made up of 515,000 nodes which were found to be sufficient to resolve the flow accurately. This was verified by comparing the generated velocity, and other variables, to DNS and experimental data as mentioned in Chapter 3.

Since the goal of identifying a model of this scenario was to design a controller scheme, as will be discussed in Chapter 6, a single-input single-output SISO approach to the modelling was initially undertaken. The main reason for this being that MIMO models increase the difficulty of designing a controller and sometimes may be completely unsuitable, depending on the form of the model (Camacho & Bordons-Alba, 2003; Rossiter, 2003).

Considering that a generalized predictive control scheme was to be designed, the models identified are required to have certain properties, as will be discussed in the next section.

After some tests with the implementation of the controller, it was noted that the SISO approach to the control did not provide results with

an acceptable performance. Therefore, multiple-input single-output MISO models were then identified.

Two different variables were chosen as outputs for the SISO and MISO case. For the former the pressure coefficient, C_p, near the top of the step wall and for the latter the velocity magnitude, $|V|$, at a node within the recirculation zone were chosen. For convenience, the SISO pressure coefficient model will be referred to as M_{Cp} and the MISO velocity magnitude models as M_{V2}, M_{V4} according to the number of actuators used in the simulations.

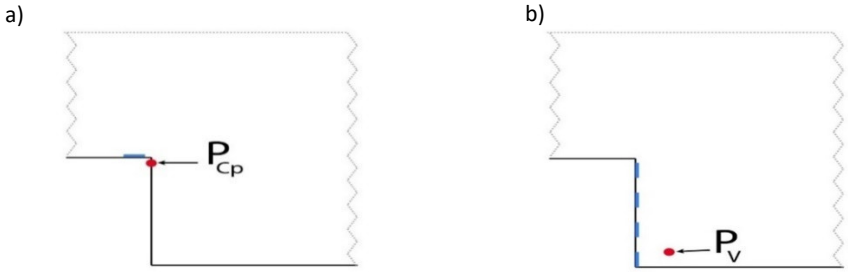

Figure 4.8. Schematic showing the location for the extraction of data from flow over the BFS domain. a) C_p location using one actuator upstream of the step. b) $|V|$ location using two and four actuators on the step wall.

The locations where this data was extracted can be seen in Figure 4.8 where $P_{Cp} = [0,0.0095]$ and $P_V = [0.0025,0.00098]$. The time step set for the training and validation data sets was $T_s = 0.005$, and $T_s = 0.001$ seconds for the $M_{Cp}$and M_V models, respectively.

Considering these variables together with the defined time-step, the data which was generated from the LES simulations was split into a subset used for the training of the models and the remainder for validation purposes. Figure 4.9 shows the data divisions for C_p and Figure 4.10 the division for $|V|$ with the actuation signals. In the case of the velocity magnitude data, both the case with two and four actuators are presented in Figure 4.10 a) and b) respectively.

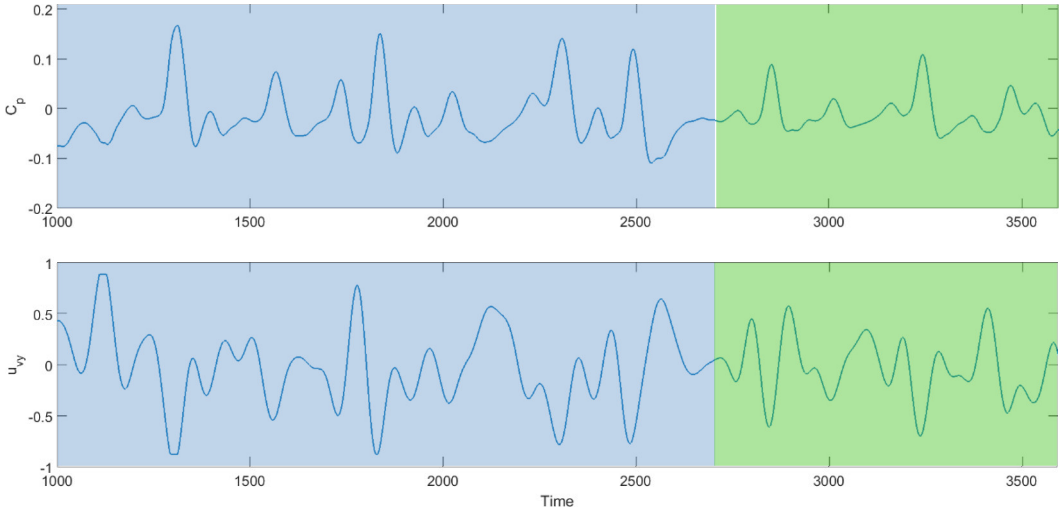

Figure 4.9. Time series for C_p data (Top) and actuation signal applied (bottom), blue and green highlighted zones represent data points used for model training and validation, respectively.

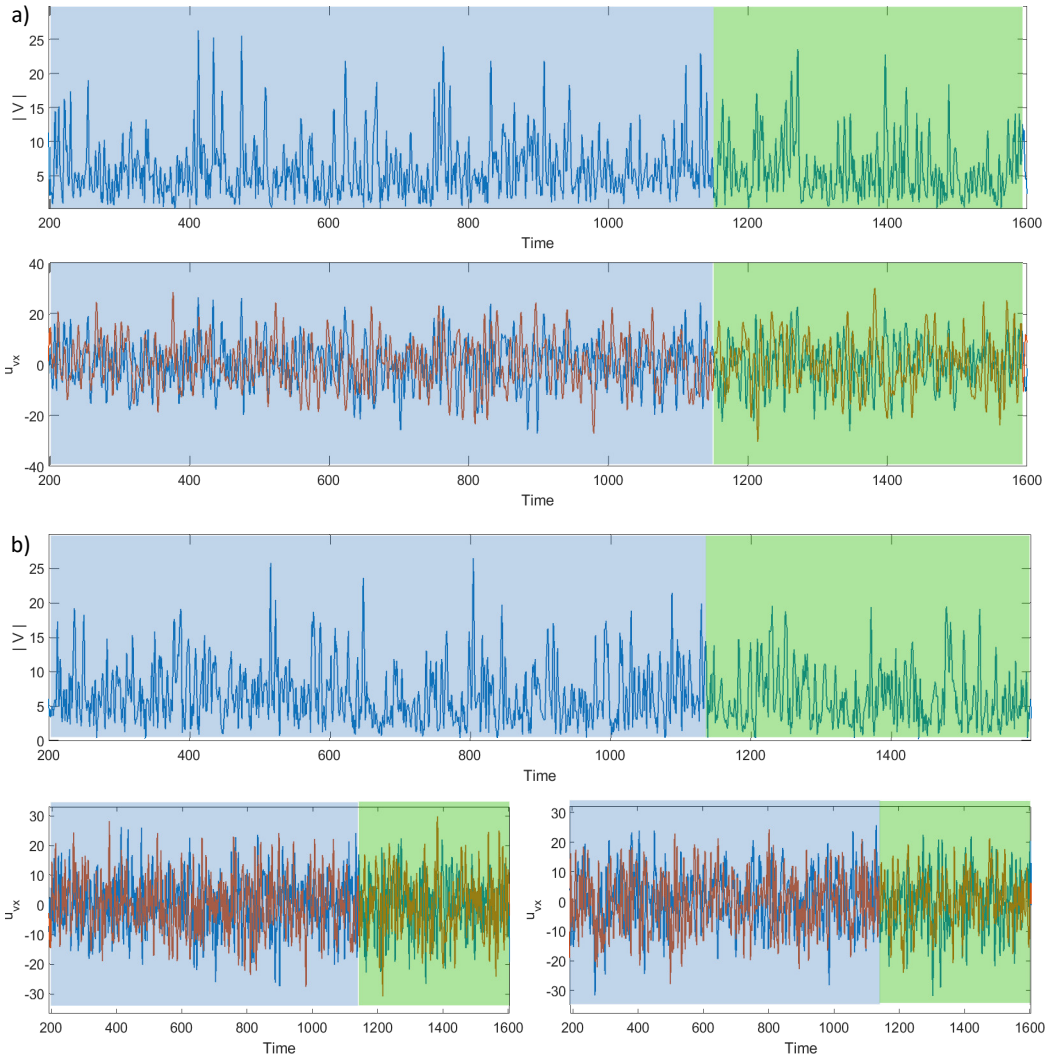

Figure 4.10. Time series for $|V|$ data and actuation signals applied, blue and green highlighted zones represent data points used for model training and validation, respectively. a) Two actuators on step wall Top: $|V|$ time series. Bottom: Actuation. b) Four actuators on step wall Top: $|V|$ time series. Bottom: Actuation.

4.4.2 Structure selection & parameter estimation

The structure selection and parameter identification algorithm was used on the training data. Unlike in the channel flow case, where quadratic models were sought to allow for an inclusion of more input and output signals without a great increase in model complexity. For the $M_{Cp}$and M_V models sought from the BFS data, higher degrees were permitted to account for the reduced amount of information being fed into the model.

Additionally, since as mentioned previously a predictive controller scheme was to be designed at a later stage, the models needed to have certain properties. These include the need for them to be input affine, and ensuring that non-linearities with respect to future terms are not included, particularly if the model is used recursively (Camacho & Bordons-Alba, 2003; Rossiter, 2003). To account for this, a routine which eliminated the candidate terms that did not comply with these conditions was included in the structure selection stage.

Tests showed that this limitation of the candidate terms had a negative impact on the performance of the models, which were slightly less accurate when certain terms were removed from the candidate set. However, this was a required trade-off since without the removal of those terms, the application of the predictive controller would have been difficult and the computational burden increased during the required calculations. The latter goes against the very motivation for deriving such models, and so it was decided to choose the best performing models that were suitable for the controller scheme.

Table 4.5. Range of variables used in the SISO system identification of the C_p and $|V|$ data.

Variable	Meaning	Value
n	Order of non-linearity	$2, 3, 4$
P_p	Process terms	$5, \dots, 25$
n_y	Output lag	$2, \dots, 5$
n_u	Input lag	$2, \dots, 20$

Here the model orders, lags and the number of process terms were tested in the range shown in Table 4.5. The final number of terms was defined by allowing the algorithm to run with an increasing limit, while

monitoring the evolution of the NMRSE of each identified model and selecting the best one.

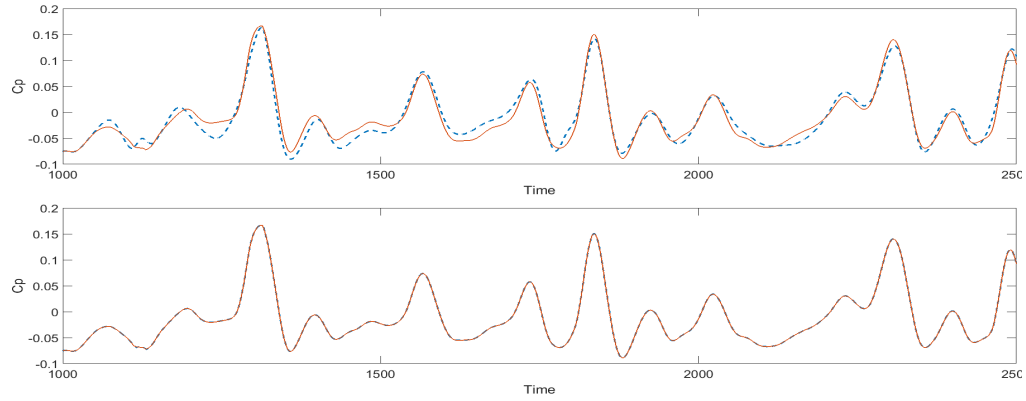

Figure 4.11. Top: Model predicted output (in blue) and measured signal (in red) of training data for C_p fluctuation using M_{Cp}. The $NRMSE = 12.75\%$. Bottom: One step ahead predictions (in blue) and measured signal (in red) for C_p fluctuation using M_{Cp}. The $NRMSE = 0.25\%$.

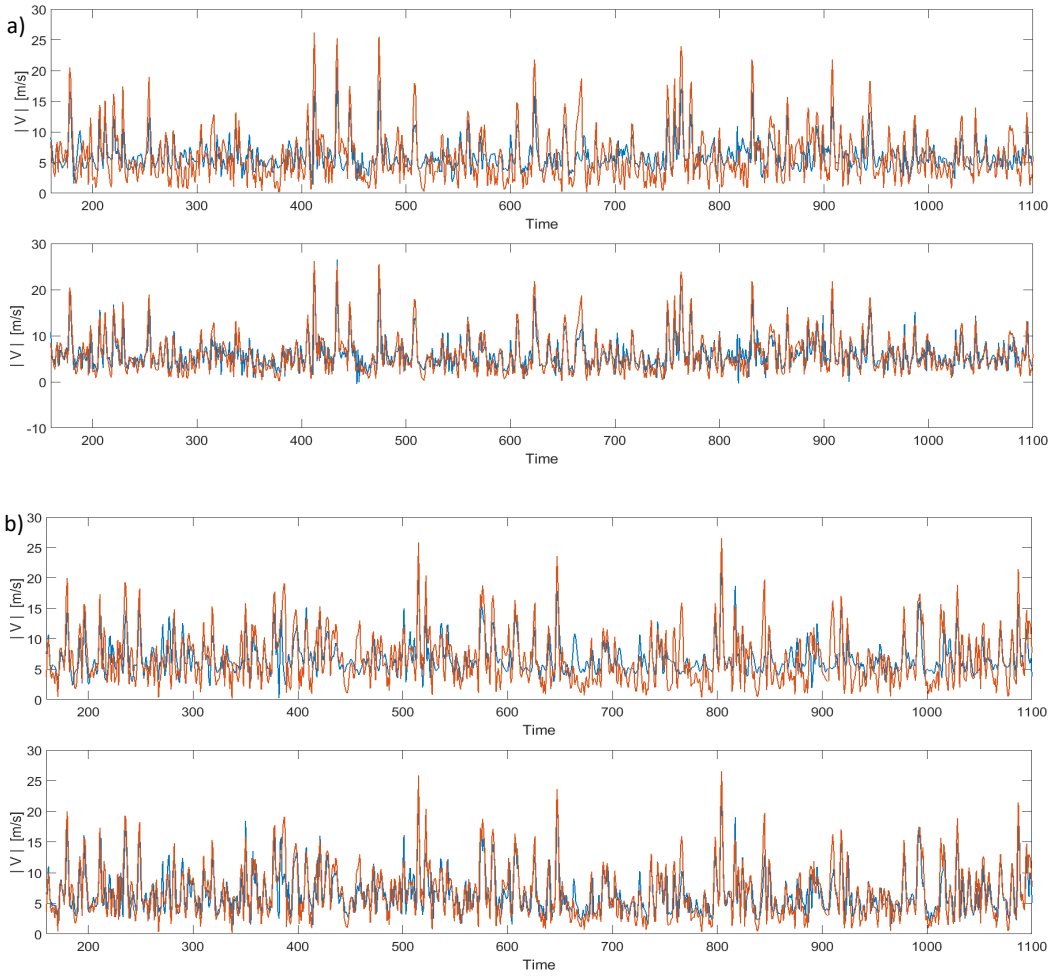

Figure 4.12. a) Top: Model predicted output (in blue) and measured signal (in red) of training data of $|V|$ fluctuation using M_{V2}. The $NRMSE = 37.16\%$. Bottom: One step ahead predictions (in blue) and measured signal (in red) of training data of $|V|$ fluctuation using M_{V2}. The $NRMSE = 28.95\%$. b) Top: Model predicted output (in blue) and measured signal (in red) of training data of $|V|$ fluctuation using M_{V4}. The $NRMSE = 39.44\%$. Bottom: One step ahead predictions (in blue) and measured signal (in red) of training data of $|V|$ fluctuation using M_{V4}. The NRMSE=30.77%.

Figure 4.11 shows the performance of MPO of the M_{Cp} model on the training data. Likewise, Figure 4.12 a) and b) presents the MPO for the M_{V2}, M_{V4} models, on the training data.

Table 4.6. Model structure and parameters for M_{Cp}.

Parameter	Model M_{Cp}	
-0.000651	0	0
1.942	$y_1(k-1)$	0
-0.963	$y_1(k-2)$	0
-0.05751	$u_1(k-1)$	0
0.003786	$u_1(k-1)$	$u_1(k-6)$
0.10892	$u_1(k-2)$	0
-0.053079	$u_1(k-3)$	0
-0.002812	$u_1(k-6)$	$u_1(k-6)$

The terms and parameters identified for the M_{Cp} model are given in Table 4.6. Similar tables containing the M_{V2} and M_{V4} model structures have been reported in Appendix B.3 to save space. The M_{Cp} model has very good prediction accuracy with an $NRMSE = 12\%$. On the other hand, the models identified from the $|V|$ data using two and four actuators have higher $NRMSE$, even though the predictions have good accuracy as can be visually verified. This is thought to be due to the formulation of the NRMSE, where the smaller and larger errors are given different a penalty (De Gooijer & Hyndman, 2006; Hyndman & Koehler, 2006). Alternative prediction error measures were considered, however the NRMSE was the most consistent for both the channel flow and flow over the BFS data.

As will be discussed in Chapter 6, the controller strategy using the M_{V2} and M_{V4}models did not have a good performance. This was mainly attributed to the accumulation of error while calculating the multi-step-ahead (MSA) predictions of the flow, when using the models recursively. Therefore, the identification of multi-step-ahead predictors identified directly from the data was carried out to improve performance (Bai, 2010; Bai & Coca, 2008, 2011). This direct approach has been shown to be more accurate than using recursive methods (Atiya, El-Shoura, Shaheen, & El-Sherif, 1999; Zhang, Eddy Patuwo, & Y. Hu, 1998).

The j-step-ahead predictors of the NARX model are given by:

$$\hat{y}(k+1|k) = f_1\left(y(k), \dots, y\left(k-n_y+1\right), u(k), \dots, u(k-n_u+1)\right),$$
$$\hat{y}(k+2|k) = f_2\left(y(k), \dots, y\left(k-n_y+1\right), u(k+1), u(k), \dots, u(k-n_u+1)\right),$$
$$\vdots$$
$$\hat{y}(k+j|k) = F_j\left(y(k), \dots, y\left(k-n_y+1\right), u(k+j-1), \dots, u(k), \dots, u(k-n_u+1)\right) \quad (4.5)$$

Where $\hat{y}(k+j|k)$ denotes the estimated value of y, j steps ahead in the future given past data up to instant k and $F(\cdot)_i\ i = 1 \dots j$ are the same non-linear functions to be identified from the data as in equation (4.1), except for the change in the included terms.

The practical way to achieve this identification is by shifting the multi-step-ahead predictors of equation (4.5) j-steps backwards in time, so that the identified functions $f\left(x(k)\right)$ will be dependent on:

$$x(k) = [y(k-j), \dots, y\left(k-n_y-j+1\right), u(k-1), \dots, u(k), \dots, u(k-n_u-j+1)]$$

This is reduced to eliminating the candidate terms which include output data from times which do not comply with this expression. The predictor needs to be shifted forward in time once the identification procedure has been completed to be readily used in the model predictive controller schemes.

The models which are identified in this manner increase in complexity as the prediction horizon increases, and so during the structure selection stage, higher orders, number of lags as well as process terms were tested.

Table 4.7. Range of variables used in the MISO system identification of the velocity fluctuations.

Variable	Meaning	Value
n	Order of non-linearity	$2, 3, 4$
P_p	Process terms	$5, \dots, 50$
n_y	Output lag	$2, \dots, 10$
n_u	Input lag	$2, \dots, 30$

Table 4.7 shows the range of parameters used in the direct identification of the MSA predictors. The identified model structures and parameters can be found in Appendix B.5.

4.4.3 Model validation

Once more, after the structure identification and parameter estimation procedures were completed, the model validation was carried out.

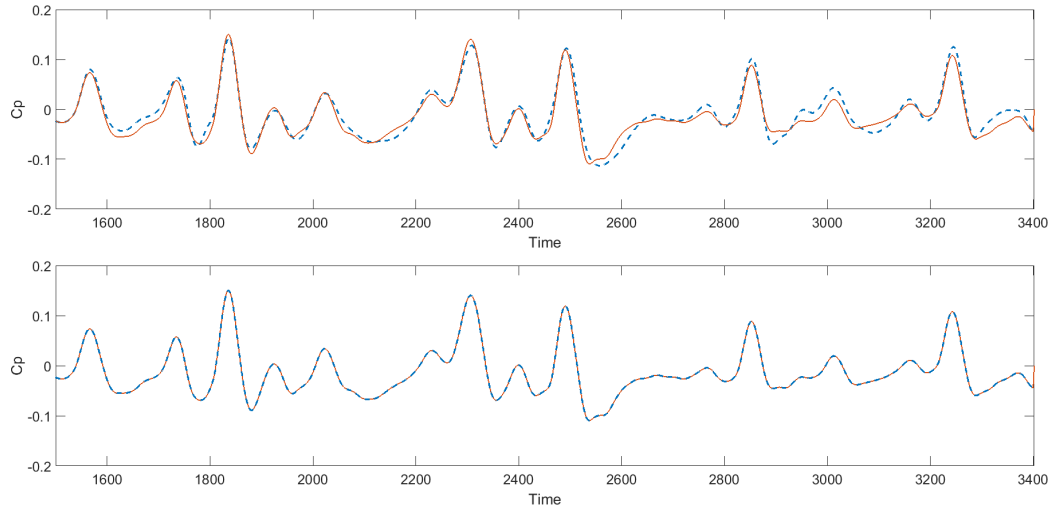

Figure 4.13. Top: Model predicted output (in blue) and measured signal (in red) of validation data for C_p fluctuation using M_{Cp}. The $NRMSE = 15.37\%$. Bottom: One step ahead predictions (in blue) and measured signal (in red) for C_p fluctuation using M_{Cp}. The $NRMSE = 1.8\ 5\%$.

First, the validation of the M_{Cp} was carried out. For this the MPO was obtained by stimulating the model with the validation data and comparing it with the measurements. The NMRSE was obtained to evaluate the performance of these models, the simulation results can be seen in Figure 4.13. As it can be seen the predictions on the unseen data have almost the same accuracy as those on the training set with an $NRMSE = 15.3\%$. This indicates that the model is an adequate representation of the system and not simply a good fit to the data.

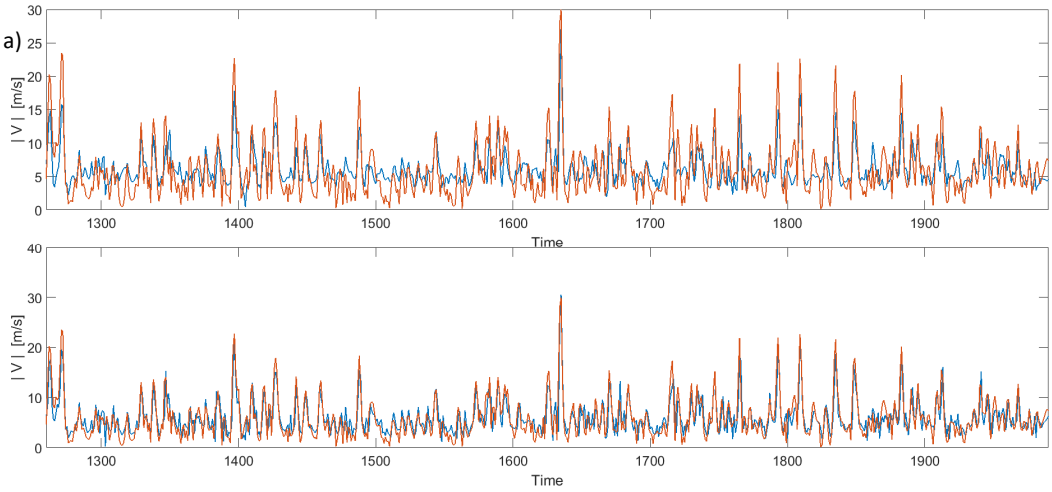

For caption see next page

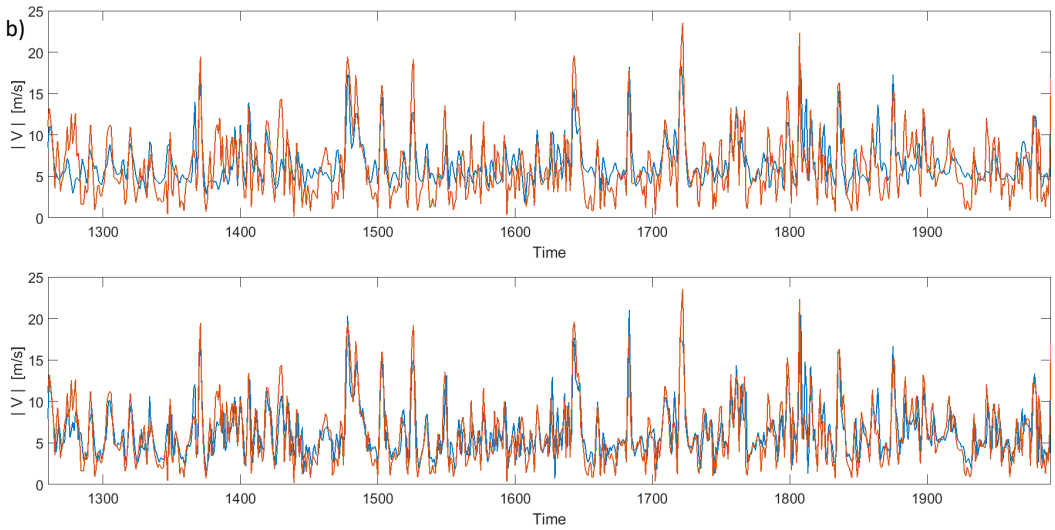

Figure 4.14. a) Top: Model predicted output (in blue) and measured signal (in red) of validation data of $|V|$ fluctuation using M_{V2}. The $NRMSE = 34.74\%$. Bottom: One step ahead predictions (in blue) and measured signal (in red) of validation data of $|V|$ fluctuation using M_{V2}. The $NRMSE = 26.53\%$. b) Top: Model predicted output (in blue) and measured signal (in red) of validation data of $|V|$ fluctuation using M_{V4}. The $NRMSE = 38.63\%$. Bottom: One step ahead predictions (in blue) and measured signal (in red) of validation data of $|V|$ fluctuation using M_{V4}. The NRMSE=29.84%.

The MPO of the M_V models on the validation data were obtained for both cases, with two and four actuators. The NRMSE was computed to evaluate the performance, and the simulation can be seen in Figure 4.14. The NRMSE has decreased slightly in the validation data compared to the training, and this is likely to be due to the different weights given to small and large errors by the NRMSE as mentioned previously.

Visually it can be seen that the predictions have a similar performance, where the main peaks and valleys are simulated with good accuracy, while smaller dynamics are not always followed. This is likely to be due to the high influence that surrounding nodes have on the current one, which in the MISO models is not present.

Table 4.8. NMRSE of the MPO for M_{V2} over training and validation data for the MSA predictors. Also shown are number of process terms, order, and maximum input/output lags.

M_{V2} MSA	Training NMRSE	Validation NMRSE	P_p	Order	n_u	n_y
2	37.84%	38.15%	21	2	10	2
3	40.73%	41.77%	15	2	14	7
4	40.65%	42.63%	9	3	10	6
5	40.79%	42.90%	9	2	14	6

In the case of the MSA predictors, the performance of each can be analysed by simulating them individually, the results of this can be seen

in Appendix B.4, while the NRMSE for each of the M_{V2} and M_{V4}, j-step ahead models are given in Table 4.8 and Table 4.9, respectively.

Table 4.9. NMRSE of the MPO for M_{V4} over training and validation data for the MSA predictors. Also shown are number of process terms, order, and maximum input/output lags.

M_{V4} MSA	Training NMRSE	MPO NMRSE	P_p	Order	n_u	n_y
2	40.39%	40.54%	21	2	10	2
3	40.23%	41.5%	15	2	14	7
4	41.76%	44.75%	9	3	10	6
5	44.52%	43.04%	9	2	14	6

Here the performance of the models deteriorates slightly with the increase of number of steps-ahead predicted. However, as is visible in the graphs of Appendix B.4, the predictions of the main trends are sufficiently accurate to be used. Additionally, the control tests using these models were successful, which also shows that the models replicate the behaviour of the flow sufficiently accurately.

4.5 Discussion

The current chapter has presented the development of reduced order models identified using measured data from simulations of flow in two scenarios. The models were identified using system identification, specifically the NARMAX methodology using a polynomial expansion for the model (Billings, 2013).

A section of the generated data in each case was assigned as training and the remainder as validation. The identified models were tested and proved to be an accurate representation of the system and its underlying dynamics and not simply a fit to the specific data set.

In the case of the channel flow data, a MIMO model made up of 27 different sub-types was identified from measurements of the velocity components of the flow. The nodes of the domain were categorized into different classes and sub-types with a structure identified for each. The number of inputs, lags and model order varied for each sub-type, with a constant three outputs at each one. Each of the structures was tested on an unseen data set and the NRMSE calculated for each to ensure it was acceptable. Additionally, a visual inspection of the superimposed time

series was carried out to verify that the main dynamics had been reproduced by the MPO.

As for the data from the flow over a BFS, three models were obtained. A SISO model has been identified which represents the input/output behaviour of the pressure coefficient C_p (at location P_{Cp}), in the presence of an external actuation, in the form of suction and blowing upstream of the step wall. Considering the fluctuations of the velocity $|V|$, two MISO models were obtained, one with two and one with four actuators on the step wall considered as inputs, and the velocity magnitude at position P_V as the output.

Again, the performance of the models was visually inspected and the NRMSE monitored during the structure selection to ensure the models were accurate, and later validated using new data.

The identified OSA predictors were used to design and implement a predictive controller of flow over the BFS. The results obtained were not adequate, therefore, multi-step-ahead predictors were identified using the same data. These have been shown to be more accurate than using one-step ahead models recursively (Atiya, El-Shoura, Shaheen, & El-Sherif, 1999; Zhang, Eddy Patuwo, & Y. Hu, 1998). Additionally, since the j-step ahead predictors depend only on data up to instant k, they can be evaluated simultaneously (Bai, 2010; Billings, 2013). Thus, allowing for parallel schemes to be implemented and calculation speeds to be minimized. Something that is key when implementing controllers on fast systems such as a fluid flow (Ho & Tai, 1998; Lofdahl & Gad-El-Hak, 1999).

As with any system identification technique, the NARMAX methodology requires that the data used in the scheme have certain properties. This work has attempted to fulfil these as much as possible, however due to the numerical methods and other limitations, some approximations have had to be made. The limitation of the actuation magnitude by the CFD package of both flow scenarios, mean that the simulated flow has not been excited by the full range of magnitudes which could have been applied to the real system. This is of course undesirable, however, since limitations on actuation and sensing exist in any real system, there can never be a truly persistently exciting

actuation nor the perfectly sampled signal. Approximations and trade-offs have to be made where necessary to study the application and decide the boundaries that need to be set (Billings, Chen, & Korenberg, 1989).

To improve the validity of the identified models, in future work, it would be of interest to study available sensors and actuators. This is so that, in addition to carrying out the studies on a domain with realistic dimensions, as in this work, the sampling rate and frequency/magnitude limitations of actuations are included. Hence, the models obtained using this set-up would be a better approximation to an implementable system. As long as the necessary calculations can be made in real-time.

A final matter to consider is the evaluation of the accuracy of the model, to determine that it is an adequate representation of the system and not a good fit to a certain data set. This has been studied extensively but remains a key question (Billings & Zhu, 1995; Haynes & Billings, 1994; Ljung, 2010). Two possible reasons for this is firstly, that measures of accuracy, such as the NRMSE, vary the way in which errors of different magnitudes are penalized (De Gooijer & Hyndman, 2006). This means that a well performing model may have a high NRMSE, if the data set contains large peaks or is close to zero for example, whereas a bad model may have a low NRMSE. Secondly, to evaluate if the model has been over/under fitted, it is necessary to carry out dynamical and statistical tests (Billings, 2013; Billings & Voon, 1986; Zheng & Billings, 1999). That is, calculate the MPO over validation data to ensure that the performance of the model remains close to constant with that of the training (Ayala Solares & Wei, 2015; Billings, 2013; Zheng & Billings, 1999).

The issue with finding a correct measure of accuracy has been encountered in the current work, were the MSA predictors have shown good performance on the validation set as well as the implementation of a predictive controller, as detailed in Chapter 6, but have relatively high NRMSE. As mentioned before, other measures were tested but the discrepancy between the scores given to the different models tested in addition to a visual inspection were more inconsistent, thus the NRMSE was chosen to evaluate the identified models.

Regarding the second issue, to determine if the models are over/under fitted they have been tested on new data. However, for the

models identified for the flow over the BFS case, it would be of interest to test the models with data obtained from simulations with different flow properties, like Reynolds number. This to verify that the model truly represents the dynamics of the flow and is not simply performing well with the validation data, which has not been '*seen*' by the model but may have similar behaviour since it is of the same flow.

Finally, regarding the choice of variables used in the identification of the models, it should be mentioned that the velocity components and magnitude were used since this has been done successfully in previous studies and experimental set-up's (Bewley, 2001; Le, Moin, & Kim, 1997; Lumley & Blossey, 1998; Moser, Kim, & Mansour, 1999). Additionally, after trial model identification using other variables, the velocity fluctuations were found to be more suitable, and their models performed better than the wall-shear for example.

It is known that the latter is useful to determine the reattachment point. However, since it is a time averaged value and a method to obtain the 'correct' instantaneous position could not be determined, it was decided to study the alternative variables.

CHAPTER 5

Review of control strategies for fluid flows

5.1 Introduction

Natural and man-made systems that interact with fluid flows are subject to considerable flow-induced forces that often have a detrimental effect on these systems (Kubo, Modi, Kotsubo, Hayashida, & Kato, 1996; Obeid, Jha, & Ahmadi, 2012). For example, turbulent flow around a wing leads to increase in drag, a decrease in lift and overall heightened fuel consumption (De Giorgi, De Luca, Ficarella, & Marra, 2015; Obeid, Jha, & Ahmadi, 2012; Wu, Z., Wong, Wang *et al.*, 2015). In contrast, turbulent flow of the air-fuel mixture inside of the combustion chamber of an engine is beneficial for an efficient combustion (Kim, J. & Bewley, 2007).

In both examples, and many other systems, the passive (i.e. the optimization of wing profile) or active (i.e. dynamic actuation on the flow) manipulation of the flow can enhance performance (Cattafesta Iii, Song, Williams, Rowley, & Alvi, 2008; De Giorgi, De Luca, Ficarella, & Marra, 2015).

One of the most notable impacts that flow control can have in modern society is in the transport industry where drag, due to skin-friction, accounts for 40-80% of the total drag (Davidson, Kaneda, & Sreenivasan, 2013; Ipcc, 2014; Viswanath, 2002). Huge monetary savings, in addition to ecological benefits brought on at the same time by the lessening of CO_2 emissions are expectable (Ipcc, 2014; Kim, J. & Bewley, 2007; Scott Collis, Joslin, Seifert, & Theofilis, 2004). The Advisory Council for Aerospace Research in Europe (ACARE) have set a target for 2020 that fuel consumption and emissions are to be reduced by 50%, relative to 2000 (De Giorgi, De Luca, Ficarella, & Marra, 2015; Glynn, 2011).

Flow control has been studied for many years (Bewley, 2001; Kim, J., 2003; Kim, J. & Bewley, 2007; Scott Collis, Joslin, Seifert, & Theofilis, 2004). Some argue (Scott Collis, Joslin, Seifert, & Theofilis, 2004; Uruba, Jonáš, & Mazur, 2007) that flow control has its origins in 1904 when Prandtl defined the aerodynamic boundary layer in his seminal paper (Prandtl, 1905).

Since then several strategies for controlling fluid flows have been developed (Bewley, 2001; Choi, H., Moin, & Kim, 1994; De Giorgi, De Luca, Ficarella, & Marra, 2015; Gad-El-Hak, 1989; Kim, J., 2003; Kim, J. & Bewley, 2007; Lumley & Blossey, 1998; Pollard, 1998; Rathnasingham & Breuer, 2003; Scott Collis, Joslin, Seifert, & Theofilis, 2004). These can be classified according to different criteria such as (Bewley, 2001; Gad-El-Hak, 1989; Kim, J. & Bewley, 2007; Lumley & Blossey, 1998; Pollard, 1998; Scott Collis, Joslin, Seifert, & Theofilis, 2004):

- The way in which the flow is modified – using passive or active means
- The type of actuator – using riblets, synthetic jets or plasma actuators, for example
- The objective of the controller – to induce drag reduction, separation delay, or mixing enhancement
- Type of control scheme used – open- or closed-loop (with further sub-divisions for the latter depending on the implemented algorithms)

This Chapter provides a literature review of theoretical and practical flow control approaches with an emphasis on studies carried out on wall bounded flows, as these are most relevant to the current work.

The Chapter is organized as follows. Passive approaches for flow control are described in Section 5.2. Existing sensors and actuators are summarized in Sections §5.3.1. Section 5.3.2 provides a review of active open-loop methodologies whereas closed-loop approaches are reported in Section 5.3.3. A discussion of the presented methodologies considering current issues identified is given in Section 5.4

5.2 Passive flow control approaches

Passive flow control methods are those which, as the name implies, do not require any type of external energy, momentum, or mass to carry out their function (Heenan & Morrison, 1998; Li, Jessen, Roggenkamp *et al.*, 2015; Perlin, Dowling, & Ceccio, 2016; Pollard, 1998; Sattarzadeh, Fransson, Talamelli, & Fallenius, 2014). These type of schemes (typically) do not change with time and often consist of an alteration to the domain boundaries (Perlin, Dowling, & Ceccio, 2016; Viswanath, 2002). Different types of structures and coatings have been used to modify the behaviour of the flow (Perlin, Dowling, & Ceccio, 2016; Viswanath, 2002).

The major interest in this type of control scheme lies precisely in the fact that after the initial design and implementation of the wall or fluid modification, no further energy or input is required (Fransson, 2015; Perlin, Dowling, & Ceccio, 2016). Hence, there is an improvement of the specific goal or performance at a low cost and effort.

Different types of wall modifications have been reported, the most common being riblets, grooves, large eddy break-up devices (LEBU's) (Sutardi & Ching, 1999; Wahidi, Chakroun, & Al-Fahed, 2005), compliant and super-hydrophobic surfaces have also been implemented and more recently the application of biologically inspired textures, such as replicating shark skin (Choi, H., Moin, & Kim, 1993; Dean & Bhushan, 2012; Lee, S. J. & Lee, 2001; Perlin, Dowling, & Ceccio, 2016; Pollard, 1998; Scott Collis, Joslin, Seifert, & Theofilis, 2004; Spalart, Strelets, & Travin, 2006).

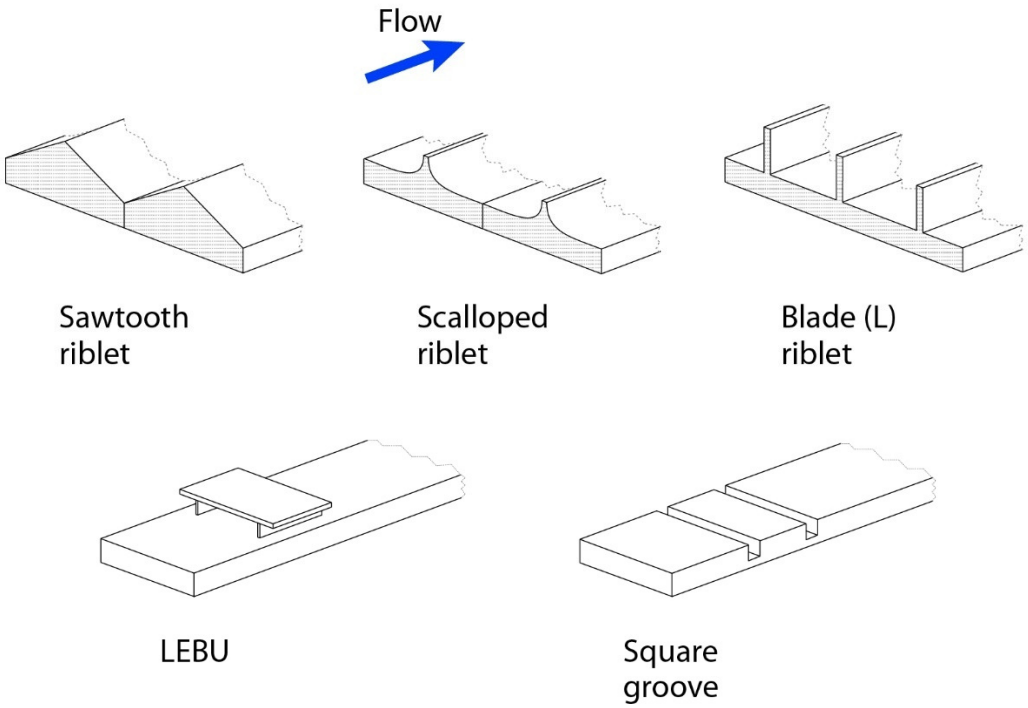

Figure 5.1 Schematic of different passive methods to alter the boundary layer in channel flow.

In the case of channel flow, grooves, riblets and LEBU's have been the most implemented (Choi, H., Moin, & Kim, 1993; Dean & Bhushan, 2012; Lee, S. J. & Lee, 2001; Li, Jessen, Roggenkamp *et al.*, 2015; Perlin, Dowling, & Ceccio, 2016; Viswanath, 2002). These are slots or protrusions which cross the entire domain in the streamwise or spanwise direction (Choi, H., Moin, & Kim, 1993; Dean & Bhushan, 2012; Li, Jessen, Roggenkamp *et al.*, 2015) as seen in Figure 5.1, except for the LEBU which is finite (Neumann & Wengle, 2003; Spalart, Strelets, & Travin, 2006).

Studies have been carried out in plane or channel flows as in (Choi, H., Moin, & Kim, 1993; Dean & Bhushan, 2012; Gad-El-Hak, 1989; Perlin, Dowling, & Ceccio, 2016; Pollard, 1998), or over aerofoils (Park, Sun, & Kim, 2014; Viswanath, 2002).

A few authors have looked at the effect of different slot shapes and sizes in flows with varying Reynolds number (Sutardi & Ching, 1999; Wahidi, Chakroun, & Al-Fahed, 2005). Additionally, (Li, Jessen, Roggenkamp *et al.*, 2015) has performed tests using riblets on a moving wall, thus increasing the effect which they can have. This is one of the first examples of a mixture of active and passive approaches.

It is thought that riblets and alike devices impede cross-flow motion, and weaken near-wall streamwise vortices (Dean & Bhushan, 2012; Lee,

S. J. & Lee, 2001; Viswanath, 2002), whereas grooves weaken the boundary layer hence turbulence is reduced and further instabilities dampened (Sutardi & Ching, 1999; Wahidi, Chakroun, & Al-Fahed, 2005).

The cases which report a decrease in drag force have found that there is a correlation between the dimensions of the riblet/groove and the drag reduction possible (Choi, H., Moin, & Kim, 1993; Dean & Bhushan, 2012; Li, Jessen, Roggenkamp *et al.*, 2015; Perlin, Dowling, & Ceccio, 2016; Viswanath, 2002). Additionally, several authors have found that in the case of grooves, a sharp increase in skin-friction C_f occurs immediately downstream, followed by a decrease and a slow oscillatory return to the smooth-wall value (Choi, H., Moin, & Kim, 1993; Dean & Bhushan, 2012; Gad-El-Hak, 1989; Li, Jessen, Roggenkamp *et al.*, 2015; Pollard, 1998). It was also found that the effects of the riblets and grooves remain largely within the boundary layer, and have little effect on the mean flow where bulk velocity and turbulent energy for example, remain largely unchanged (Sutardi & Ching, 1999).

Most of the studies mentioned here present a drop between 1% and 6% of drag reduction when using either of these methods under specific flow and riblet / groove dimensions (Perlin, Dowling, & Ceccio, 2016; Spalart, Strelets, & Travin, 2006; Sutardi & Ching, 1999; Wahidi, Chakroun, & Al-Fahed, 2005). Further, the effect was seen to usually increase proportionally with Reynolds number up to a certain limit (Wahidi, Chakroun, & Al-Fahed, 2005). However, drag increase has also been found with certain parameters, such as arrays of micro-grooves (Bewley, 2001; Gad-El-Hak, 1989; Li, Jessen, Roggenkamp *et al.*, 2015; Pollard, 1998; Scott Collis, Joslin, Seifert, & Theofilis, 2004).

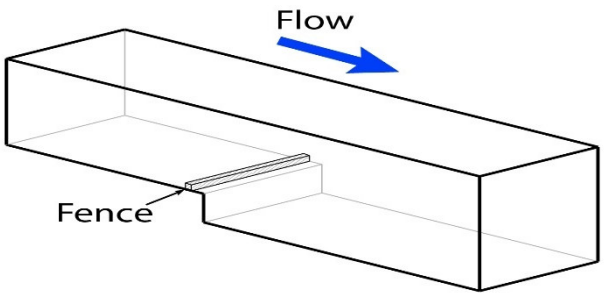

Figure 5.2. Schematic of the flow over the BFS domain using upstream square fence to control the reattachment length.

In the case of flow over the BFS, studies where a *fence* is added on the inlet wall, as seen in Figure 5.2, have shown that its position and height have a strong effect on the size of the recirculation zone downstream of the step (Neumann & Wengle, 2003; Terekhov, Smul'skii, & Sharov, 2012). Neumann et al. and Terekhov have carried out similar studies, the former using DNS and LES methods and the latter through experiments (Neumann & Wengle, 2003; Terekhov, Smul'skii, & Sharov, 2012). The experimental results showed a drop of around 30% of the reattachment distance X_r, with respect to the base flow, whereas the simulations indicated a smaller decrease of 13% (Neumann & Wengle, 2003; Terekhov, Smul'skii, & Sharov, 2012). This discrepancy can be attributed to the slight geometrical differences of the domains studied in each case (Driver & Jovic, 1994; Le, Moin, & Kim, 1997), in addition to a greater impact of the numerical and discretization error on this more complicated flow (Neumann & Wengle, 2003; Terekhov, Smul'skii, & Sharov, 2012).

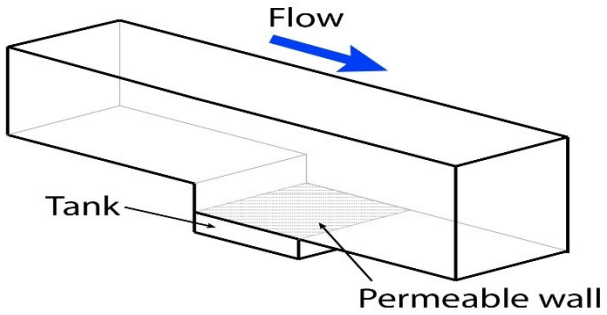

Figure 5.3. Schematic of the flow over the BFS domain using passive permeable wall to control the reattachment length.

Two final passive schemes which have been reported are using a permeable reattachment surface on the outlet wall of the flow over the BFS domain (Heenan & Morrison, 1998), as shown in Figure 5.3, and the so-called reinforced passive control over a flat plate (Sattarzadeh, Fransson, Talamelli, & Fallenius, 2014). The permeable wall method by Hennan and Morrison, consists of the traditional BFS geometry with a plenum of "quiescent" fluid beneath the permeable section of the outlet wall, this is sealed so that there is zero net mass-flux (Heenan & Morrison, 1998).

This technique increases the reattachment distance by around 20%, however, the flow downstream of the step is stabilized. This is likely to

be due to an inhibition of unsteady pressure convection and vorticity from the recirculation zone back to the step (Heenan & Morrison, 1998).

On the other hand, the reinforced passive control consists of a mixture of a groove on a flat plate, with arrays of vortex generators further downstream to extend the stabilizing effect (Sattarzadeh, Fransson, Talamelli, & Fallenius, 2014). Comparing the un-manipulated flow, flow with a single groove and flow with a groove and vortex generator mix, Sattarzadeh et al. have managed to delay the transition onset from $X_{tr} = 1.3m$, to $X_{tr} = 2.9m$ and in the last case completely removing it from the considered plate, that is $X_{tr} > 4m$. Considering this, the overall drag can be calculated using the Blasius skin-friction relation for the laminar section of the boundary layer, and an empirical relation for the turbulent part, giving a reduction of 39% and 65% of drag force compared to the uncontrolled case (Sattarzadeh, Fransson, Talamelli, & Fallenius, 2014).

The situation where a slight change in the dimension of the implemented device, be it a riblet or fence, leads to a radical change in performance, can be considered as a clear example of the drawback to using passive methods (Choi, H., Moin, & Kim, 1993; Perlin, Dowling, & Ceccio, 2016; Viswanath, 2002). They are inherently limited to deliver the expected results only while operating under conditions like those of their design (Bewley, 2001; Gad-El-Hak, 1989; Perlin, Dowling, & Ceccio, 2016; Scott Collis, Joslin, Seifert, & Theofilis, 2004). Thus, drag reduction for example, can be lower than anticipated, or altogether increased if the nominal flow conditions are surpassed. This, coupled with the need to react to changes instantaneously, are the main reasons that active control methods have been developed (Choi, H., Moin, & Kim, 1994; Gad-El-Hak, 1989; Perlin, Dowling, & Ceccio, 2016; Scott Collis, Joslin, Seifert, & Theofilis, 2004).

5.3 Active flow control approaches

To overcome the fact that passive controllers provide a relatively small benefit, and can quickly become a burden if the conditions of the system change. In addition to the desire of gaining a higher increase of

performance, active control approaches have been studied with increasing frequency in all manner of applications. Fluid control is no exception and more methods have been considered over the past few decades (Bewley, 2001; Gad-El-Hak, 1989; Perlin, Dowling, & Ceccio, 2016; Scott Collis, Joslin, Seifert, & Theofilis, 2004).

Active controllers are defined as those which require a form of external energy input to be able to affect the system, in this case the fluid flow, and this is often delivered by means of unsteady actuators (Choi, H., Moin, & Kim, 1994; Chung & Talha, 2011; Gad-El-Hak, 1989; Perlin, Dowling, & Ceccio, 2016; Pollard, 1998; Rathnasingham & Breuer, 2003; Scott Collis, Joslin, Seifert, & Theofilis, 2004).

The schemes that fall into this kind can be further categorized according to the actuation, as mentioned, but a more significant method is by the way in which the controller responds to changes in the flow (Bewley, 2001; Gad-El-Hak, 1989; Kim, J. & Bewley, 2007; Lumley & Blossey, 1998; Pollard, 1998; Scott Collis, Joslin, Seifert, & Theofilis, 2004). That is, by defining if the method is open- or closed-loop, where the former does not react to change in the flows, rather it is prescribed, and the latter includes the feedback of a measured quantity that the controller uses to calculate future actuations to drive the system to the desired state (Bewley, 2001; Gad-El-Hak, 1989; Scott Collis, Joslin, Seifert, & Theofilis, 2004). Open-loop control is often viewed as an under-utilization of the possibility of reacting according to the system's state (Scott Collis, Joslin, Seifert, & Theofilis, 2004).

One of the main advantages of active controllers is that, theoretically, a larger impact on flow behaviour is possible by means of localized sensing and actuation, than that achievable by passive means (Scott Collis, Joslin, Seifert, & Theofilis, 2004; Zhou & Bai, 2011). The optimal arrangement of sensors and actuators is not something that can be easily determined, and research is still ongoing. (Bewley, Moin, & Temam, 2001; Gad-El-Hak, 1989; Perlin, Dowling, & Ceccio, 2016; Scott Collis, Joslin, Seifert, & Theofilis, 2004; Zhou & Bai, 2011).

5.3.1 Sensors and actuators used in active flow control

This section provides a brief description of available actuators and an overview of sensors, which are both essential elements of both open- and closed-loop control. The details of how such devices are used in flow control are saved for the next sections where the controller schemes are introduced.

Most of the implementations presented here are using wall bounded flows. These actuators have been known to be used in other configurations, however, initial studies are often performed on this geometry to test their performance and study the mechanisms by which the flow behaviour is changed.

There are two main types of actuators which involve the injection of fluid into the main flow (De Giorgi, De Luca, Ficarella, & Marra, 2015; Kim, J., 2003). The source of this additional fluid can be external in the case of jets, or from the same flow, as synthetic jets (Bewley, 2001; De Giorgi, De Luca, Ficarella, & Marra, 2015; Gad-El-Hak, 1989; Pollard, 1998; Scott Collis, Joslin, Seifert, & Theofilis, 2004; Xu, Gao, Ming *et al.*, 2015).

This kind of actuators have been studied in simulations and experimental set-ups (De Giorgi, De Luca, Ficarella, & Marra, 2015; Rathnasingham & Breuer, 2003; Scott Collis, Joslin, Seifert, & Theofilis, 2004). There have been trials with single actuators or arrays, which in turn, are localized or spread throughout the domain (Chung & Talha, 2011; Ricco & Dilib, 2010; Uruba, Jonáš, & Mazur, 2007). In simulations, these actuators are often used as wall transpiration, which represents arrays of jets that provide wall-normal velocity at different locations (De Giorgi, De Luca, Ficarella, & Marra, 2015; Rathnasingham & Breuer, 2003).

The current work uses these actuators in both flow cases. For the channel flow case, the velocity is added at all computational nodes on the boundary.

Therefore, it can be considered that the actuator nozzle is of the same dimensions of the domain, or that there is an actuator at each of the nodes. On the other hand, in the flow over the BFS case, the control action is in the form of an array of actuators, here each of them have a

pre-defined size and position. At the current stage, the dimensions of these actuators have been set based on previous studies or limitations of the domain and CFD package, rather than properties of real devices.

Overall jets have been found to be able to produce a larger effect since the pressure at which they operate can be defined externally (De Giorgi, De Luca, Ficarella, & Marra, 2015). On the other hand, synthetic jets often depend on membranes that oscillate, or moving walls within a cavity to create movement of the flow which is pushed through an opening on the wall, which greatly limits the force available (De Giorgi, De Luca, Ficarella, & Marra, 2015; Okada, Miyaji, Fujii *et al.*, 2010; Scott Collis, Joslin, Seifert, & Theofilis, 2004; Xu, Gao, Ming *et al.*, 2015). In some studies, it has been reported that the net energy saving of jets is found to be small if not negative due to the large amount of energy that is required by the actuator (Lumley & Blossey, 1998; Perlin, Dowling, & Ceccio, 2016; Pollard, 1998). This in usually not the case with synthetic jets, which can have a great impact if the limited actuation manages to modify the flow considering the low input energy required (De Giorgi, De Luca, Ficarella, & Marra, 2015; Wang, Luo, Xia, Liu, & Deng, 2012).

Mechanical actuators are generally those which create a deformation of the boundary or movement of certain elements such as flaps (Wang, Luo, Xia, Liu, & Deng, 2012). Arrays of micro-electromechanical-systems (MEMS) can deliver wall deformations of different amplitudes and at high frequencies (Ho & Tai, 1998; Lofdahl & Gad-El-Hak, 1999a, 1999b; Segawa, Kawaguchi, Kikushima, & Yoshida, 2002; Varadan & Varadan, 2000). Experiments have also been performed using oscillating sections of wall (Ricco, Ottonelli, Hasegawa, & Quadrio, 2012; Zhao, Wu, & Luo, 2004).

Trials using groups of vibrating walls have been used to simulate wave-like deformations of the wall. Results have been varied and the frequency at which the wall(s) vibrate, or of the travelling wave have a great impact on the success of the scheme (Pollard, 1998; Quadrio, Ricco, & Viotti, 2009; Ricco & Quadrio, 2008; Ricco & Wu, 2004; Segawa, Kawaguchi, Kikushima, & Yoshida, 2002). The main idea behind these type of actuators is that the oscillating surface can alter the flow

momentum in the boundary layer, which in turn reduces the turbulence intensity (Wang, Luo, Xia, Liu, & Deng, 2012).

The use of plasma actuators, consisting of two electrodes placed on either side of a thin dielectric material, that create an ionized region capable of accelerating the fluid in its vicinity, has increased in previous years (Pouryoussefi, Mirzaei, & Hajipour, 2015; Wang, Luo, Xia, Liu, & Deng, 2012; Wu, Z., Wong, Wang *et al.*, 2015). This mainly due to the high flow speeds which can be generated by such devices, in addition to the ease of implementation and lack of moving parts. A similar effect to a jet which is parallel to the flow is obtained using these actuators, however it has a higher response rate (Pouryoussefi, Mirzaei, & Hajipour, 2015; Wang, Luo, Xia, Liu, & Deng, 2012).

Experimental trials have been carried out as will be discussed later. However, simulations have not been thoroughly investigated to better understand the way in which the plasma interacts with the flow since it is difficult to model this phenomenon (Perlin, Dowling, & Ceccio, 2016).

The final type of actuation to be discussed is that of using non-intrusive forces on the flow. An important example of this is the use of the Lorentz force, generated when an electrically conducting fluid flows through a magnetic field (Zhou & Bai, 2011). Using this force different types of actuation can be simulated such as wall-normal suction and blowing, streamwise forcing and spanwise travelling waves (Huang, L., Fan, & Dong, 2010). This shows that it can be a versatile tool, since it is likely to be the most re-configurable, however, this type of actuation can only be applied to very specific fluids (Huang, L., Fan, & Dong, 2010).

In the case of sensors, many technologies have been studied and stablished to measure a wide range of variables in flows of different fluids and properties (Wang, Luo, Xia, Liu, & Deng, 2012). In this discipline, care should be taken to ensure that the required scales can be measured when implementing a real sensor (Lofdahl & Gad-El-Hak, 1999a, 1999b). Much debate surrounding the adequate resolution and distance between arrays of sensors for example, has been generated over the years (Kasagi, Suzuki, & Fukagata, 2009; Lofdahl & Gad-El-Hak, 1999a, 1999b; Varadan & Varadan, 2000). This has been helped by the creation of MEMS since they allow for smaller scales to be identified, however if

measurements near the wall are required, then even these might prove to be insufficient (Lofdahl & Gad-El-Hak, 1999b).

The main variables in a flow are the velocity, pressure and also of importance is the wall shear (Frank, 2011). Sensors which focus on measuring these quantities have existed for many years.

Pressure sensors use piezo-electric or -resistive configurations, where vibrations cause a small diaphragm to deflect, and depending on the type of sensor this will cause a small voltage to be generated. Capacitive sensors have also been implemented (Lofdahl & Gad-El-Hak, 1999a, 1999b).

For the determination of wall shear stress, the application defines the resolution that is necessary. However, for this variable not only the mean shear is necessary but also its fluctuations, particularly in the case of turbulent flows (Haritonidis, 1989; Lofdahl & Gad-El-Hak, 1999a). The wall shear can be obtained through direct measurements using floating element sensors or inferred from other quantities as with correlation methods or momentum balance techniques (Haritonidis, 1989; Ho & Tai, 1998; Lofdahl & Gad-El-Hak, 1999a, 1999b; Varadan & Varadan, 2000). Examples of these are too many to be discussed here and the reader is referred to (Haritonidis, 1989) for a review of methods.

5.3.2 Open-loop flow control

Many approaches have been taken using open-loop strategies by different authors where these techniques incorporate the use of actuators which have a predefined function (Bewley, 2001; Gautier & Aider, 2014b; Kim, J., 2003; Pollard, 1998; Zhao, Wu, & Luo, 2004; Zhou & Bai, 2011). In addition, they have no way of sensing the current state of the flow to adjust their behaviour. The benefit of these control schemes over passive ones, is that they can easily be adjusted if new knowledge or circumstances are presented (Bewley, 2001; Joshi, Speyer, & Kim, 1997; Kim, J., 2003; Pollard, 1998).

Plasma actuators have been used mainly on the flow over the BFS geometry, where different authors have studied the effect of actuator positioning (Koide, Sasaki, Kameya, & Motosuke, 2015; Pouryoussefi,

Mirzaei, & Hajipour, 2015; Wang, Luo, Xia, Liu, & Deng, 2012; Wu, Z., Wong, Wang *et al.*, 2015). In a study by (Pouryoussefi, Mirzaei, & Hajipour, 2015), the effects of a dielectric barrier discharge (DBD) actuator have been experimentally studied over a range of Reynolds numbers.

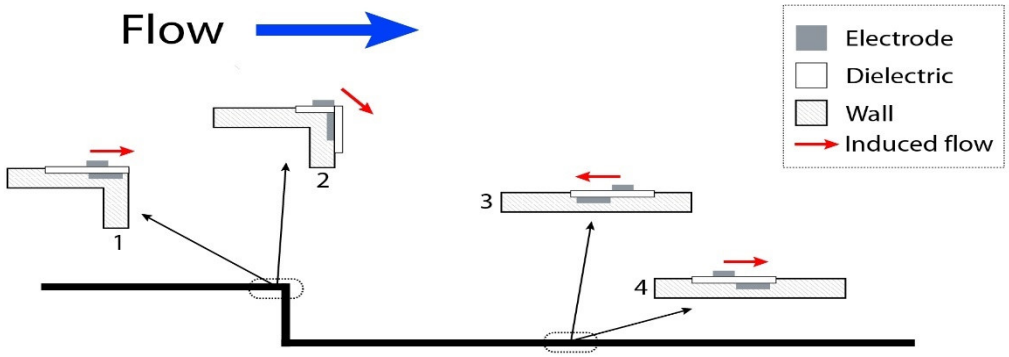

Figure 5.4. Schematic of the flow over the BFS domain using a plasma actuator on the step edge to control the reattachment length.

Four actuation positions were tested, two on the step edge which yielded an induced flow parallel to the free-stream flow or diagonally flowing into the recirculation zone, in each case. And two others downstream of the step, one inducing flow towards the step and the remaining towards the outlet. The arrangements can be seen in Figure 5.4, a schematic of the plasma actuator configuration at tach location is presented where the induced flow is directed from the exposed to the hidden electrode (Pouryoussefi, Mirzaei, & Hajipour, 2015). Each of the positions were tested individually using both, continuous and oscillating actuation with varying frequencies, the tested values chosen as multiples of the vortex shedding frequency (Pouryoussefi, Mirzaei, & Hajipour, 2015).

It was found that the actuator at position 1 was better suited to reduce the length of the recirculation zone. This was obtained by using oscillating control with a frequency equal to that of the vortex shedding of un-manipulated flow (Pouryoussefi, Mirzaei, & Hajipour, 2015). The remaining configurations showed little improvement, however it was evident that as the free stream velocity increased, the impact of the actuation became less significant regardless of the position of the actuator (Pouryoussefi, Mirzaei, & Hajipour, 2015). With this study, they defined that in flow over the BFS, the most significant ways to achieve a reduction of the reattachment length is to increase shear layer

entrainment and promote a mixture with the mean flow, or to influence the streams of the recirculation zone directly (Pouryoussefi, Mirzaei, & Hajipour, 2015). In this work, the direct manipulation of the streams in the recirculation zones was tested using the actuators placed on the step wall. The upstream actuator was used in an attempt to modify the shear-layer; however, the control was not as effective as will be discussed.

Several authors have investigated wall oscillations (Choi, K. S., 2002; Choi, K. S., Debisschop, & Clayton, 1998; Quadrio & Ricco, 2004; Ricco & Quadrio, 2008; Ricco & Wu, 2004). Studies have been performed with one and both domain walls being actuated. Additionally, tests were performed with sub-sections of the wall under actuation. It was found that the possible drag reduction using this type of control depends strongly on the maximum wall velocity and period of oscillation, where certain combinations provided up to 45% drag reduction whereas experimental trials reported lower drag reductions of approximately 25-37% (Choi, K. S., Debisschop, & Clayton, 1998; Ricco & Quadrio, 2008; Ricco & Wu, 2004). A parameter which relates the scaling of drag reduction according to the values mentioned previously is firstly proposed by (Choi, K. S., 2002; Choi, K. S., Debisschop, & Clayton, 1998), and formally defined and investigated by (Quadrio & Ricco, 2004; Ricco & Quadrio, 2008). This parameter is seen to be a powerful predictive tool to determine the drag reduction quantity over a defined threshold of wall velocity, and period of oscillations (Ricco & Quadrio, 2008).

A drawback of the simulation and experimental trials reported, is that they have been performed at moderately low Reynolds numbers (Choi, K. S., Debisschop, & Clayton, 1998; Ricco & Quadrio, 2008; Ricco & Wu, 2004). Even though the effect of the Reynolds number has been investigated, and shown to decrease the drag reduction and net energy saving across conservative values, it is not known if the same methods will continue to provide benefit at flows with more practical properties (Choi, K. S., 2002; Choi, K. S., Debisschop, & Clayton, 1998; Quadrio & Ricco, 2004; Quadrio, Ricco, & Viotti, 2009; Ricco, Ottonelli, Hasegawa, & Quadrio, 2012; Ricco & Quadrio, 2008; Ricco & Wu, 2004). The discrepancy between experimental and simulations results is thought to be due to the difference of the setup. In an experimental set-up, results

are obtained using sections of oscillating walls, while simulations often rely on periodic boundary conditions which represent infinitely long oscillating walls (Ricco, Ottonelli, Hasegawa, & Quadrio, 2012; Ricco & Quadrio, 2008).

Flow control using stream- and span-wise travelling waves generated by external forcing, such as Lorentz force, or through suction and blowing can be considered as variants to wall oscillations since they both aim to modify or eliminate streamwise streaks directly with the actuation method (Huang, L., Fan, & Dong, 2010; Quadrio, Ricco, & Viotti, 2009; Zare, Lieu, & Jovanovic, 2012; Zhao, Wu, & Luo, 2004). Using these approaches similar results of around 40-50% drag reduction were obtained (Huang, L., Fan, & Dong, 2010; Quadrio, Ricco, & Viotti, 2009; Zare, Lieu, & Jovanovic, 2012; Zhao, Wu, & Luo, 2004).

The final form of open-loop control to be discussed, which is the most extensively studied, and uses the form of actuation implemented in the current work, is that of steady and unsteady suction and blowing. The use of jets and synthetic jets are considered simultaneously, since similar mechanisms of drag-reduction are exploited using both types of actuators (De Giorgi, De Luca, Ficarella, & Marra, 2015; Okada, Miyaji, Fujii *et al.*, 2010). The difference between them lies in source of the injected flow, and how the energy is transferred as mentioned in the previous section.

In the case of flow over the BFS, (Uruba, Jonáš, & Mazur, 2007) have carried out experimental control tests using suction and blowing on a spanwise slot at the base of the step. They tested two shapes and several actuation areas, with uniform actuation across the entire step width. It was found that the orifice geometry does not affect the shortening of the recirculation zone when using constant suction, rather it is dependant only on the force applied (Uruba, Jonáš, & Mazur, 2007). Further, they found that constant blowing is also dependant on the force but more sensitive to the contact volume, i.e. the geometry of the slot.

An optimization of an actuator with varying jet angle upstream of the step was done by (Xu, Gao, Ming *et al.*, 2015). In addition to finding the optimal angle of operation, variations of the frequencies of the oscillating jet were considered. It was found that an upstream facing jet,

with the non-linear oscillations of this actuator, has a strong effect on the entrainment of the shear layer and helps it to curve inward towards the step. Thus, reducing the size of the recirculation zone.

Finally, (Gautier & Aider, 2014a) performed experimental tests using variations of jet frequency and amplitude/duty-cycle. They managed to reduce the size of the recirculation zone using various combinations of the parameters. It was noted that with certain optimal jet amplitudes, the duty-cycle could be lowered to around 10% and still yield reductions of the reattachment length of 90%. Gautier et. al. claim that this upper bound of performance is due to the actuator imperfections rather than the actual method used. However, if the jet amplitude exceeded certain values, the recirculation zone was greatly increased.

Numerical analysis by (Kim, K. & Sung, 2006) of periodic blowing on a channel flow were carried out. A single geometry for the slot was used and variation of the frequency of the jet oscillations analysed. Using this technique, drag reduction of up to 70% were obtained by unsteady blowing as well as steady force. These results have been confirmed experimentally and drag reductions of up to 50% have been obtained (Kim, J., 2003; Kim, K. & Sung, 2006).

(Ricco & Dilib, 2010) have performed simulations of the effect that wall transpirations have on the vorticity disturbances of the incompressible Blasius boundary layer. Here they found that wall suction can attenuate both two- and three-dimensional fluctuations. Lower frequency structures are attenuated and high frequency are merely shifted towards the inner flow. This is enough to reduce the turbulent energy of the flow; however, it is dependent on the magnitude of the actuation.

5.3.3 Closed-loop flow control

Taking into consideration the limitations of open-loop controllers, in addition to the need to react in real-time to the state of the flow, the development of closed-loop strategies has been studied by several authors (Bewley, Moin, & Temam, 2001; Henning & King, 2007; Obeid, Jha, & Ahmadi, 2012; Pollard, 1998; Scott Collis, Joslin, Seifert, &

Theofilis, 2004; Wu, G. C., Baleanu, Zeng, & Deng, 2015; Wu, Z., Wong, Wang *et al.*, 2015). The previous open-loop approaches and the knowledge gained, has helped to develop a better comprehension of the different phenomena and overall flow behaviour. Using this, better models of the flow can now be obtained, which lead to development of improved closed-loop controllers, and may also contribute with the development of actuators (Kim, J., 2003; Lofdahl & Gad-El-Hak, 1999b; Scott Collis, Joslin, Seifert, & Theofilis, 2004).

The most significant and relevant approaches, described below, have been grouped by the type of control method used, such as classical and modern control, neural networks, optimal control, and finally data-based model methods (Pollard, 1998; Scott Collis, Joslin, Seifert, & Theofilis, 2004). The latter were isolated since they are the most closely related approaches to the current work.

Considering that turbulence production near the wall is related to the large coherent structures, which can be modelled by linear dynamical equations (Pollard, 1998; Rathnasingham & Breuer, 2003), a MIMO linear filter was used by Rathnasingham to estimate a transfer function between three spanwise wall sensors and three downstream sensors, designated outputs/control points. A second transfer function is estimated from the actuators (inputs), which lie between the first set of sensors and the control points themselves.

The control method consisted in minimizing a cost function defined from measured values at the control points. This was implemented in a wind tunnel, initial tests to validate the identified transfer functions were performed, the predictions obtained by the model were found to be accurate. Actuated trials were then performed with one and three actuators. The results were that the streamwise velocity fluctuations could be reduced by around 25% using both configurations, when measuring the velocity at the control points. This translates roughly to a reduction of around 7% of the drag force in the flow (Rathnasingham & Breuer, 2003).

Another study using linear control scheme is that of (Joshi, Speyer, & Kim, 1997), where, using the linearized Navier-Stokes equations, they develop a finite dimensional SISO state space model, using a Galerkin

method to transform from the partial differential equations. A PI controller was implemented using x-direction wall-shear measurements, this approach was used to stabilize 2-D plane flow. It was noted that the position of the actuator and type of sensing can lead to changes in the pole/zeros of the model (Joshi, Speyer, & Kim, 1997). Some sensor locations lead to minimum-phase systems while others to non-minimum phase, which are inherently more difficult to control. Their control was robust to varying Reynolds number, however, it was noticed that the feedback control can result in high amplitude transients. These may exceed the range for which the linear model is valid, and impede the stabilization of the flow if the disturbance is reinforced through nonlinear means (Joshi, Speyer, & Kim, 1997; Scott Collis, Joslin, Seifert, & Theofilis, 2004).

(Choi, H., Moin, & Kim, 1994) came up with the so-called opposition control. This involves suction/blowing at the wall, where the magnitude of the actuation is the opposite of the velocity measured at a certain distance y_d (Bewley, 2001; Chung & Talha, 2011; Kim, J., 2003; Scott Collis, Joslin, Seifert, & Theofilis, 2004). Therefore, the applied value is given by:

$$V_{(\cdot)}(x, 0, z; t) = -k_p * v(x, y_d, z; t)$$

Several numerical simulations were performed to test different components of velocity imposed at the wall, these being wall-normal V_y, and spanwise V_z control.

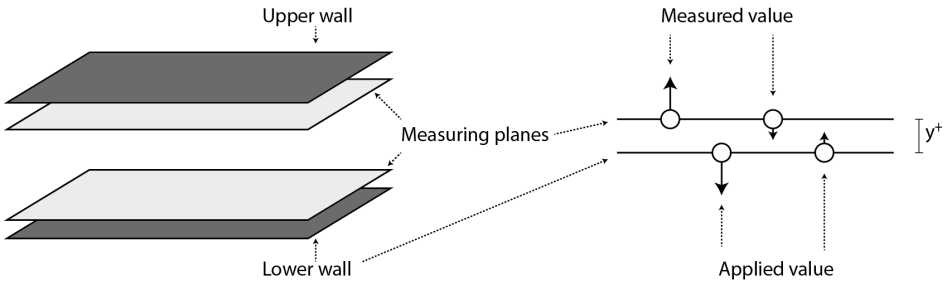

Figure 5.5. Schematic of the channel flow domain using opposition control, the measuring planes at height y^+ and out-of-phase actuation are shown.

Tests were performed using smaller regions of the wall for actuation, in addition to tests where the reactive signal was applied only when events exceeded a threshold value V_{th}. In their studies the optimal sensing height was found to be $y_d = 10$. A 25% skin friction reduction was obtained with both the V_y and V_z controllers. When using 25% of the wall

for actuation, and applying the opposing signal at strong events, a skin friction reduction of 20% was achieved. When 5% of the surface was used in the same configuration a drop of 15% was achieved (Choi, H., Moin, & Kim, 1994). This indicates that selective and localized actuation can have great effect on the flow if properly applied. This controller can be considered as a proportional controller with a negative gain, k_p, and a schematic representing the method is given in Figure 5.5.

The conditions for this control are somewhat unrealistic regarding the measuring of the velocity, since this approach is hard to implement. Hence, Choi et al. implemented wall-based measurements, using the leading term in a Taylor series expansion of the velocity near the wall, and managed to get a 6% reduction in skin friction. Since these initial studies of opposition control, similar approaches have been tested with varying sensing heights, increased proportional gains, in addition to different approximations to obtain flow information using wall measurements (Chung & Talha, 2011; Ricco & Dilib, 2010). However, great differences in the reduction of skin friction have not been achieved, and remain around 5-15%, additionally it was noticed that if the actuation exceeds a certain value, the drag force reduction decreases (Bewley, 2001; Chung & Talha, 2011).

Modern control techniques which explicitly account for model uncertainty as well as disturbances have also been implemented.

(Fattorini & Sritharan, 1992) proposed an existence theorem for optimal control of viscous bounded and unbounded flows in different geometries. Barbu and Sritharan (Barbu & Sritharan, 1998) proposed the use of infinite-dimensional state-space formulation of the H^{∞}-control of the Navier-Stokes equation to address the robustness of optimal closed-loop methods in the presence of exogeneous forces regarding fluid dynamics. They stablish that once a suboptimal solution is found for the H^{∞}-control of the linearized system, the corresponding H^{∞}-control problem has a solution for small perturbations of the steady solution (Barbu & Sritharan, 1998).

In (Barbu, Havârneanu, Popa, & Sritharan, 2003; Havârneanu, Popa, & Sritharan, 2006), the local exact controllability of both, the magnetohydrodynamic equations and the Navier-Stokes equations was

studied. It was found that both are locally exactly controllable around sufficiently smooth stationary solutions. In the case of the Navier-Stokes equations, this can be achieved by suitable locally distributed actuation dictated by an internal controller (Havârneanu, Popa, & Sritharan, 2006). The Navier-Stokes equation analysis was based on a domain with a Navier-slip boundary condition. (Barbu & Triggiani, 2004) showed that a finite-dimensional closed-loop controller, which depends on the largest algebraic multiplicity of the unstable eigenvalues of the linearized Navier-Stokes equations, is capable of locally stabilizing to any steady-state solution. The controller is supported in an open set $w \subset \Omega$ where Ω is an open smooth bounded domain and is of the form (Barbu & Triggiani, 2004; Yan, Coca, & Barbu, 2008):

$$u(x,t) = -\sum_{k=1}^{2K} u_k(t)\psi_k(x)$$

Where $u(\cdot)$ is the control signal, $\{\psi_i\}_{i=1}^{2K}$ is a constructed system of functions related to the unstable eigenvalues of the linearized Navier-Stokes operator and K is the maximum algebraic multiplicity of such unstable eigenvalues (Barbu & Triggiani, 2004; Yan, Coca, & Barbu, 2008).

Yan, Coca, et. al. (Yan, Coca, & Barbu, 2008) developed an algorithm to implement the proposed control law, considering that the need to solve an infinite dimensional operator Riccati equation does not allow direct implementation. The developed algorithm is based on the Galerkin finite element method and these results were extended to apply to wider range on semi-linear parabolic systems in (Barbu, Coca, & Yan, 2005; Yan, Coca, & Barbu, 2009).

(Barbu, 2007) presents an open-loop control for two-dimensional channel flow using wall normal actuation (φ, ψ) of the form

$$\varphi(t,x) = \sum_{|k|\leq M} \varphi_k(t)e^{ikx}\ , \qquad \psi(t,x) = \sum_{|k|\leq M} \psi_k(t)e^{ikx}$$

Where (φ, ψ) are functions that exponentially stabilize the system. This shows that the stabilization of steady-state flows can be achieved using a finite number M of Fourier modes (Barbu, 2007).

(Raymond, 2006) studied the stabilization of the linearized Navier-Stokes equations using a feedback boundary control in two-dimensions. The pointwise (in time) closed-loop control law was determined through

the solution of an LQ problem. Raymond used an extension of the exact controllability results using internal control of the linearized governing equations from (Fernández-Cara, Guerrero, Imanuvilov, & Puel, 2004). A similar approach had been taken by (Fursikov, 2001), however, in this case the feedback operator is not pointwise and the eigenfunctions and eigenvalues of the Oseen operator are required (Raymond, 2006). (Raymond, 2007) then studied the three-dimensional case, which is not a straightforward expansion from his previous results, since the feedback control law could not be characterized by a well posed Riccati equation. For the case when both Dirichlet and Neumann type boundary conditions are present, (Nguyen & Raymond, 2015) have obtained a feedback control law by stabilizing the linearized Navier-Stokes equations, additionally, proved that the full system is also stabilized around the neighbourhood of an unstable stationary solution.

$\mathscr{H}_2$ (or Linear-Quadratic Gaussian – LQG) and $\mathscr{H}_\infty$ methods have also been implemented by (Bewley, 2001; Bewley & Liu, 1998; Bewley, Moin, & Temam, 2001). Bewley used an adjoint-based optimal control, where the control objective was minimized over finite time. Using this approach, a drag reduction of around 50% was obtained in channel flow at low Reynolds number. A suboptimal approach was taken by (Lee, C., Kim, & Choi, 1998) where it was no longer necessary to solve the governing equations iteratively. Additionally, the adjoint formulation could be taken only regarding the linear part of the discretized Navier-Stokes equations. These methods have been implemented on flows at low Reynolds numbers.

Controllers based on reduced order models have also been implemented using similar methods. (Lee, K. H., Cortelezzi, Kim, & Speyer, 2001) used LQG strategy to synthesize a two-dimensional controller based on the linearized Navier-Stokes equations. The gradients of the streamwise velocity fluctuations as outputs and blowing/suction at the wall as inputs were used and a reduction of skin-friction by 10% obtained. The controller was then replicated in the spanwise direction to create a three-dimensional controller which delivered a 17% reduction of skin-friction.

(Jones, Heins, Kerrigan, Morrison, & Sharma, 2015) used model refinement techniques on a state space approximation of the channel flow perturbation equations, to derive a low order model, which was used to synthesise a $\mathscr{H}_\infty$ loop-shaping controller. Their objective was to minimize the streamwise wall-shear stress perturbation through measurements of this variable, and used the voltage applied to actuators as the controlled input. They suggest that there are three problems to be addressed when dealing with the control of turbulence through linear control theory, which are the linearization, spatial discretisation, and the method to go from a system of partial differential equations to one of ordinary differential equations. More recently, (Heins, Jones, & Sharma, 2016) designed a passivity-based control using similar means. In this new study, they found that the ten lowest streamwise Fourier modes, considering only the linear dynamics of channel flow, are responsible for a large part of the energy production. Their control objective was to minimise the energy bound of these modes, which leads to a reduction of the skin-friction of the flow.

Another technique that has been explored is that of neural networks (NN), (Lee, C., Kim, Babcock, & Goodman, 1997) developed a linear and non-linear neural network which was able to predict the velocities at certain locations from measurements of wall-sheer stresses. Both neural networks were trained off-line using data from a numerical simulation of a fully controlled flow based on the previously described *opposition control* method. They were applied as controllers to a turbulent flow giving an 18% drop in drag force reduction in both cases (Lee, C., Kim, Babcock, & Goodman, 1997). This showed that there is a strong correlation between the shear stresses at the boundary, and the actuation required to control the flow. Additionally, the notion that in some cases it is sufficient to apply linear schemes to obtain considerable results is reinforced. However, since the networks had been trained on an already controlled flow, this approach is unlikely to be useful with other scenarios (Kim, J., 2003; Lee, C., Kim, Babcock, & Goodman, 1997).

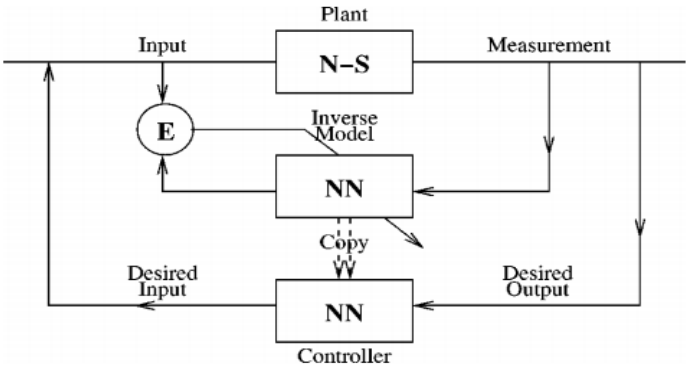

Figure 5.6. Schematic of neural network based control used by Lee.

A second approach was studied, where a new network was trained on-line to serve as an adaptive inverse model of the Navier-Stokes equations, the plant. The setup for this procedure is shown in the schematic in Figure 5.6.

In this method, a NN models the inverse plant that maps from the shear stresses at the wall to the actuation required. The model is copied to act as controller, with the shear stresses that are being sought as input to the plant. This approach resulted in a 20% drag force reduction, although it is not a considerable increase from the previous cases, it was achieved from the direct study of a time varying system and therefore has a greater likelihood of successful application in a wider range of scenarios (Lee, C., Kim, Babcock, & Goodman, 1997).

A model free approach was taken by (Santillo, Hoagg, Bernstein, & Powell, 2006). Firstly, a system identification technique was applied to determine the coefficients of the transfer function relating the control inputs to the performance variables. Following, an ARMARKOV adaptive disturbance rejection algorithm was implemented to stabilize one- and two-dimensional flows. Two actuators were used, one on each of the walls of a channel flow, with measured, and performance variables being the velocity components of the flow at the sensor locations. The method was proven to be feasible, although the authors felt that the two-dimensional performance could be further improved. Due to the low complexity of this approach, it is possible to implement in an easier manner than other techniques mentioned here (Santillo, Hoagg, Bernstein, & Powell, 2006).

As it can be seen, many of the previously mentioned techniques which use reduced order models are often based on the linearized

Navier-Stokes equations. However, to the authors knowledge, there have been few attempts of using system identification techniques to obtain data-based reduced-order models to be used with the control schemes. (Huang, S. C. & Kim, 2008) is an example of this approach, where separation control was implemented through a LQG controller in the flow over the BFS case. This used state estimation from a Kalman filter that was in turn, based on linear models identified directly from input-output data. Two different models were identified, firstly a least-squares based approach is used to obtain an ARX model, and secondly, a subspace method was implemented to obtain a state space representation. The LQG strategy was designed to minimise a cost function dependant on the energy of pressure fluctuations and the controller input itself. With this strategy, the recirculation zone was greatly reduced. It was found that the state space model was better suited than the ARX model obtained.

(Hervé, Sipp, Schmid, & Samuelides, 2012) too worked on the separation control of flow over the BFS. They identified an ARMAX model from the measured data, the coefficients of the identified model were set according to physical knowledge, such as the maximum lag between the application of the actuation and its effect downstream (Hervé, Sipp, Schmid, & Samuelides, 2012). A feed-forward control is implemented and proved to be able to reduce the total turbulent kinetic energy of the system by 50%. Encouraging results were also obtained when the sensors and actuators were considered as corrupted by noise of different magnitudes, where the stability was not compromised and an expected decrease of performance was observed. Other approaches using alternative methods of system identification have been noticed, named data-based mechanistic methods. These have not been applied to wall bounded flows but have been found in studies relating to environmental flows such as rivers or airflow (Desta, Brecht, Meyers, Baelmans, & Berckmans, 2004; Young, 2006).

5.4 Discussion

A review of recent applications of flow control strategies in wall bounded domains, has been presented. The author is aware that more examples of the strategies described here exist, however, only the most representative were chosen to be included. A number of reviews have been found and the reader is directed to them, and the references therein, for further information (Bewley, 2001; Bewley & Liu, 1998; Chung & Talha, 2011; Gad-El-Hak, 1989; Kim, J., 2003; Kim, J. & Bewley, 2007; Lumley & Blossey, 1998; Perlin, Dowling, & Ceccio, 2016; Pollard, 1998; Rathnasingham & Breuer, 2003; Scott Collis, Joslin, Seifert, & Theofilis, 2004; Wang, Luo, Xia, Liu, & Deng, 2012; Zhou & Bai, 2011).

A few matters have to be addressed regarding the control methods and the elements required by them.

Firstly, on the topic of actuators and sensors, it should be noted that available technologies make the implementation of many controller strategies a real possibility (Ho & Tai, 1998; Lofdahl & Gad-El-Hak, 1999b; Varadan & Varadan, 2000). However, many studies, including the current work, have used methods, measurements or concepts that cannot be directly implemented in real systems. This is due to several reasons, such as the impossibility of having full state information, or using variables that are hard to measure. Additionally, computationally expensive methods cannot be implemented, especially in the case of closed-loop control, due to the fast dynamics of the systems which require equally fast solutions (Bewley, 2001; Scott Collis, Joslin, Seifert, & Theofilis, 2004). Lastly, actuators and sensors have limitations on the scales, frequencies and magnitudes which can be achieved, in many cases this has not been considered during the controller design. It is also of importance to keep in mind that the measurements will be corrupted by noise so a method to validate the controllers before such conditions should also be incorporated in the studies to ensure that the controllers derived are robust (Bewley, 2001; Hervé, Sipp, Schmid, & Samuelides, 2012; Scott Collis, Joslin, Seifert, & Theofilis, 2004). These issues need to be amended before many of the controllers currently designed can be implemented on full-scale systems.

Regarding the controller methods, expensive methods cannot be implemented in real-time due to the small time-scales that flows exhibit (Lee, K. H., Cortelezzi, Kim, & Speyer, 2001). This is the main motivation for the use of reduced order models, to reduce the computational burden and remove the need to perform iterative computations, complex optimizations or the calculations of the adjoint of large systems (Lee, K. H., Cortelezzi, Kim, & Speyer, 2001). Concerning the use of classical controllers, it is important to consider that these methods do not account for the initial transient, and so it must be taken into account separately, as this can easily lead to instabilities which take the flow beyond the validity of the model (Kim, J. & Bewley, 2007; Scott Collis, Joslin, Seifert, & Theofilis, 2004).

As for the types of models used to approximate the full flow, it is observed that many authors use linear structures (Kim, J. & Bewley, 2007). The use and capability of this practice has been validated through experimental tests and it is widely believed that controlling the linear dynamics of a flow is sufficient to prevent transition for example (Kim, J. & Bewley, 2007; Scott Collis, Joslin, Seifert, & Theofilis, 2004). However, it is necessary to remember that when using linearizations, the validity of the model is always limited to a certain operating point. If this point is surpassed, no guarantees can be made regarding the performance of the model and any control based on it (Kim, J., 2003).

The use of non-linear models has not been identified in the literature, this is likely due to the difficulty in identifying accurate models, as well as designing controllers which are compatible with them (Allgower, Findeisen, & Nagy, 2004; Billings, 2013). This issue is worsened by the nature of the infinite-dimensional system with such a complex behaviour (Joshi, Speyer, & Kim, 1997; Kim, J. & Bewley, 2007). However, the implementation of such methods would likely yield an improvement in the predictions and the range of validity of the control methods.

The final point to be addressed is the selection of the sensing and actuation methods, as well as the location of application. This is as important as the control strategy and models employed, since it directly defines and limits the former. A correct selection of the measurement variables and position of sensors and actuations can determine if the

plant is observable, controllable and non-minimum phase, or otherwise (Kim, J. & Bewley, 2007). This however, is not something that has a unique solution, nor can it be easily determined (Bewley, 2001; Kim, J., 2003; Pollard, 1998; Scott Collis, Joslin, Seifert, & Theofilis, 2004). Therefore, methods to help to identify optimal sensing and actuation as well as the most significant variables should be studied in greater depth depending on the application, so that the developed strategies can fulfil expectations.

CHAPTER 6

Non-linear model predictive control of flow over the backward facing step

6.1. Introduction

Several model-based control approaches to flow control have been proposed and demonstrated, both numerical and experimentally (Bewley, 2001; Choi, Moin, & Kim, 1994; Gad-El-Hak, 1989; Heins, Jones, & Sharma, 2016; Hervé, Sipp, Schmid, & Samuelides, 2012; Scott Collis, Joslin, Seifert, & Theofilis, 2004). For practical reasons, controller design is often carried out based on models derived from simplified versions of the governing equations (Bewley, 2001; Hervé, Sipp, Schmid, & Samuelides, 2012; Scott Collis, Joslin, Seifert, & Theofilis, 2004). More specifically, for a control scheme to be implemented on a real system, it should not have resource intensive characteristics or rely on data that is difficult to obtain (Bewley, 2001; Kim, 2003; Scott Collis, Joslin, Seifert, & Theofilis, 2004). Therefore, developing implementable control strategies require sufficiently accurate reduced-order models of the fluid flow.

In the case of the flow over a backward step, a typical goal is to control the position of the reattachment point (Heenan & Morrison, 1998; Hervé, Sipp, Schmid, & Samuelides, 2012; Neumann & Wengle, 2003; Uruba, Jonáš, & Mazur, 2007). This geometry is often considered as a benchmark to study the effects of control schemes to be used with amplifier flows (Gautier & Aider, 2013, 2014b). These are flow in which instabilities are, as the name implies, amplified due to the geometry itself, in the current case, due to the expansion of the channel (Ruisi, Zare-Behtash, Kontis, & Erfani, 2016; Zheng, Zhang, & Zhang, 2011).

The separation and reattachment of the flow are also of importance in many applications, such as turbines and heat exchangers, among others, where the goal is to enhance lift and reduce drag or vibrations by the reduction of the unstable recirculation bubble (Gautier & Aider, 2013; Hervé, Sipp, Schmid, & Samuelides, 2012; Le, Moin, & Kim, 1997; Neumann & Wengle, 2003; Ruisi, Zare-Behtash, Kontis, & Erfani, 2016; Uruba, Jonáš, & Mazur, 2007; Xu, Gao, Ming *et al.*, 2015; Zheng, Zhang, & Zhang, 2011).

The separation of the flow at the edge of the step causes a (separated) shear layer to appear, which reattaches further downstream (Gautier & Aider, 2014b; Le, Moin, & Kim, 1997; Zheng, Zhang, & Zhang, 2011). It has been noted that the altering of this shear layer can influence the properties of the recirculation bubble (Gautier & Aider, 2014a; Henning & King, 2007; Hervé, Sipp, Schmid, & Samuelides, 2012; Pouryoussefi, Mirzaei, & Hajipour, 2015; Ruisi, Zare-Behtash, Kontis, & Erfani, 2016; Uruba, Jonáš, & Mazur, 2007; Zheng, Zhang, & Zhang, 2011).

The latter is characterised as having two main recirculation's, the larger of the two being caused by the main separation and which defined the reattachment point of the flow over the BFS, and the smaller present in the lower corner of the step (Gautier & Aider, 2014a; Le, Moin, & Kim, 1997; Zheng, Zhang, & Zhang, 2011). Both cause changes in the pressure felt by the channel walls, hence, cause variations of the wall-shear stress, commonly used to identify the reattachment point. Further, it is thought that the increase of mixing between the free-flow and the shear layer can also aid in the reduction of the reattachment length

(Pouryoussefi, Mirzaei, & Hajipour, 2015; Ruisi, Zare-Behtash, Kontis, & Erfani, 2016).

Model predictive control has its origin in the 1960's (García, Prett, & Morari, 1989), since then a number of different algorithms have been proposed, each with strengths and weaknesses (Allgower, Findeisen, & Nagy, 2004; Camacho & Bordons-Alba, 2003; Clarke, Mohtadi, & Tuffs, 1987a; García, Prett, & Morari, 1989; Henson, 1998; Lee, 2011; Mayne, 2014; Morari & Lee, 1999). Most of the approaches have been based on linear representations of the systems, using impulse- and step-response models, or identified input/output mappings (Camacho & Bordons-Alba, 2003; García, Prett, & Morari, 1989; Lee, 2011; Morari & Lee, 1999; Qin & Badgwell, 2003).

Linear approaches have been shown to be successful while there are few, or no variations of the set point, so that a sufficiently accurate model remains valid (Henson, 1998; Mayne, 2014; Morari & Lee, 1999). In the case that the conditions change significantly, non-linear effects may become significant and therefore the response of the controller may be unacceptable (Henson, 1998; Mayne, 2014).

In these cases, the use of non-linear models is warranted, however, this introduces the need to use expensive non-linear optimization, in addition to the use of complicated algorithms to identify accurate models and compute the future predictions (Bai, 2010; Camacho & Bordons-Alba, 2003; Henson, 1998; Mayne, 2014).

Model predictive control does not refer to a single algorithm, but a methodology that consists of the following set of elements (Camacho & Bordons-Alba, 2003; Clarke & Mohtadi, 1989; Clarke, Mohtadi, & Tuffs, 1987a; Rossiter, 2003):

- Explicit model. It is used to forecast the evolution of the system over the prediction horizon, N_2. Many forms can be used such as state-space, transfer function and difference equation models such as in this work.
- Measurements of past data. Needed to initialize the algorithm and obtain the control sequence. Data up to instant $(k-1)$ is needed for the actuation signals, u, and up to (k) for the outputs, y.

- Cost function. It is optimized at each time-step to compute the control sequence which minimizes the error between the measured and desired state. In addition, it can include penalization on the input(s), output(s) and their rates of change.

MPC relies on iterative finite-horizon optimizations of the model which requires accurate prediction of the system response over a finite number of steps in the future, and not infinitely as is the case with other optimal control strategies (Bewley, 2001; Clarke & Mohtadi, 1989; Rossiter, 2003).

This methodology can be applied to SISO as well as to MIMO system configurations and allows the incorporation of constraints at design stage (Camacho & Bordons-Alba, 2003; García, Prett, & Morari, 1989; Rossiter, 2003). These properties make MPC suited to flow control applications that involve large-scale multi-input-multi-output models – typically obtained as finite-element approximations of the governing partial differential equations – and are subject to various constrains imposed by the actuators and sensors. Control approaches that handle constraints at design stage rather than during the implementation is highly desirable (Clarke & Mohtadi, 1989; Clarke, Mohtadi, & Tuffs, 1987a).

The development and implementation of MPC strategies for flow control applications pose several challenges. Specifically, the numerical models are high-dimensional and non-linear leading to computationally intensive algorithms that are difficult to implement in real-time.

This chapter investigates a non-linear model predictive control strategy based on reduced-order one- and multi-step ahead non-linear predictors identified directly from data (Bai & Coca, 2008, 2011), generated by an accurate simulation of the governing partial differential equations, which can provide a possible solution to these challenges.

Assuming that such multi-step predictors are available, this approach can be applied in principle to wide range of control problems (Bai & Coca, 2008; Rossiter, 2003).

The approach, which is similar to the generalized predictive control (GPC) (Camacho & Bordons-Alba, 2003; Clarke, Mohtadi, & Tuffs, 1987a), has the advantage that it relies on input-affine nonlinear predictors,

which lead to fast algorithms that are suited to real-time implementation.

The Chapter is organized as follows. Section 6.2 provides an overview of existing linear and non-linear MPC schemes. Section 6.3 introduces a NARMAX based non-linear MPC strategy derived from the GPC algorithm. The results of simulations trials with noise-free, measurement noise and measurement noise in addition to disturbances for the M_{Cp} SISO model are given in Section 6.4.1. Section 6.4.2 presents the expansion of the algorithm to accommodate multivariate MISO predictors. Simulation results are once more presented, studying the three noise/disturbance scenarios as before.

Finally, Section 6.4 contains a discussion of these results, including their validity and possible improvements which could be made in the future.

6.2. Review of non-linear model predictive control strategies

As previously stated, MPC schemes are those which predict the evolution of the state, and aim to compute a control sequence which minimizes a cost function while satisfying constraints. Most algorithms in this family implement a receding horizon which means that only one input is applied to the plant and the process repeated at every time-step.

An example of the MPC method can be seen in Figure 6.1. Where, for a given system, the control horizon ends at $(k + N_u)$ and the prediction horizon at $(k + N_2)$, the controller increments are Δu and the control actions are assumed constant for all $j > N_u$.

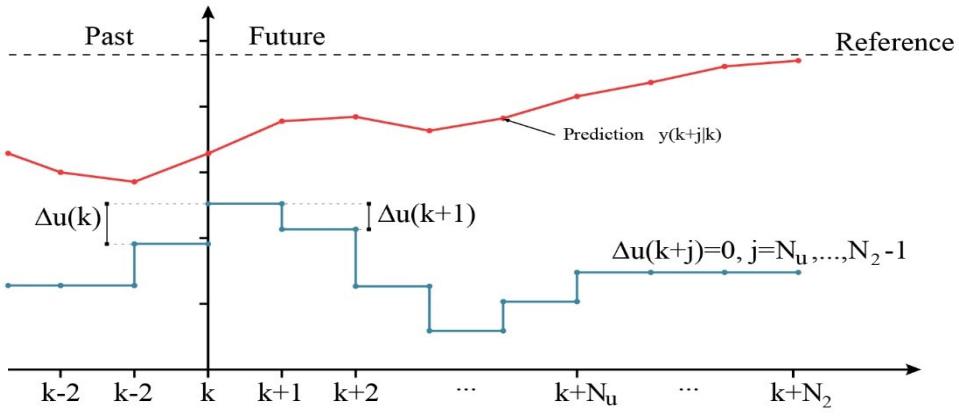

Figure 6.1. Schematic of the MPC strategy, showing the predictions based on past data up to instant (k) and the future control increments Δu.

The variants of MPC are differentiated depending on the length of the prediction and control horizon, as well as the type of models that can be controlled successfully. That is, what form the model is in, such as state space or transfer function, or to which kind of plant-model mismatch they are most sensitive to, such as over-parametrization or the correct selection of dead-time (Clarke & Mohtadi, 1989).

Both linear and non-linear MPC exist, where the former has been studied extensively and is well documented (Clarke, Mohtadi, & Tuffs, 1987a; García, Prett, & Morari, 1989; Henson, 1998; Morari & Lee, 1999). These methods incorporate linear models and constraints, together with a quadratic cost function (Clarke, Mohtadi, & Tuffs, 1987a). Rigorously speaking, the closed-loop dynamics of linear MPC methods are non-linear due to the inclusion of constraints and the quadratic cost function. however, they are considered linear since the models are of this form (García, Prett, & Morari, 1989; Morari & Lee, 1999).

The methods considered as non-linear MPC (NMPC) are those based on non-linear models and/or make use of non-linear constraints and the cost function may not be quadratic (Camacho & Bordons-Alba, 2003; Henson, 1998; Rossiter, 2003). NMPC has not been as widely studied and few industrial applications exist in either simulation or experimental set-up (Henson, 1998). This is mainly due to the increased computational expense when calculating the predictions, and performing the non-linear optimization. The latter is generally non-quadratic and non-convex (Henson, 1998; Rossiter, 2003). Further, the difficulty in obtaining reliable models using system identification is viewed as a great disadvantage (Billings, 2013). This however, can be circumvented by using the NARMAX methodology, as is the case of this work. Additionally, by restricting the terms included in the model, and considering some variable changes, the advantage of using NMPC can be obtained without its characteristic computational burden. This will be explained in greater detail below.

Regardless of whether the model used is linear or non-linear, there are several variants of MPC, which have been proposed by different authors (Camacho & Bordons-Alba, 2003; Clarke, Mohtadi, & Tuffs, 1987a; García, Prett, & Morari, 1989; Lee, 2011). Several reviews exist (Allgower,

Findeisen, & Nagy, 2004; García, Prett, & Morari, 1989; Henson, 1998; Lee, 2011; Mayne, 2014; Mayne, Rawlings, Rao, & Scokaert, 2000; Morari & Lee, 1999). Considering that there are many types, each customized for a certain type of application and in some cases, with sub-classifications, a comprehensive review is beyond the scope of the current work. The most representative schemes found in the literature are dynamic matrix control (DMC), quadratic DMC, GPC, internal model control (IMC), unified predictive control (UPC), extended model based predictive control (EMPC) and extended prediction self-adaptive control (EPSAC) (Camacho & Bordons-Alba, 2003; Clarke, Mohtadi, & Tuffs, 1987a; Henson, 1998; Lee, 2011).

The linear GPC algorithm proposed by (Clarke, Mohtadi, & Tuffs, 1987a), uses an explicit formulation of the model, often in the controlled auto-regressive integral moving-average (CARIMA) form. This is chosen since it accounts for non-stationary uncertainty (Clarke, Mohtadi, & Tuffs, 1987a; Rossiter, 2003). In the current work, however, the control is implemented using the identified NARMAX models. Some modifications will be performed to include integral action and ensure an offset-free steady-state.

The prediction horizon considered is finite and set according to the application, it is recommended that it be equal or slightly greater to the settling time of the system (Clarke, Mohtadi, & Tuffs, 1987a, 1987b). The control horizon can be equal to that of the predictions or shorter. In GPC, it is assumed that all control increments beyond this horizon are equal to zero, which means that the control is assumed to be at a constant value after the control horizon (Clarke, Mohtadi, & Tuffs, 1987a, 1987b).

A control sequence is obtained by minimising the cost function subject to the constraints. At the following time-step the process is repeated using the new measurements and thus, a receding horizon method is obtained (Camacho & Bordons-Alba, 2003; Clarke, Mohtadi, & Tuffs, 1987a; Rossiter, 2003).

6.3. NARMAX based non-linear model predictive control

The NARMAX model NMPC approach introduced in (Bai & Coca, 2008) is adopted in this work. This method uses a non-linear model, which is input-affine for future terms, with linear constraints, and a quadratic cost function. Therefore, this approach maintains the accuracy achievable only with non-linear models, without requiring the solution of non-linear optimizations (Bai & Coca, 2011).

In the GPC framework, the predictors are derived through the solution of a set of Diophantine equations, however this cannot be performed using non-linear models (Bai & Coca, 2008). To circumvent this, Bai and Coca proposed the use of j-step ahead non-linear predictors identified directly from data. The j-step-ahead predictors of the NARX model are given by (Bai, 2010; Bai & Coca, 2008):

$$\begin{gathered}\hat{y}(k+1|k) = f_1\left(y(k), \dots, y\left(k-n_y+1\right), u(k), \dots, u(k-n_u+1)\right),\\ \hat{y}(k+2|k) = f_2\left(y(k), \dots, y\left(k-n_y+1\right), u(k+1), u(k), \dots, u(k-n_u+1)\right),\\ \vdots\\ \hat{y}(k+j|k) = F_j\left(y(k), \dots, y\left(k-n_y+1\right), u(k+j-1), \dots, u(k),\right.\\ \left.\dots, u(k-n_u+1)\right)\end{gathered} \tag{6. 1}$$

By shifting the predictors from equation (6. 1) j-steps backwards in time, the functions $F_j(x(k))$ will depend on

$$\begin{gathered}x(k) = \left[y(k-j), \dots, y\left(k-n_y-j+1\right), u(k-1),\right.\\ \left.\dots, u(k), \dots, u(k-n_u-j+1)\right]\end{gathered}$$

Therefore, the terms included in the model will ensure that it is input affine, which means linear with respect to terms that include $u(k+j)$ for $j = 0, 1, \dots, N_u$. Since values for input(s) and output(s) are known up to instant $(k-1)$ and (k), respectively, the model can be evaluated and the predictions obtained in terms of the future inputs as the only unknown.

In (Bai & Coca, 2008) these predictors are identified directly in terms of the future input increments. In this work, this has been performed after the identification, in addition to using the output increments.

Once the change of variable is performed, the predictors correspond to the linearization of equation (6. 1) around the previous control input $u(t)$.

$$\hat{y}(k+j|k) = f_j(x(k) + \sum_{i=1}^{\min(j,N_u)} \left.\frac{\partial f_j(x)}{\partial u(k+i)}\right|_{u(t)} \Delta u(k+i)$$

This approach is somewhat like the extended linear MPC, originally proposed for the DMC controller. In their case, the linear prediction equation was augmented with a non-linear term, which in turn was calculated by minimizing the difference between the prediction of the linear and full non-linear model (Camacho & Bordons-Alba, 2003). In this work however, the full non-linear model is always considered.

There has been great interest in the topic of linear MPC stability and robustness and methods such as using infinite prediction horizon or setting terminal in/equality constraints have been developed to ensure this (Keerthi & Gilbert, 1988; Mayne & Michalska, 1990). In the case of NMPC there is still no general theoretical results regarding closed-loop stability, however, the aforementioned processes can also be applied (Mayne & Michalska, 1990).

The use of infinite horizon is the most straightforward manner of assuring convergence, this is of course unfeasible and made even more so in the case of non-linear optimizations, the use of terminal constraints is also difficult due to the inherent complexity of non-linear models (Bai, 2010). Therefore, in practice, when nominal stability cannot be guaranteed, closed-loop stability is ensured by the tuning of the parameters (Camacho & Bordons-Alba, 2003; Henson, 1998).

Finally, regarding the robustness of MPC, it has been noted that in many LMPC and NMPC applications, the models employed are wholly deterministic and so do not account for model/plant mismatch. The current work will consider the use of integral action during the design of the controller to obtain robustness. Additionally, multi-step-ahead models are employed which also aid with this objective. Should the system under study contain measurement and process noise, the NARMAX methodology can be used to identify a linear or non-linear noise model to obtain a stochastic predictor (Billings, 2013; Billings, Chen, & Korenberg, 1989).

6.4. NARMAX based NMPC for flow over the backward facing step

This section describes the methodology used to carry out the model predictive control of the identified models. The methodology will be illustrated for the SISO model M_{Cp}. The required modifications to the models and other details elaborated and finally, results of simulations with and without measurement noise and disturbances given.

6.4.1. NARMAX based NMPC for M_{Cp} using recursive predictors

For control implementation purposes, the one-step-ahead SISO predictor of the system is the reduced-order NARMAX model identified from data, introduced in Chapter 4, given by

$$\hat{y}(k) = F\big(y(k-1), \dots, y\big(k-n_y\big), u(k-1), \dots, u(k-n_u), e(k-1), \dots, e(k-n_e)\big) + e(k) \tag{6. 2}$$

The identified predictor M_{Cp} is input-affine with respect to the future control input $u(k+j-1)$, for $j = 1, \dots, N_c$.

As mentioned in Chapter 4, the exclusion of terms in the candidate set, required to ensure input-affinity, has caused a slight degradation of the prediction performance of the identified models. However, the models are still more accurate and include richer dynamics than linear ones, so the trade-off was believed to be warranted.

The future control input considering known data up to instant $(k-1)$, is defined as

$$u(k+j-1) = u(k-1) + \sum_{i=0}^{j-1} \Delta u\,(k+i) \tag{6. 3}$$

where the control increments are

$$\Delta u(k+j) = u(k+j) - u(k+j-1) \qquad j = 0,1, \dots, N_u \tag{6. 4}$$

With this change of variable, the j-step ahead predictor, equation (6. 2), can be written as

$$\hat{y}(k+j|k) = F_j\big(y(k), \dots, y\big(k-n_y+1\big), \Delta u(k+j-1), \dots, \Delta u(k), u(k-1) \dots, u(k-n_u+1)\big) \tag{6. 5}$$

Table 6.1. Model structure and parameters for M_{Cp} with incremental actuation.

Parameter	Model M_{Cp}	
-0.00065	1	1
1.942068	$y_1(k)$	1
-0.96332	$y_1(k-1)$	1
-0.05751	$\Delta u_1(k)$	1
-0.05751	$u_1(k-1)$	1
0.003786	$\Delta u_1(k)$	$u_1(k-5)$
0.003786	$u_1(k-1)$	$u_1(k-5)$
0.108961	$u_1(k-1)$	1
-0.05308	$u_1(k-2)$	1
-0.00281	$u_1(k-5)$	$u_1(k-5)$

The model terms and corresponding parameters of the OSA model with the change of variable are listed in Table 6.1.

The one-step-ahead predictor M_{Cp} was used to derive the multi-step-ahead predictors assuming a control horizon $N_2 = 5$. The structure identified is such that, the j-step ahead predictor, $1 < j \leq 5$, obtained by iteration of model M_{Cp}, is still input affine with respect to future control actions. Higher prediction horizons can be considered but this would require the direct identification of the predictors for $j > 5$.

Separating terms that include future control increments, equation (6. 5) can be written as

$$y(k+j|k) = f_j\big(x(k)\big) + \sum_{i=1}^{j} g_{ji}(x(k))\Delta u(k+i-1)$$

or simplified,

$$y(k+j|k) = f_j\big(x(k)\big) + G_j(x(k))\Delta u(k+i-1) \tag{6. 6}$$

where

$$x(k) = \big[y(k), \dots, y\big(k-n_y+1\big), u(k-1)\dots, u(k-n_u+1)\big]$$

Arranging equation (6. 6) in matrix form, yields

$$\boldsymbol{y} = \boldsymbol{G}\cdot\Delta\boldsymbol{u} + \boldsymbol{F} \tag{6. 7}$$

In equation (6. 7), each of the variables are defined as:

$$\boldsymbol{y} = \begin{bmatrix} y(k+1|k) \\ y(k+2|k) \\ \vdots \\ y(k+N_2|k) \end{bmatrix},\ \Delta\boldsymbol{u} = \begin{bmatrix} \Delta u(k) \\ \Delta u(k+1) \\ \vdots \\ \Delta u(k+N_u-1) \end{bmatrix},\ \boldsymbol{F} = \begin{bmatrix} f_1\big(x(k)\big) \\ f_2\big(x(k)\big) \\ \vdots \\ f_{N2}\big(x(k)\big) \end{bmatrix},$$

$$\boldsymbol{G} = \begin{bmatrix} g_{11}(x(k)) & 0 & \cdots & 0 \\ g_{21}(x(k)) & g_{22}(x(k)) & \cdots & 0 \\ \vdots & \vdots & \ddots & \vdots \\ g_{N_2\,1}(x(k)) & g_{N_2\,2}(x(k)) & \dots & g_{N_2\,N_u}(x(k)) \end{bmatrix} \tag{6. 8}$$

Matrix $\boldsymbol{G}$ needs to be updated at each time-step since it depends on past measurements.

To deal with load disturbances and ensure zero steady-state error (Henson, 1998), predictors are modified to incorporate integral action by applying the operator $\Delta = 1 - z^{-1}$ to equation (6. 6), which gives

$$\Delta y(k+j|k) = \Delta f_j\big(x(k)\big) + \Delta G_j(z^{-1})\Delta u(k+j-1)$$

and leads to

$$\begin{aligned} y(k+j|k) = y(k+j-1|k) &+ f_j\big(x(k)\big) - f_j\big(x(k-1)\big) \\ &+ G_j(z^{-1})[\Delta u(k+j-1) - \Delta u(k+j-2)] \end{aligned}$$

In matrix form this is written as

$$\mathbf{y} = \boldsymbol{G}_{int} \cdot \Delta \boldsymbol{u} + \boldsymbol{F}_{int} \tag{6. 9}$$

with

$$\boldsymbol{G}_{int} = \begin{bmatrix} g_{11} & 0 & \cdots & 0 \\ g_{21} - g_{22} + g_{11} & g_{22} & \cdots & 0 \\ \vdots & \vdots & \ddots & \vdots \\ g_{N_2\,1} - g_{N_2\,2} + g_{(N_2-1)\,1} & g_{N_2\,2} - g_{N_2\,3} + g_{(N_2-1)\,2} & \cdots & g_{N_2\,N_u} \end{bmatrix},$$

$$\boldsymbol{F}_{int} = \begin{bmatrix} -g_{11} \\ -(g_{21} + g_{11}) \\ \vdots \\ -(g_{N_2\,1} + \cdots + g_{21} + g_{11}) \end{bmatrix} \cdot \Delta u(k-1) + \begin{bmatrix} f_{int\,1}(x(k)) \\ f_{int\,2}(x(k)) \\ \vdots \\ f_{int\,N2}(x(k)) \end{bmatrix},$$

$$\begin{bmatrix} f_{int\,1}(x(k)) \\ f_{int\,2}(x(k)) \\ \vdots \\ f_{int\,N2}(x(k)) \end{bmatrix} = \begin{bmatrix} f_1(x(k)) - f_1(x(k-1)) + y(k) \\ f_2(x(k)) - f_2(x(k-1)) + f_{int\,1}(x(k)) \\ \vdots \\ f_{N_2}(x(k)) - f_{N_2}(x(k-1)) + f_{int\,(N_2-1)}(x(k)) \end{bmatrix} \tag{6. 10}$$

In the previous expression, the $g_{ji}(x(k))$ notation was dropped to help readability of the matrices; likewise, the subscript of equation (6. 9) will be dropped. The predictor will be used in the form of equation (6. 9) for the remainder of this description.

The only remaining elements to define are the desired trajectory and the constraints. The former is dependent on the application; several

different trajectories were tested as will be described later. In the case of the constraints, these can be imposed on the inputs, u, outputs, y , and their rate of change, Δu or Δy (Clarke, Mohtadi, & Tuffs, 1987a, 1987b; Rossiter, 2003).

The inclusion of constraints during the design stage is one of the most valuable characteristics of MPC methodologies, since this ensures adequate closed-loop performance (Clarke & Mohtadi, 1989; Clarke, Mohtadi, & Tuffs, 1987a). In the case of GPC, these can be used as tuning parameters to enhance the performance of the controlled system, in addition to specifying the operational limits of the system (Clarke & Mohtadi, 1989; Clarke, Mohtadi, & Tuffs, 1987a, 1987b).

In the current work, only constraints of the input and its rate of change have been considered. The MPC optimization problem can be formulated as follows

$$J(N_1, N_2, N_u) = \sum_{j=N_1}^{N_2} \delta[y(k+j|k) - \omega(k+j)]^2 + \sum_{j=1}^{N_u} \lambda(j)[\Delta u(k+j-1)]^2 \quad (6.\ 11)$$

Subject to the following constraints

$$\begin{gathered} \boldsymbol{u}_{min} \leq \boldsymbol{u} \leq \boldsymbol{u}_{max} \\ \Delta\boldsymbol{u}_{min} \leq \Delta\boldsymbol{u} \leq \Delta\boldsymbol{u}_{max} \\ \boldsymbol{y}_{min} \leq \boldsymbol{y} \leq \boldsymbol{y}_{max} \end{gathered} \quad (6.\ 12)$$

In equation (6. 11), ω is the reference signal, N_1 is the minimum prediction horizon which determines at which instant it becomes desirable for the output to follow the reference, and λ, δ are weighing sequences ($\delta = 1$).

In equation (6. 12), the constraint on the input needs to be written in terms of the input increments. Therefore, it becomes

$$\begin{bmatrix} \boldsymbol{I} \\ -\boldsymbol{I} \end{bmatrix} \cdot \boldsymbol{A} \cdot \begin{bmatrix} \boldsymbol{\Delta u(k)} \\ \boldsymbol{\Delta u(k+1)} \\ \vdots \\ \boldsymbol{\Delta u(k+N_u-1)} \end{bmatrix} + \begin{bmatrix} \boldsymbol{q} \\ \boldsymbol{q} \end{bmatrix} \cdot \boldsymbol{u(k-1)} \leq \begin{bmatrix} \boldsymbol{q} & \boldsymbol{0} \\ \boldsymbol{0} & \boldsymbol{q} \end{bmatrix} \cdot \begin{bmatrix} \boldsymbol{u_{max}} \\ \boldsymbol{-u_{min}} \end{bmatrix} \quad (6.\ 13)$$

and the constraint on the input increments remains

$$\begin{bmatrix} I \\ -I \end{bmatrix} \cdot \begin{bmatrix} \Delta u(k) \\ \Delta u(k+1) \\ \vdots \\ \Delta u(k+N_u-1) \end{bmatrix} \leq \begin{bmatrix} \boldsymbol{q} & \boldsymbol{0} \\ \boldsymbol{0} & \boldsymbol{q} \end{bmatrix} \cdot \begin{bmatrix} \Delta u_{max} \\ \Delta u_{min} \end{bmatrix} \quad (6.\ 14)$$

Where $\boldsymbol{q}$ is a vector of ones of dimensions ($N_u \times 1$) and $\boldsymbol{A}$ a lower triangular matrix ($N_u \times N_u$), with unit entries below the diagonal:

$$\boldsymbol{A} = \begin{bmatrix} 1 & 0 & \cdots & 0 \\ 1 & 1 & \cdots & 0 \\ 1 & 1 & \ddots & \vdots \\ 1 & 1 & \ldots & 1 \end{bmatrix}$$

$\boldsymbol{I}$ is a square identity matrix of dimensions N_u and $\mathbf{0}$ denotes a zero matrix of adequate dimensions. In this example $N_u = N_2$.

As mentioned, constraints on the outputs can also be enforced, a similar approach is followed where equation (6. 9) is used to substitute the prediction $y(k+j)$ in terms of the past measurements and the future control increments vector. In the current work this was not implemented.

Substituting equation (6. 9) in (6. 11), considering equation (6. 4) and expressing the result in matrix form gives

$$\boldsymbol{J} = [\boldsymbol{G} \cdot \Delta\boldsymbol{u} + \boldsymbol{F} - \boldsymbol{\omega}]^T \cdot [\boldsymbol{G} \cdot \Delta\boldsymbol{u} + \boldsymbol{F} - \boldsymbol{\omega}] + \Delta\boldsymbol{u}^T \cdot \boldsymbol{\Lambda} \cdot \Delta\boldsymbol{u} \quad (6.\ 15)$$

with Λ being a diagonal matrix of $\left[\lambda_1, \lambda_2, \ldots, \lambda_{N_u}\right]^T$ and $\bar{\boldsymbol{u}} = \boldsymbol{L} \cdot u(k-1)$, where $\boldsymbol{L}$ is a vector of ones of appropriate dimensions.

The set of control increments which minimises the cost function (6. 15) can be found by solving

$$\frac{\partial \boldsymbol{J}}{\partial \Delta\boldsymbol{u}} = 0 \quad (6.\ 16)$$

Subject to the constraints defined by equations (6. 13) and (6. 14) . The unconstrained sequence is given by

$$\Delta\boldsymbol{u} = (\boldsymbol{G}^T \cdot \boldsymbol{G} + \boldsymbol{\Lambda})^{-1}(\boldsymbol{G}^T \cdot \boldsymbol{\omega} - \boldsymbol{G}^T \cdot \boldsymbol{F}) \quad (6.\ 17)$$

Where only the first value of the vector $\Delta\boldsymbol{u}$ is applied to the process.

Different cost functions can be formulated depending on the required performance and needs of the application (Clarke, Mohtadi, & Tuffs, 1987a).

The prediction horizons, N_1 and N_2, in addition to the control horizon, N_u, and weighing matrix, Λ , are the tuning parameters available to modify this controller (Clarke & Mohtadi, 1989; Clarke, Mohtadi, & Tuffs, 1987a). The prediction horizons determine the response that the controlled system will exhibit (Camacho & Bordons-Alba, 2003; Mayne & Michalska, 1990).

To define the value, it is necessary to consider the rise time of the plant. Ideally it is important to ensure that N_2 is large enough to anticipate deviations from the set-point or constraint violations, for example, and compensate for them accordingly. Meanwhile, value of N_1 is most important if the plant includes delays or dead-times and should be greater than these, since any actuation applied before will not influence the output (Clarke, Mohtadi, & Tuffs, 1987a, 1987b).

The control horizon determines how aggressive or sluggish the controlled response of the system will be. Setting lower values of N_u is requiring that the desired value be reached faster, whereas increasing the value allows for a smoother response (Clarke, Mohtadi, & Tuffs, 1987a, 1987b; Henson, 1998). The weighing matrix, Λ, also affects this response as it influences the cost of the control increments, Δu. It is difficult to determine the optimal values *a priori* and so fine tuning through simulations if often employed (Clarke, Mohtadi, & Tuffs, 1987a, 1987b; Henson, 1998).

Table 6.2. Values tested as tuning parameters of the MPC algorithm

Variable	Meaning	Value
N_1	Minimum prediction horizon	1
N_2	Maximum prediction horizon	5
$\mathrm{N_u}$	Control horizon	5
λ	Weighing sequence	$1\times10^{-5}, \ldots, 1$

Table 6.2 shows the values assigned to the tuning parameters. These were evaluated through numerical simulation. The maximum prediction horizon tested, which achieved desired performance, was $N_2 = 5$.

Since the flow has no dead-time, the minimum prediction horizon was set to $N_1 = 1$. The control horizon was set to be equal to the prediction horizon $N_2 = N_u = 5$. Numerical simulations show the performance decreasing considerably for $N_u < 4$, however, performance did not improve using horizons larger than $N_u = 5$. The constraints of the input should be set were set per the limitations of the actuators implemented, both in magnitude and response speed. In the case of simulations this bound can be implemented in a straightforward manner.

For the current work, during the system identification stage, an input with the highest magnitude acceptable by the package Fluent was implemented, to ensure it was persistently exciting. The control limit will therefore be set at this value, that is the magnitude had to be lower than $\pm 1 \frac{m}{s}$, as for the input increments, the threshold was varied to tune the response speed of the system.

The MPC algorithm was implemented using Matlab, the plant evolution was simulated by the OSA predictor defined in Table 4.6 and the controller applied with the different tuning parameters mentioned previously. Initially, several simulations were run to tune the control increment weighing parameter.

Regarding the set-points or desired trajectories, various sequences were designed by analysing the range of the measured output, and creating a mixture of a stepped signal of different magnitudes with a sinusoidal which are in the appropriate range.

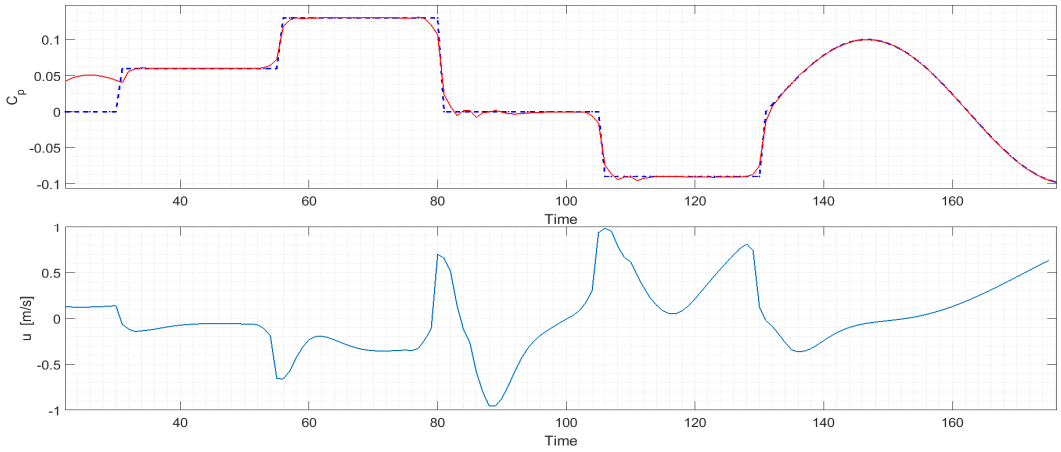

Figure 6.2. Top: Simulation of noise-free controlled M_{Cp} model. Plant output in red and desired trajectory in blue. Bottom: Actuation signal $u(k)$. $N_2 = 5$, $N_u = 5$ and $\lambda = 0.001$, $NRMSE = 7.77\%$

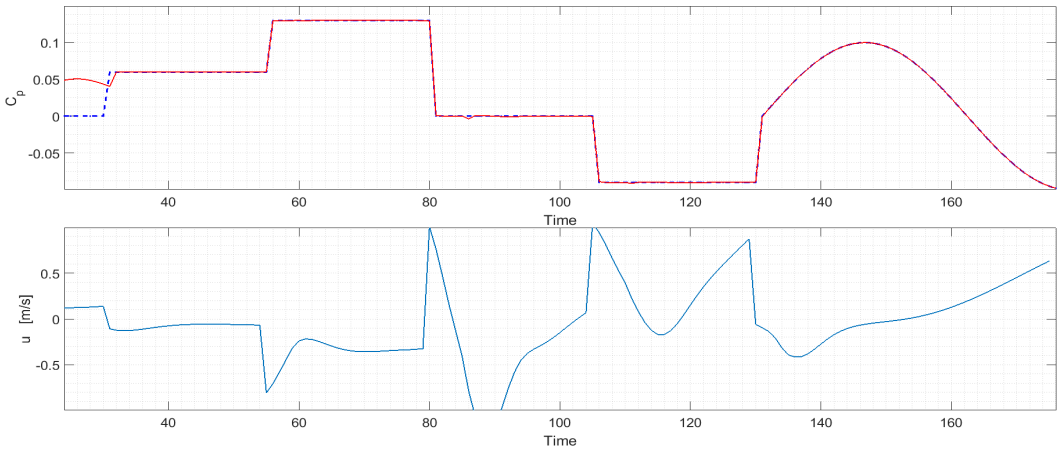

Figure 6.3. Top: Simulation of noise-free controlled M_{Cp} model. Plant output in red and desired trajectory in blue. Bottom: Actuation signal $u(k)$. $N_2 = 5$, $N_u = 5$ and $\lambda = 2 \times 10^{-5}$, $NRMSE = 5.22\%$

Figure 6.2 and Figure 6.3 shows the performance of the control with two values of λ. It can be seen that the smaller value of λ has better tracking of the trajectory, however the changes in the control signal are more sudden and have sharper changes. Depending on the actuator used, this may not be achievable or it may cause damage to the system or itself.

Therefore, the implemented value would depend on the limitations and requirements of the real system.

To validate the controller further, the measured signal was corrupted with noise, additionally, load disturbances were added throughout the simulation time to see the capability of the controller to compensate for them.

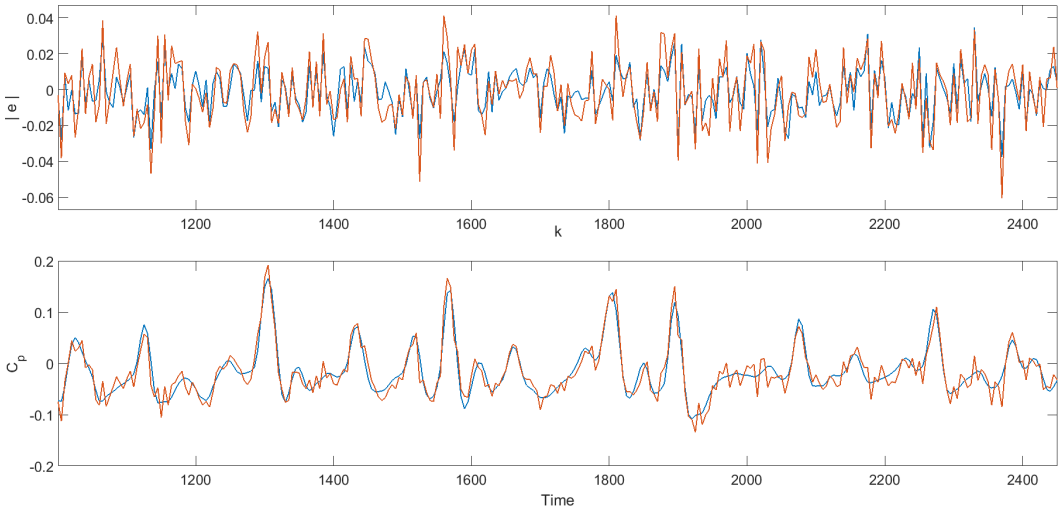

Figure 6.4. Top: White noise signal $e(k)$ in blue and measurement noise $e_m(k)$ in red. Bottom: Comparison of clean data in blue, and noise corrupted signal in red of C_p fluctuations.

The measurement noise signal, $e_p(k)$,was generated by filtering a white noise signal $e(k)$ with variance $\sigma^2 = 1.537\times10^{-4}$ using the filter

$$H(z) = 1 - \frac{0.5}{z}$$

This yielded the signal shown in Figure 6.4 with $\mu = -1.12\times10^{-4}$ and $\sigma^2 = 3.101\times10^{-4}$. The load disturbances introduced $d(k)$ are given by

$$d(k) = \begin{cases} .0055 & 60 \leq k \leq 75 \\ -.0055 & 135 \leq k \leq 150 \\ 0 & otherwise \end{cases}$$

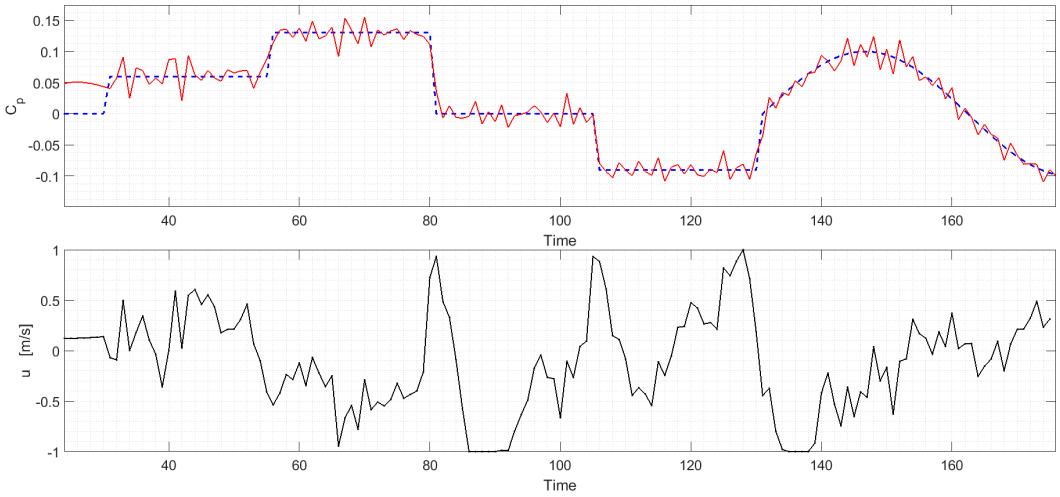

Figure 6.5. Top: Simulation of controlled M_{Cp} model with measurement noise $e_m(k)$. Plant output in red and desired trajectory in blue. Bottom: Actuation signal $u(k)$. $N_2 = 5$, $N_u = 5$ and $\lambda = 0.001$, $NRMSE = 20.5\%$

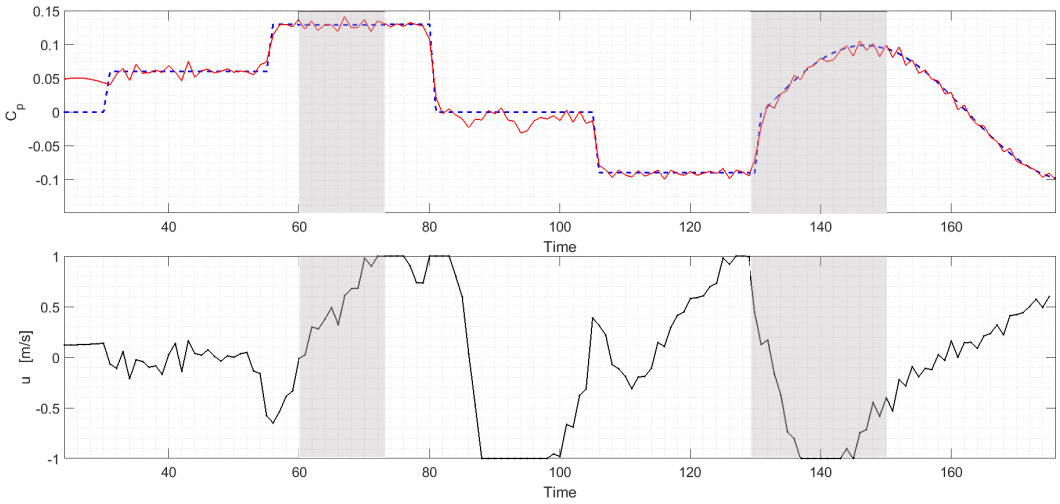

Figure 6.6. Top: Simulation of controlled M_{Cp} model with measurement noise $e_m(k)$ and load disturbances $d(k)$ (in grey). Plant output in red and desired trajectory in blue. Bottom: Actuation signal $u(k)$. $N_2 = 5$, $N_u = 5$ and $\lambda = 0.001$, $NRMSE = 12.43\%$

As it can be seen, the controller is able to maintain the system at the desired trajectory despite the presence of measurement noise as in Figure 6.5, and measurement noise with load disturbances, shown in Figure 6.6. The inputs are maintained within operational limits, and for the most part not overly aggressive.

For the simulation including the load disturbance, the measurement noise signal $e_m(k)$ was attenuated by 20% so that the effects of the disturbance could be more identified more easily.

6.4.2. NARMAX based NMPC for M_{V2} and M_{V4} using multi-step ahead predictors

A similar procedure was carried out to implement the MPC using the identified predictors for each of the $M_{V(\cdot)}$ models. However, as these are MISO models, an expansion of the algorithm was performed.

Firstly, for a system with s inputs, equations (6. 3) and (6. 4) have to be defined for each of the inputs. The change of variable from future input values, to input increments should be performed to obtain the MISO version of equation (6. 5), given by

$$\hat{y}(k+j|k) = F_j\big(y(k), \dots, y\big(k-n_y+1\big), \Delta u^1(k+j-1), \dots, \Delta u^1(k), u^1(k-1) \dots, u^1(k-n_u+1), \dots, \Delta u^s(k+j-1), \dots, \Delta u^s(k), u^s(k-1) \dots, u^s(k-n_u+1)\big) \quad (6.\ 18)$$

Here, as during the system identification, n_u is considered constant for all inputs. The input number is used as a superscript to avoid confusion in the following operations.

The predictor in the form of equation (6. 18) is once again split into terms which include future control increments and those that do not, hence the following is obtained for the j-step ahead predictor:

$$y(k+j|k) = f_j\big(\boldsymbol{x}(k)\big) + \sum_{m=1}^{s}\sum_{i=1}^{j} g_{ji}^{m}(\boldsymbol{x}(k))\Delta u^m(k+i-1) \quad (6.\ 19)$$

where

$$\boldsymbol{x}(k) = \big[y(k), \dots, y\big(k-n_y+1\big), u^1(k-1) \dots, u^1(k-n_u+1), \dots, u^s(k-1) \dots, u^s(k-n_u+1)\big] \quad (6.\ 20)$$

Substituting equation (6. 20) into (6. 19), and writing them out in vector form gives the same result as (6. 7), mainly, $\boldsymbol{y} = \boldsymbol{G} \cdot \Delta\boldsymbol{u} + \boldsymbol{F}$. However, for the MISO case the extended variables are defined as

$$\Delta\boldsymbol{u} = \begin{bmatrix} \Delta\boldsymbol{u}(k) \\ \Delta\boldsymbol{u}(k+1) \\ \vdots \\ \Delta\boldsymbol{u}(k+N_u-1) \end{bmatrix}, \quad \boldsymbol{F} = \begin{bmatrix} f_1\big(\boldsymbol{x}(k)\big) \\ f_2\big(\boldsymbol{x}(k)\big) \\ \vdots \\ f_{N2}\big(\boldsymbol{x}(k)\big) \end{bmatrix},$$

$$\boldsymbol{G} = \boldsymbol{G}(\boldsymbol{x}(k)) = \begin{bmatrix} \boldsymbol{G}_{11}(\boldsymbol{x}(k)) & 0 & \cdots & 0 \\ \boldsymbol{G}_{21}(\boldsymbol{x}(k)) & \boldsymbol{G}_{22}(\boldsymbol{x}(k)) & \cdots & 0 \\ \vdots & \vdots & \ddots & \vdots \\ \boldsymbol{G}_{N_2\,1}(\boldsymbol{x}(k)) & \boldsymbol{G}_{N_2\,2}(\boldsymbol{x}(k)) & \ldots & \boldsymbol{G}_{N_2\,N_u}(\boldsymbol{x}(k)) \end{bmatrix} \tag{6. 21}$$

where

$$\Delta\boldsymbol{u}(k) = \begin{bmatrix} \Delta u^1(k) \\ \vdots \\ \Delta u^s(k) \end{bmatrix}, \quad \Delta\boldsymbol{u}(k+j-1) = \begin{bmatrix} \Delta u^1(k+j-1) \\ \vdots \\ \Delta u^s(k+j-1) \end{bmatrix}$$

and

$$\boldsymbol{G}_{i\,l}^{m}(\boldsymbol{x}(k)) = [g_{i\,l}^{m}(\boldsymbol{x}(k))], \quad i = 1, \ldots, j \quad l = 1, \ldots, N_u, \text{ and } m = 1, \ldots, s.$$

Here, each $g(\boldsymbol{x}(k))$ is of dimension $[1, s]$.

Using this new definition of the relevant variables, the same procedure used in the SISO case is applied to introduce integral action to the predictor (6. 19).

Similarly, the constraints imposed on the system have to be re-structured.

Most of the modifications which are required are the adjustment of identity matrices and unit vectors. The main difference is the new definition of the vector $\Delta\boldsymbol{u}$ as given by equation (6. 21). For the current work, the limits u_{min} and u_{max}, as well as Δu_{min} and Δu_{max}, have been set as equal to all the inputs. As mentioned in the previous section, these bounds were defined to be the maximum magnitude possible and not based on real actuator performance at this stage. This can easily be modified to accommodate actuators with different characteristics.

A new cost function is defined by

$$J(N_1, N_2, N_u) = \sum_{j=N_1}^{N_2} \delta[y(k+j|k) - \omega(k+j)]^2 + \sum_{j=1}^{N_u} \|\Delta\mathbf{u}(k+j-1)\|_{\Lambda}^2 \tag{6. 22}$$

Which is subject to the constraints

$$\begin{cases} u_{min} \le u^i(k+j-1) \le u_{max}, & i = 1, \ldots, s, \quad j = 1, \ldots, N_u \\ \Delta u_{min} \le \Delta u^i(k+j-1) \le \Delta u_{max}, & i = 1, \ldots, s, \quad j = 1, \ldots, N_u \end{cases}$$

Likewise, in matrix form, equation (6. 22) is given by

$$\boldsymbol{J} = [\boldsymbol{G} \cdot \Delta\boldsymbol{u} + \boldsymbol{F} - \boldsymbol{\omega}]^T \cdot [\boldsymbol{G} \cdot \Delta\boldsymbol{u} + \boldsymbol{F} - \boldsymbol{\omega}] + \Delta\boldsymbol{u}^T \cdot \boldsymbol{\Lambda} \cdot \Delta\boldsymbol{u} \tag{6. 23}$$

Taking into account the new definition of the variables.

The solution is found using equation (6. 16) and the control implemented to the system is

$$\boldsymbol{u}(k) = \boldsymbol{u}(k-1) + \Delta\boldsymbol{u}(k)$$

This MISO MPC algorithm was again implemented using Matlab and tested on both the M_{V2} and M_{V4} models identified for the velocity magnitude fluctuations. The lower and upper bounds for the actuation signal in this case were $\pm 30\frac{m}{s}$ and again, the weighing matrix λ was modified during the simulations to manipulate the controller performance.

As in the previous section, the algorithm was tested using the OSA predictors as the plant. Firstly, the case with no measurement noise or disturbances was applied to the model M_{V2}.

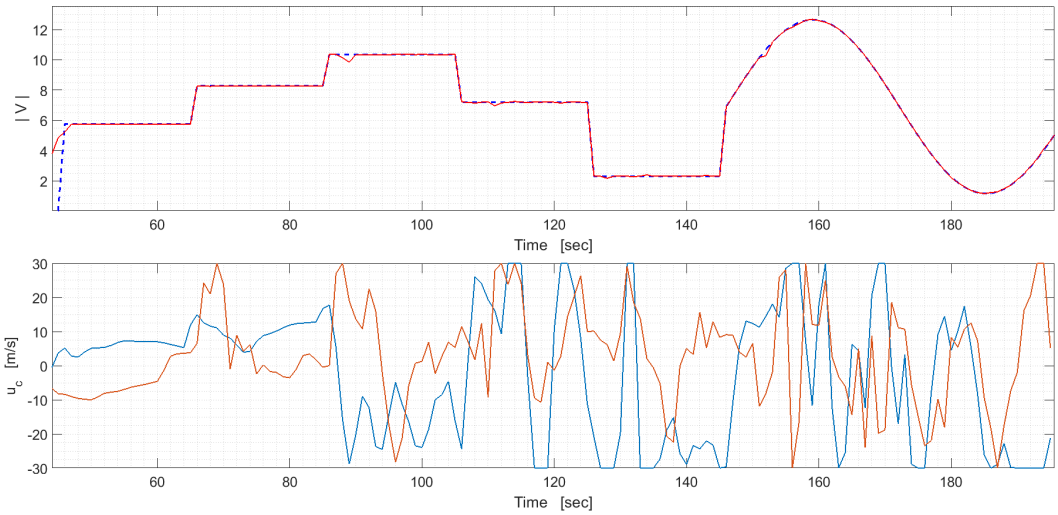

Figure 6.7. Top: Simulation of noise-free controlled M_{V2} model. Plant output in red and desired trajectory in blue. Bottom: Actuation signals $u_i(k)$. $N_2 = 5$, $N_u = 5$ and $\lambda = 0.0001$, $NRMSE = 2.41\%$

This case considered two inputs, therefore s=2 was set in the algorithm and the matrices formed to the appropriate size. In Figure 6.7 it can be seen that using two actuators, the required actuation to maintain the system at the desired trajectory has large oscillations and is saturated at some points due to the constraints. Even so, the controller can maintain good tracking performance and minimise the error.

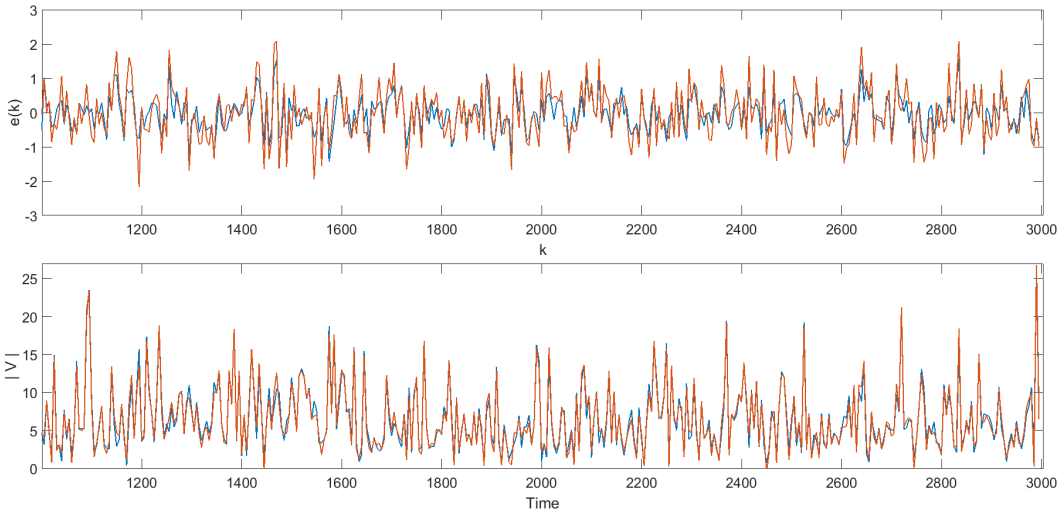

Figure 6.8. Top: White noise signal $e(k)$ and measurement noise $e_m(k)$. Bottom: Comparison of measured and noisy data of $|V|$ fluctuations.

A new noise signal $e(k)$ was generated as in the previous section, for this scenario the variance was set as $\sigma^2 = 5.92\times10\text{^} - 2$. The signal was filtered giving the measurement noise $e_m(k)$ as seen in Figure 6.8, with $\mu = -1.5\times10^{-3}$ and $\sigma^2 = 5.165\times10^{-1}$. The load disturbances introduced $d(k)$ are given by

$$d(k) = \begin{cases} 1.5 & 65 \leq k \leq 80 \\ -1.5 & 110 \leq k \leq 120 \\ 1.5 & 150 \leq k \leq 170 \\ 0 & otherwise \end{cases}$$

The algorithm was then implemented including only the measurement noise, and then measurement noise with load disturbances.

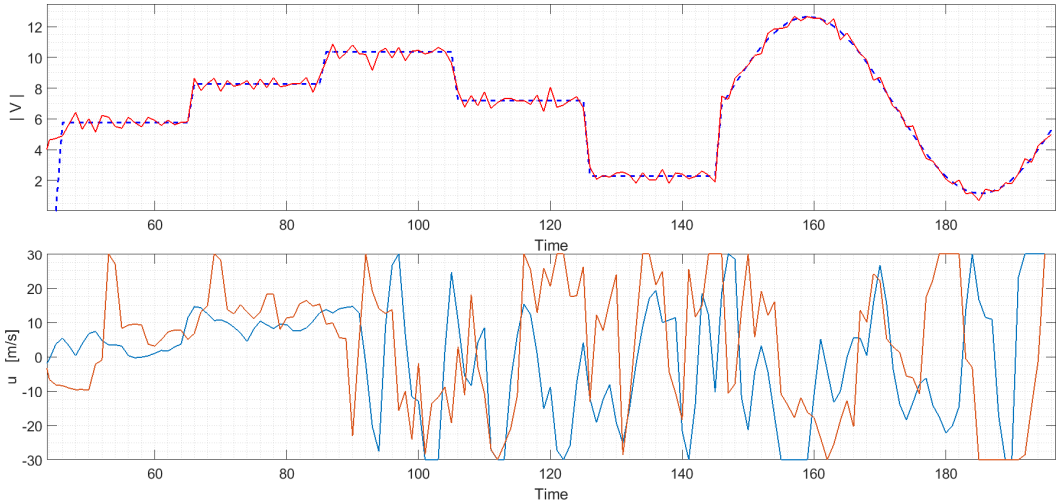

Figure 6.9. Top: Simulation of controlled M_{V2} model with measurement noise $e_m(k)$. Plant output in red and desired trajectory in blue. Bottom: Actuation signals $u_i(k)$. $N_2 = 5$, $N_u = 5$ and $\lambda = 0.0001$, $NRMSE = 10.46\%$

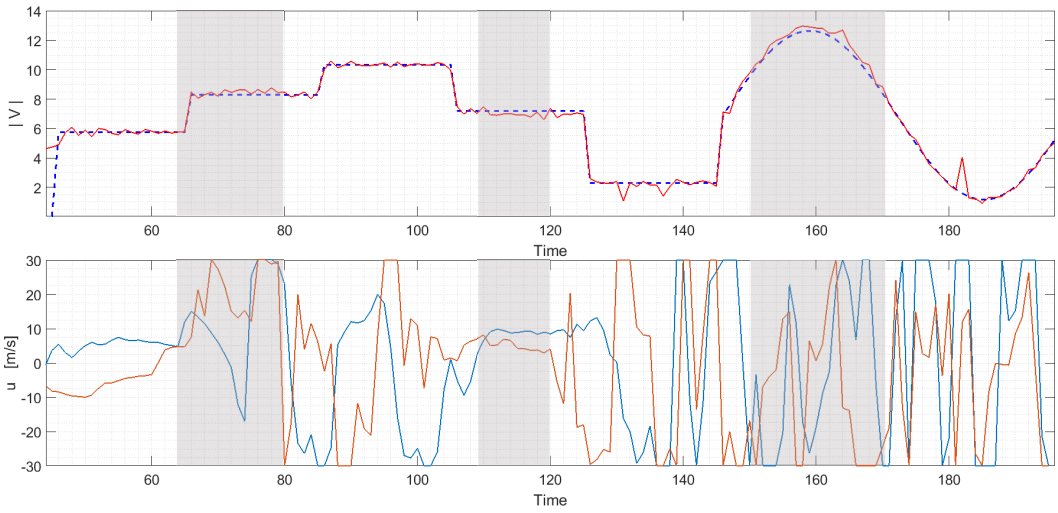

Figure 6.10. Top: Simulation of controlled M_{V2} model with measurement noise $e_m(k)$ and load disturbance $d(k)$ (in grey). Plant output in red and desired trajectory in blue. Bottom: Actuation signals $u_i(k)$. $N_2 = 5$, $N_u = 5$ and $\lambda = 0.0001$, $NRMSE = 10.46\%$

Figure 6.9 and Figure 6.10 once again show that the controller has good performance even in the presence of noise and load disturbances. This is of due to the integral action obtained by using input and output increments rather than the whole values. However, the actuations are saturated for a portion of the simulations. It is clear that when this occurs, the performance of the controller is decreased. The magnitude of the measurement noise was again decreased when introducing the load disturbances so that its effect could be seen more clearly.

After these tests had been performed, the same procedure was implemented using the M_{V4} multi-step-ahead predictors. Once again, a noise free case was performed to define the weighing parameters.

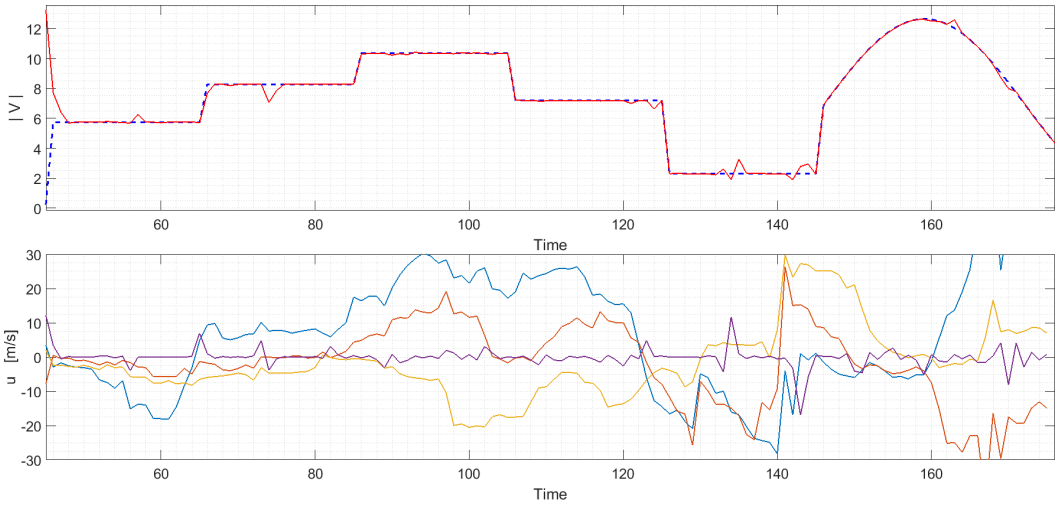

Figure 6.11. Top Simulation of noise-free controlled M_{V4} model. Plant output in red and desired trajectory in blue. Bottom: Actuation signals $u_i(k)$. $N_2 = 5$, $N_u = 5$ and $\lambda = 0.01$, $NRMSE = 9.28\%$

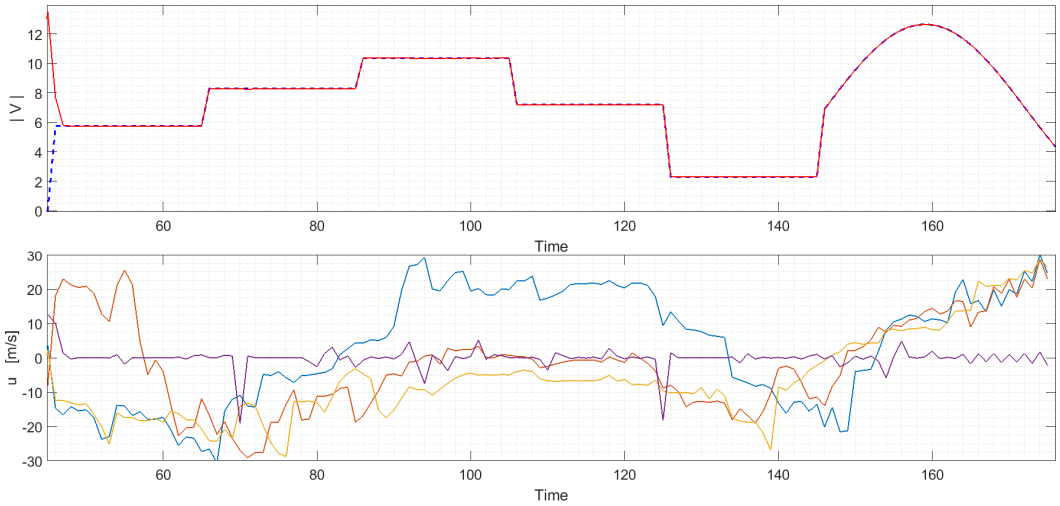

Figure 6.12. Top: Simulation of noise-free controlled M_{V4} model. Plant output in red and desired trajectory in blue. Bottom: Actuation signals $u_i(k)$. $N_2 = 5$, $N_u = 5$ and $\lambda = 0.0001$, $NRMSE = 5.8\%$

The system is successfully controlled even with the relatively high value for λ as can be seen in Figure 6.11. Figure 6.12 shows that the performance can be increased using the weighing matrix, however this makes the actuation slightly more aggressive at some points and the improvement of performance for the current case is not greatly enhanced.

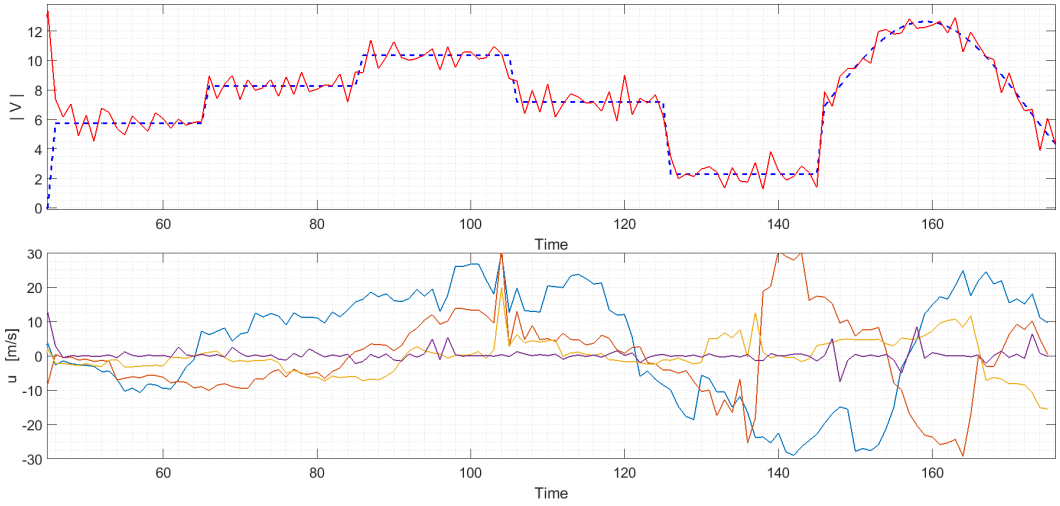

Figure 6.13. Top: Simulation of controlled M_{V4} model with measurement noise $e_m(k)$. Plant output in red and desired trajectory in blue. Bottom: Actuation signals $u_i(k)$. $N_2 = 5$, $N_u = 5$ and $\lambda = 0.01$, $NRMSE = 23.28\%$

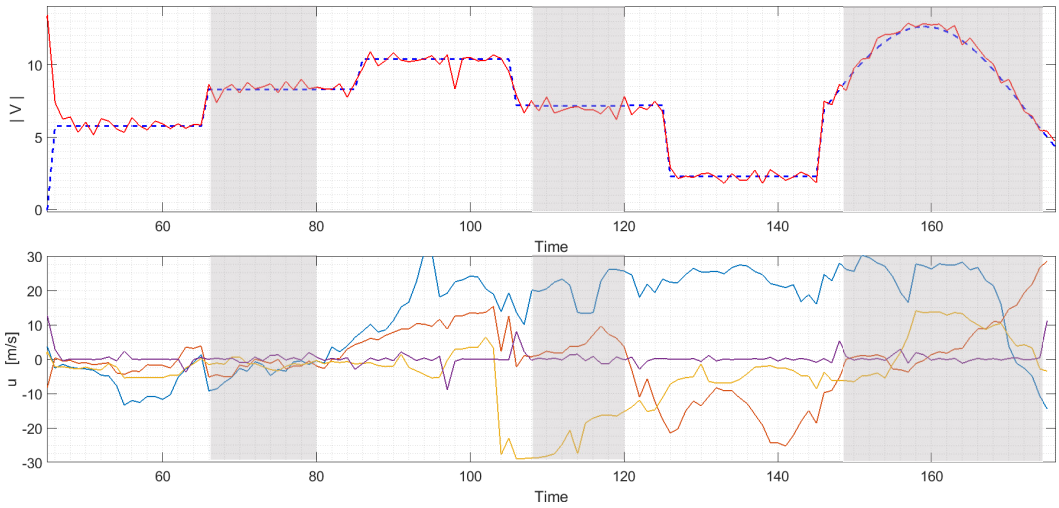

Figure 6.14. Top: Simulation of controlled M_{V2} model with measurement noise $e_m(k)$ and load disturbance $d(k)$. Plant output in red and desired trajectory in blue. Bottom: Actuation signals $u_i(k)$. $N_2 = 5$, $N_u = 5$ and $\lambda = 0.01$, $NRMSE = 14.73\%$

Likewise, a trial using only measurement noise, and one with measurement noise and disturbance were carried out. The results of these can be seen in Figure 6.13 and Figure 6.14, respectively. The same noise signal and disturbances used in the M_{V2} case were applied here. Like the previous case, the measurement error was attenuated in the simulation including the load disturbance to study the performance of the controller before these events.

As it can be seen, the algorithm can take the system to the desired state and track changes in the set-point in the presence of measurement noise and load disturbances.

6.5. Discussion

This chapter has presented a brief overview of the MPC algorithm, with a special focus on the non-linear GPC approach that relies on identified input-affine NARX/NARMAX predictors, introduced by (Bai & Coca, 2008).

The algorithm was to control the fluctuations of the pressure coefficient on the step wall. Additionally, using two MISO models, M_{V2} and M_{V4} the control of the velocity fluctuations at a node downstream of the step was also performed.

In the M_{Cp} case, the j-step ahead predictions are obtained recursively using a OSA predictor and with the MISO models, each of the predictors were identified directly from data. All of the simulations have been

carried out with modified versions of the models which use the increments of input and output variables rather than the whole signals, leading to integral action of the controller and enhancing robustness (Camacho & Bordons-Alba, 2003; Rossiter, 2003).

The controller schemes have proved to be successful in all the cases. Each of them was tested firstly with no noise, then considering measurement noise obtained from a filtered white noise sequence, and lastly, with measurement noise and load disturbances. In the case of the M_{Cp} control, the signal to noise ratio defined is

$$SNR = 10\log\left(\frac{\sigma^2_{signal}}{\sigma^2_{noise}}\right) \approx 9dB$$

while in the cases used with the velocity magnitude, $SNR \approx 15dB$.

The disturbances added were approximately 8-10% of the largest magnitudes of the signal used in the system identification in each case. This shows that the method proposed has good performance overall and the capability to reject disturbances and operate with corrupted measurements.

It can be observed that both $M_{V(\cdot)}$ models performed better than the M_{Cp}. This can be attributed to two reasons. The first is that for the M_{Cp} model, a single OSA predictor was used, and the five-step-ahead predictions obtained through recursive calculations. This approach leads to a build-up of error at each step due to the use of past predictions rather than data (Bai, 2010). Therefore, the control sequence computed will not drive the real system to the desired state. On the other hand, the use of directly identified multi-step-ahead predictors, as used in this work, greatly improves the accuracy of the projected evolution of the system, allowing for the truly required control signal to be computed.

The predictors identified using the NARMAX methodology are parsimonious compared to those obtained through linearizations or first-principle models, and therefore controllers can be designed with greater ease (Bewley, 2001; Billings, 2013; Scott Collis, Joslin, Seifert, & Theofilis, 2004).

This is enhanced further by the fact that they contain only linear terms with respect to future input. Therefore, the advantage of a wholly NMPC strategy is obtained, without the associated complexity and

computational cost as fast QP methods can be used to carry out the optimization. A last advantage to using the NARMAX methodology, is that when using corrupted measurements for the identification, stochastic predictors can easily be identified, which can improve the robustness of the designed control law since it would not depend only on the tuning parameters as the model itself accounts for noise and disturbances (Bai & Coca, 2011).

The second reason behind the increased performance of $M_{V(\cdot)}$ over M_{Cp} is that the former has a single degree of freedom to control the system. This single actuation is able to track the desired trajectory, however, since it does not perform as well as expected, it is likely that the real system will not be adequately controlled. This is also visible in the fact that the M_{V4} model outperforms the M_{V2}, again showing an improvement with increased actuators.

The control actions of the four-input case are smoother and of a lower magnitude compared to those of two actuators, which even saturates in some instances. Nonetheless, the stability is maintained and performance recovered at later time-steps for all the cases.

It may be possible to improve the performance of the controller further by carrying out tests using either an increased prediction horizon, or a higher number of actuators. Although it has been seen that using $N_2 = 5$ has yielded positive results, an increase of the prediction horizon is guaranteed to improve the performance, given that an infinite horizon leads to nominal stability (Keerthi & Gilbert, 1988; Mayne & Michalska, 1990; Mayne, Rawlings, Rao, & Scokaert, 2000). This of course, increases the computational burden, however depending on the sampling time and complexity of the model, it may not be of great concern unless extremely high horizons are sought. In the current work this was not perfumed due to the decrease of prediction performance that was seen after five-steps-ahead. However, the use of alternate NARMAX formulations may allow for better predictors to be identified at longer prediction horizons.

As it was mentioned in the last chapter, the number and location of the actuators contribute greatly to the effectiveness of the control

scheme in the case of fluid flows (Kim, 2003; Lofdahl & Gad-El-Hak, 1999; Scott Collis, Joslin, Seifert, & Theofilis, 2004).

In this work, three arrangements have been studied, one actuator one the inlet wall and two or four on the step wall. These have shown that a SISO case is likely to be unfeasible, as it is barely able to control a reduced-order model of the system with adequate performance. The two and four actuator cases have showed promising results, however, these could be improved if further analysis using different dimensions and additional actuators were introduced, to find the optimal settings.

CHAPTER 7

Frequency analysis of fluid flows

7.1. Introduction

Turbulence has been studied for many years, yet a comprehensive understanding of it, and its onset is still out of reach (George, P., 2003; Li, 2013; Moin & Mahesh, 1998). In fact, some believe that turbulence is even "more than" chaos, since it has been shown that depending on the Reynolds number, it may not be caused by, or even due to the same effects as chaos; but rather due to rough dependence[1] on the initial data (Li, 2013, 2014).

The NARMAX models identified from simulation data of flow over the BFS have been shown to capture the dynamics of the flow encountered in this geometry. An analysis using nonlinear reduced-order models of turbulent flow can be used to grow the understanding of fluid behaviour, in an attempt to shed some light on the turbulence phenomena. Non-linear models are clearly required for such a task since

[1] Chaos and moderate Reynolds number turbulence is said to be due to sensitive dependence on initial data, whereas high Reynolds number is due to rough dependence on initial data. That is, in the former, a perturbation takes time to accumulate and in the latter it can grow to a significant amount instantly ((Li, 2013))

their linear counterpart cannot represent dynamical behaviours such as chaos, harmonics, intermodulation, among others (Lang & Billings, 2004; Peyton Jones & Choudhary, 2012a; Yue, Billings, & Lang, 2005a). This however, greatly increases the difficulty of the analysis since the well-established methods of linear analysis in both the time- and frequency-domain cannot be easily applied in the non-linear case (Lang & Billings, 2004).

The study of non-linear systems in the frequency domain has received more attention over the past few decades (Lang & Billings, 1997; Lang, Billings, Yue, & Li, 2007; Yue, Billings, & Lang, 2005a), mainly due to the increase of computational power and development of tools which allow for this kind of analysis, such as the generalized frequency response function (GFRF) (Billings & Tsang, 1989a; George, D. A., 1959), the output frequency response function (OFRF) (Billings & Lang, 2002; Lang & Billings, 1997, 2004), and the describing function method (Nuij, Bosgra, & Steinbuch, 2006), to name a few. Another reason for the interest in the analysis of non-linear systems, is the fact that if these complex phenomena, such as energy transfer between frequencies, are not understood and considered in the design of any structure, be it architectonic, automotive or otherwise, it can lead to a catastrophic outcome should a resonance be triggered, for example (Lang & Billings, 2004).

Frequency domain analysis of non-linear systems is useful, both, in the case that the time-domain models have physically meaningful parameters or if, as is the case of identified models, the terms and coefficients are not related to any physical properties of the system (Jing, Lang, & Billings, 2008). This is because the frequency representation can be explicitly mapped from the model coefficients and so the observed non-linear phenomena can be directly linked to the physical system (Jing, Lang, & Billings, 2008; Lang, Billings, Yue, & Li, 2007). Additionally, identified models with no physical meaning are often not unique, therefore it is difficult to compare them in the time-domain. However, their frequency domain representation will show the invariant features of the *system*, and therefore will be the same (Billings, 2013; Jing, Lang, & Billings, 2008; Lang, Billings, Yue, & Li, 2007).

This chapter presents an analysis of identified NARMAX models in the frequency domain. These models represent the input-output behaviour between four nodes in the domain, two upstream and two downstream of the step. Additionally, the interaction between both upstream nodes will be studied.

The chapter is divided as follows. Section 7.2 presents a brief introduction to the frequency domain properties of non-linear systems. Section 7.3 introduces the concept of the GFRF and OFRF, additionally the method to compute them is presented in section 7.3.1 and 7.3.2, respectively.

Section 7.4 presents the computation and analysis of the GFRF's for the identified models. Likewise, Section 7.5 presents the estimated OFRF's. Both, the GFRF's and OFRF's are presented up to third order. Finally, Section 7.6 presents a discussion of the results and their relevance.

7.2. Non-linear systems in the frequency domain

Linear systems have been studied in the frequency domain with great success for many years, and many theories exists, allowing for analysis and design of systems across many disciplines (Billings, 2013; Billings & Lang, 2002; Lang & Billings, 2004).

The main benefit of linear models is that they can be directly mapped between the time and frequency domain (Billings, 2013; Billings & Lang, 2002; Lang & Billings, 2004). Therefore, the relationship between the input spectra and the output response can be easily obtained (Billings & Lang, 2002; Lang & Billings, 2004). The time domain system response, $y(t)$, is given by

$$y(t) = \int_{-\infty}^{\infty} h(\tau)u(t-\tau)d\tau$$

Here, $h(\tau)$ is the impulse response and $u(t)$ the input.

Applying the Fourier transform gives the frequency domain counterpart

$$Y(j\omega) = H(j\omega) \cdot U(j\omega) \tag{7. 1}$$

Where $Y(j\omega)$ and $U(j\omega)$ are the spectrum[2] of the output and input respectively and $H(j\omega)$ is the (linear) frequency response function. Additionally, $j^2 = -1$ is the imaginary unit.

The need for non-linear systems arises from the fact that linear ones cannot exhibit many dynamics and phenomena that are present and significant to most real systems (Billings & Tsang, 1989a; Lang & Billings, 2004). The following phenomena are the mechanisms through which the output frequency content of a non-linear system is enriched and becomes significantly different to that of a linear system excited by the same input signal (Billings, 2013; Billings & Tsang, 1989a; Lang & Billings, 2004; Yue, Billings, & Lang, 2005a).

- Inter-modulation: the way in which two or more components are combined to form the output frequency. The frequencies created in this way are limited to those which cannot be obtained through the rest of the mechanisms described here.
- Harmonics: defined as frequency components which are multiples of the input frequency, i.e. if the input frequency is $\omega = \omega_1$ the output will include elements at $\omega = 2\omega_1, 3\omega_1, \ldots$
- Desensitisation: is the interference caused to the response at frequency ω_1 by the application of another sinusoidal of frequency component ω_2. The gain at ω_1 will depend on the magnitude of the second signal of frequency ω_2
- Gain compression or expansion: is the change of the system gain due to variation of the input magnitude, where it is not proportional as with linear models. Expansion is an increase of the gain beyond the linear gain, and compression the opposite.

[2] In this work $Y(j\omega)$ is used to represent the Fourier transform of $y(t)$, some of the literature also uses $Y(\omega)$.

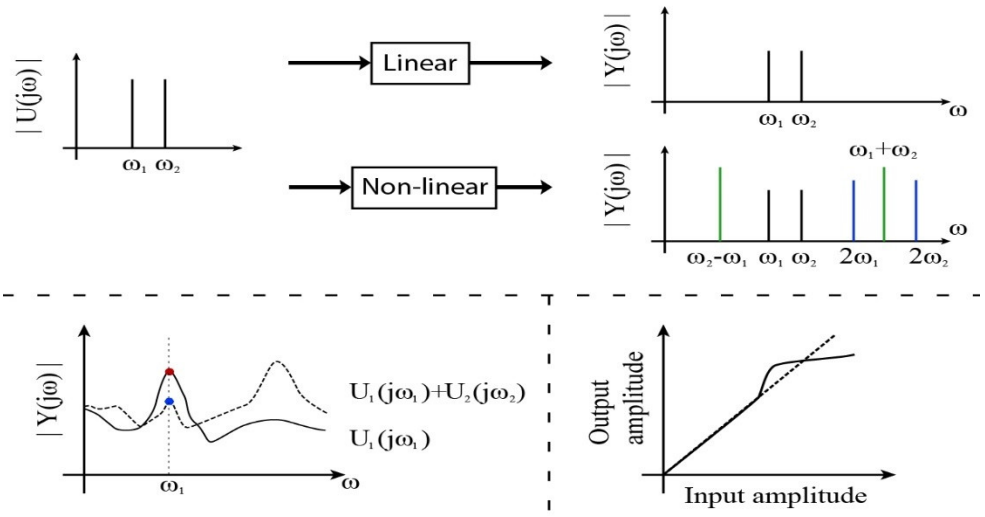

Figure 7.1. Examples of non-linear frequency generation phenomena. Top: Harmonics and intermodulation. Bottom left: Desensitisation and Bottom right: Gain expansion/compression.

Visual examples of these phenomena are given in Figure 7.1. The top image compares the linear and non-linear frequency response of a system under a two-tone input. Harmonics (in blue) and inter-modulation effects (in green) are shown (Billings & Tsang, 1989a, 1989b; Yue, Billings, & Lang, 2005a). The image on the bottom left presents desensitisation of the original output spectrum (when excited by $U_1(j\omega_1)$), when an additional input $U_2(j\omega_2)$ is applied. The value of the spectrum at ω_1 (red dot) is lowered non-linearly due to the presence of the second frequency component (Billings & Tsang, 1989a, 1989b). The bottom right image shows a typical curve of the gain variation of a linear (dotted) and non-linear (solid) system. Gain expansion is observed as the solid line surpasses the dashed and compression is present when the former is found below (Billings & Tsang, 1989a, 1989b; Yue, Billings, & Lang, 2005a).

It is clear that the output spectrum of a non-linear system is much richer than the input (Billings & Lang, 2002; Billings & Tsang, 1989a; Jing, Lang, & Billings, 2008, 2010; Lang & Billings, 1997, 2004; Peyton Jones & Choudhary, 2012b). Therefore, the techniques applied to the study of linear systems cannot be applied in the non-linear case and extensions have been proposed (Billings & Lang, 2002; Billings & Tsang, 1989a, 1989b; Jing, Lang, & Billings, 2010; Lang & Billings, 1997, 2004; Peyton Jones, 2007; Peyton Jones & Choudhary, 2012a; Yue, Billings, & Lang, 2005a).

7.3. The generalized and output frequency response functions

The GFRF is an extension of the linear frequency response function, to the nonlinear case (Billings & Lang, 2002; Billings & Tsang, 1989a; Peyton Jones & Choudhary, 2012b; Yue, Billings, & Lang, 2005a). There are several methods to calculate the GFRF's, such as using higher order extensions of the fast Fourier transform (Kim & Powers, 1988; Nam & Powers, 1994) or the transformation of a model using exponential inputs, the power series method, through a direct mapping of coefficients or computing the response to multi-tonal inputs (Billings & Lang, 2002; Lang & Billings, 1997; Peyton Jones & Choudhary, 2012b; Wei, Lang, & Billings, 2007).

A disadvantage of the FFT methods is the need to compute higher order spectra, in addition to the limited ability of analysing systems of up to third order due to computational expense (Billings & Lang, 2002; Yue, Billings, & Lang, 2005a). Additionally, requirements often unachievable concerning the input signals, and a great difficulty in obtaining a Volterra series representation of many systems exist (Billings & Lang, 2002; Yue, Billings, & Lang, 2005a). In this work, an approach based on the mapping of the NARMAX models to the frequency domain will be used (Billings & Lang, 2002; Lang & Billings, 1997; Peyton Jones & Billings, 1989; Peyton Jones & Choudhary, 2012b).

Considering a class of non-linear systems, that is stable near a zero-equilibrium point, and can be represented by the Volterra series (Lang & Billings, 1996; Sandberg, 1983), the output is given by

$$y(t) = \sum_{n=1}^{N} \int_{-\infty}^{\infty} \dots \int_{-\infty}^{\infty} h_n(\tau_1, \dots, \tau_n) \prod_{i=1}^{n} u(t-\tau_i) d\tau_i \tag{7. 2}$$

Where N is the maximum non-linearity order, and $h_n(\cdot)$ represents the n^{th} order Volterra kernel. Equation (7. 2) can also be written as

$$y(t) = \sum_{n=1}^{N} y_n(t) \tag{7. 3}$$

Where, $y_n(t)$ is the contribution of the n^{th} order non-linearity to the output, given by

$$y_n(t) = \int_{-\infty}^{\infty} \dots \int_{-\infty}^{\infty} h_n(\tau_1, \dots, \tau_n) \prod_{i=1}^{n} u(t-\tau_i) d\tau_i \tag{7. 4}$$

The Fourier transform of the Volterra kernel is given by the expansion to the n^{th} order non-linear case of

$$H(j\omega) = \int_{-\infty}^{\infty} h(\tau) e^{-j\omega\tau} d\tau$$

which yields

$$H_n(j\omega_1, \dots, j\omega_n) = \int_{-\infty}^{\infty} \dots \int_{-\infty}^{\infty} h_n(\tau_1, \dots, \tau_n) e^{-j(\omega_1 \cdot \tau_1 + \dots + \omega_n \cdot \tau_n)} \, d\tau_1, \dots, d\tau_n$$

for $n = 1,2, \dots, N$ (7. 5)

Equation (7. 5) is the definition of the n^{th} order generalized frequency response function (GFRF) (George, D. A., 1959).

Given that the Volterra kernel can be written a number of ways depending on the order of the terms within the integration, it is necessary to define a way to obtain unique representations (Billings, 2013). The symmetric GFRF is therefore defined as

$$H_{n\,sym}(j\omega_1, \dots, j\omega_n) = \frac{1}{n!} \sum_{\pi(\cdot)} H_n\left(j\omega_{\pi(1)}, \dots, j\omega_{\pi(n)}\right) \tag{7. 6}$$

In equation (7. 6), $\pi(\cdot)$ denotes all permutations of integers $1, \dots, n$.
Using the definition of the GFRF in equation (7. 4) and considering an input defined by

$$u(t) = \frac{1}{2\pi} \int_{-\infty}^{\infty} U(j\omega) e^{j\omega t} d\omega$$

The output $y(t)$ can be written as

$$y(t) = \sum_{n-1}^{N} \frac{1}{(2\pi)^n} \int_{-\infty}^{\infty} \dots \int_{-\infty}^{\infty} H_n(j\omega_1, \dots, j\omega_n) \prod_{i=1}^{n} U(j\omega_i) e^{j(\omega_1 + \dots + \omega_n)t} d\omega_1, \dots, d\omega_n \tag{7. 7}$$

After some manipulations and change of variables (Billings, 2013; Lang & Billings, 1996), equation (7. 7) can be written in the frequency domain as:

$$Y(j\omega) = \sum_{n=1}^{N} Y_n(j\omega) \tag{7. 8}$$

with

$$Y_n(j\omega) = \frac{1}{\sqrt{n} \cdot (2\pi)^{n-1}} \int_{\omega_1 + \cdots + \omega_n = \omega} H_n(j\omega_1, \dots, j\omega_n) \prod_{i=1}^{n} U(j\omega_i) d\sigma_\omega \tag{7. 9}$$

Where $\int_{\omega_1+,\dots,+\omega_n=\omega}(\cdot)$ denotes the integration of the argument over the n-dimensional hyperplane $\omega = \omega_1+, \dots, +\omega_n$ and $d\sigma_\omega$ denotes the area of a minute element on the hyperplane.

From equation (7. 9), and considering $U_n(j\omega)$ as the extension of an input spectrum $U(j\omega)$ to the n^{th} order non-linear case as

$$U_n(j\omega) = \frac{1}{\sqrt{2} \cdot (2\pi)^{n-1}} \int_{\omega_1 + \cdots + \omega_n = \omega} \prod_{i=1}^{n} U(j\omega_i)\, d\sigma_\omega$$

It can be shown that

$$Y_n(j\omega) = \frac{\int_{\omega_1 + \cdots + \omega_n = \omega} H_n(j\omega_1, \dots, j\omega_n) \prod_{i=1}^{n} U(j\omega_i) d\sigma_\omega}{\int_{\omega_1 + \cdots + \omega_n = \omega} \prod_{i=1}^{n} U(j\omega_i)\, d\sigma_\omega} \cdot \frac{1}{\sqrt{n} \cdot (2\pi)^{n-1}} \cdot \int_{\omega_1 + \cdots + \omega_n = \omega} \prod_{i=1}^{n} U(j\omega_i)\, d\sigma_\omega$$

Defining

$$G_n(j\omega) = \frac{\int_{\omega_1 + \cdots + \omega_n = \omega} H_n(j\omega_1, \dots, j\omega_n) \prod_{i=1}^{n} U(j\omega_i) d\sigma_\omega}{\int_{\omega_1 + \cdots + \omega_n = \omega} \prod_{i=1}^{n} U(j\omega_i)\, d\sigma_\omega} \tag{7. 10}$$

it is clear that

$$Y_n(j\omega) = G_n(j\omega) \cdot U_n(j\omega) \tag{7. 11}$$

$G_n(j\omega)$ is the output frequency response function (OFRF) that relates the input spectrum and system parameters, in the form of the GFRF, to the output response (Billings, 2013; Lang & Billings, 2004). As it can be seen, this is an equivalent formulation to equation (7.1) for the non-linear case.

7.3.1. Derivation of the Generalized Frequency Response Functions

Due to the difficulties encountered in obtaining the Volterra series representation of non-linear systems, different methods have been developed to derive the GFRFs (Billings, 2013; Billings & Tsang, 1989a; Nam & Powers, 1994). Such methods either involve direct identification of the GFRF from input-output data (Billings, 2013; Kim & Powers, 1988), or through a harmonic probing method based on parametric models (Billings, 2013; Billings & Tsang, 1989a; Lang & Billings, 2000).

(Peyton Jones & Billings, 1989) proposed a method to map NARMAX models, such as those identified in this work, to the frequency domain. This method has been used and is implemented as follows.

Firstly, the input needs to be re-written as an n-tone signal which is zero-mean given by:

$$u(k) = e^{j\omega_i k} + \cdots + e^{j\omega_n k}$$

Additionally, it is assumed that an asymptotically stable equilibrium of the system is reached (Billings, 2013; Peyton Jones & Billings, 1989).
Then, considering the NARMAX model re-written as:

$$y(k) = \sum_{m=1}^{M} \sum_{\substack{p=0 \\ p+q=m}}^{m} \sum_{l_1,\ldots,l_{p+q}=1}^{K} c_{pq}(l_1,\ldots,l_{p+q}) \prod_{i=1}^{p} y(k-l_i) \times \prod_{i=p+1}^{p+q} u(k-l_i) \quad (7.12)$$

and $p+q=m$. A recursive method to obtain the GFRF is given by:

$$\begin{aligned}
&\left[1 - \sum_{l_1=1}^{K} c_{10}(l_1) \exp[-j(\omega_1 + \cdots, \omega_n) l_1]\right] H_n(\omega_1 + \cdots + \omega_n) \\
&= \sum_{l_1,\ldots,l_n=0}^{K} c_{0n}(l_1,\ldots,l_n) \exp[-j(\omega_1 l_1 + \cdots, \omega_n l_n)] \\
&+ \sum_{q=1}^{n-1} \sum_{p=1}^{n-q} \sum_{l_1,\ldots,l_n=0}^{K} c_{pq}(l_1,\ldots,l_n) \exp\left[-j\left(\omega_{n-q+1} l_{p+1} + \cdots + \omega_n l_{p+q}\right)\right] H_{n-q,p}\left(\omega_1 + \cdots + \omega_{n-q}\right) \\
&+ \sum_{p=2}^{n} \sum_{l_1,\ldots,l_p=0}^{K} c_{p0}\left(l_1,\ldots,l_p\right) \exp[-j(\omega_1 + \cdots + \omega_n)]
\end{aligned} \quad (7.13)$$

where

$$H_{n,p}(j\omega_1,\ldots,j\omega_n) = \sum_{i=1}^{n-p+1} H_i(j\omega_1,\ldots,j\omega_i) H_{n-i,p-i}(j\omega_{i+1},\ldots,j\omega_n) \exp[-j(\omega_1 + \cdots + \omega_i)^{l_p}] \quad (7.14)$$

and

$$H_{n,1}(j\omega_1, \dots, j\omega_n) = H(j\omega_1, \dots, j\omega_n) \exp[-j(\omega_1 + \cdots + \omega_n)^{l_1}] \tag{7. 15}$$

The recursive algorithm set by equations (7. 13)-(7. 15) is only defined for data and models which are zero-mean and are stable around a zero-equilibrium point (Billings, 2013; Peyton Jones & Billings, 1989, 1993). Data used for system identification and the models obtained are usually not of this form, therefore the mean in addition to the DC offset of the model must be removed (Peyton Jones & Billings, 1989, 1993; Peyton Jones & Choudhary, 2012b).

The NARMAX model is re-written using a change of variable

$$\tilde{u}(t) = u(t) - \bar{u} \tag{7. 16}$$

where

$$\bar{u} = \frac{1}{N_l} \sum_{i=1}^{N_l} u_i$$

and N_l is the length of the data sequence. Substituting $u(t)$ from equation (7. 16) into the NARMAX model of equation (4.1) gives

$$\begin{aligned} \boldsymbol{y}(k) = \boldsymbol{F}\Big(&\boldsymbol{y}(k-1), \dots, \boldsymbol{y}\big(k-n_y\big), \tilde{\boldsymbol{u}}(k-1) + \bar{\boldsymbol{u}}, \dots, \tilde{\boldsymbol{u}}(k-n_u) \\ &+ \bar{\boldsymbol{u}}, \boldsymbol{e}(k-1), \dots, \boldsymbol{e}(k-n_e)\Big) + \boldsymbol{e}(k) \end{aligned} \tag{7. 17}$$

In order to remove the DC component, consider

$$\tilde{y}(t) = y(t) + y_0 \tag{7. 18}$$

Where y_0 is the models internal constant, $\tilde{y}(t)$ the output including the DC term and $y(t)$ is the offset-free output (Peyton Jones & Choudhary, 2012b). Again, substituting (7. 18) into the modified predictor of equation (7. 17) yields

$$\begin{aligned} \boldsymbol{y}(k) - \boldsymbol{y}_0 = \boldsymbol{F}\Big(&\boldsymbol{y}(k-1) - \boldsymbol{y}_0, \dots, \boldsymbol{y}\big(k-n_y\big) - \boldsymbol{y}_0, \tilde{\boldsymbol{u}}(k-1) \\ &+ \bar{\boldsymbol{u}}, \dots, \tilde{\boldsymbol{u}}(k-n_u) + \bar{\boldsymbol{u}}, \boldsymbol{e}(k-1), \dots, \boldsymbol{e}(k-n_e)\Big) + \boldsymbol{e}(k) \end{aligned}$$

The internal constant is then obtained by solving $\sum c_{00} * y_0 + C = 0$, where c_{00} are all terms affected by y_0 and are labelled per equation (7. 12) and C are the constant terms.

During each of these substitutions, the model coefficients need to be recalculated, and some terms will be added or removed. Once these

modifications have been made, the model is ready to be used for the estimation of the GFRF (Billings, 2013; Peyton Jones & Billings, 1989, 1993; Peyton Jones & Choudhary, 2012b).

7.3.2. Derivation of the Output Frequency Response Functions

The GFRFs can be used to analyse the non-linear model. However, as they are multivariable function in higher order frequency space, they are difficult to interpret, and even their visualisation is complicated after second order (Billings, 2013; Billings & Tsang, 1989a, 1989b; Yue, Billings, & Lang, 2005a, 2005b).

Nevertheless, methods have been implemented such as subdomain division to analyse individual contribution by each term (Peyton Jones & Billings, 1989), or using graphical techniques, for example (Billings, 2013; Billings & Tsang, 1989b; Billings, Tsang, & Tomlinson, 1990; Yue, Billings, & Lang, 2005a, 2005b).

A better approach is to perform the analysis using OFRF's as defined in equation (7. 10) and (7. 11). These are functions of a single complex variable (Lang & Billings, 2004). The non-linear OFRF allows for the system to be analysed in the style of linear systems, therefore it is possible to define the non-linear behaviour and determine how the frequency generation occurs (Billings, 2013; Billings & Lang, 2002; Lang & Billings, 2004).

The OFRF is obtained by integrating the product of the GFRF and input spectrum over the hyper-plane $\omega_1+,\dots,+\omega_n = \omega$, for each ω of the output spectrum $Y(j\omega)$.

The output response of a third order system, according to equation (7. 8), will be

$$Y(j\omega) = Y_1(j\omega) + Y_2(j\omega) + Y_3(j\omega) \tag{7. 19}$$

Using (7. 9)

$$Y(j\omega) = 1 \cdot \int_{\omega_1=\omega} H_1(j\omega_1) \cdot U(j\omega_1) d\sigma_{\omega 1} +$$

$$0.1125 \cdot \int_{\omega_1+\omega_2=\omega} H_2(j\omega_1, j\omega_2) \cdot U(j\omega_1) \cdot U(j\omega_2) d\sigma_{\omega 1} d\sigma_{\omega 2} +$$

$$0.0146 \cdot \int_{\omega_1+\omega_2+\omega_3=\omega} H_3(j\omega_1, j\omega_2, j\omega_3) \cdot U(j\omega_1) \cdot U(j\omega_2) \cdot U(j\omega_3) d\sigma_{\omega 1} d\sigma_{\omega 2} d\sigma_{\omega 3}$$

The contribution of the first, second and third order non-linearities can be studied individually as seen in (7. 9).

7.4. Computation and analysis of the GFRF's for the BFS

The analysis of a NARMAX model using frequency domain methods is capable of shedding light into the energy transfer mechanisms between the input and output (Billings, 2013; Billings & Lang, 2002). For the case of flow over the BFS, it was decided to study how flow upstream of the step influences the downstream (of the step) behaviour.

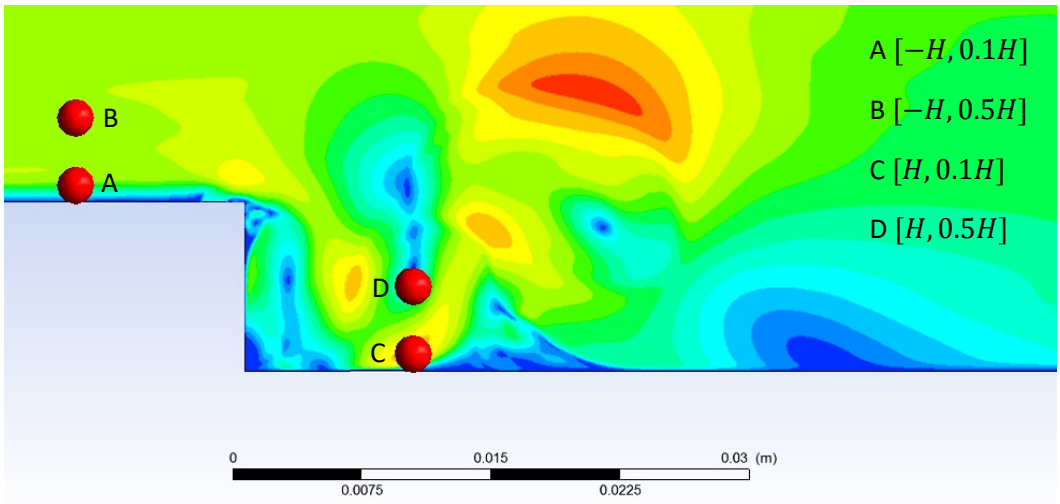

Figure 7.2. Location of the nodes considered for the study of the flow in the frequency domain.

A method to obtain the GFRF's was introduced in Section 7.3.1 and has been implemented on this system. Firstly, NARMAX models using data from the locations given in Figure 7.2 were obtained.

Table 7.1. Label and location of the input/output data of the identified NARMAX models

Model name	Input	Output
M_{AD}	A	D
M_{AE}	A	E
M_{BD}	B	D
M_{BE}	B	E
M_{AB}	A	B

The input/output models between the selected locations were identified. The methodology introduced in Chapter 4 was carried out on data from the relevant nodes to obtain OSA, non-linear SISO predictors. The models were trained and validated on different data sets. The coefficient and model structures for each of the five models are given in Appendix C.1.

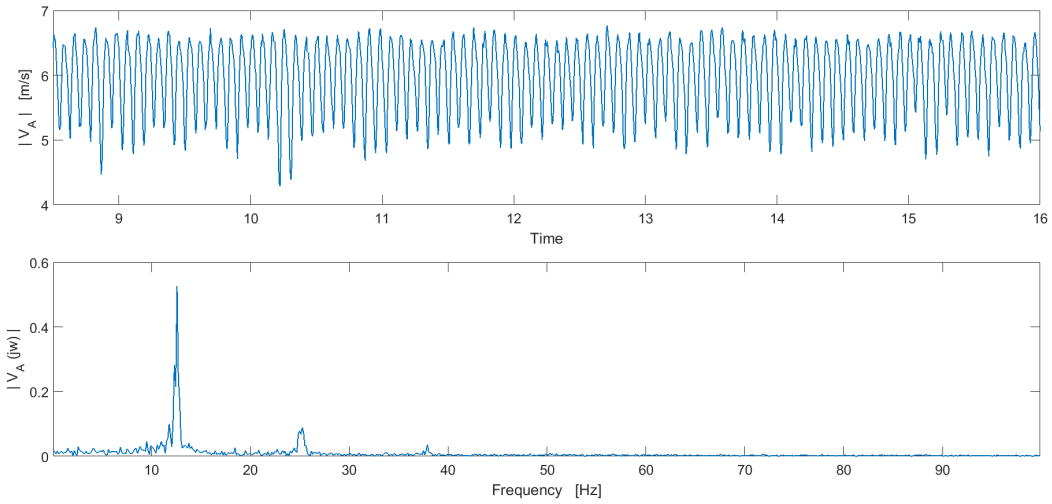

Figure 7.3. Time series and spectrum of the input signals V_A

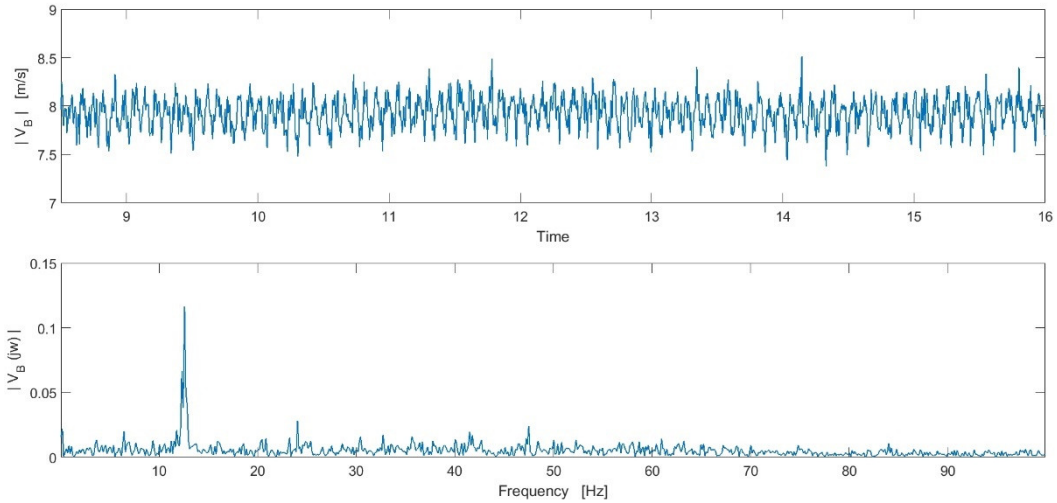

Figure 7.4. Time series and spectrum of the input signals V_B

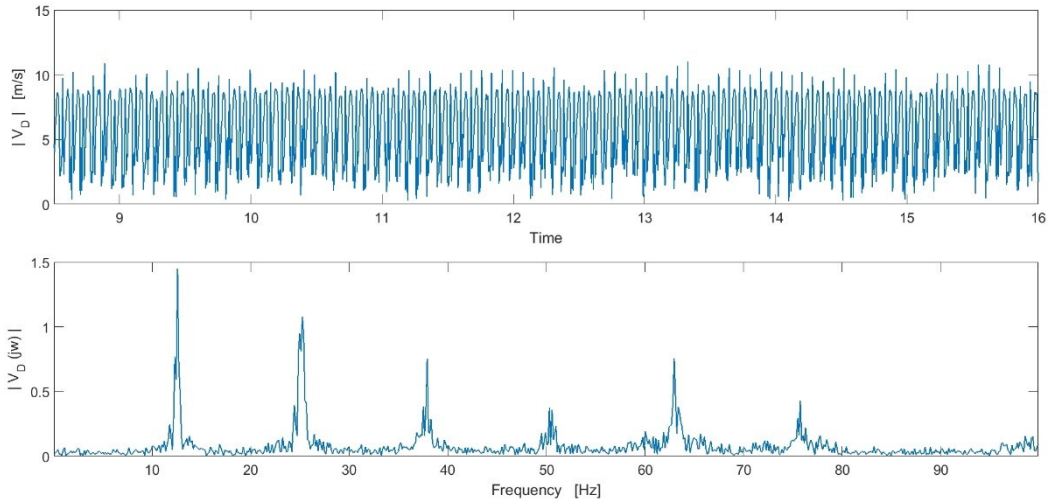

Figure 7.5. Time series and spectrum of the output signals V_D

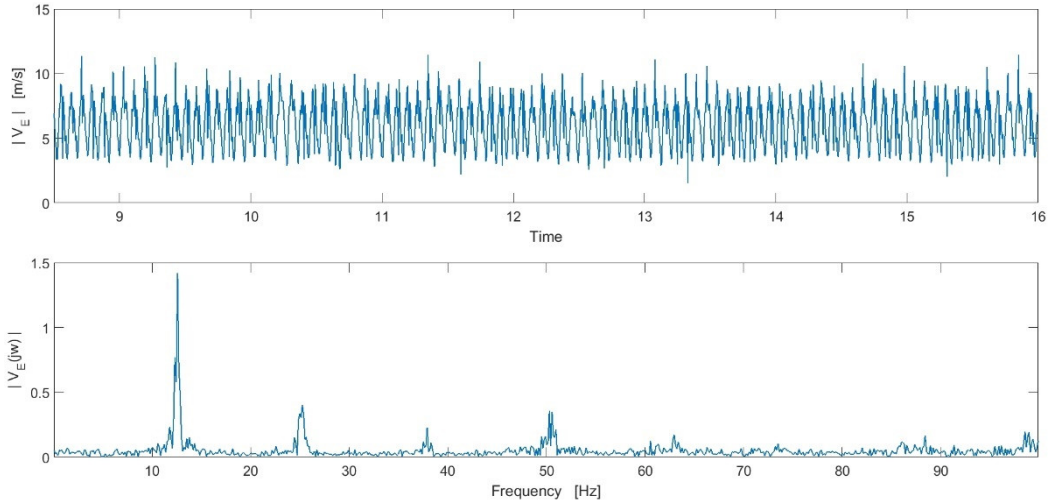

Figure 7.6. Time series and spectrum of the output signals V_E

The input and output data as well as their spectrum are given in Figure 7.3, Figure 7.4 for the inputs (point A and B) and Figure 7.5, Figure 7.6 for the outputs (points D and E).

Table 7.2. Magnitude, $|Y(j\omega)|$, and frequency, F_1, of the most significant peaks of the outputs.

Output D		Output E		Output B	
F_1	$\lvert Y(j\omega)\rvert$	F_1	$\lvert Y(j\omega)\rvert$	F_1	$\lvert Y(j\omega)\rvert$
12.59	1.449	12.59	1.42	12.59	0.1165
25.25	1.081	25.25	0.40	24.05	0.028
37.91	0.753	37.91	0.229	41.51	0.019
50.3	0.374	50.3	0.356	47.5	0.024
62.96	0.756	60.56	0.123	60.96	0.014
75.75	0.43	62.96	0.172	-	-
-	-	88.41	.167	-	-

Significant peaks are seen in both inputs around $F = 12.59$Hz and a smaller one at $F = 25.25$Hz, whereas the outputs show peaks at $F \approx 12, 25, 37, 50, 62, 75$Hz. A summary of the location and magnitudes of the peaks is given in Table 7.2. The output frequencies are almost multiples of the input frequency; therefore, they are likely to be harmonics. The current analysis, in addition to the OFRF's will allow for the precise determination of how these frequencies are generated.

The algorithm proposed by (Peyton Jones & Billings, 1989) to compute the GFRF's is defined for models that has a zero-mean and stable around a zero-equilibrium point. To ensure this, the modifications according to equation (7. 16) and (7. 18) were performed on each of the models. After the mean removal, the coefficients are recalculated and terms grouped where possible, the removal of the constant is then carried out and again, the model coefficients are updated and terms grouped. For this case, $\bar{u}_A = 5.9663$m/s and $\bar{u}_B = 7.9821$m/s over the training data and different internal constants were identified. The modified models are given in Appendix C.2

Once the models were of appropriate form, the GFRF computation was performed using the Non-linear System Frequency Response Analysis Toolkit (Yue, Lang, & Billings, 2004). Using this Matlab toolbox, both the symbolic expressions and graphical representations of the GFRF of the first, second and third order GFRF were obtained. For many non-linear systems, these GFRF's are sufficient to characterize such a system (Zhang & Billings, 1993).

The expression for the linear, quadratic and cubic GFRF's for system AD are:

$$Y_1(j\omega_1) = -\left(\frac{4.880\, e^{-2\,j\,\omega_1} - 5.962 e^{-j\,\omega_1} + 1.707 e^{-3j\omega_1} - 3.447\, e^{-5\,j\,\omega_1}}{0.125 e^{-2\,j\omega_1} - 0.187 e^{-3j\omega_1} + 1}\right.$$
$$+\frac{1.707 e^{-11\,j\,\omega_1} + 1.127 e^{-13j\,\omega_1} - 0.173 e^{-14\,j\,\omega_1} - 3.447\, e^{-16\,j\,\omega_1} + 1.951 e^{-18\,j\,\omega_1}}{0.125 e^{-2\,j\,\omega_1} - 0.187 e^{-3j\omega_1} + 1}$$
$$\left.+\frac{0.940 e^{-19\,j\,\omega_1} - 1.083 e^{-20\,j\,\omega_1})}{0.125 e^{-2\,j\,\omega_1} - 0.187 e^{-3j\omega_1} + 1}\right)$$

$$Y_2(j\omega_1, j\omega_2) = -\left(\frac{0.286\, e^{-j\,(3\omega_1 + 11\,\omega_2)} - 0.578\, e^{-j\,(5\,\omega_1 + 16\,\omega_2)}}{0.125\, e^{-2\,j(\omega_1 + \omega_2)} - 0.187\, e^{-3\,j\,(\omega_1 + \omega_2)} + 1}\right.$$
$$\left.+\frac{0.818\, e^{-j(2\omega_1 + 20\omega_2)} + 0.327\, e^{-j\,(18\omega_1 + 19\omega_2)} - B + C + D}{0.125\, e^{-2\,j(\omega_1 + \omega_2)} - 0.187\, e^{-3\,j\,(\omega_1 + \omega_2)} + 1}\right)$$

where

$$A = 4.880e^{-2\,j\,w1c} - 5.962e^{-j\,\omega_1} + 1.707e^{-3j\,\omega_1} - 3.447\,e^{-5j\,\omega_1} + 1.707\,e^{-11j\,\omega_1} + 1.127\,e^{-13j\,\omega_1} - 0.173\,e^{-14j\,\omega_1} - 3.447\,e^{-16\,j\,\omega_1} + 1.951\,e^{-18\,j\,\omega_1} + 0.940\,e^{-19j\,w1c} - 1.083e^{-20\,j\,\omega_1}$$

$$B = \frac{0.204e^{-2\,j\omega_1}e^{-13\,j\,\omega_2}A}{0.125e^{-2\,j\,\omega_1} - 0.187e^{-3j\,\omega_1} + 1}$$

$$C = \frac{0.031e^{-3j\omega_1}\,e^{-14\,j\,\omega_2}}{0.125e^{-2\,j\,\omega_1} - 0.187e^{-3j\omega_1} + 1}$$

$$D = \frac{0.183e^{-2\,j\,\omega_1}\;e^{-19j\,\omega_2}}{0.125e^{-2\,j\,\omega_1} - 0.187e^{-3j\,\omega_1} + 1}$$

and lastly,

$$Y_3(j\omega_1, j\omega_2, j\omega_3) = -\left(\frac{F - G + H}{0.125e^{-2j(\omega_1+\omega_2+\omega_3)} - 0.187e^{-3j\,(\omega_1+\omega_2+\omega_3)} + 1}\right)$$

with

$$A = \left(\frac{4.88e^{-2j\,\omega_1} - 5.963e^{-j\,\omega_1} + 1.707e^{-3j\,\omega_1} - 4.447\,e^{-5j\,\omega_1}}{(0.125e^{-2j\,\omega_1} - 0.187e^{-3j\omega_1} + 1)} + \frac{1.707\,e^{-11j\,\omega_1} + 1.127\,e^{-13\,j\,\omega_1} - 0.173\,e^{-14\,j\,\omega_1} - 3.447\,e^{-16j\,\omega_1} + 1.951\,e^{-18\,j\,\omega_1}}{(0.125e^{-2j\,\omega_1} - 0.187e^{-3j\omega_1} + 1)} + \frac{0.94\,e^{-19j\omega_1} - 1.083e^{-20j\,\omega_1}}{(0.125e^{-2j\,\omega_1} - 0.187e^{-3j\omega_1} + 1)}\right)$$

$$B = \frac{0.204e^{-2j\,\omega_1}e^{-13j\,\omega_2}}{(0.125e^{-2j\,\omega_1} - 0.187e^{-3j\omega_1} + 1)}A$$

$$C = \frac{0.031e^{-3j\,\omega_1}\,e^{-14j\,w2c}}{(0.125e^{-2j\,\omega_1} - 0.187e^{-3j\omega_1} + 1)}A$$

$$D = \frac{0.183e^{-2j\,\omega_1}e^{-19j\,\omega_2}}{(0.125e^{-2j\,\omega_1} - 0.187e^{-3j\omega_1} + 1)}A$$

$$E = 0.286\,e^{-j\,(3\,\omega_1\,+11\omega_2)} - 0.578\,e^{-j(5\,\omega_1\,+16\omega_2)} + 0.818\,e^{-j\,(2\omega_1\,+20\,\omega_2)} + 0.327\,e^{-j(18\omega_1\,+19\omega_2)} - A + B + C$$

$$F = \frac{0.031e^{-3j\,(\omega_1\,+\omega_2)}e^{-14\,j\,\omega_3}\,E}{0.125e^{-2j(\omega_1\,+\omega_2)} - 0.187e^{-3j\,(\omega_1\,+\omega_2)} + 1}$$

$$G = \frac{0.204e^{-2j(\omega_1\,+\,\omega_2)}e^{-13\,j\,\omega_3}E}{0.125e^{-2j(\omega_1+\,\omega_2)} - 0.187e^{-3j\,(\omega_1\,+\,\omega_2)} + 1}$$

$$H = \frac{0.183e^{-2j(\omega_1\,+\,\omega_2)}e^{-2j(\omega_1\,+\,\omega_2)}e^{-19j\,\omega_3}\,E}{0.125e^{-2j(\omega_1\,+\,\omega_2)} - 0.187e^{-3j\,(\omega_1\,+\,\omega_2)} + 1}$$

The complexity of these functions is shown in this example.

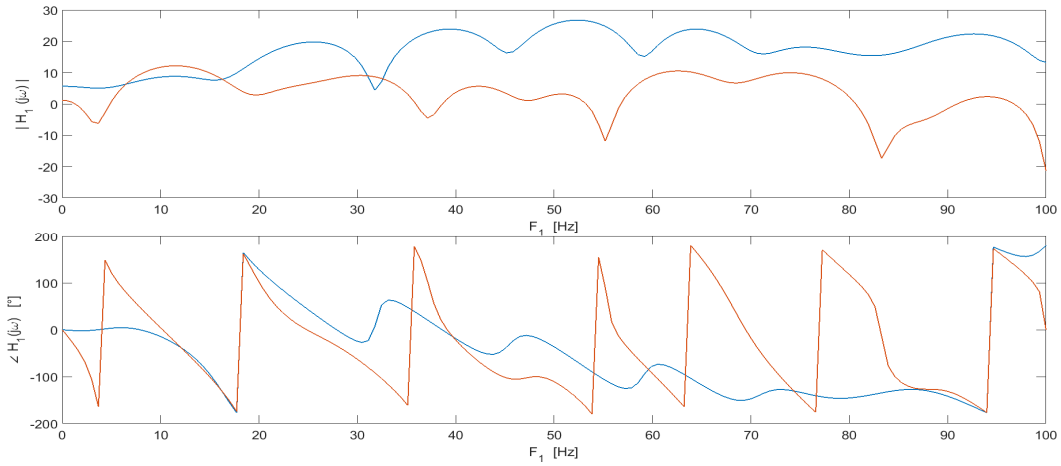

Figure 7.7. Top: Magnitude $|H_1(j\omega_1)|$, Bottom: phase $\angle H_1(j\omega_1)$ plots for the first order GFRF's of model M_{AD} (blue) and M_{BD} (red).

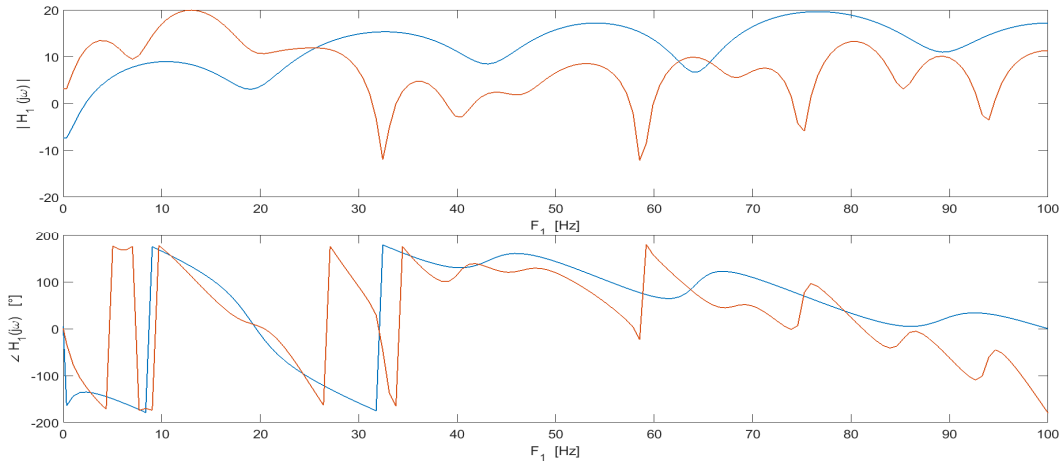

Figure 7.8. Top: Magnitude $|H_1(j\omega_1)|$, Bottom: phase $\angle H_1(j\omega_1)$ plots for the first order GFRF's of model M_{AE} (blue) and M_{BE} (red).

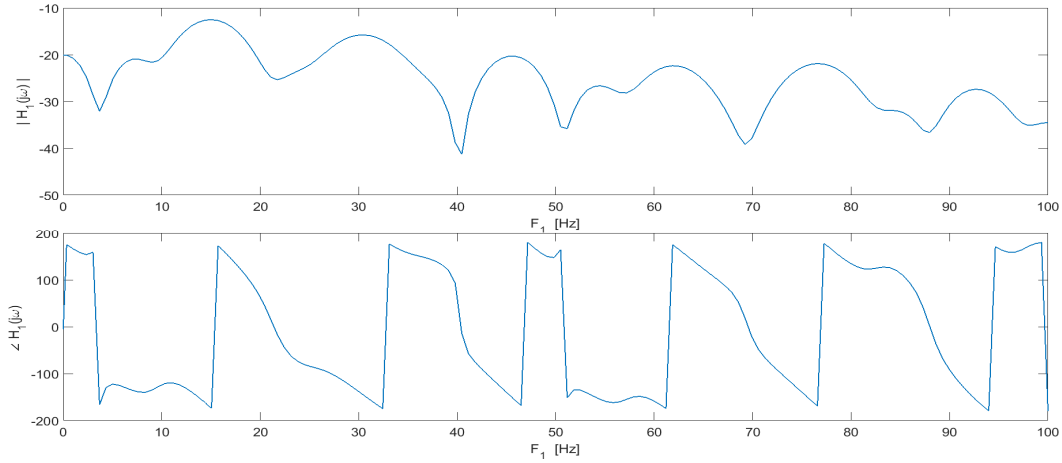

Figure 7.9. Top: Magnitude $|H_1(j\omega_1)|$, Bottom: phase $\angle H_1(j\omega_1)$ plots for the first order GFRF's of model M_{AB} (blue).

The above images compare the first order GFRF's of the different input-output models identified. It can be observed that overall, both the $|H_1^{AD}(j\omega_1)|$ and $|H_1^{AE}(j\omega_1)|$ (shown in blue in their corresponding plots)

are larger than $|H_1^{BD}(j\omega_1)|$ and $|H_1^{BE}(j\omega_1)|$ (shown in red in their respective plots) for frequencies $F_1 > 15$Hz. Whereas below that frequency, $|H_1^{BD}(j\omega_1)|$ is greater in the $3 < F_1 < 9$ Hz range and $|H_1^{BE}(j\omega_1)|$ is larger for all frequencies below $F_1 < 26$Hz. Both systems AD and AE show a high-pass filter behaviour where the gain is seen to increase slightly towards larger frequencies, whereas BD and BE are the opposite, with a slightly negative incline.

Figure 7.9 shows that at all frequencies, the first order effect of the input U_A is dampened considering Y_B as the output and therefore will have a low contribution to the output spectrum.

The phase plots show a saw-tooth behaviour for the systems analysed, except M_{AB}. Additionally, there is a sharp phase change shown by both the M_{AD} and M_{BD} models at $F_1 = 19.94$Hz, and by the AE and BE models at $F_1 \approx 9,32$ Hz, where in the latter, M_{BE} is around 2Hz behind M_{AE}. This last change in phase is also present in model M_{AB}.

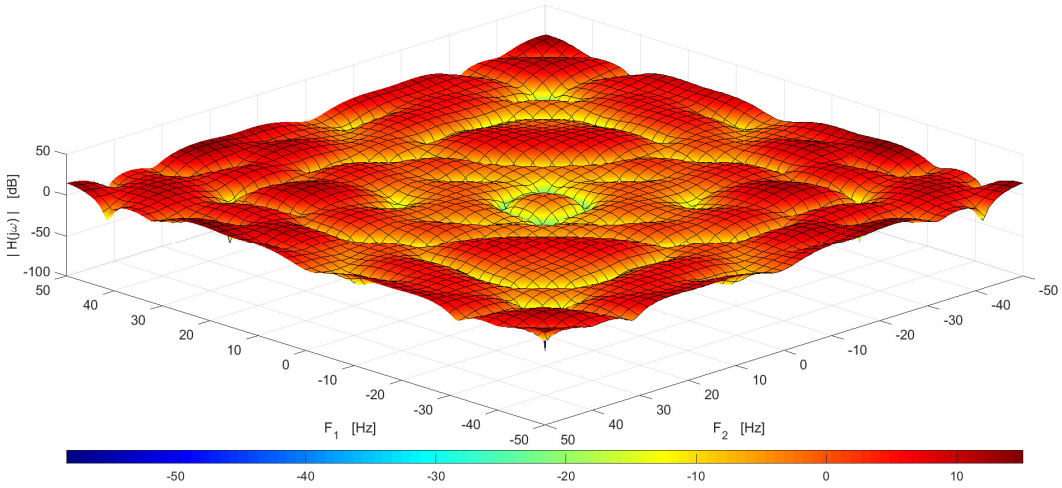

Figure 7.10. Magnitude of $|H_2(j\omega_1, j\omega_2)|$ of second order GFRF of model M_{AD}.

The magnitude of the second order GFRF of model M_{AD} is given in Figure 7.10. Here it can be seen that overall, the non-linear effects are amplified, as the GFRF is largely positive. There are peaks of up to 14.5 dB at $F_1 = \pm 22.8$Hz, $F_2 = \pm 50$. There are two significant anti-resonances at $F = \pm(-36.44, 36.44)$Hz. The complexity of these functions can be seen in these plots, which demonstrate the difficulty of interpreting them due to the high number of peaks and ridges, which hide the mechanisms of output frequency generation (Billings & Lang, 2002; Lang & Billings,

1996; Yue, Billings, & Lang, 2005a, 2005b; Zhang & Billings, 1993). The phase plots for all GFRF's are given in Appendix C.3.

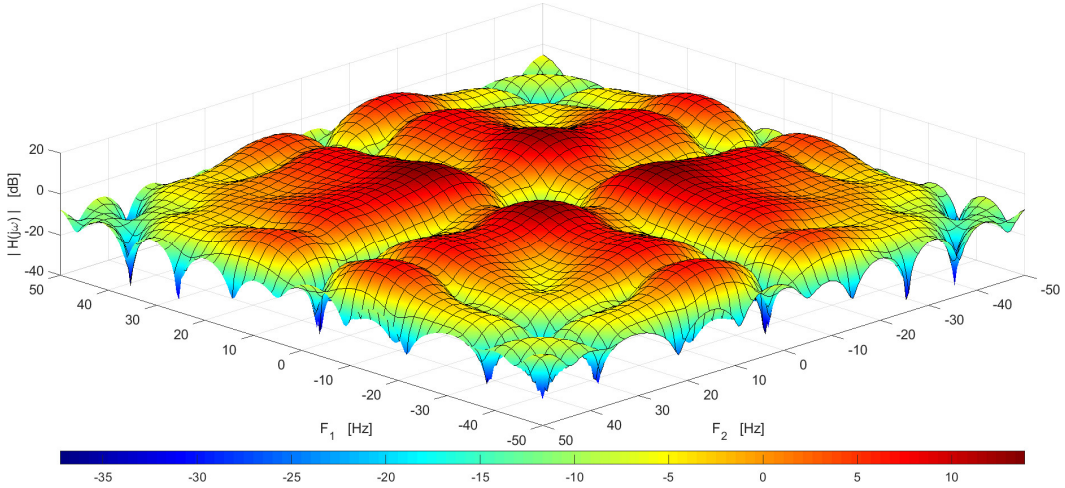

Figure 7.11. Magnitude of $|H_2(j\omega_1, j\omega_2)|$ of second order GFRF of model M_{BD}.

The second order GFRF of M_{BD} in Figure 7.11 shows a generally lower gain than that of M_{AD}. Peaks at $F_1 = F_2 = \pm 12.2$Hz have a gain of 13.41dB which is nearly equal to M_{AD}. However, the remainder drops quickly. There are significant valleys where the gain is lower than -5dB at approximately $F_1 = F_2 = 0$Hz.

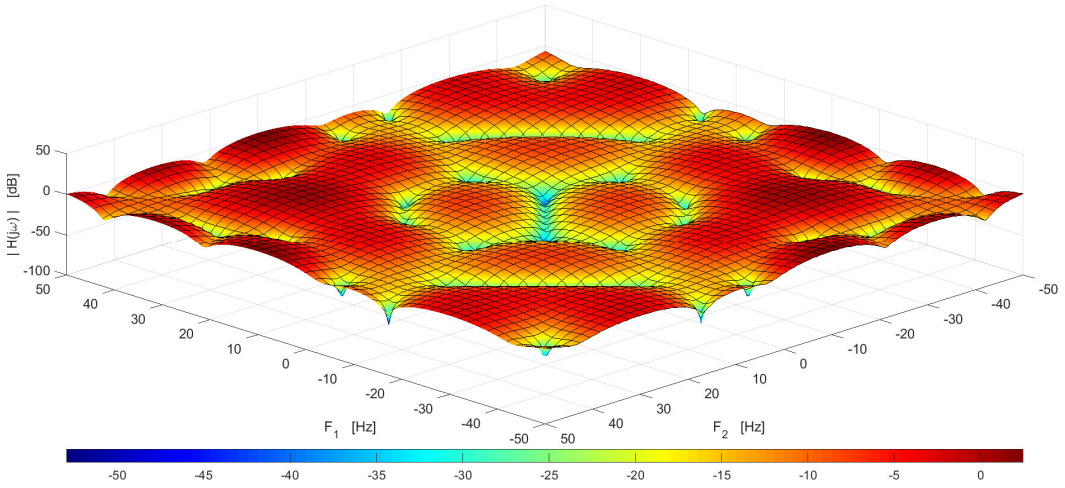

Figure 7.12. Magnitude of $|H_2(j\omega_1, j\omega_2)|$ of second order GFRF of model M_{AE}.

The GFRF of M_{AE} in Figure 7.12 has a much lower magnitude to the previous. The highest peaks have a magnitude of around 2.4dB in gain and are found at $F_1 = \pm 50$Hz, $F_2 = \pm 9.6$Hz.

There are ridges at $F_1 + F_2 = 59.28$Hz and $F_1 + F_2 = 59.28$Hz.

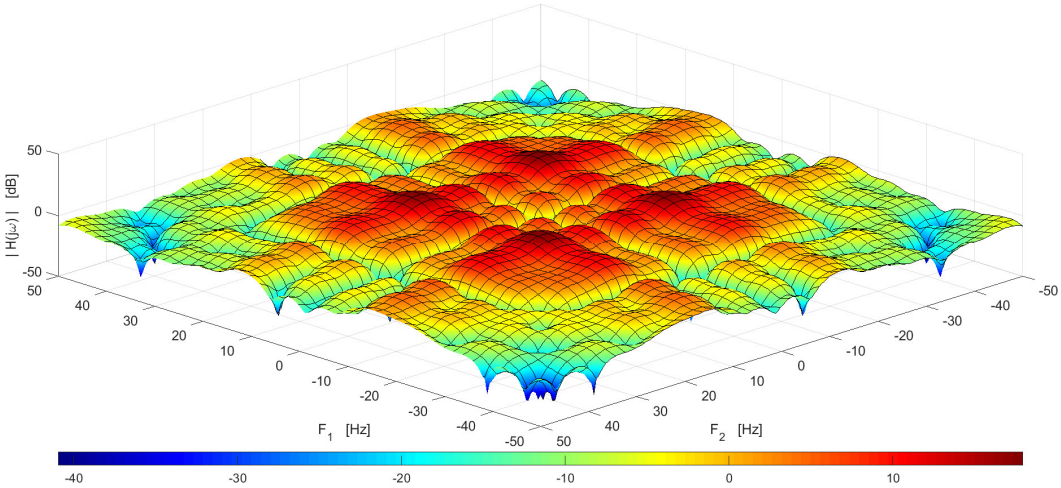

Figure 7.13. Magnitude of $|H_2(j\omega_1, j\omega_2)|$ of second order GFRF of model M_{BE}

This second order GFRF for model M_{BE} has a maximum gain of 17.92dB which is slightly higher than all previous GFRF's. This shows that the contribution from the second order GFRF to the frequency response at $F_1 = F_2 = \pm 13.3$Hz will be significant. However, only frequencies in the $-28 < F_1, F_2 < 2$Hz have a positive gain, the remaining effects are dampened.

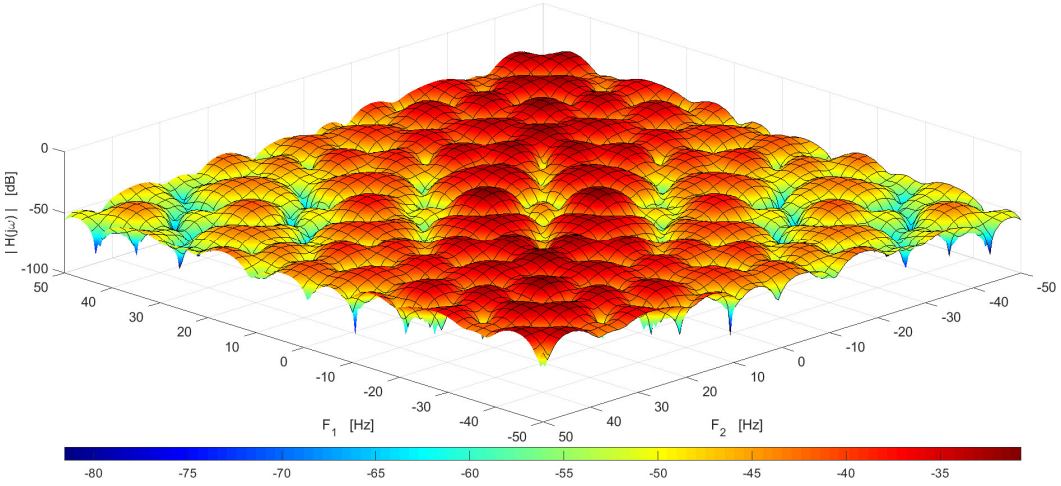

Figure 7.14. Magnitude of $|H_2(j\omega_1, j\omega_2)|$ of second order GFRF of model M_{AB}.

Finally, the second order GFRF from the M_{AB} model show that the response will not be made up from contributions of this function. The entire gain is negative, that is, dampening the effects at all frequencies.

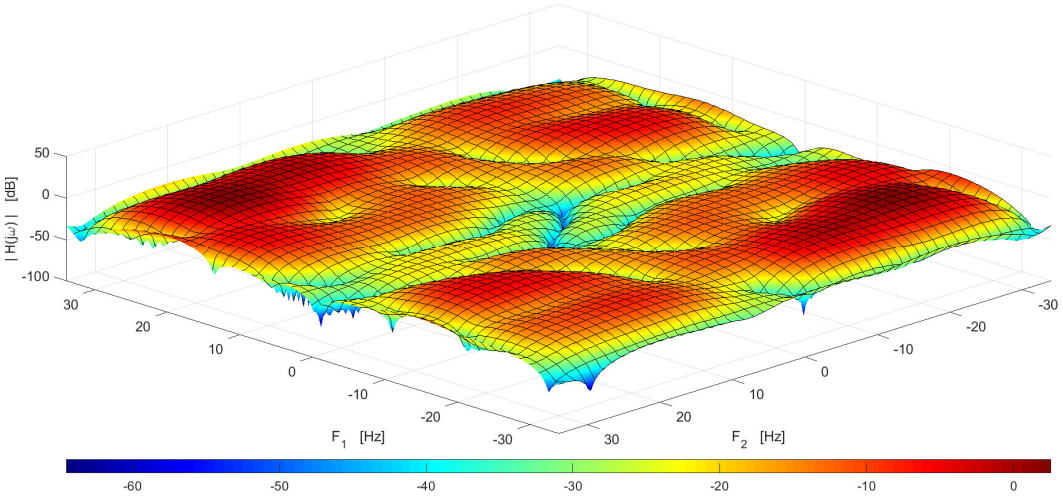

Figure 7.15. Magnitude of $|H_3(j\omega_1, j\omega_2, j\omega_3)|$ of second order GFRF of model M_{AD}.

A slice of the third order GFRF at with $\omega_3 = \omega_2$ for model M_{AD} is shown in Figure 7.15. It can be seen that the contribution of this function to the response will be lower than the second order GFRF's for all frequencies. The highest gain in this case is 2.4dB but most of the values are negative.

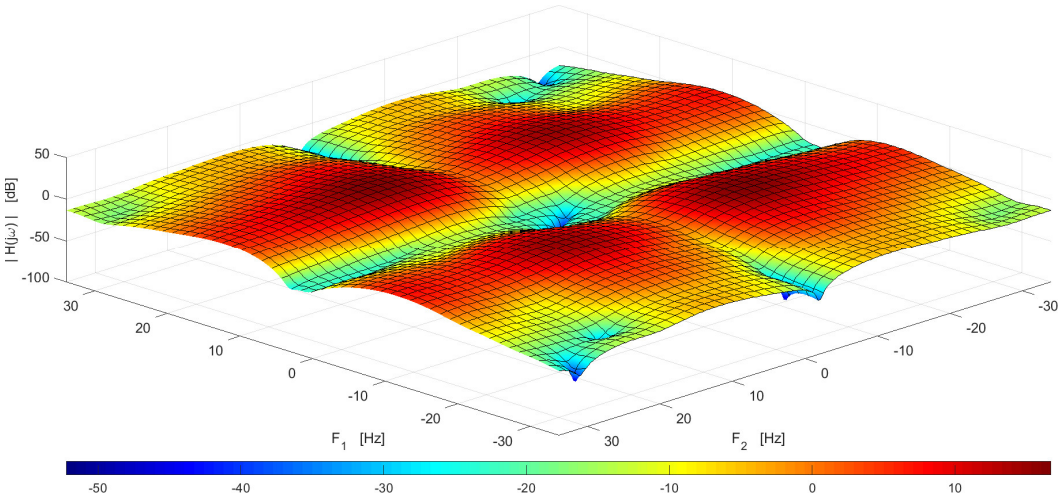

Figure 7.16. Magnitude of $|H_3(j\omega_1, j\omega_2, j\omega_3)|$ of second order GFRF of model M_{BD}.

The third order GFRF for model has a gain which is higher than that of the second order. Peaks at $F_1 = F_2 = 12.814$Hz have a gain of 16.72dB and $F_1 = F_2 = 12.46$Hz of 14.8dB, both of which are higher than the peaks of the second order GFRF of the same model. However, most of the remaining frequencies are dampened.

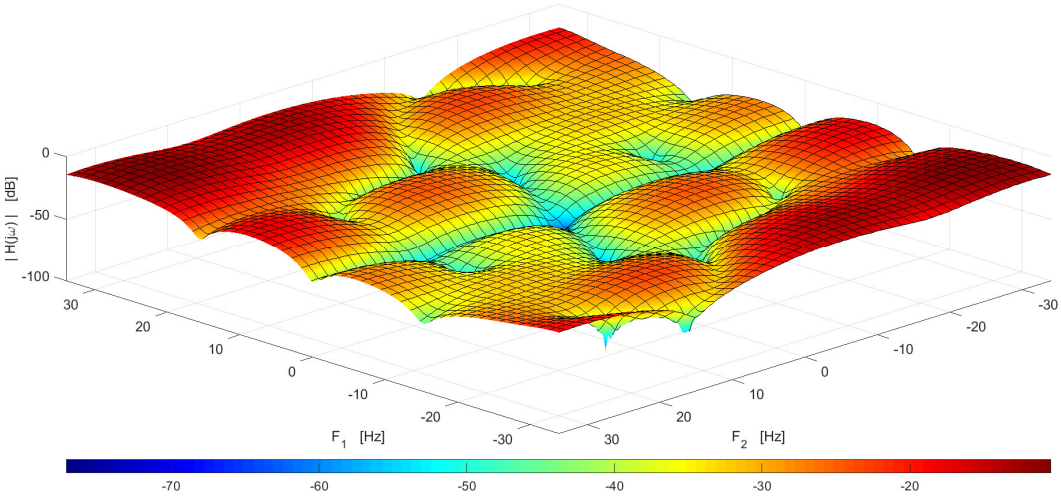

Figure 7.17. Magnitude of $|H_3(j\omega_1, j\omega_2, j\omega_3)|$ of second order GFRF of model M_{AE}.

The entire magnitude of the third order GFRF for model M_{AE} in Figure 7.17 is negative. As the second order only had small sections which were positive, it can be inferred that most of the output response is due to the linear effects.

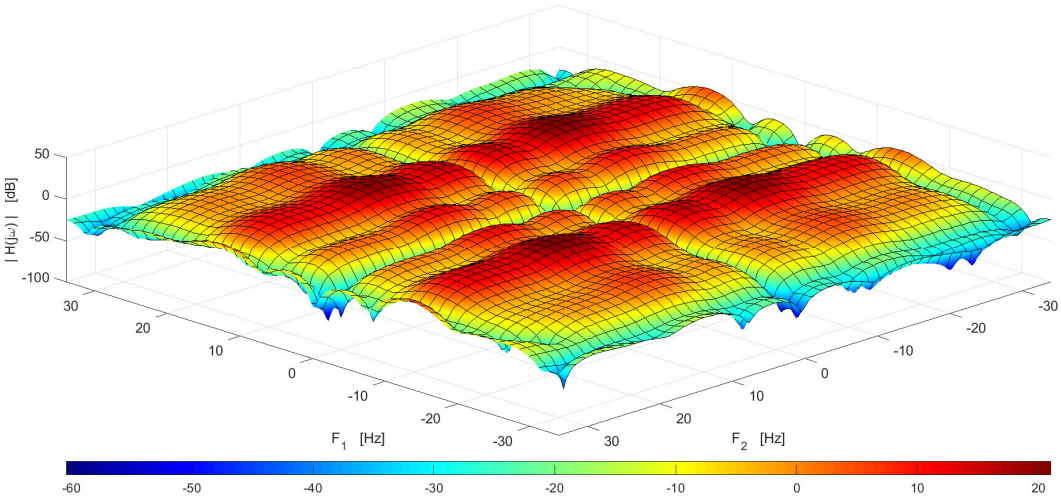

Figure 7.18. Magnitude of $|H_3(j\omega_1, j\omega_2, j\omega_3)|$ of second order GFRF of model M_{BE}.

The third order GFRF for M_{BE} has a high resonant peak at $F_1 = F_2 = 12.814$Hz with a gain of 20.5dB, likewise a ridge is found at $8 < F_1 < 18$Hz, $-30 < F_2 < 30$Hz. The remainder of the frequencies are dampened as seen in Figure 7.18.

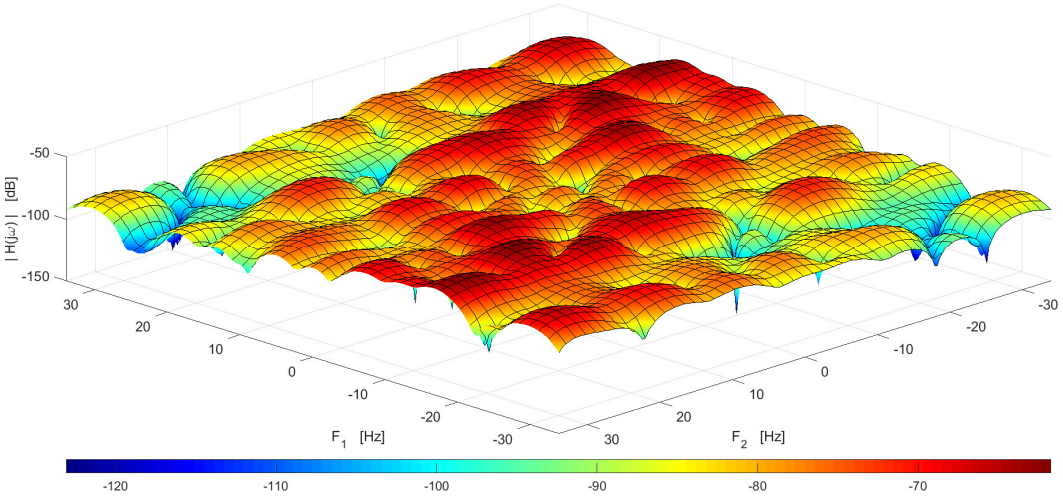

Figure 7.19. Magnitude of $|H_3(j\omega_1, j\omega_2, j\omega_3)|$ of second order GFRF of model M_{AB}.

Lastly, the third order GFRF of M_{AB} has a lower gain than the second order counterpart, suggesting once more that the contribution to the output at these frequencies is dampened.

In this section the GFRF's have been studied, where it is possible to have an idea of the amount of contribution that each order will have on the output spectrum (Billings & Tsang, 1989b; Billings, Tsang, & Tomlinson, 1990). However, the actual way in which the contribution takes place is not transparent, mainly due to the high dimensionality and non-linear processes that are present in the functions, such as intermodulation of two or more frequencies, for the second and third order case, respectively (Lang & Billings, 2004; Yue, Billings, & Lang, 2005a). It is necessary to consider all possible combinations of ω's that make up a single output frequency which can be daunting.

7.5. Computation and analysis of the OFRF's for the BFS

Considering the difficulty of gaining insight into the system from the computed GFRF, the OFRF's of each of the systems were studied.

The OFRF were computed and evaluated per equation (7. 9) and compared to the FFT of the measured output signals at each location.

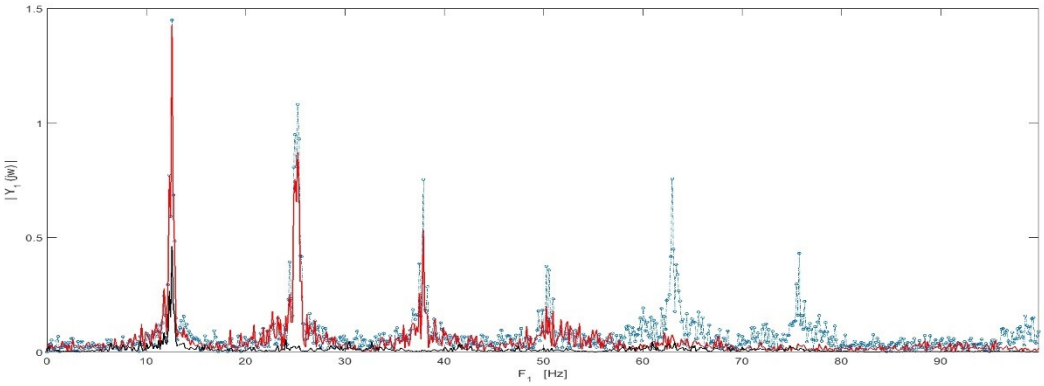

Figure 7.20. Magnitude of $|Y_1(j\omega)|$ for M_{AD} (in red) and M_{BD} (in black) to the measured frequency response, $Y(j\omega)$ (in dashed blue).

The contributions that the first order OFRF's have on the output spectrum for model M_{AD} and M_{BD} are shown in Figure 7.20. in red and black respectively. The largest peaks for both $|Y_1^{AD}(j\omega)|$ and $|Y_1^{BD}(j\omega)|$ are at the frequency $F_1 = 12.59$Hz which is expected since it is also found in the input. Furthermore, the linear contribution to $|Y_1^{AD}(j\omega)|$ is also significant to the peaks at $F_1 = 25.25, 37.2, 50.3$Hz, whereas $|Y_1^{BD}(j\omega)|$ only makes up 31.8% of the output frequency at $F_1 = 12.59$Hz and is negligible for the remaining values.

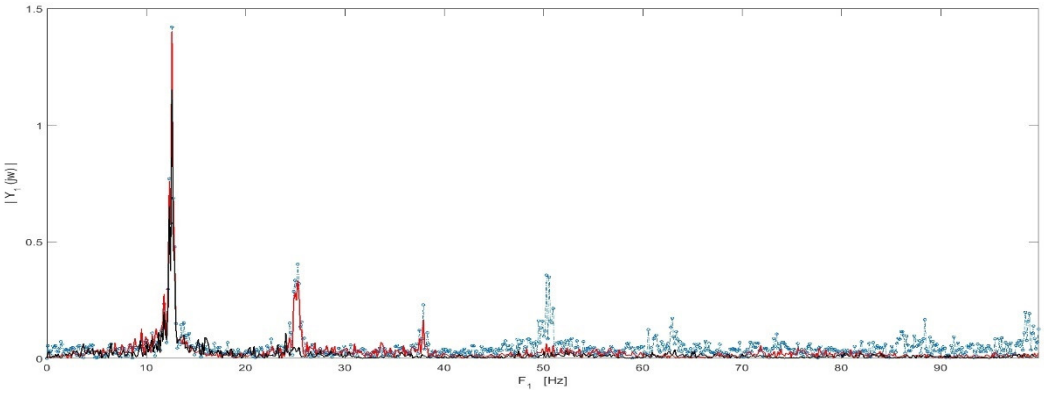

Figure 7.21. Magnitude of $|Y_1(j\omega)|$ for M_{AE} (in red) and M_{BE} (in black) to the measured frequency response, $Y(j\omega)$ (in dashed blue).

Figure 7.21 shows the contribution to the output spectrum by $|Y_1^{AE}(j\omega)|$ and $|Y_1^{BE}(j\omega)|$. The largest peaks are found at the frequency $F_1 = 12.59$Hz. Further, once again the $|Y_1^{AE}(j\omega)|$ is close to that of the measured response, contributing 98.6% and makes up a significant percentage of the peaks at $F_1 = 25.25, 37.2$Hz. In this case $|Y_1^{BE}(j\omega)|$ contributes 81% of the magnitude of the output spectrum but is only significant around this frequency.

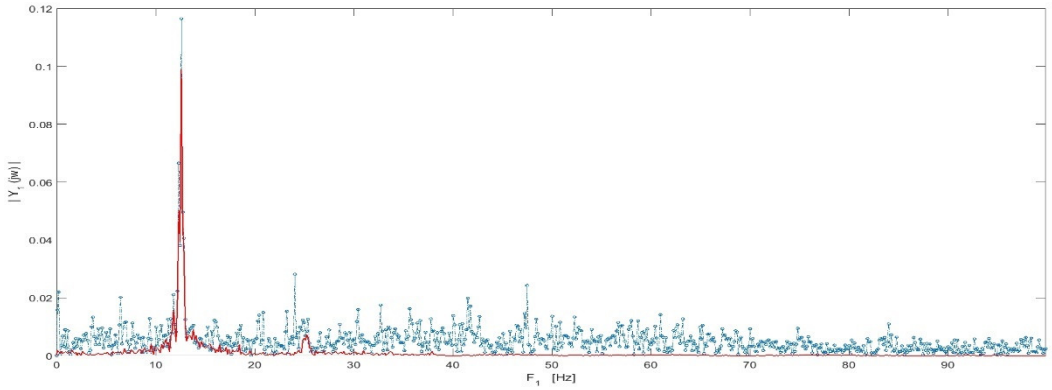

Figure 7.22. Comparison of the magnitude of $|Y_1(j\omega)|$ for M_{AB} (in red) to the measured frequency response, $Y(j\omega)$ (in dashed blue).

This last Figure 7.22, shows how the measured output frequency response is much lower than that of the other models studied. In this case $|Y_1^{AB}(j\omega)|$ contributes 85% to the output frequency component at $F_1 = 25.25$Hz and 55.38% of the peak at 25.38Hz, however, the nearest resonant peak is around 1Hz lower.

The second order OFRF's have also been evaluated to study the system in response to pairs of frequencies that satisfy $\omega = \omega_1 + \omega_2$ (Billings, 2013; Billings & Tsang, 1989a).

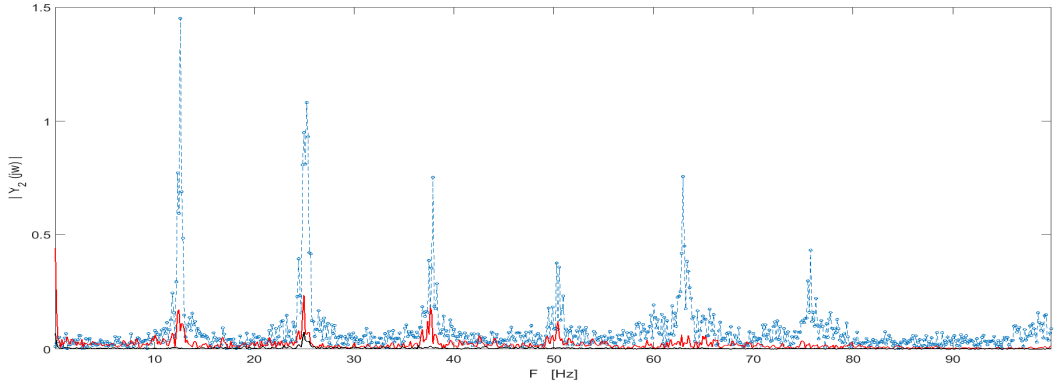

Figure 7.23. Comparison of the magnitude of $|Y_2(j\omega)|$ for M_{AD} (in red) and M_{BD} (in black) to the measured frequency response, $Y(j\omega)$ (in blue).

The second order OFRF shown in Figure 7.23 has a lesser contribution to the output spectrum than the linear part, this is expected considering the gain of the second order GFRF for both models. However, the non-linear effects are visible at the higher resonant frequencies, where three-wave interaction exists and is partially responsible for the harmonics, particularly for M_{AD}.

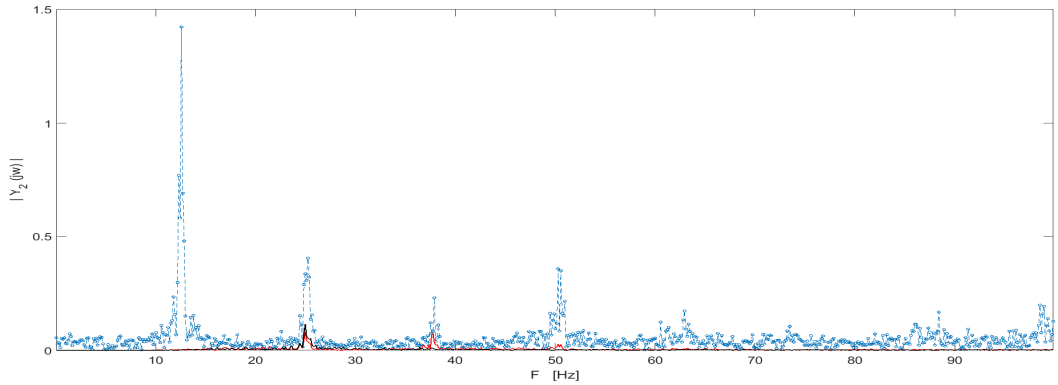

Figure 7.24. Comparison of the magnitude of $|Y_2(j\omega)|$ for M_{AE} (in red) and M_{BE} (in black) to the measured frequency response, $Y(j\omega)$ (in blue).

Figure 7.24 shows a similar outcome, where the second order OFRF magnitude, $|Y_2(j\omega)|$, shows a slight contribution from three-wave interactions at $F = 24.98$Hz. The contribution at this frequency for both M_{AE} and M_{BE} is quite similar. However, there is a slight contribution at $F = 37.77$Hz for M_{AE} whereas M_{BE} is largely insignificant.

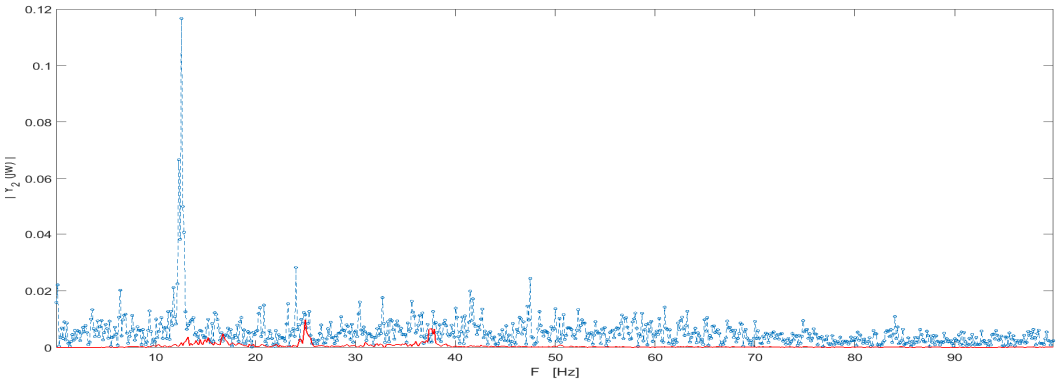

Figure 7.25. Comparison of the magnitude of $|Y_2(j\omega)|$ for M_{AB} (in red) to the measured frequency response, $Y(j\omega)$ (in blue).

Considering that the most relevant peaks of the output spectrum for M_{AB} have been seen to be due to the linear effects, Figure 7.25 shows an expected low contribution from the second order OFRF $|Y_2(j\omega)|$. It is worth noting that two small peaks are visible which once again, show that three-wave interaction does account for some of the dynamics of the output.

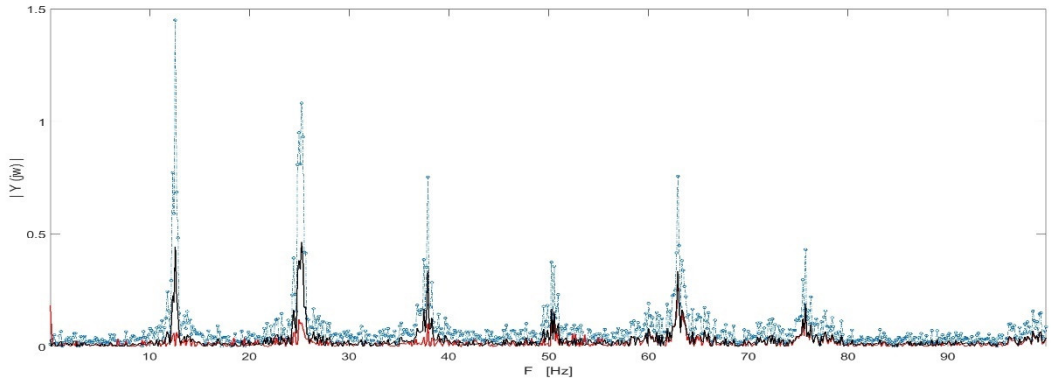

Figure 7.26. Comparison of the magnitude of $|Y_3(j\omega)|$ for M_{AD} (in red) and M_{BD} (in black) to the measured frequency response, $Y(j\omega)$ (in blue).

The contribution of the third order OFRF can be seen in Figure 7.26. It is clear that four-wave interactions have a great impact on the output spectrum for both M_{AD} and M_{BD}. Several of the higher frequency resonances are generated due to these third order non-linear mechanisms for model M_{AD}, whereas almost the entire spectrum has a significant contribution for M_{BD}.

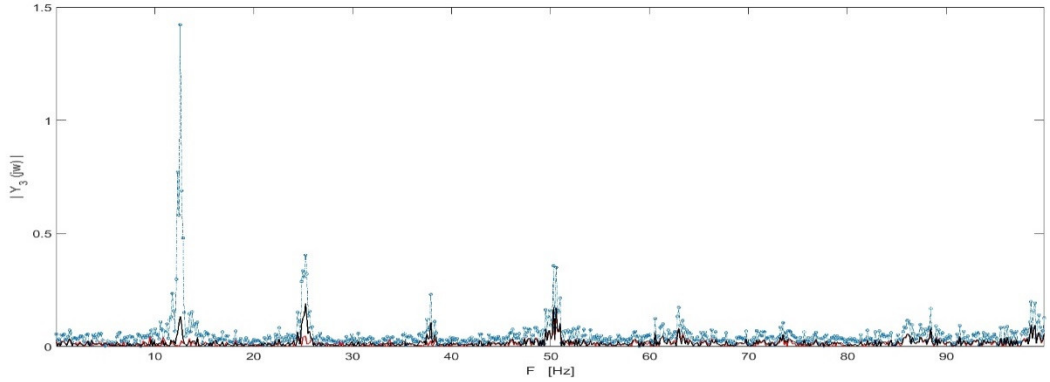

Figure 7.27. Comparison of the magnitude of $|Y_3(j\omega)|$ for M_{AE} (in red) and M_{BE} (in black) to the measured frequency response, $Y(j\omega)$ (in blue).

For M_{BE} it is visible in Figure 7.27 that the third order OFRF also has a significant contribution to the output spectrum, especially in the higher frequencies. In the case of M_{AE}, the contribution is lower overall.

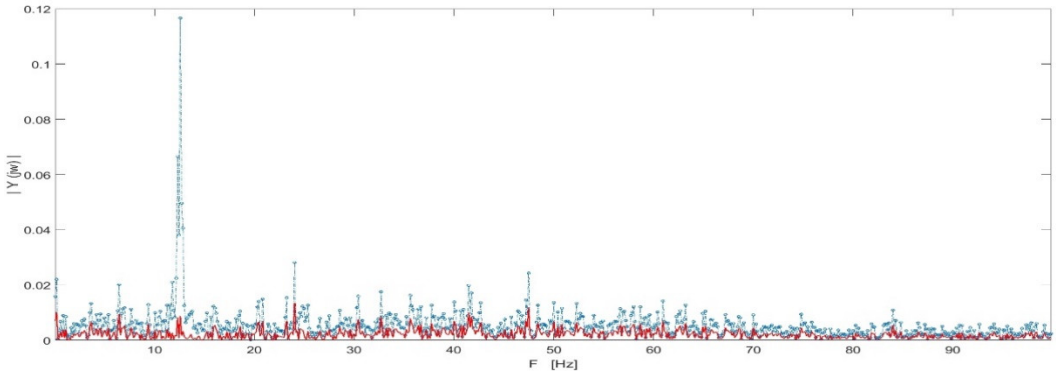

Figure 7.28. Comparison of the magnitude of $|Y_3(j\omega)|$ for M_{AB} (in red) to the measured frequency response, $Y(j\omega)$ (in blue).

Finally, the contribution to the output spectrum of the third order OFRF for model M_{AB} is seen to be relatively high for most frequencies except for the resonance at $F = 12.59$Hz which had been almost completely made up from the linear effects.

The OFRF's for higher orders can be obtained as long as the GFRF's can be identified, however, for many systems it is sufficient to study up to third order effects (Zhang & Billings, 1993). Therefore, the following step in the analysis of these systems is to assess how much of the measured output response has been estimated using the combination of the n-th order frequency responses computed from the model (Lang & Billings, 2004).

For this, a simple summation is performed to obtain an estimated output frequency response $\hat{Y}(jw)$ using

$$\hat{Y}(j\omega) = Y_1(j\omega) + Y_2(j\omega) + Y_3(j\omega)$$

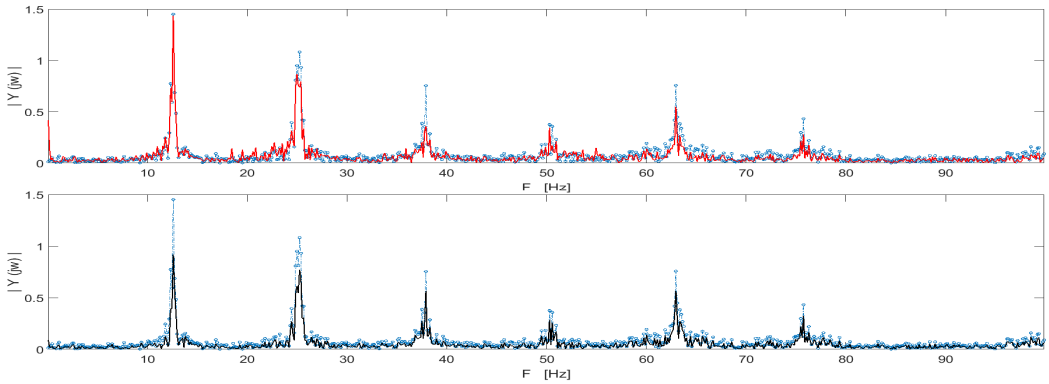

Figure 7.29. Top: Comparison of the magnitude of $|\hat{Y}(j\omega)|$ for M_{AD} (in red) to the measured frequency response, $Y(j\omega)$ (in blue). Bottom: Comparison of the magnitude of $|\hat{Y}(j\omega)|$ for M_{BD} (in black) to the measured frequency response, $Y(j\omega)$ (in blue).

Figure 7.29 shows the comparison between the measured and estimated frequency responses. For model M_{AD}, the main resonant frequencies are estimated almost entirely, whereas for M_{BD} the estimated response predicts the location of the peaks well, however the magnitude is not accurate at the lower frequencies but is seen to improve towards higher values.

Table 7.3. Comparison between measured $|Y(j\omega)|$ and estimated $|\hat{Y}(j\omega)|$ output frequency response for M_{AD} and M_{BD}

Peak frequency [Hz]	$\|Y(j\omega)\|$	$\|\hat{Y}(j\omega)\|$		% of Error	
		M_{AD}	M_{BD}	M_{AD}	M_{BD}
12.59	1.45	1.433	0.918	1.172	36.6
25.25	1.082	0.754	0.772	30.24	28.63
37.91	0.754	0.357	0.566	52.59	24.89
50.3	0.375	0.342	0.282	8.74	24.8
62.96	0.757	0.549	0.567	27.37	25.07
75.75	0.431	0.2778	0.322	35.54	25.29

A summary of the error between the predicted and measured value of the output response of model M_{AD} and M_{BD} at the resonant frequencies is given in Table 7.3.

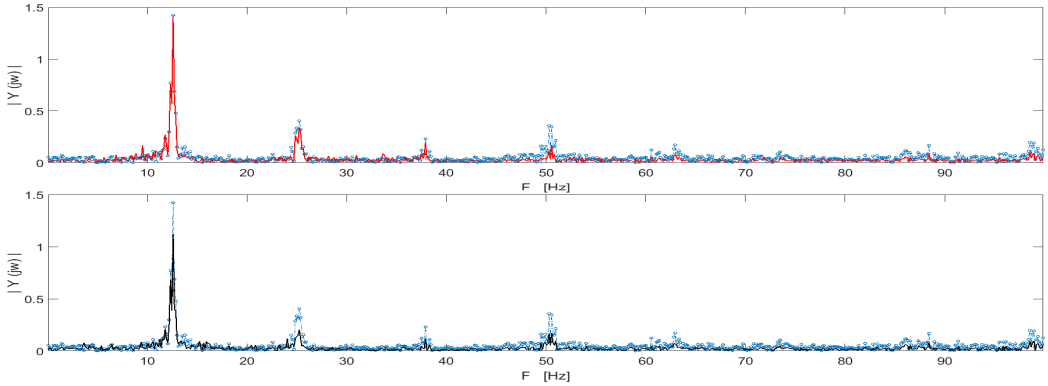

Figure 7.30. Top: Comparison of the magnitude of $|\hat{Y}(j\omega)|$ for M_{AE} (in red) to the measured frequency response, $Y(j\omega)$ (in blue). Bottom: Comparison of the magnitude of $|\hat{Y}(j\omega)|$ for M_{BE} (in black) to the measured frequency response, $Y(j\omega)$ (in blue).

Similarly, Figure 7.30 shows the approximated and measured frequency response for models M_{AE} and M_{BE}. In this case both models yielded GFRF's and OFRF's capable of estimating the output response of the system accurately. Once again, the model whose input is data from point A is seen to predict most of the response accurately.

Table 7.4. Comparison between measured $|Y(j\omega)|$ and estimated $|\hat{Y}(j\omega)|$ output frequency response for M_{AE} and M_{BE}

Peak frequency [Hz]	$\|Y(j\omega)\|$	$\|\hat{Y}(j\omega)\|$		% of Error	
		M_{AE}	M_{BE}	M_{AE}	M_{BE}
12.59	1.422	1.403	1.121	1.33	21.16
25.25	0.404	0.341	0.203	15.39	49.60
37.91	0.231	0.189	0.119	18.01	48.13
50.57	0.3491	0.172	0.173	50.50	50.27

A summary of the main peaks, and the amount of the output response predicted using the OFRF's of model M_{AE} and M_{BE} is given in Table 7.4.

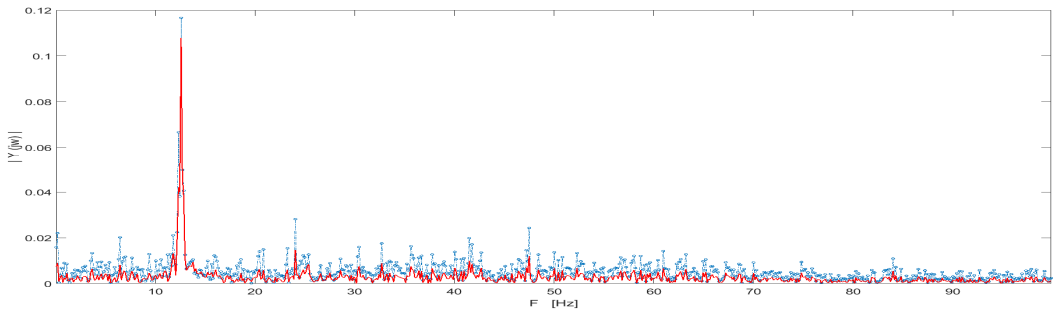

Figure 7.31. Comparison of the magnitude of $|\hat{Y}(j\omega)|$ for M_{AB} (in red) to the measured frequency response, $Y(j\omega)$ (in blue).

Lastly, the approximation of the output response for model M_{AB} can be seen to be accurate in Figure 7.31. Here most of the peak at $F = 12.59$Hz is accounted for by the approximation and the location of lesser peaks is also captured precisely.

Table 7.5. Comparison between measured $|Y(j\omega)|$ and estimated $|\hat{Y}(j\omega)|$ output frequency response for M_{AB}

Peak frequency [Hz]	$\lvert Y(j\omega)\rvert$	$\lvert\hat{Y}(j\omega)\rvert$	% of Error
12.59	0.1165	0.1078	7.46
24.05	0.028	0.0147	47.5
41.51	0.019	0.009	52.63
47.5	0.024	0.0119	50.41

A summary of the main peaks, and the amount of the output response predicted using the OFRF's of model M_{AE} and M_{BE} is given in Table 7.4.

7.6. Discussion

To understand turbulence, it is necessary to deduce a description of the observed dynamics, that is, the composition of the turbulence, such as the energy distribution, and linear and non-linear, energy transfer processes (Balikhin, Bates, & Walker, 2001).

This chapter has presented a study of turbulent flow over the BFS in the frequency domain, for the first time using GFRF's and OFRF's. This was achieved by identifying several polynomial SISO NARMAX model from data extracted at different points up and downstream of the flow. These models were mapped into the frequency domain to obtain the GFRF's proposed by (George, D. A., 1959) using the NSFRA toolbox, based on the harmonic probing approach (Billings & Lang, 2002; Billings &

Tsang, 1989a; Lang & Billings, 2004; Peyton Jones & Billings, 1989; Peyton Jones & Choudhary, 2012b; Yue, Lang, & Billings, 2004).

The first order GFRF's for the models showed that there are some local maxima near the resonant frequencies observed in the output, such as $F \approx 12, 25, 37, 53, 65$,75Hz for all the identified models. The second and third order GFRF's are harder to interpret, as they are multivariable and high-dimensional functions. However, they can be used to have an idea of the amount of contribution that each of the non-linear processes will have on the output spectrum (Billings, 2013; Billings & Tsang, 1989a, 1989b; Peyton Jones & Choudhary, 2012b).

The second and order effects for model M_{BD} and M_{BE} are likely to have the highest contribution to their corresponding frequency response since the gain of the GFRF is of a similar or even larger magnitude than the linear effects. On the other hand, model M_{BD} and M_{AD} have decreasing gains for the second and third order GFRF's for most frequencies. Finally, model M_{AB} has negative gains for all GFRF's.

An analysis of the OFRF's has been performed to study the way in which the n-th order frequency responses are formed, and in turn, how much of the output frequency response is explained by linear, quadratic and cubic effects using the identified models (Billings, 2013; Lang & Billings, 1997, 2004).

The linear energy transfer mechanism is dominant in all five cases. In particular, the output frequency response at the frequency F=12.59 Hz, $|Y(j12.59)|$ can be explained almost entirely in terms of the linear frequency response function. Additionally, for models M_{AD} and M_{AE}, a significant contribution to higher resonant frequencies can be seen, as mentioned these are approximately at the local maxima of the first order GFRF.

The second order OFRF's have a minimal contribution to the output response for the BD and BE systems. The most significant peaks make up less than 28% of the output response at $F \approx 25, 37$Hz. However, three-wave interactions are present in the flow, in systems AD/AE the magnitude of $|Y_2(j\omega)|$ at $F = 25.25, 37.9$Hz has clear resonant peaks, which will ultimately contribute to the output response at those frequencies. On the other hand, the third order contribution is seen to

be quite significant for M_{BD} and M_{BE}, this is foreseeable considering the gain of the corresponding GFRF. Additionally, the $|Y_3(j\omega)|$ is expected to be lower for the M_{AD} and M_{AE} since the linear and quadratic output responses have already accounted for a large part of the output response. M_{AB} is seen to be largely linear, where the second and third order effects are negligible for most of the frequencies with the exceptions of slight peaks at the resonant frequencies of the input.

In a study on turbulence, (Ritz & Powers, 1986) showed that in turbulent plasma, the position of the measuring probes changes the effects which are measured. For measurements from neighbouring points, the effects are mainly linear since structures seen at the input are still present, and dominate the behaviour at the output, whereas larger distance between probes yields an increase capture of non-linear interactions between the waves (Ritz & Powers, 1986).

In this work, this remains valid, the distance between the studied nodes is small and linear effects dominate the energy transfer for all systems, hence the input frequency has a strong presence in the output response. Between nodes AD, the quadratic effect is significant whereas AE shows almost entirely linear behaviour. System BD has strong cubic contributions whereas BE does not.

It is understandable to see that AE has mainly linear dynamics, since the two nodes are separated by a short wall-normal distance (0.5H) and node E is close to the dividing streamline between the recirculation and free flow (shear layer). However, it is interesting to see that AD has again mainly linear dynamics, with a slight contribution from three-wave interactions (quadratic effects), considering that the vertical separation is almost a whole step height, and in addition, point D is immersed in the recirculation zone.

On the other hand, system BE is mostly linear with some cubic effects, whereas BD is almost entirely dominated by cubic effects. Further investigation into the energy transfer and the variation of these mechanisms across the spatial domain, in addition to variations of flow properties is required. It may also be of interest to study if the energy transfer mechanisms can be used to determine the direction of the energy transfer, from smaller to larger eddies or vice versa, however this

would have to be done using three-dimensional data to obtain a more realistic behaviour including vortices.

In the case of the study by Ritz, it was found that a linear transfer function was sufficient to represent the turbulent plasma system since the quadratic effects were insignificant and they did not pursue higher order due to limitations of the method implemented (Ritz & Powers, 1986). In the analysis performed here, linear effects indeed dominate the energy transfer the studied positions, however, cubic and perhaps higher order interactions are also important. These play an important role in the transfer of energy from the input to output frequencies, which by definition, cannot be done through linear means (Billings & Lang, 2002; Lang & Billings, 2004), and as shown using the linear OFRF's, the output response is not adequately represented using only this component.

CHAPTER 8

Conclusions and future work

8.1. Summary

This work proposed an alternative approach to the development of reduced-order models of fluid flows for flow control applications, using non-linear system identification rather than finite-element approximations. This approach has been applied to two classic benchmark models, the three-dimensional channel flow and two-dimensional flow over the backward facing step.

The identification approach was used to develop a non-linear model predictive control strategy, based on input-affine multi-step ahead nonlinear predictors. The methodology was demonstrated through numerical simulations to control the flow over the backward facing step. Furthermore, non-linear models identified from simulated data were used to carry out higher-order frequency response analysis of turbulent flow, over the backward facing step using the generalized and output frequency response functions.

Simulations were performed using dedicated computational fluid dynamics software. The ChannelFlow package (Gibson, 2012) was employed for direct numerical simulations of three-dimensional

channel flow, whereas Ansys Fluent (Ansys, 2016) was used to perform Large Eddy simulations of two-dimensional flow over the backward facing step. These simulations were designed and carried out considering flow properties, parameters and dimensions used in the literature, to ensure their accuracy and validity of the data (Driver & Jovic, 1994; Gibson, Halcrow, & Cvitanović, 2008; Heins, 2015; Le, Moin, & Kim, 1997).

A Fourier analysis was performed on the data from both scenarios to identify the system's bandwidth and generate a persistently exciting input (Leontaritis & Billings, 1987; Ljung, 2004). This signal was implemented on actuated versions of the scenarios (Heins, 2012). The actuation used was suction and blowing applied as normal velocity on the wall nodes (Ricco & Dilib, 2010; Uruba, Jonáš, & Mazur, 2007).

Input/output data from a simulation using the designed stimuli was used to identify one-step ahead MIMO predictors (Billings, 2013; Chen & Billings, 1989; Leontaritis & Billings, 1985). In the case of channel flow, a six-input and three-output configuration was considered. A structure was identified for nodes belonging to different classes, such as wall, edge and vertex, resulting in 27 sub-models. Quadratic and cubic predictors with input and output lag $n_u = 7$, $n_y = 4$, respectively, and varying number of terms were identified. The best performing over the training data were tested on an unseen data set for validation, the final model for each structure was chosen based on the NRMSE, parameters were re-calculated for each node of the corresponding sub-type.

A similar approach was taken to identify SISO OSA predictors for the fluctuations of the pressure coefficient C_p, on the top of the step, and MISO MSA predictors for the variations of the velocity magnitude at a point within the recirculation zone. The inputs were a single actuator on the inlet wall for the M_{Cp} case, and two or four actuators on the step wall for the $M_{V(\cdot)}$ configurations, once again using suction and blowing. The candidate term set for the models identified of flow over the BFS was tailored to ensure input affinity, which allows for a predictive control strategy to be readily implemented (Bai & Coca, 2008, 2011).

A linear/non-linear *hybrid* model predictive control approach (Bai & Coca, 2008) is used based on the GPC algorithm (Camacho & Bordons-

Alba, 2003; Clarke, Mohtadi, & Tuffs, 1987a). This method uses the full non-linear model, which contains terms that allow for the posterior optimization to be performed using fast QP methods. The identified non-linear predictors, formulated with input and output increments to incorporate integral action (Bai & Coca, 2008), are used to generate predictions of future states over the N_2 horizon. A control sequence is computed which minimizes a defined cost function of the error between the actual and desired state, additionally it can penalize the actuation and output signal (Clarke, Mohtadi, & Tuffs, 1987a).

A predictive control scheme was chosen due to the compatibility with non-linear models, in addition to the capability of imposing constraints during the control design stage (Camacho & Bordons-Alba, 2003; Clarke, Mohtadi, & Tuffs, 1987a; Rossiter, 2003). This is of great importance since real systems all have constraints on the actuation, output and rates of change of these variables.

The control algorithm was applied to the three identified models, M_{Cp}, M_{V2} and M_{V4}. Simulations using the corresponding OSA predictor as the plant were performed, and the control was shown to be able to maintain the system on the desired trajectory, even in the presence of measurement noise and load disturbances.

Lastly, an analysis of the energy transfer between two up and downstream nodes, in addition to the interaction of both upstream points was realized. To achieve this, the NARMAX system identification methodology (Billings, 2013) was implemented on data from these points and OSA SISO predictors were identified. These were mapped into the frequency domain to yield the linear, quadratic and cubic GFRF's (George, 1959), which were analysed and subsequently used to compute the OFRF's (Lang & Billings, 1997, 2004). The latter show the contribution of each n-th order frequency response to the total output response.

It was found that linear mechanisms dominate the energy transfer for the selected points, however quadratic and cubic effects are significant for the AD and BD systems, respectively.

8.1.1. System identification of non-linear reduced order models and predictive control of flow over the backward facing step

System identification using the NARMAX methodology was carried out for the first time using data from simulations of turbulent flow in two geometries. This approach has been shown to be effective in capturing the dynamics of the system using SISO, MISO and MIMO predictors. Validation techniques have shown the accuracy of models identified in this manner, additionally, a predictive control strategy was designed and tested using the NARMAX models and shown to be able to drive the system to the desired state. Which once again shows that the dynamics captured are representative of the system.

The main issues recognised in the current work regarding system identification are related to the experiment design. This stage is crucial for any application (Leontaritis & Billings, 1987; Ljung, 2004), however in the case of fluid flows and their control, it is particularly difficult considering the complexity and incomplete understanding of their behaviour (Bradshaw, 1994; Davidson, Kaneda, & Sreenivasan, 2013).

Experimental tests are difficult and often costly to perform (John, 1995), due to the iterative nature of system identification, they are not an optimal source of data. Simulations on the other hand can provide the required data, however, the selection of parameters, flow properties and design of meshes needs to be done carefully and is often a repetitive, and time consuming process until an adequate simulation can be obtained (Ansys, 2016; John, 1995). Putting these matters aside, the definition of the adequate sensing and actuation position, and sampling rate, as well as the variables themselves is a further challenge (Chung & Talha, 2011; Lofdahl & Gad-El-Hak, 1999a; Scott Collis, Joslin, Seifert, & Theofilis, 2004).

Currently, actuators exist which can be readily implemented and so their behaviour can be simulated in a straight forward manner considering the response rate, dimensions and other characteristics (Ho & Tai, 1998; Lofdahl & Gad-El-Hak, 1999a, 1999b).

Similarly, current sensor technology can make measurements of wall-based values, and some can record flow information small distances from the boundary (Lofdahl & Gad-El-Hak, 1999a). Therefore, the

selection of a quantity which can be readily measured is of importance if controllers based on these models are to be implemented on real systems.

In the current work, the velocity measurements for the MISO models are not easily obtained. However, these variables were considered as a first attempt of employing non-linear system identification approaches and predictive controllers in a simulation environment. These can be refined or modified to consider more realistic measurements, and sampling times for example, to generate feasible controllers.

The use of non-linear models in fluid control is of great importance since numerical solutions of the Navier-Stokes equations are prohibitively expensive for any purpose other than off-line analysis (Scott Collis, Joslin, Seifert, & Theofilis, 2004). On the other hand, linearized or simplified versions of the governing equations can only represent a limited set of flow dynamics, and are usually defined around small neighbourhoods of states (Pollard, 1998; Scott Collis, Joslin, Seifert, & Theofilis, 2004; Yue, Billings, & Lang, 2005). In reality, flow behaviour changes dramatically, and many applications have properties such as Reynolds numbers, which make some of the previously reported approaches no longer valid (Davidson, Kaneda, & Sreenivasan, 2013; Frank, 2011).

The predictive control approach proposed in this work has the accuracy of non-linear models to forecast the evolution of the flow, with the ease of implementation of a linear predictive approach, given that the identified MSA predictors are input affine and do not require non-linear optimization methods. Additionally, since all future predictions depend on measured data up to instant (k), they can be evaluated in parallel and so are feasible for use in real-time applications.

The control scheme incorporates integral action using input and output increments rather than the whole variable. Therefore, it is well suited to account for exogeneous disturbances, which have a significant presence in real flows.

Lastly, as stated, the position of the actuator has a great impact on the effectiveness of the control approach. Therefore, the simulation of the system before actuation with practical dimensions and limitations,

will help to elucidate the true impact that an implementable control can produce.

8.1.2. Frequency analysis of turbulent fluid flows

The analysis made on the five systems of the flow over the backward facing step has shown the way in which the output frequency response is made up by *n*-th order mechanisms (Lang & Billings, 2004). It has been shown that the linear effects dominate but quadratic and cubic effects can be significant depending on the position of the input considered. This study was based on NARMAX SISO predictors which can be mapped directly into the frequency domain, hence some of the issues regarding the system identification also need to be addressed here.

The position of the input and output will define the dynamics captured, small separation between measurement points result in dominant linear characteristics whereas more separation allows for the non-linear effects to increase in significance (Ritz & Powers, 1986). The frequency domain tools such as the OFRF's can be used to study the positions which have greater effect on other locations of the flow, or which effects are better transmitted, and so a better decision on the type and location of the actuation and sensing can be taken.

The study of the OFRF can also be applied to determine the specific frequencies which contribute to the generation of resonances and the way in which energy is transferred (Billings & Lang, 2002; Lang & Billings, 2004). A further study between the spatial variations of frequency and time domain properties, can lead to the determination of which events give rise to instabilities and how these are propagated across the domain. Hence it can be possible to design controllers which attenuate the relevant modes. An approach using a similar strategy is used by (Heins, Jones, & Sharma, 2016) and has been shown to be effective.

8.2. Conclusions

The current work has successfully implemented the NARMAX system identification methodology using data obtained from numerical simulations of turbulent flow in two different geometries. Two numerical methods were used to generate the data, DNS and LES methods for the channel, and flow over the BFS, respectively. The geometry, flow properties, and simulation parameters were set according to previous studies.

Models of the SISO, MISO and MIMO types were obtained for different variables from these geometries, these being the components of velocity fluctuations from three-dimensional channel flow and the velocity magnitude and pressure coefficient variations from two-dimensional flow over the BFS. In the case of the latter geometry, both OSA and MSA predictors were identified, and were later used in a non-linear model predictive control scheme. The proposed NMPC approach has been shown to be robust and capable of following a desired trajectory using localized actuation and sensing.

Finally, a frequency domain analysis has been performed between two upstream and two downstream nodes of the step, in addition to the interaction between the two upstream locations. New SISO OSA predictors were identified from measured data. The GFRF's were computed to study the linear, quadratic and cubic effects visible through the gain of the magnitude, the phase and dependence on the combinations of frequencies. The OFRF's have been evaluated and the individual contributions of the n-th frequency responses studied.

It was determined that for the selected positions, the linear effects dominate the energy transfer, however for two of the locations the quadratic and cubic non-linearities also make a significant contribution. It was shown that the effects up to third order can explain most of the output frequency response, including the additional resonances observed on the output, which are due to harmonic and intermodulation effects.

8.3. Recommendations for future work

This thesis has presented developments obtained in the system identification, control and analysis of turbulent fluid flows. However, a number of issues and challenges remain in each of these areas. The following recommendations are avenues for future work on this multidisciplinary subject.

- The NARMAX system identification methodology has been used in this work using turbulent flow data. A polynomial expansion was selected, however, the use of alternate formulations may be beneficial to improve the accuracy of the multi-step ahead predictors to be used in the control approach (Billings, 2013). Further, an improvement of the validity of the identified models and subsequent control can be obtained through the use of three-dimensional simulations to generate more realistic data (De Brederode & Bradshaw, 1978). In addition, the consideration of existing device properties of actuators and sensors, coupled with a matching sampling rate and the use of feasible variables and measurements is essential for the development of realistic control strategies based on these models.
- The proposed control scheme has been tested using the identified OSA predictor as the plant. The next step is to implement this algorithm into the CFD package and study the performance on the "true" system, that is, the LES of the Navier-Stokes equations, and with this, validate its usefulness. It is also of importance to study the effect of the control and prediction horizons, as within the simulations performed in this work, the values selected were sufficient. However, considering the increased complexity of the full simulation, it may be necessary to expand one or both parameters, as well as a performing a re-tuning of the weighting function(s) (Clarke, Mohtadi, & Tuffs, 1987a). Further, if the measurements used for the identification are considered as noisy, the NARMAX methodology can easily incorporate a noise sub-model to ensure that the parameters

computed are not biased (Chen, Billings, & Luo, 1989; Leontaritis & Billings, 1985), and the NMPC scheme can be extended to account include this addition (Bai, 2010; Bai & Coca, 2008; Clarke, Mohtadi, & Tuffs, 1987a, 1987b).

- The extension and adaptation of the control approach to the MIMO channel flow case also studied in this work can show the scalability and range of systems to which such an approach can be applied to. This can be a first step into the establishment of a complete methodology for turbulent flow control which encompasses from the experiment design, system identification and ends with controller implementation.
- GFRF's and OFRF's have shown the energy transfer mechanisms present between node-pairs up and downstream of flow over the BFS. Using this initial knowledge, events of interest can be sought in the computed GFRF's and OFRF's of different order to further study them. A precise decomposition of each event can be performed to determine the specific contributions that input frequencies have, and how the output behaviour is constructed (Lang & Billings, 2004). In addition, a study of higher order functions may be of interest to obtain a more accurate approximation to the spectrum of the measured output, in addition to determining the importance of five- or higher-wave interactions for different flow arrangements (Ritz & Powers, 1986; Zhang & Billings, 1993).
- The frequency analysis tools can be used to determine the spatial variation of energy transfer within the flow by carrying out a frequency domain analysis of more systems. Using this new insight into turbulence and its behaviour, it may be possible to determine the locations which have the biggest effects on the recirculation zone, for example, and thus identify the best position for actuation systematically. A similar approach may be able to elucidate the optimal spatial arrangement of actuators and sensors.

Appendix A

A.1 Additional fluid mechanics and dynamics concepts

- Dynamic viscosity (μ): This quantity depends on the temperature of the fluid and the surrounding pressure. It has SI units $\left[\frac{kg}{ms}\right]$.
- Kinematic viscosity (ν): ratio of the dynamic viscosity to the density of the fluid denoted by $\nu = \frac{\mu}{\rho}$ with SI units $\left[\frac{m^2}{s}\right]$.
- Velocity (**U**): It stands for $\boldsymbol{U} = \boldsymbol{i}u + \boldsymbol{j}v + \boldsymbol{k}w$, where $u = f_1(x, y, x, t)$, $v = f_2(x, y, x, t)$ and $w = f_3(x, y, x, t)$ are the directional components with SI units $\left[\frac{m}{s}\right]$.
- Reynolds number (Re): Care has to be taken when using this since the ranges that define the type of flow vary greatly depending on the geometry of the domain. When calculating it, L is the characteristic length of the flow, which is related for example, to the diameter of pipes or the distance travelled by the fluid.
- Boundary layer: This concept has allowed for the simplification of the Navier-Stokes equations and enables the study of a number of practical problems which were unreachable beforehand (Scott Collis, Joslin et al. 2004).
- Density (ρ): Is the amount of mass of a fluid contained within a unit volume, with international system (SI) units $\left[\frac{kg}{m^3}\right]$.

- Pressure (P): It is the property that represents the compressive stress within the fluid and has the same magnitude in all directions, it has SI units $\left[\frac{N}{m^2}\right]$.
- Turbulence: It is usually found when a Re value is exceeded (depending on the geometry), where a transitional flow occurs which may be part laminar, part turbulent. If the Re value is increased further the flow will usually become fully turbulent. Turbulent flow is always three-dimensional with high interaction of ordered structures, particularly in the boundary layer which itself becomes unstable.
- Turbulent kinetic energy or TKE (k): it is the measure of the mean kinetic energy per unit mass of the turbulent fluctuations u', v', w' with SI units $[\frac{J}{kg} = \frac{m^2}{s^2}]$.
- Turbulent kinetic energy dissipation rate (ϵ): it is the rate at which the TKE is converted into thermal energy, with SI units $[\frac{J}{kg*s} = \frac{m^2}{s^3}]$

Appendix B

B.1 Channel flow model structures

Vertex [1,1,1]

Structure v_x		Structure v_y		Structure v_z	
y_1(k-1)	1	y_2(k-1)	1	y_3(k-1)	1
y_1(k-2)	1	y_2(k-2)	1	y_3(k-2)	1
u_2(k-1)	1	u_8(k-1)	1	u_10(k-1)	y_3(k-1)
u_17(k-1)	y_2(k-2)	u_26(k-1)	1	u_24(k-1)	u_16(k-1)
u_13(k-1)	u_11(k-1)	u_22(k-1)	u_11(k-1)	u_27(k-1)	y_3(k-1)
u_14(k-1)	1	u_24(k-1)	u_20(k-1)	u_19(k-1)	u_12(k-1)
u_24(k-1)	1	u_15(k-1)	y_3(k-1)	u_26(k-1)	y_1(k-1)
		y_3(k-2)	y_3(k-1)	u_14(k-1)	u_7(k-1)
		u_2(k-1)	1	u_26(k-1)	y_1(k-2)
		u_22(k-1)	u_12(k-1)	u_16(k-1)	y_3(k-2)
		u_16(k-1)	y_3(k-1)	u_9(k-1)	y_3(k-2)
		u_13(k-1)	y_3(k-2)	u_22(k-1)	u_9(k-1)
		u_22(k-1)	u_21(k-1)		
		y_3(k-2)	y_1(k-1)		
		u_25(k-1)	y_3(k-1)		
		u_11(k-1)	y_1(k-1)		
		u_20(k-1)	y_1(k-2)		
		u_25(k-1)	u_11(k-1)		
		u_26(k-1)	u_11(k-1)		
		u_4(k-1)	1		
		u_13(k-1)	1		
		u_13(k-1)	y_1(k-1)		
		y_1(k-2)	y_1(k-2)		
		y_3(k-1)	y_3(k-1)		
		u_19(k-1)	u_15(k-1)		
		u_21(k-1)	u_16(k-1)		
		u_25(k-1)	y_3(k-2)		
		u_24(k-1)	y_1(k-2)		

Vertex [30,1,1]

Structure v_x		Structure v_y		Structure v_z	
y_1(k-1)	1	y_2(k-1)	1	y_3(k-1)	1
y_1(k-2)	1	y_2(k-2)	1	y_3(k-2)	1
u_7(k-2)	1	u_8(k-1)	1	u_9(k-2)	1
u_7(k-1)	1	u_26(k-1)	u_17(k-1)	u_27(k-1)	u_23(k-2)
y_1(k-1)	1	u_26(k-2)	u_11(k-2)		

Vertex [1,1,25]

Structure v_x		Structure v_y		Structure v_z	
y_1(k-1)	1	y_2(k-1)	1	1	1
u_13(k-3)	u_13(k-3)	u_8(k-3)	1	y_3(k-1)	1
u_10(k-2)	y_3(k-1)	u_14(k-2)	1	u_15(k-2)	1
u_10(k-2)	1	u_6(k-3)	1	u_15(k-1)	1
u_22(k-2)	u_9(k-2)	u_20(k-1)	u_14(k-1)	u_15(k-3)	1
u_22(k-1)	u_13(k-1)	u_4(k-1)	1	u_24(k-1)	u_22(k-1)
u_22(k-1)	u_13(k-2)	u_8(k-1)	1	u_13(k-1)	y_1(k-1)
u_22(k-1)	u_13(k-3)	u_8(k-2)	1	u_13(k-2)	y_1(k-1)
u_22(k-3)	u_13(k-3)	u_26(k-2)	1	u_20(k-1)	u_15(k-3)
u_24(k-3)	u_10(k-1)	u_26(k-1)	1	u_13(k-3)	u_12(k-1)
y_3(k-1)	y_1(k-1)	u_26(k-3)	1	u_12(k-3)	u_7(k-2)
u_24(k-2)	u_22(k-3)	u_14(k-1)	1	u_24(k-1)	y_3(k-1)
u_27(k-1)	u_10(k-1)	u_21(k-2)	u_18(k-2)	u_22(k-3)	u_12(k-3)
u_13(k-2)	1	u_14(k-3)	1	u_22(k-1)	u_10(k-1)
u_13(k-1)	1	u_26(k-3)	u_9(k-1)	u_13(k-3)	u_12(k-2)
u_13(k-3)	1	u_24(k-3)	u_24(k-2)	u_24(k-1)	u_10(k-1)
u_13(k-3)	u_10(k-3)	u_16(k-1)	u_15(k-3)		
u_13(k-3)	u_10(k-1)	u_25(k-1)	u_13(k-1)		
u_8(k-3)	1				

Vertex [30,1,25]

Structure v_x		Structure v_y		Structure v_z	
y_1(k-1)	1	y_2(k-1)	y_1(k-2)	y_3(k-1)	1
u_13(k-2)	u_10(k-2)	u_8(k-2)	1	u_15(k-2)	1
u_13(k-1)	u_10(k-2)	u_8(k-1)	1	u_15(k-1)	1
u_25(k-2)	u_7(k-2)			u_21(k-2)	y_1(k-1)
u_24(k-2)	u_22(k-1)			u_12(k-1)	u_10(k-2)
u_13(k-2)	u_7(k-1)			u_10(k-1)	1
u_13(k-1)	u_7(k-1)				
u_24(k-2)	u_22(k-2)				
u_16(k-2)	u_14(k-2)				
u_10(k-2)	y_1(k-1)				
u_25(k-2)	u_19(k-1)				
u_13(k-2)	1				

Vertex [1,29,1]

Structure v_x		Structure v_y		Structure v_z	
y_1(k-1)	1	y_2(k-1)	y_1(k-2)	y_3(k-1)	1
u_13(k-2)	1	u_8(k-2)	1	u_15(k-2)	1
u_13(k-1)	1	u_8(k-1)	1	u_15(k-1)	1
u_10(k-1)	u_10(k-1)	u_14(k-2)	1	u_15(k-1)	y_2(k-1)
u_13(k-1)	u_8(k-1)	u_26(k-2)	1	u_12(k-1)	u_10(k-1)
		u_26(k-1)	1		
		u_14(k-1)	1		
		u_15(k-1)	1		
		y_3(k-1)	1		

Vertex [1,29,25]

Structure v_x		Structure v_y		Structure v_z	
y_1(k-1)	1	y_2(k-1)	1	u_15(k-1)	1
u_25(k-1)	y_1(k-1)	u_4(k-1)	1	u_27(k-1)	u_23(k-1)
u_13(k-1)	u_7(k-1)	u_9(k-1)	u_9(k-1)	u_15(k-1)	u_14(k-1)
u_18(k-1)	u_12(k-1)	u_17(k-1)	1		
		u_19(k-1)	u_18(k-1)		

Vertex [30,29,1]

Structure v_x		Structure v_y			Structure v_z	
y_1(k-1)	1	y_2(k-1)	1	1	y_3(k-1)	1
u_25(k-1)	1	u_17(k-1)	y_2(k-1)		u_19(k-1)	u_9(k-1)
u_19(k-1)	u_15(k-1)	y_2(k-1)	y_2(k-1)		u_12(k-1)	u_10(k-1)
u_24(k-1)	u_13(k-1)				u_24(k-1)	u_13(k-1)
					u_13(k-1)	u_12(k-1)
					u_12(k-1)	u_12(k-1)
					u_25(k-1)	u_10(k-1)
					u_15(k-1)	u_13(k-1)

Vertex [30,29,25]

Structure v_x		Structure v_y		Structure v_z	
y_1(k-1)	1	y_2(k-1)	1	u_15(k-1)	1
u_25(k-2)	u_25(k-2)	u_8(k-2)	u_7(k-1)	u_15(k-2)	1
u_25(k-1)	u_13(k-2)	u_8(k-1)	1	u_15(k-1)	u_14(k-2)
u_25(k-1)	u_13(k-1)			u_9(k-2)	u_7(k-2)
u_7(k-2)	1			u_15(k-2)	u_8(k-2)

Edge [1,1,~]

Structure v_x		Structure v_y		Structure v_z	
y_1(k-1)	1	y_2(k-1)	1	u_18(k-1)	1
u_16(k-2)	u_15(k-1)	u_8(k-2)	1	u_18(k-2)	1
u_16(k-1)	1	u_8(k-1)	u_8(k-1)	u_18(k-1)	u_17(k-1)

Edge [30,1,~]

Structure v_x		Structure v_y		Structure v_z	
y_1(k-1)	1	y_2(k-1)	1	u_18(k-1)	1
y_1(k-2)	1	u_8(k-1)	1	y_3(k-2)	1
u_7(k-1)	1	y_2(k-2)	1	u_38(k-1)	u_9(k-1)
u_37(k-1)	u_17(k-1)	u_38(k-1)	1	u_35(k-1)	u_18(k-1)
u_16(k-1)	y_2(k-2)	u_17(k-1)	1	u_28(k-1)	u_18(k-1)
u_16(k-1)	y_2(k-1)	y_3(k-1)	y_3(k-1)	u_38(k-1)	u_38(k-1)
u_38(k-1)	u_34(k-1)	y_3(k-2)	y_3(k-2)		

Edge [~,1,1]

Structure v_x		Structure v_y		Structure v_z	
y_1(k-1)	1	y_2(k-1)	1	y_3(k-1)	1
y_1(k-2)	1	y_2(k-2)	1	y_3(k-2)	1
u_7(k-1)	1	u_8(k-1)	1	u_36(k-1)	1
u_37(k-1)	u_23(k-1)	u_11(k-1)	1	u_39(k-1)	u_23(k-1)
u_16(k-1)	1	u_21(k-1)	y_1(k-1)	u_32(k-1)	u_18(k-1)
u_35(k-1)	u_16(k-1)	u_38(k-1)	u_23(k-1)	u_19(k-1)	y_3(k-1)
u_32(k-1)	u_9(k-1)	y_1(k-1)	y_1(k-1)	u_36(k-1)	u_31(k-1)
1	1			u_39(k-1)	u_32(k-1)
				u_13(k-1)	y_3(k-1)

Edge [~,1,25]

Structure v_x		Structure v_y		Structure v_z	
y_1(k-1)	1	u_8(k-1)	1	y_3(k-1)	1
y_1(k-2)	1	y_2(k-2)	1	y_3(k-2)	1
u_31(k-1)	y_1(k-2)	y_2(k-1)	1	u_24(k-1)	y_1(k-1)
u_34(k-1)	1	u_3(k-1)	1	u_15(k-1)	u_13(k-1)
u_9(k-1)	y_1(k-1)	u_35(k-1)	u_35(k-1)	u_37(k-1)	u_36(k-1)
u_31(k-1)	u_18(k-1)	u_2(k-1)	1	u_31(k-1)	1
u_16(k-1)	u_13(k-1)	u_1(k-1)	1		

Edge [1,29,~]

Structure v_x		Structure v_y		Structure v_z	
y_1(k-1)	1	u_14(k-1)	u_14(k-2)	y_3(k-1)	1
u_22(k-1)	u_13(k-2)	u_14(k-2)	1	u_18(k-2)	1
u_22(k-1)	u_13(k-1)	1	1	u_18(k-1)	1
u_16(k-2)	u_16(k-2)			u_31(k-1)	u_31(k-1)
u_16(k-1)	u_16(k-1)				
1	1				
u_34(k-1)	u_19(k-2)				

Edge [30,29,~]

Structure v_x		Structure v_y		Structure v_z	
y_1(k-1)	1	y_2(k-1)	y_2(k-1)	u_18(k-1)	1
u_7(k-2)	1	u_23(k-2)	1	u_18(k-2)	1
u_17(k-1)	u_16(k-2)	u_23(k-1)	1	u_32(k-1)	u_9(k-2)
u_17(k-2)	u_16(k-1)	u_17(k-2)	1	u_38(k-2)	u_9(k-1)
u_17(k-1)	y_1(k-1)	u_29(k-2)	1	u_18(k-2)	u_17(k-1)
u_38(k-2)	u_16(k-1)	u_29(k-1)	1	u_18(k-2)	u_17(k-2)
u_16(k-1)	1	u_38(k-2)	1	u_13(k-1)	y_3(k-1)
				u_39(k-2)	u_13(k-1)
				u_15(k-1)	y_3(k-1)

Edge [~,20,1]

Structure v_x		Structure v_y		Structure v_z	
y_1(k-1)	y_1(k-2)	y_2(k-1)	1	y_3(k-1)	1
u_7(k-1)	1	u_29(k-1)	u_17(k-1)	u_9(k-1)	1
u_18(k-1)	1	u_38(k-1)	u_11(k-1)	u_18(k-1)	u_16(k-1)
1	1	u_4(k-1)	1		
		u_2(k-1)	1		
		u_5(k-1)	1		
		1	1		

Edge [~,29,25]

Structure v_x		Structure v_y		Structure v_z	
y_1(k-1)	1	y_2(k-1)	y_2(k-2)	u_18(k-1)	1
u_17(k-1)	u_16(k-2)	u_20(k-2)	1	u_18(k-2)	1
u_17(k-2)	u_16(k-1)	u_20(k-1)	1	u_35(k-1)	u_9(k-2)
u_35(k-2)	u_34(k-2)	u_17(k-2)	1	u_18(k-1)	u_17(k-2)
u_17(k-2)	u_7(k-2)	u_23(k-2)	1	u_35(k-2)	u_9(k-2)
u_37(k-2)	u_24(k-2)	u_23(k-1)	1	u_17(k-1)	u_9(k-1)
u_18(k-2)	u_17(k-2)	u_17(k-1)	1	u_17(k-2)	u_9(k-1)
1	1			u_25(k-1)	u_21(k-2)
				u_36(k-2)	u_16(k-1)

Edge [1,~,1]

Structure v_x		Structure v_y		Structure v_z	
y_1(k-1)	1	y_2(k-1)	1	y_3(k-1)	1
u_16(k-2)	1	u_17(k-2)	1	u_18(k-2)	1
u_16(k-1)	1	u_17(k-1)	1	u_18(k-1)	1
u_13(k-1)	1	u_14(k-1)	1	u_28(k-1)	1
1	1	u_28(k-1)	u_17(k-1)	u_18(k-1)	u_13(k-1)
		u_31(k-2)	u_13(k-1)	1	1

Edge [1,~,25]

Structure v_x		Structure v_y		Structure v_z	
y_1(k-1)	1	y_2(k-1)	1	y_3(k-1)	1
u_16(k-2)	1	u_14(k-2)	1	u_15(k-2)	1
u_16(k-1)	1	u_14(k-1)	y_1(k-1)	u_18(k-2)	1
u_13(k-1)	u_13(k-2)	1	1	u_18(k-1)	1
u_13(k-2)	1			u_15(k-1)	u_14(k-1)

Edge [30,~,1]

Structure v_x		Structure v_y		Structure v_z	
y_1(k-1)	1	y_2(k-1)	1	y_3(k-1)	1
u_7(k-2)	1	u_8(k-2)	1	u_9(k-2)	1
u_13(k-2)	1	u_17(k-2)	1	u_15(k-2)	1
u_13(k-1)	1	u_17(k-1)	1	u_15(k-1)	1
u_34(k-2)	1	u_14(k-1)	1	u_36(k-2)	1
u_16(k-2)	u_16(k-2)	u_14(k-2)	1	u_33(k-1)	u_24(k-1)
u_30(k-1)	u_16(k-1)	u_17(k-1)	u_7(k-1)	u_36(k-1)	1
1	1	u_39(k-2)	u_33(k-1)	u_39(k-2)	u_16(k-1)
		u_8(k-1)	1	u_15(k-1)	y_1(k-1)
		u_21(k-2)	u_16(k-1)	u_33(k-1)	u_13(k-1)
		u_24(k-1)	u_16(k-2)		
		u_27(k-1)	u_23(k-2)		
		u_25(k-2)	u_8(k-2)		
		u_31(k-1)	u_14(k-1)		
		u_33(k-1)	u_26(k-2)		
		u_34(k-2)	u_20(k-2)		
		u_38(k-1)	u_15(k-2)		
		u_27(k-2)	y_1(k-1)		
		u_32(k-1)	y_3(k-1)		
		u_29(k-2)	u_19(k-1)		
		u_37(k-2)	u_22(k-2)		
		u_16(k-1)	y_2(k-1)		

Edge [30,~,25]

Structure v_x		Structure v_y		Structure v_z	
y_1(k-1)	1	y_2(k-1)	1	u_15(k-1)	1
u_37(k-2)	u_7(k-2)	u_14(k-2)	1	u_15(k-2)	1
u_13(k-2)	1	u_14(k-1)	1	u_36(k-2)	u_16(k-1)
u_13(k-1)	1	u_35(k-1)	1	u_18(k-2)	1
u_37(k-2)	u_13(k-1)	u_29(k-2)	1	u_18(k-1)	y_1(k-1)
u_13(k-1)	u_8(k-2)	u_26(k-1)	u_19(k-2)	u_36(k-1)	u_14(k-1)
u_16(k-1)	u_8(k-1)	u_33(k-1)	u_27(k-1)	u_18(k-2)	u_13(k-1)

Wall [~,1,~]

Structure v_x		Structure v_y		Structure v_z	
y_1(k-1)	y_1(k-1)	y_2(k-1)	1	y_3(k-1)	1
u_7(k-2)	1	u_8(k-2)	1	u_51(k-3)	1
1	1	u_50(k-3)	y_1(k-1)	u_22(k-1)	u_12(k-1)
		u_26(k-3)	u_7(k-3)	u_51(k-2)	u_49(k-2)
		u_50(k-1)	u_16(k-3)		
		u_11(k-1)	1		
		u_53(k-1)	u_13(k-2)		

Wall [~,29,~]

Structure v_x		Structure v_y		Structure v_z	
y_1(k-1)	y_1(k-2)	y_2(k-1)	1	u_21(k-1)	1
u_7(k-2)	1	u_11(k-2)	1	u_21(k-2)	1
u_19(k-2)	1	u_11(k-1)	1	u_32(k-2)	y_3(k-1)
u_19(k-1)	1	u_20(k-2)	1	u_52(k-2)	u_9(k-2)
1	1	u_20(k-1)	1	1	1
		u_56(k-1)	1		
		u_56(k-2)	1		

Wall [1,~,~]

Structure v_x		Structure v_y		Structure v_z	
y_1(k-1)	1	y_2(k-1)	1	y_3(k-1)	1
u_7(k-1)	1	u_43(k-1)	u_41(k-1)	u_15(k-1)	1
u_10(k-1)	1	u_47(k-1)	u_37(k-1)	1	1
u_25(k-1)	1	u_41(k-1)	u_28(k-1)		
u_17(k-1)	1	u_48(k-1)	u_27(k-1)		
1	1	u_8(k-1)	1		
		u_40(k-1)	u_11(k-1)		
		u_6(k-1)	1		

Wall [30,~,~]

Structure v_x		Structure v_y		Structure v_z	
y_1(k-1)	1	y_2(k-1)	1	y_3(k-1)	1
u_7(k-1)	1	u_53(k-1)	1	u_24(k-1)	1
u_37(k-1)	u_27(k-1)	u_35(k-1)	1	u_15(k-1)	1
u_49(k-1)	u_31(k-1)	u_14(k-1)	1	u_20(k-1)	1
u_45(k-1)	1	u_24(k-1)	u_23(k-1)	u_33(k-1)	u_31(k-1)
u_15(k-1)	1	u_54(k-1)	u_53(k-1)	u_31(k-1)	u_15(k-1)
		u_17(k-1)	1	u_47(k-1)	u_35(k-1)
				u_10(k-1)	u_10(k-1)
				u_25(k-1)	u_19(k-1)
				u_25(k-1)	u_13(k-1)
				u_16(k-1)	u_12(k-1)

Wall [~,~,1]

Structure v_x		Structure v_y		Structure v_z	
y_1(k-1)	1	y_2(k-1)	1	y_3(k-1)	1
u_46(k-1)	1	u_47(k-1)	1	u_9(k-1)	1
u_10(k-1)	1	u_11(k-1)	1	u_57(k-1)	1
u_7(k-1)	1	u_50(k-1)	u_23(k-1)	u_15(k-1)	1
u_47(k-1)	u_19(k-1)	1	1	u_50(k-1)	u_19(k-1)
u_50(k-1)	u_49(k-1)			u_55(k-1)	u_50(k-1)
u_17(k-1)	1			u_50(k-1)	u_46(k-1)
u_20(k-1)	1			u_53(k-1)	u_18(k-1)
u_16(k-1)	u_15(k-1)			u_53(k-1)	u_42(k-1)
u_41(k-1)	u_30(k-1)			u_53(k-1)	u_32(k-1)
u_50(k-1)	1			u_21(k-1)	u_17(k-1)
				u_18(k-1)	u_11(k-1)
				u_56(k-1)	u_43(k-1)
				u_39(k-1)	u_35(k-1)

Wall [~,~,25]

Structure v_x		Structure v_y		Structure v_z	
y_1(k-1)	1	y_2(k-1)	y_2(k-1)	y_3(k-1)	1
u_7(k-1)	1	u_50(k-1)	1	u_51(k-1)	1
u_52(k-1)	1			u_54(k-1)	u_50(k-1)
u_49(k-1)	u_47(k-1)			u_21(k-1)	1
u_47(k-1)	u_7(k-1)			u_29(k-1)	u_21(k-1)
u_52(k-1)	u_13(k-1)			u_51(k-1)	u_30(k-1)
u_50(k-1)	u_13(k-1)			u_54(k-1)	u_53(k-1)
0	0			u_26(k-1)	y_3(k-1)

Inner flow [~,~,~]

Structure v_x		Structure v_y		Structure v_z	
y_1(k-1)	1	y_2(k-1)	1	y_3(k-1)	1
u_7(k-1)	u_6(k-1)	u_26(k-1)	1	u_27(k-1)	u_27(k-1)
u_10(k-1)	1	u_68(k-1)	1	u_72(k-1)	1
		u_58(k-1)	u_8(k-1)		
		u_23(k-1)	1		

B.2 Probability density functions for the NRMSE of each velocity component over the entire channel flow domain

Probability density function of NRMSE of models of the streamwise velocity component across the channel flow domain

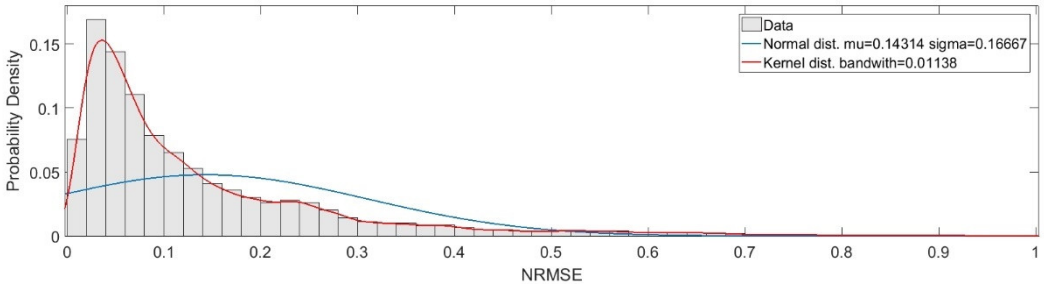

Probability density function of NRMSE of models of the wall-normal velocity component across the channel flow domain

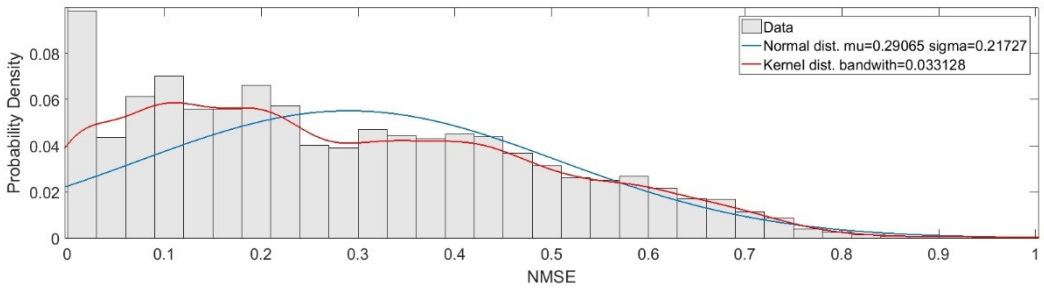

Probability density function of NRMSE of models of the spanwise velocity component across the channel flow domain

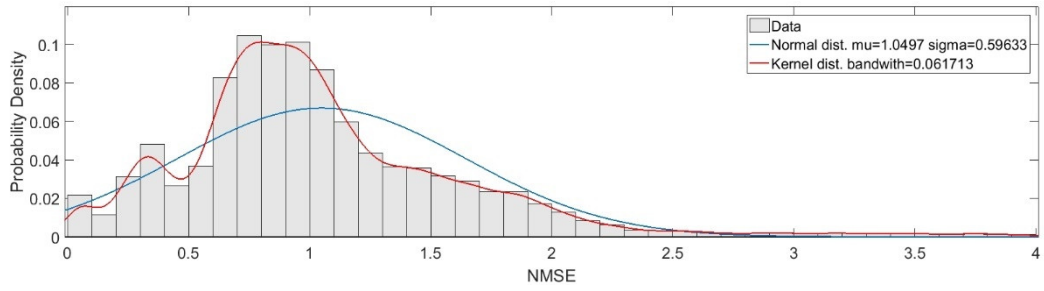

B.3 Model structures and parameters for OSA predictors of $|V|$ data of flow over the BFS

M_{V2} Model

Parameter	Structure	
2.53797	1	1
0.755998	y_1(k-1)	1
-0.01108	y_1(k-1)	y_1(k-2)
-0.00518	y_1(k-1)	u_1(k-4)
0.003086	y_1(k-1)	u_2(k-5)
-0.23781	y_1(k-2)	1
0.007318	y_1(k-2)	y_1(k-3)
0.253627	u_1(k-1)	1
0.001529	u_1(k-1)	y_1(k-3)
0.100254	u_1(k-1)	u_1(k-2)
-0.14836	u_1(k-1)	u_1(k-3)
0.103555	u_1(k-1)	u_1(k-4)
-0.03578	u_1(k-1)	u_1(k-5)
-0.29675	u_1(k-2)	1
-0.16042	u_1(k-2)	u_1(k-2)
0.220081	u_1(k-3)	1
0.378664	u_1(k-3)	u_1(k-2)
-0.20632	u_1(k-3)	u_1(k-3)
-0.08243	u_1(k-4)	1
-0.24637	u_1(k-4)	u_1(k-2)
0.254099	u_1(k-4)	u_1(k-3)
-0.07313	u_1(k-4)	u_1(k-4)
0.079872	u_1(k-5)	u_1(k-2)
-0.07343	u_1(k-5)	u_1(k-3)
0.03338	u_1(k-5)	u_1(k-4)
0.001652	u_2(k-1)	u_1(k-5)
0.002332	u_2(k-4)	u_1(k-1)
0.002282	u_2(k-6)	u_1(k-5)
-0.00183	u_2(k-7)	u_2(k-2)

M_{V4} Model

Parameter	Structure	
1.552415	1	1
0.739311	y_1(k-1)	1
-0.01552	y_1(k-1)	y_1(k-2)
0.002856	u_3(k-3)	u_1(k-2)
0.084472	u_4(k-1)	1
0.005077	u_4(k-1)	y_1(k-3)
-0.00283	u_4(k-1)	u_1(k-2)
0.282455	u_4(k-1)	u_4(k-2)
-1.0773	u_4(k-1)	u_4(k-3)
2.13992	u_4(k-1)	u_4(k-4)
-2.93899	u_4(k-1)	u_4(k-5)
2.987156	u_4(k-1)	u_4(k-6)
-2.27135	u_4(k-1)	u_4(k-7)
1.25803	u_4(k-1)	u_4(k-8)
-0.46837	u_4(k-1)	u_4(k-9)
0.089137	u_4(k-1)	u_4(k-1)
0.010947	u_4(k-2)	u_4(k-2)
-0.05311	u_4(k-3)	1

B.4 Validation of MSA predictors of $|\boldsymbol{V}|$ data from flow over the BFS

M_{V2} model

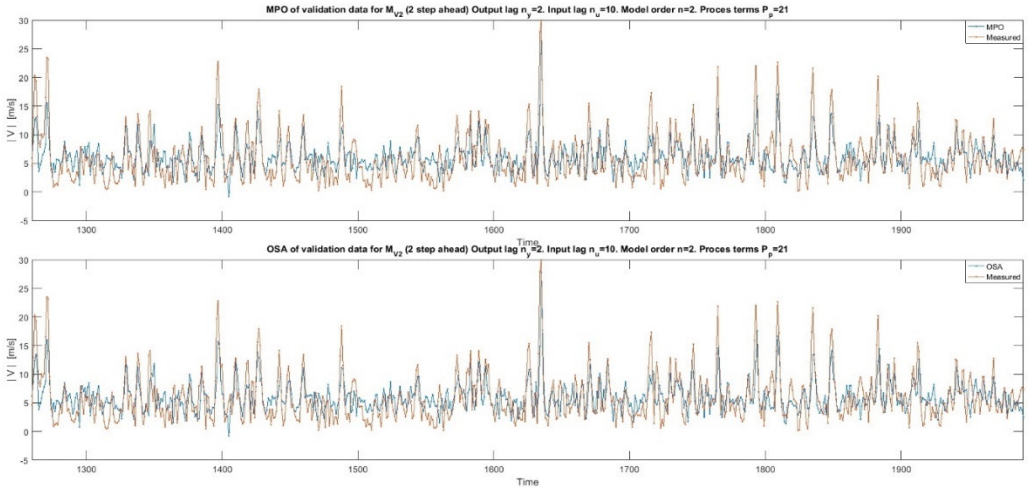

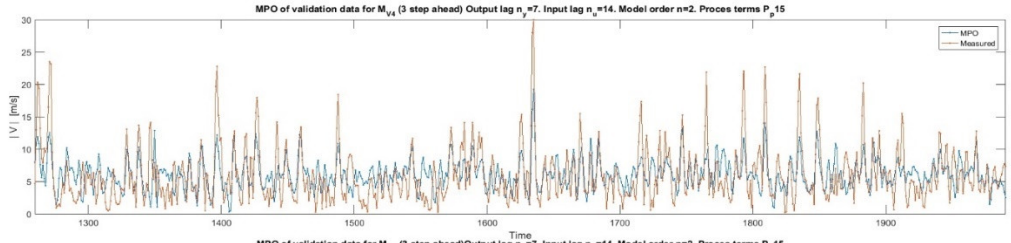

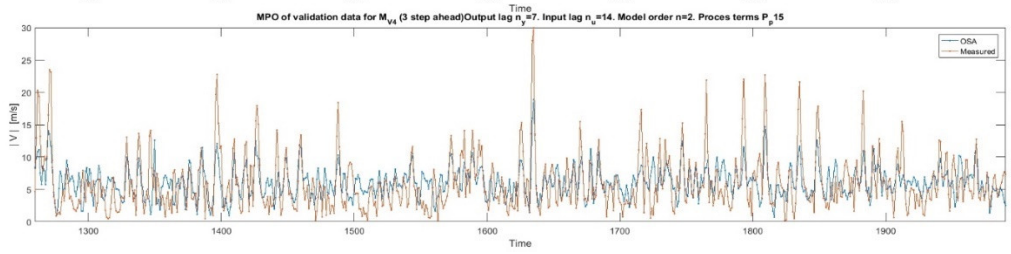

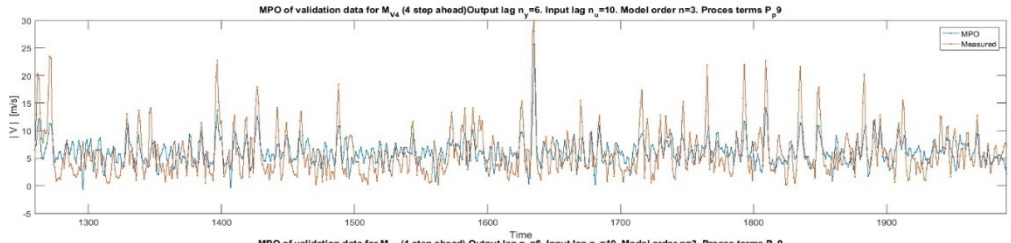

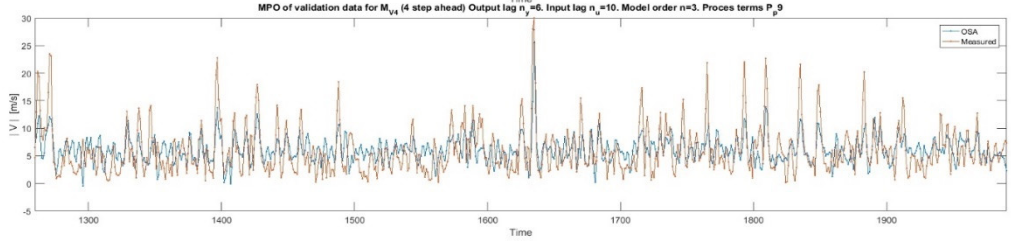

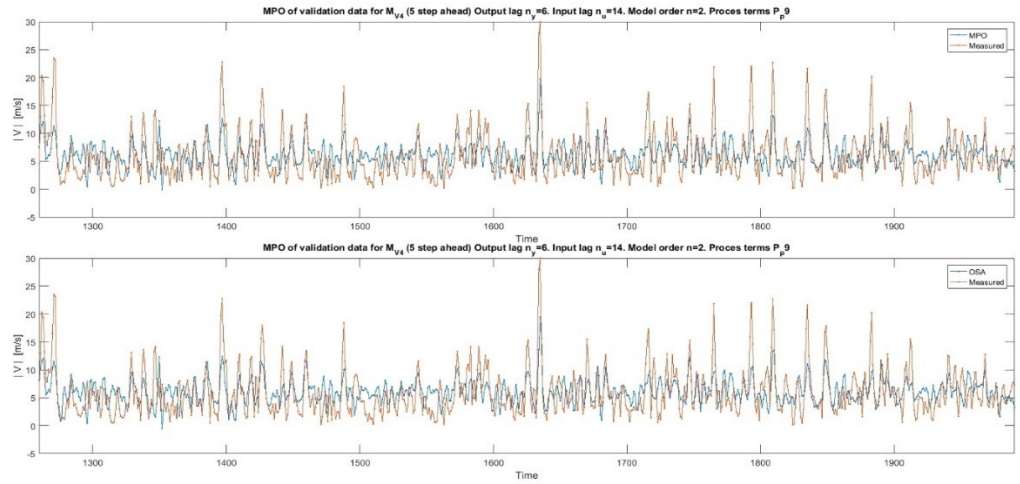
MPO of validation data for M_{V4} (5 step ahead) Output lag n_y=6. Input lag n_u=14. Model order n=2. Proces terms P_p=9
MPO
Measured
| V | [m/s]
Time
MPO of validation data for M_{V4} (5 step ahead) Output lag n_y=6. Input lag n_u=14. Model order n=2. Proces terms P_p=9
OSA
Measured
| V | [m/s]
Time

M_{V4} Model

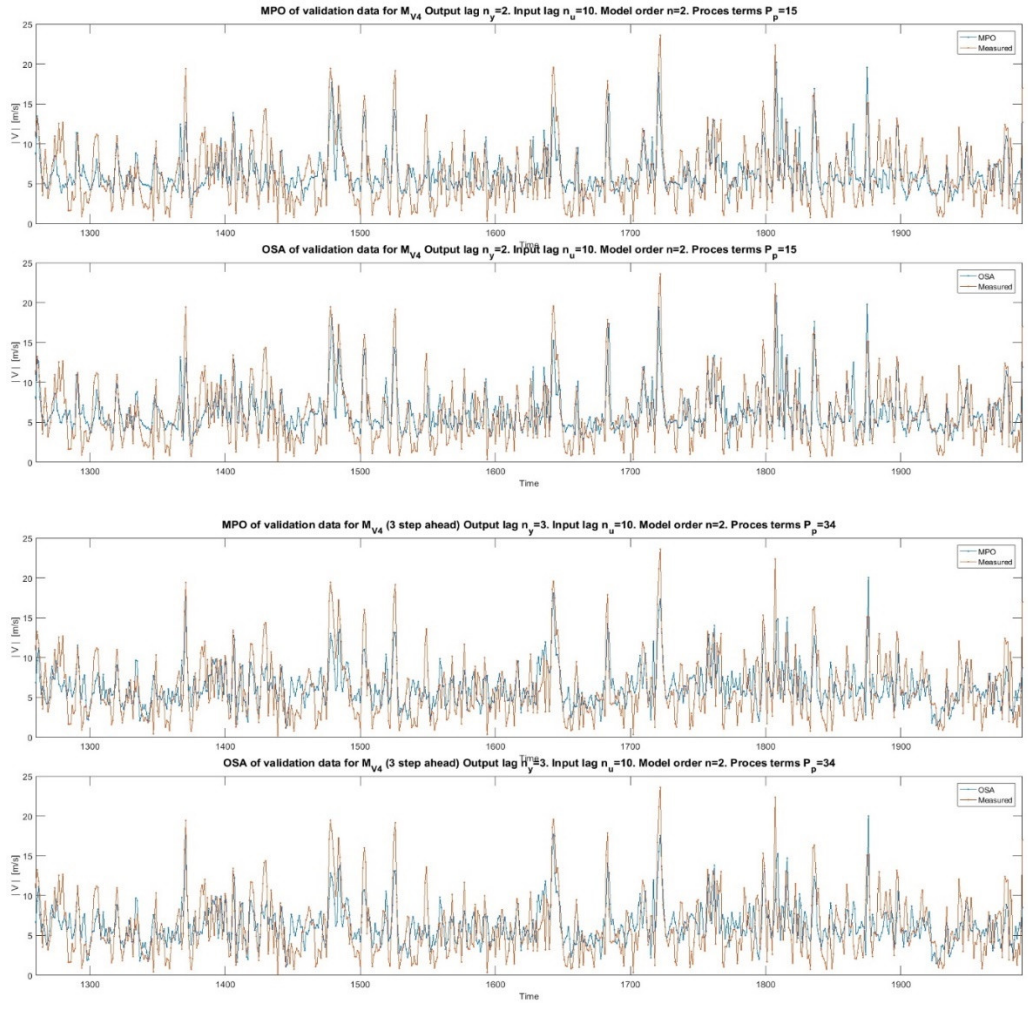
MPO of validation data for M_{V4} Output lag n_y=2. Input lag n_u=10. Model order n=2. Proces terms P_p=15
MPO
Measured
| V | [m/s]
OSA of validation data for M_{V4} Output lag n_y=2. Input lag n_u=10. Model order n=2. Proces terms P_p=15
OSA
Measured
| V | [m/s]
Time
MPO of validation data for M_{V4} (3 step ahead) Output lag n_y=3. Input lag n_u=10. Model order n=2. Proces terms P_p=34
MPO
Measured
| V | [m/s]
OSA of validation data for M_{V4} (3 step ahead) Output lag n_y=3. Input lag n_u=10. Model order n=2. Proces terms P_p=34
OSA
Measured
| V | [m/s]
Time

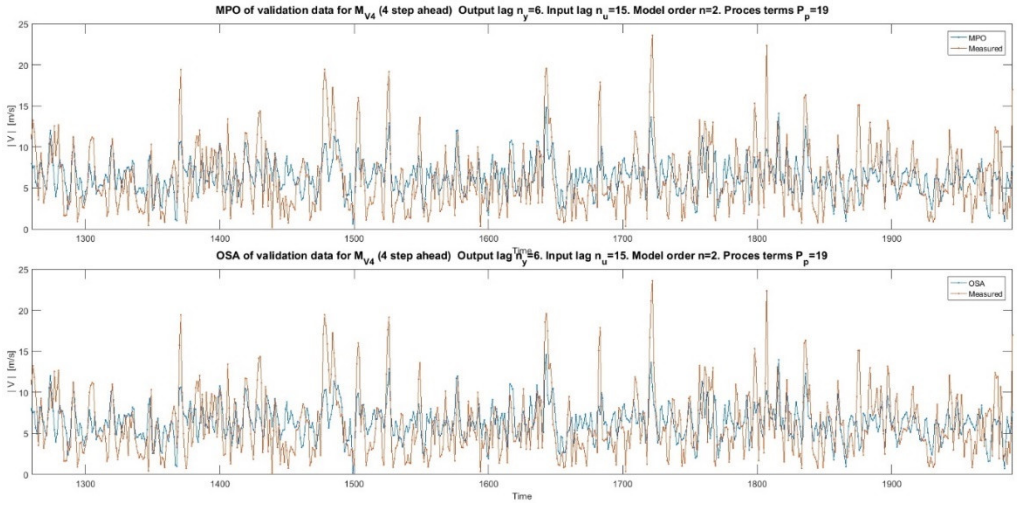
MPO of validation data for M_{V4} (4 step ahead) Output lag n_y=6. Input lag n_u=15. Model order n=2. Proces terms P_p=19
MPO
Measured
|V| [m/s]
OSA of validation data for M_{V4} (4 step ahead) Output lag n_y=6. Input lag n_u=15. Model order n=2. Proces terms P_p=19
OSA
Measured
|V| [m/s]
Time

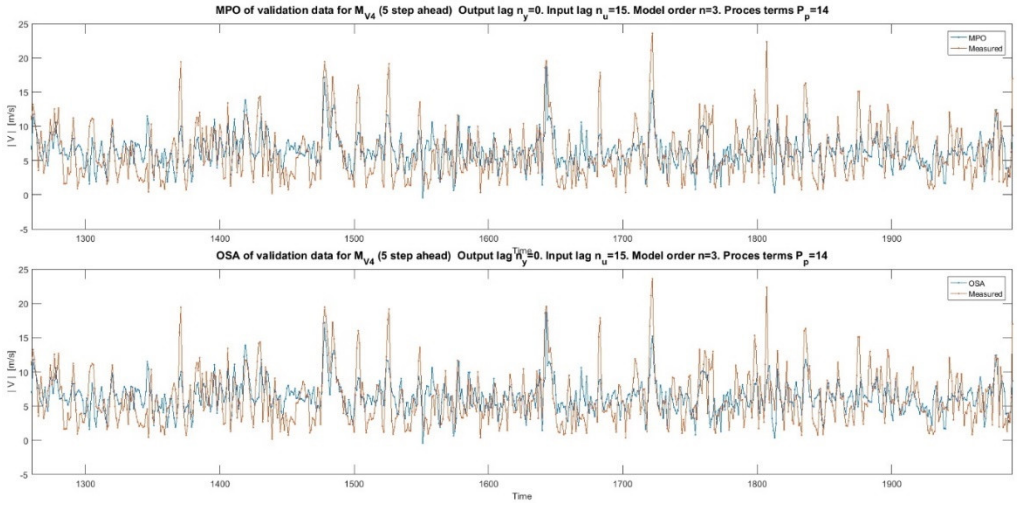
MPO of validation data for M_{V4} (5 step ahead) Output lag n_y=0. Input lag n_u=15. Model order n=3. Proces terms P_p=14
MPO
Measured
|V| [m/s]
OSA of validation data for M_{V4} (5 step ahead) Output lag n_y=0. Input lag n_u=15. Model order n=3. Proces terms P_p=14
OSA
Measured
|V| [m/s]
Time

B.5 Model structures and parameters for MSA predictors of $|V|$ data from flow over the BFS

M_{V2} Model

Parameter	Structure (2SA)	
2.53797	1	1
0.755998	y_1(k-1)	1
-0.01108	y_1(k-1)	y_1(k-2)
-0.00518	y_1(k-1)	u_1(k-4)
0.003086	y_1(k-1)	u_2(k-5)
-0.23781	y_1(k-2)	1
0.007318	y_1(k-2)	y_1(k-3)
0.253627	u_1(k-1)	1
0.001529	u_1(k-1)	y_1(k-3)
0.100254	u_1(k-1)	u_1(k-2)
-0.14836	u_1(k-1)	u_1(k-3)
0.103555	u_1(k-1)	u_1(k-4)
-0.03578	u_1(k-1)	u_1(k-5)
-0.29675	u_1(k-2)	1
-0.16042	u_1(k-2)	u_1(k-2)
0.220081	u_1(k-3)	1
0.378664	u_1(k-3)	u_1(k-2)
-0.20632	u_1(k-3)	u_1(k-3)
-0.08243	u_1(k-4)	1
-0.24637	u_1(k-4)	u_1(k-2)
0.254099	u_1(k-4)	u_1(k-3)
-0.07313	u_1(k-4)	u_1(k-4)
0.079872	u_1(k-5)	u_1(k-2)
-0.07343	u_1(k-5)	u_1(k-3)
0.03338	u_1(k-5)	u_1(k-4)
0.001652	u_2(k-1)	u_1(k-5)
0.002332	u_2(k-4)	u_1(k-10)
0.002282	u_2(k-6)	u_1(k-5)
-0.00183	u_2(k-7)	u_2(k-2)

Parameter	Structure (5SA)		
5.951107	1	1	1
0.001229	y_1(k-4)	y_1(k-6)	u_2(k-6)
0.307119	u_1(k-1)	1	1
-0.00687	u_1(k-1)	u_1(k-5)	1
0.000669	u_1(k-1)	u_1(k-5)	u_2(k-7)
-0.00058	u_1(k-1)	u_2(k-5)	u_2(k-5)
0.019445	u_2(k-1)	1	1
-0.07164	u_1(k-2)	1	1
0.0058	u_2(k-4)	u_1(k-10)	1

Parameter	Structure (4SA)	
5.675127	1	1
0.00763	y_1(k-3)	u_2(k-11)
0.00766	y_1(k-6)	y_1(k-5)
0.309818	u_1(k-1)	1
-0.01083	u_1(k-1)	u_1(k-4)
-0.18185	u_1(k-2)	1
0.092169	u_1(k-3)	1
-0.01138	u_1(k-5)	y_1(k-6)
0.005533	u_1(k-10)	y_1(k-7)
0.011809	u_2(k-1)	1
0.008235	u_2(k-5)	y_1(k-5)
0.007701	u_2(k-5)	u_1(k-11)
0.006083	u_2(k-6)	u_1(k-14)
-0.00369	u_2(k-9)	u_1(k-14)
-0.01091	u_2(k-11)	y_1(k-7)

Parameter	Structure (3SA)	
4.551515	1	1
0.114738	y_1(k-2)	1
-0.00305	y_1(k-2)	u_1(k-5)
0.004083	y_1(k-2)	u_2(k-5)
0.356015	u_1(k-1)	1
0.058835	u_1(k-1)	u_1(k-3)
-0.16428	u_1(k-1)	u_1(k-4)
0.239917	u_1(k-1)	u_1(k-5)
-0.2549	u_1(k-1)	u_1(k-6)
0.206357	u_1(k-1)	u_1(k-7)
-0.12808	u_1(k-1)	u_1(k-8)
0.055316	u_1(k-1)	u_1(k-9)
-0.01657	u_1(k-1)	u_1(k-10)
-0.29867	u_1(k-2)	1
0.216621	u_1(k-3)	1
-0.10567	u_1(k-4)	1
0.027062	u_1(k-9)	1
0.002591	u_2(k-2)	u_1(k-5)
-0.00337	u_2(k-2)	u_2(k-8)
0.004473	u_2(k-4)	u_1(k-10)
0.005115	u_2(k-6)	u_1(k-5)

M_{V4} Model

Parameter	Structure (2SA)	
4.038423	1	1
0.180865	y_1(k-2)	1
-0.00571	y_1(k-2)	u_4(k-4)
-0.00462	u_2(k-1)	u_4(k-5)
0.044338	u_2(k-10)	1
0.163482	u_4(k-1)	1
-0.00343	u_4(k-1)	u_1(k-3)
0.302551	u_4(k-1)	u_4(k-3)
-1.07788	u_4(k-1)	u_4(k-4)
2.000969	u_4(k-1)	u_4(k-5)
-2.44749	u_4(k-1)	u_4(k-6)
2.11271	u_4(k-1)	u_4(k-7)
-1.27522	u_4(k-1)	u_4(k-8)
0.500628	u_4(k-1)	u_4(k-9)
-0.10302	u_4(k-1)	u_4(k-10)

Parameter	Structure (4SA)	
6.335584	1	1
0.006438	u_1(k-3)	y_1(k-6)
0.006495	u_1(k-4)	u_1(k-12)
0.005697	u_2(k-1)	u_4(k-10)
-0.00553	u_2(k-2)	u_3(k-11)
0.00662	u_2(k-8)	u_1(k-6)
-0.00509	u_2(k-15)	u_1(k-7)
0.003938	u_3(k-1)	u_4(k-9)
-0.04817	u_3(k-13)	1
0.005869	u_3(k-13)	u_1(k-9)
-0.0073	u_3(k-13)	u_2(k-6)
0.004639	u_3(k-15)	u_2(k-5)
0.153388	u_4(k-1)	1
-0.00411	u_4(k-1)	u_2(k-14)
-0.00692	u_4(k-1)	u_4(k-5)
0.005987	u_4(k-1)	u_4(k-7)
0.004752	u_4(k-2)	u_1(k-7)
-0.00523	u_4(k-15)	u_2(k-11)
0.005372	u_4(k-15)	u_2(k-15)

Parameter	Structure (3SA)	
4.858581	1	1
0.070562	y_1(k-3)	1
0.004182	y_1(k-3)	u_2(k-4)
0.002937	u_1(k-1)	u_2(k-4)
0.003	u_1(k-2)	u_4(k-6)
0.004164	u_1(k-3)	u_3(k-4)
0.004397	u_1(k-3)	u_4(k-9)
0.001841	u_1(k-7)	u_1(k-7)
0.002976	u_1(k-9)	u_1(k-9)
-0.00551	u_2(k-1)	u_3(k-10)
-0.00587	u_2(k-1)	u_4(k-5)
0.005654	u_2(k-7)	u_1(k-5)
0.051542	u_2(k-10)	1
0.005008	u_2(k-10)	u_1(k-7)
0.002926	u_3(k-4)	u_2(k-9)
-0.02931	u_3(k-7)	1
-0.00498	u_3(k-7)	u_1(k-8)
0.003198	u_3(k-9)	u_1(k-5)
-0.00336	u_3(k-10)	u_1(k-10)
0.157153	u_4(k-1)	1
-0.00319	u_4(k-1)	u_1(k-4)
0.00423	u_4(k-1)	u_1(k-6)
-0.00311	u_4(k-1)	u_3(k-6)
0.181099	u_4(k-1)	u_4(k-4)

-0.6448	u_4(k-1)	u_4(k-5)
1.138395	u_4(k-1)	u_4(k-6)
-1.25855	u_4(k-1)	u_4(k-7)
0.9202	u_4(k-1)	u_4(k-8)
-0.42058	u_4(k-1)	u_4(k-9)
0.095465	u_4(k-1)	u_4(k-10)
-0.03545	u_4(k-4)	1
0.005941	u_4(k-5)	u_2(k-9)
0.00259	u_4(k-10)	u_2(k-10)
0.002598	u_4(k-10)	u_3(k-5)

Parameter	Structure (5SA)		
6.297355	1	1	0
0.000794	u_1(k-4)	u_3(k-9)	u_4(k-13)
-0.00053	u_2(k-3)	u_2(k-12)	u_3(k-11)
-0.00058	u_2(k-4)	u_2(k-8)	u_2(k-15)
0.000732	u_3(k-3)	u_3(k-13)	u_2(k-15)
0.127341	u_4(k-1)	1	1
-0.00149	u_4(k-1)	u_2(k-10)	u_1(k-9)
0.000787	u_4(k-1)	u_2(k-13)	u_2(k-6)
-0.00069	u_4(k-1)	u_4(k-7)	u_1(k-11)
-0.00077	u_4(k-2)	u_2(k-11)	u_1(k-6)
-0.00083	u_4(k-2)	u_2(k-14)	u_1(k-9)
-0.00071	u_4(k-12)	u_2(k-11)	u_1(k-6)
-0.00084	u_4(k-12)	u_4(k-9)	u_2(k-10)
0.000761	u_4(k-14)	u_2(k-12)	u_1(k-15)

Appendix C

C.1 Coefficients and model structures of NARMAX predictors used for frequency analysis of flow over the BFS

Parameter	Structure M_{AD}	
0.577679	u_1(k-16)	u_1(k-5)
-0.28612	u_1(k-11)	u_1(k-3)
-0.32704	u_1(k-19)	u_1(k-18)
0.999447	u_1(k-20)	u_1(k-1)
0.031293	u_1(k-14)	y_1(k-3)
-0.818	u_1(k-20)	u_1(k-2)
-0.20371	u_1(k-13)	y_1(k-2)
0.182682	u_1(k-19)	y_1(k-2)

Parameter	Structure M_{AE}	
0.235252	u_1(k-10)	u_1(k-10)
-0.5779	u_1(k-6)	u_1(k-1)
0.37175	u_1(k-6)	u_1(k-2)
-0.07538	u_1(k-10)	u_1(k-5)
-0.03017	y_1(k-2)	y_1(k-1)
8.819774	1	1

Parameter	Structure M_{BE}	
0.109226	u_1(k-7)	y_1(k-1)
0.139829	u_1(k-10)	u_1(k-9)
-0.22738	u_1(k-4)	u_1(k-1)
0.181832	u_1(k-25)	u_1(k-11)
-0.06305	y_1(k-1)	y_1(k-1)
-0.16316	u_1(k-16)	u_1(k-6)
0.122899	u_1(k-27)	u_1(k-12)

Parameter	Structure M_{AB}	
2.187493	y_1(k-1)	1
-0.11613	y_1(k-1)	y_1(k-1)
0.01427	u_1(k-14)	u_1(k-1)
-0.43072	y_1(k-2)	1
0.016801	y_1(k-3)	y_1(k-2)
-0.01018	u_1(k-21)	u_1(k-10)
0.005822	u_1(k-27)	u_1(k-21)
-0.00304	u_1(k-12)	u_1(k-3)

Parameter	Structure M_{BD}		
0.000106	u_1(k-18)	u_1(k-4)	u_1(k-2)
-0.0151	u_1(k-12)	u_1(k-11)	u_1(k-10)
0.058915	u_1(k-20)	u_1(k-17)	y_1(k-1)
-0.00521	u_1(k-13)	u_1(k-13)	y_1(k-2)
-0.05263	u_1(k-13)	u_1(k-11)	y_1(k-1)
0.025099	u_1(k-14)	u_1(k-11)	u_1(k-1)

C.2 Modified models used for frequency analysis

Parameter	Structure M_{AD}	
-0.28612	u_1(k-11)	u_1(k-3)
-0.20371	u_1(k-13)	y_1(k-2)
0.031293	u_1(k-14)	y_1(k-3)
0.577679	u_1(k-16)	u_1(k-5)
0.182682	u_1(k-19)	y_1(k-2)
-0.32704	u_1(k-19)	u_1(k-18)
-0.818	u_1(k-20)	u_1(k-2)
5.962982	1	u_1(k-20)
5.962982	1	u_1(k-1)
-1.70706	1	u_1(k-11)
-1.70706	1	u_1(k-3)
-1.21536	1	y_1(k-2)
0.186701	1	y_1(k-3)
3.446593	1	u_1(k-16)
3.446593	1	u_1(k-5)
1.089933	1	y_1(k-2)
-1.95123	1	u_1(k-19)
-1.95123	1	u_1(k-18)
-4.88044	1	u_1(k-20)
-4.88044	1	u_1(k-2)
-1.12748	u_1(k-13)	1
0.1732	u_1(k-14)	1
1.011119	u_1(k-19)	1

Parameter	Structure M_{AE}	
-0.03017	y_1(k-2)	y_1(k-1)
-0.5779	u_1(k-6)	u_1(k-1)
0.37175	u_1(k-6)	u_1(k-2)
-0.07538	u_1(k-10)	u_1(k-5)
0.235252	u_1(k-10)	u_1(k-10)
-3.4479	1	u_1(k-6)
-3.4479	1	u_1(k-1)
2.217964	1	u_1(k-6)
2.217964	1	u_1(k-2)
-0.44973	1	u_1(k-10)
-0.44973	1	u_1(k-5)
1.403577	1	u_1(k-10)
1.403577	1	u_1(k-10)
-0.18294	y_1(k-2)	1
-0.18294	y_1(k-1)	1

Parameter	Structure M_{BE}	
-0.06305	y_1(k-1)	y_1(k-1)
-0.22738	u_1(k-4)	u_1(k-1)
0.109226	u_1(k-7)	y_1(k-1)
0.139829	u_1(k-10)	u_1(k-9)
-0.16316	u_1(k-16)	u_1(k-6)
0.181832	u_1(k-25)	u_1(k-11)
0.122899	u_1(k-27)	u_1(k-12)
-1.35661	1	u_1(k-4)
-1.35661	1	u_1(k-1)
0.651675	1	y_1(k-1)
0.834258	1	u_1(k-10)
0.834258	1	u_1(k-9)
-0.97345	1	u_1(k-16)
-0.97345	1	u_1(k-6)
1.08486	1	u_1(k-25)
1.08486	1	u_1(k-11)
0.733249	1	u_1(k-27)
0.733249	1	u_1(k-12)
-0.21517	y_1(k-1)	1
-0.21517	y_1(k-1)	1
0.372748	u_1(k-7)	1

Parameter	Structure M_{AB}	
2.187493	0	y_1(k-1)
-0.11613	y_1(k-1)	y_1(k-1)
-0.43072	0	y_1(k-2)
0.016801	y_1(k-3)	y_1(k-2)
0.01427	u_1(k-14)	u_1(k-1)
-0.00304	u_1(k-12)	u_1(k-3)
-0.01018	u_1(k-21)	u_1(k-10)
0.005822	u_1(k-27)	u_1(k-21)
0.085138	1	u_1(k-14)
0.085138	1	u_1(k-1)
-0.01815	1	u_1(k-12)
-0.01815	1	u_1(k-3)
-0.06076	1	u_1(k-21)
-0.06076	1	u_1(k-10)
0.034738	1	u_1(k-27)
0.034738	1	u_1(k-21)

0.036044	y_1(k-1)	1
0.036044	y_1(k-1)	1
-0.00521	y_1(k-3)	1

Parameter	Structure M_{BD}		
-0.0151	u_1(k-12)	u_1(k-11)	u_1(k-10)
-0.05263	u_1(k-13)	u_1(k-11)	y_1(k-1)
-0.00521	u_1(k-13)	u_1(k-13)	y_1(k-2)
0.000106	u_1(k-18)	u_1(k-4)	u_1(k-2)
0.058915	u_1(k-20)	u_1(k-17)	y_1(k-1)
0.14975	1	u_1(k-14)	u_1(k-11)
0.14975	1	u_1(k-14)	u_1(k-1)
0.14975	1	u_1(k-11)	u_1(k-1)
0.893449	1	1	u_1(k-14)
0.893449	1	1	u_1(k-11)
0.893449	1	1	u_1(k-1)
-0.09009	1	u_1(k-12)	u_1(k-11)
-0.09009	1	u_1(k-12)	u_1(k-10)
-0.09009	1	u_1(k-11)	u_1(k-10)
-0.53752	1	1	u_1(k-12)
-0.53752	1	1	u_1(k-11)
-0.53752	1	1	u_1(k-10)
-0.31402	1	u_1(k-13)	y_1(k-1)
-0.31402	1	u_1(k-11)	y_1(k-1)
-1.8735	1	1	y_1(k-1)
-0.03106	1	u_1(k-13)	y_1(k-2)
-0.03106	1	u_1(k-13)	y_1(k-2)
-0.18532	1	1	y_1(k-2)
0.000634	1	u_1(k-18)	u_1(k-4)
0.000634	1	u_1(k-18)	u_1(k-2)
0.000634	1	u_1(k-4)	u_1(k-2)
0.003783	1	1	u_1(k-18)
0.003783	1	1	u_1(k-4)
0.003783	1	1	u_1(k-2)
0.351504	1	u_1(k-20)	y_1(k-1)
0.351504	1	u_1(k-17)	y_1(k-1)
2.097169	1	1	y_1(k-1)
-0.11746	u_1(k-13)	u_1(k-11)	1
-0.01162	u_1(k-13)	u_1(k-13)	1
0.131483	u_1(k-20)	u_1(k-17)	1
-0.7008	u_1(k-13)	1	1
-0.7008	u_1(k-11)	1	1
-0.06932	u_1(k-13)	1	1
-0.06932	u_1(k-13)	1	1
0.784465	u_1(k-20)	1	1
0.784465	u_1(k-17)	1	1

C.3 Phase plots for GFRF's

AD 2nd order

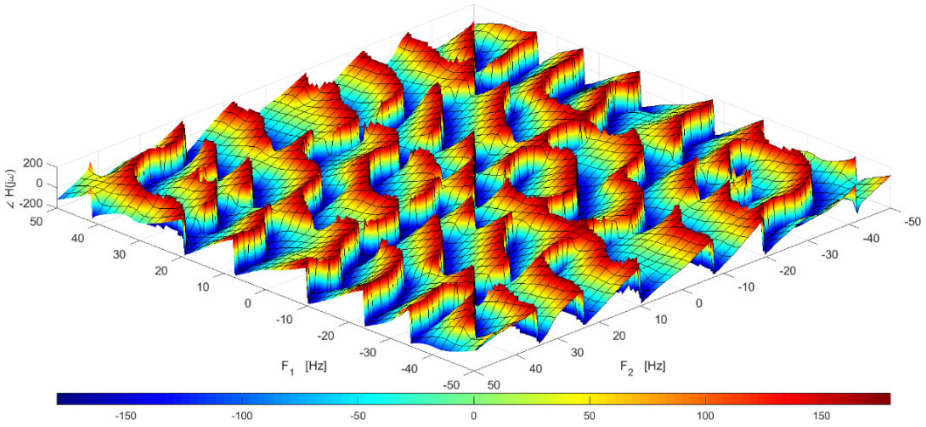

AD 3rd order

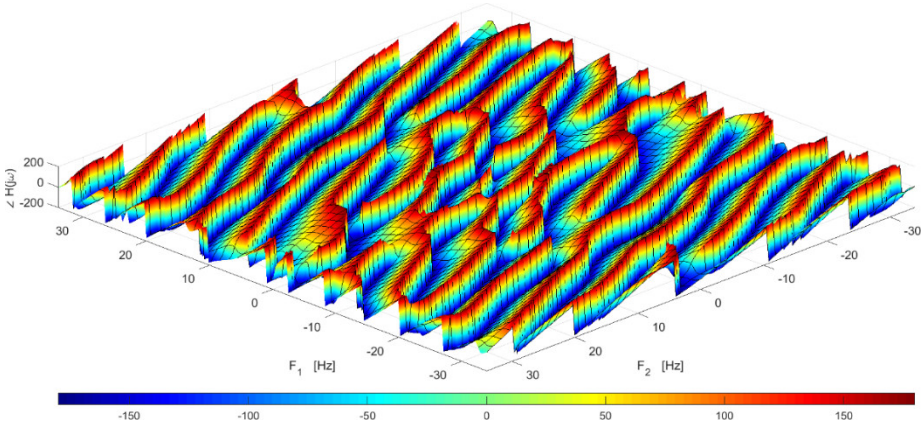

BD 2nd order

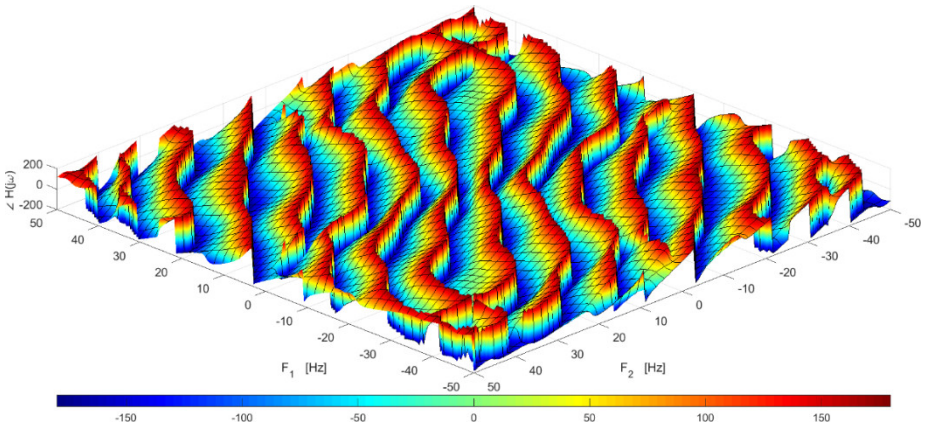

BD 3rd order

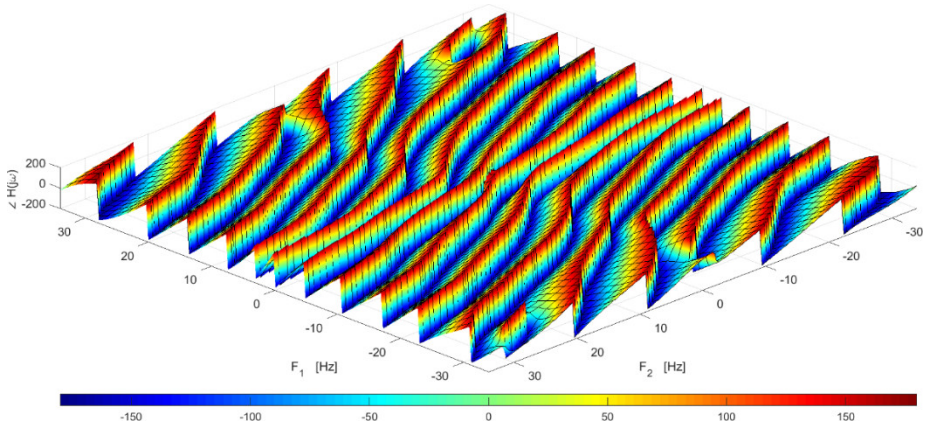

AE 2nd order

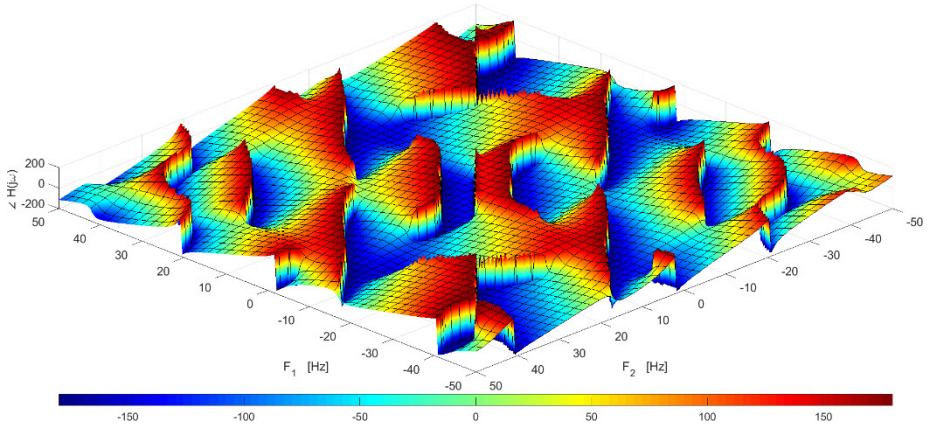

AE 3rd order

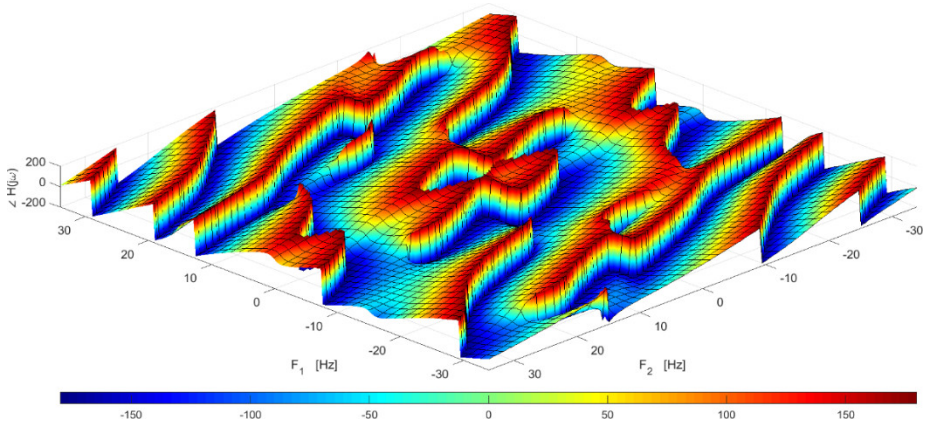

BE 2nd order

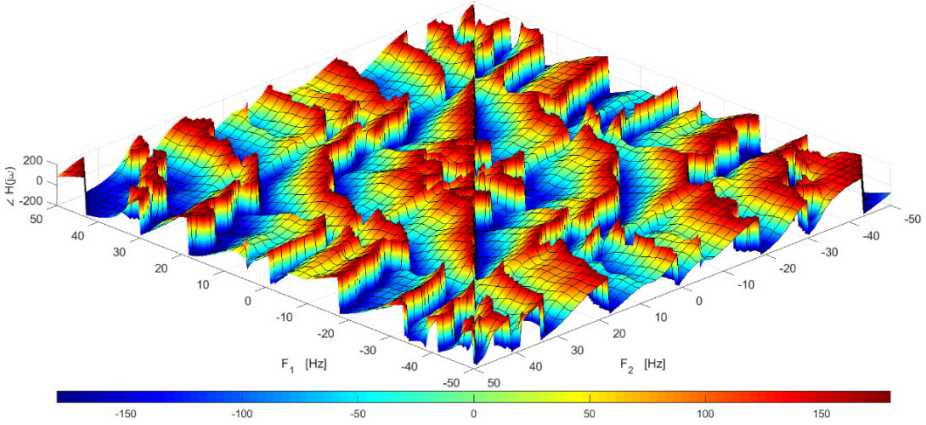

BE 3rd order

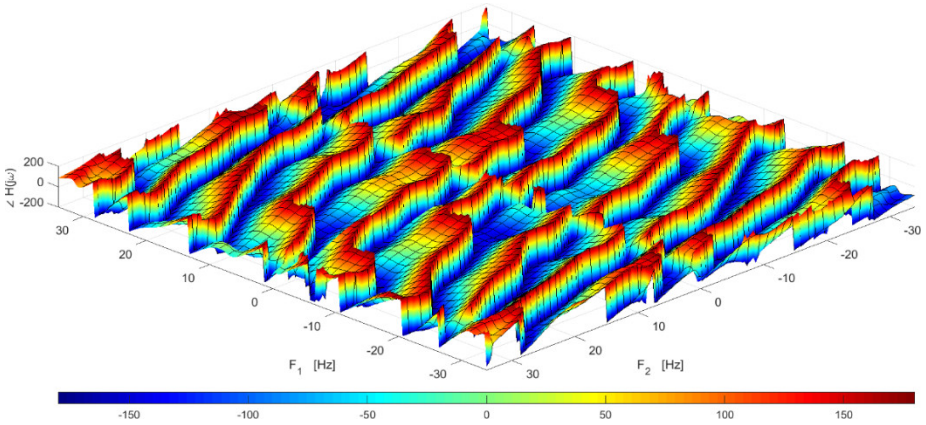

AB 2nd order

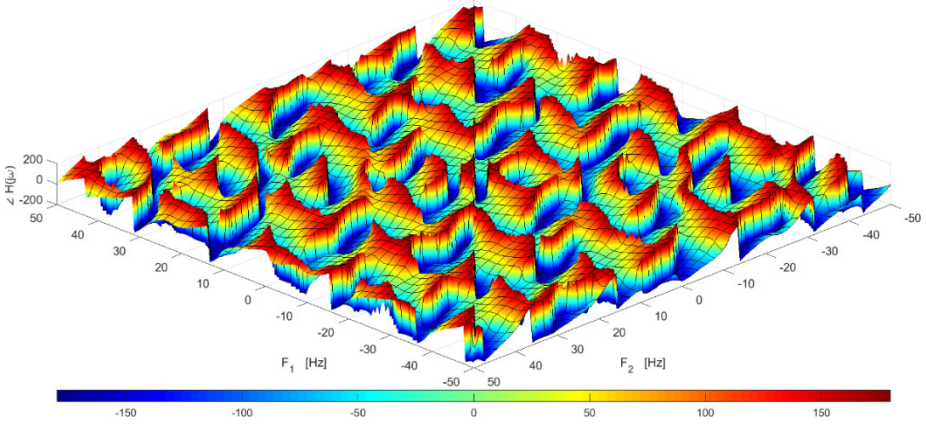

AB 3rd order

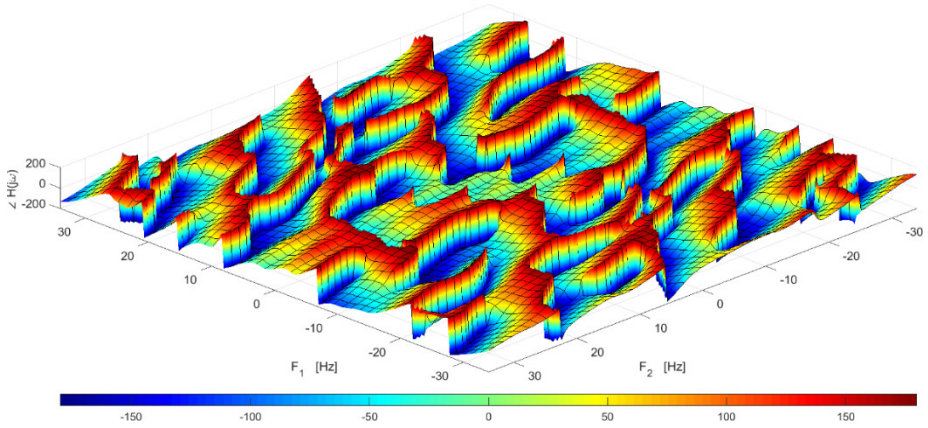
200
0
-200
∠ H(jω)
30
20
10
0
-10
-20
-30
F1 [Hz]
30
20
10
0
-10
-20
-30
F2 [Hz]
-150
-100
-50
0
50
100
150

REFERENCES

Aamo, O. M., & Fossen, T. I. (2002). Tutorial on fedback control of flows, Part I: Stabilization of fluid flows in channels and pipes. *Modeling, Identification and Control, 23*(1), 161-226.

Akanyeti, O., Rañó, I., Nehmzow, U., & Billings, S. A. (2010). An application of Lyapunov stability analysis to improve the performance of NARMAX models. *Robotics and Autonomous Systems, 58*(1), 229-238.

Åkervik, E., Hœpffner, J., Ehrenstein, U., & Henningson, D. S. (2007). Optimal growth, model reduction and control in a separated boundary-layer flow using global eigenmodes. *Journal of Fluid Mechanics, 579*(1), 305-315.

Allgower, F., Findeisen, R., & Nagy, Z. K. (2004). Nonlinear model predictive control: From theory to application. *Journal of the Chinese Institute of Chemical Engineers, 35*(1), 299-315.

Ansys. (2016). ANSYS FLUENT Academic Research (Version Release 16): Ansys Inc.

Atiya, A. F., El-Shoura, S. M., Shaheen, S. I., & El-Sherif, M. S. (1999). A comparison between neural-network forecasting techniques - Case study: River flow forecasting. *IEEE Transactions on Neural Networks, 10*(1), 402-409.

Ayala Solares, J. R., & Wei, H. L. (2015). Nonlinear model structure detection and parameter estimation using a novel bagging method based on distance correlation metric. *Nonlinear Dynamics, 82*(1), 201-215.

Bai, L. (2010). *Nonlinear Predictive Control Based on NARMAX Models.* (PhD), The University of Sheffield, Sheffield.

Bai, L., & Coca, D. (2007). *NARMAX Based Nonlinear Predictive Control*. Paper presented at the 2007 European Control Conference, Kos, Greece.

Bai, L., & Coca, D. (2008). *Nonlinear predictive control based on NARMAX models*. Paper presented at the 2008 11th International Conference on Optimization of Electrical and Electronic Equipment, Brasov, Romania.

Bai, L., & Coca, D. (2011). Internal Nonlinear Predictive Control of Semilinear Parabolic equations. *IFAC World Congress 18th, 44*(1), 5525-5530.

Baker, J., Armaou, A., & Christofides, P. D. (2000). Nonlinear Control of Incompressible Fluid Flow: Application to Burgers' Equation and 2D Channel Flow. *Journal of Mathematical Analysis and Applications, 252*(1), 230-255.

Baldacchino, T., Anderson, S. R., & Kadirkamanathan, V. (2012). Structure detection and parameter estimation for NARX models in a unified em framework. *Automatica, 48*(1), 857-865.

Baldacchino, T., Anderson, S. R., & Kadirkamanathan, V. (2013). Computational system identification for Bayesian NARMAX modelling. *Automatica, 49*(1), 2641-2651.

Balikhin, M. A., Bates, I., & Walker, S. (2001). Identification of linear and nonlinear processes in space plasma turbulence data. *Advances in Space Research, 28*(1), 787-800.

Baramov, L., Tutty, O. R., & Rogers, E. (2001). *H infinity control for non-periodic planar channel flows.* Paper presented at the 40th IEEE Conference on Decision and Control, 2001, Orlando, Florida.

Barbu, V. (1998). Optimal control of Navier-Stokes equations with periodic inputs. *Nonlinear Analysis: Theory, Methods & Applications, 31*(1), 15-31.

Barbu, V. (2003). Feedback stabilization of Navier–Stokes equations. *ESAIM: Control, Optimisation and Calculus of Variations, 9*(1), 197-205.

Barbu, V. (2007). Stabilization of a plane channel flow by wall normal controllers. *Nonlinear Analysis, Theory, Methods and Applications, 67*(1), 2573-2588.

Barbu, V., Coca, D., & Yan, Y. (2005). Stabilizing semilinear parabolic equations. *Numerical Functional Analysis and Optimization, 26*(1), 449-480.

Barbu, V., Havârneanu, T., Popa, C., & Sritharan, S. S. (2003). Exact Controllability for the Magnetohydrodynamic Equations. *Communications on Pure and Applied Mathematics, 56*(1), 732-783.

Barbu, V., Lasiecka, I., & Triggiani, R. (2006a). Abstract settings for tangential boundary stabilization of Navier-Stokes equations by high- and low-gain feedback controllers. *Nonlinear Analysis, Theory, Methods and Applications, 64*(1), 2704-2746.

Barbu, V., Lasiecka, I., & Triggiani, R. (2006b). Tangential Boundary Stabilization of Navier-Stokes Equations. In A. M. Society (Ed.), *Memoirs of the American Mathematical Society* (First ed., Vol. 852, pp. 1-128). Virginia, USA: American Mathematical Society.

Barbu, V., Lasiecka, I., & Triggiani, R. (2007). Local Exponential Stabilization Strategies of the Navier-Stokes Equations , d = 2 , 3 , via Feedback Stabilization of its Linearization. In K. Kunisch, J. Sprekels, G. Leugering, & F. Tröltzsch (Eds.), *Control of Coupled Partial Differential Equations* (Vol. 155, pp. 13-46). Basel: Birkhäuser Basel.

Barbu, V., & Sritharan, S. S. (1998). *H∞–control theory of fluid dynamics.* Paper presented at the Proceedings of the Royal Society of London. Series A: Mathematical, Physical and Engineering Sciences, London.

Barbu, V., & Triggiani, R. (2004). Internal stabilization of Navier-Stokes equations with finite-dimensional controllers. *Indiana University Mathematics Journal, 53*(1), 1443-1494.

Bewley, T. R. (2001). Flow control: New challenges for a new Renaissance. *Progress in Aerospace Sciences, 37*(1), 21-58.

Bewley, T. R., & Liu, S. (1998). Optimal and robust control and estimation of linear paths to transition. *J. Fluid Mech., 365*(1), 305-349.

Bewley, T. R., Moin, P., & Temam, R. (2001). DNS-based predictive control of turbulence: an optimal benchmark for feedback algorithms. *Journal of Fluid Mechanics, 447*(1), 179-225.

Biau, D. (2012). Laminar-turbulent separatrix in a boundary layer flow. *Physics of Fluids, 24*(1), 1-23.

Billings, S. A. (2013). *Nonlinear System Identification NARMAX Methods in the Time, Frequency, and Spatio-Temporal Domains*. London: Wiley.

Billings, S. A., & Aguirre, L. A. (1995). Effects of the Sampling Time on the Dynamics and Identification of Nonlinear Models. *International Journal of Bifurcation and Chaos, 05*(1), 1541-1556.

Billings, S. A., Chen, S., & Korenberg, M. J. (1989). Identification of MIMO non-linear systems using a forward-regression orthogonal estimator. *International Journal of Control, 49*(1), 2157-2189.

Billings, S. A., Fadzil, M. B., Sulley, J. L., & Johnson, P. M. (1988). Identification of a non-linear difference equation model of an industrial diesel generator. *Mechanical Systems and Signal Processing, 2*(1), 59-76.

Billings, S. A., & Lang, Z. Q. (2002). Non-linear systems in the frequency domain: Energy transfer filters. *International Journal of Control, 75*(1), 1066-1081.

Billings, S. A., & Li, L. M. (2000). Reconstruction of Linear and Non-Linear Continuous-Time System Models from Input/output Data Using the Kernel Invariance Algorithm. *Journal of Sound and Vibration, 233*(1), 877-896.

Billings, S. A., & Tsang, K. M. (1989a). Spectral analysis for non-linear systems, Part I: Parametric non-linear spectral analysis. *Mechanical Systems and Signal Processing, 3*(1), 319-339.

Billings, S. A., & Tsang, K. M. (1989b). Spectral analysis for non-linear systems, Part II: Interpretation of non-linear frequency response functions. *Mechanical Systems and Signal Processing, 3*(1), 341-359.

Billings, S. A., Tsang, K. M., & Tomlinson, G. R. (1990). Spectral analysis for non-linear systems, part III: Case study examples. *Mechanical Systems and Signal Processing, 4*(1), 3-21.

Billings, S. A., & Voon, W. S. F. (1983). *Structure detection and model validity tests in the identification of nonlinear systems* (0143-7054). Retrieved from Sheffield, UK:

Billings, S. A., & Voon, W. S. F. (1986). Correlation based model validity tests for non-linear models. *International Journal of Control, 44*(1), 235-244.

Billings, S. A., & Zhang, H. (1994). Analysing non-linear systems in the frequency domain--II. The phase response. *Mechanical Systems and Signal Processing, 8*(1), 45-62.

Billings, S. A., & Zhu, Q. M. (1994). Nonlinear model validation using correlation tests. *International Journal of Control, 60*(1), 1107-1120.

Billings, S. A., & Zhu, Q. M. (1995). Model validation tests for multivariable nonlinear models including neural networks. *International Journal of Control, 62*(1), 749-766.

Biserni, C., Fichera, A., Guglielmino, I. D., Lorenzini, E., & Pagano, A. (2006). A non-linear approach for the analysis and modelling of the dynamics of systems exhibiting Vapotron effect. *International Journal of Heat and Mass Transfer, 49*(1), 1264-1273.

Boaghe, O. M., Billings, S. A., Li, L. M., Fleming, P. J., & Liu, J. (2002). Time and frequency domain identification and analysis of a gas turbine engine. *Control Engineering Practice, 10*(1), 1347-1356.

Boynton, R. J., Balikhin, M. A., Billings, S. A., Sharma, A. S., & Amariutei, O. A. (2011). Data derived NARMAX Dst model. *Annales Geophysicae, 29*(1), 965-971.

Bradshaw, P. (1994). Turbulence: the chief outstanding difficulty of our subject. *Experiments in Fluids, 16-16*(1), 203-216.

Braslow, A. L. (1999). *A history of suction-type laminar-flow control with emphasis on flight research* (Vol. 13). Washington, USA: NASA History Office, Office of Policy and Plans, NASA Headquarters.

Camacho, E. F., & Bordons-Alba, C. (2003). *Model predictive control* (2nd ed. ed.). London: Springer-Verlag.

Canuto, C., Hussaini, M. Y., Quarteroni, A., & Zang, T. A. (1988). *Spectral methods in fluid dynamics*. Berlin Springer Berlin Heidelberg.

Cattafesta Iii, L. N., Song, Q., Williams, D. R., Rowley, C. W., & Alvi, F. S. (2008). Active control of flow-induced cavity oscillations. *Progress in Aerospace Sciences, 44*(1), 479-502.

Chen, S., & Billings, S. A. (1989). Representations of non-linear systems: the NARMAX model. *International Journal of Control, 49*(1), 1013-1032.

Chen, S., Billings, S. A., & Luo, W. (1989). Orthogonal least squares methods and their application to non-linear system identification. *International Journal of Control, 50*(1), 1873-1896.

Cheng, S. J., & Liu, J. J. (2015). Nonlinear modeling and identification of proton exchange membrane fuel cell (PEMFC). *International Journal of Hydrogen Energy, 40*(1), 9452-9461.

Choi, H., Moin, P., & Kim, J. (1993). Direct numerical simulation of turbulent flow over riblets. *Journal of Fluid Mechanics, 255*(1), 503-539.

Choi, H., Moin, P., & Kim, J. (1994). Active turbulence control for drag reduction in wall-bounded flows. *Journal of Fluid Mechanics, 262*(1), 75-110.

Choi, K. S. (2002). Near-wall structure of turbulent boundary layer with spanwise-wall oscillation. *Physics of Fluids, 14*(1), 2530-2542.

Choi, K. S., Debisschop, J. R., & Clayton, B. R. (1998). Turbulent boundary-layer control by means of spanwise-wall oscillation. *AIAA Journal, 36*(1), 1157-1163.

Chung, Y. M., & Talha, T. (2011). Effectiveness of active flow control for turbulent skin friction drag reduction. *Physics of Fluids, 23*(1), 1-30.

Clarke, D. W., & Mohtadi, C. (1989). Properties of generalized predictive control. *Automatica, 25*(1), 859-875.

Clarke, D. W., Mohtadi, C., & Tuffs, P. S. (1987a). Generalized predictive control—Part I. The basic algorithm. *Automatica, 23*(1), 137-148.

Clarke, D. W., Mohtadi, C., & Tuffs, P. S. (1987b). Generalized Predictive Control—Part II Extensions and interpretations. *Automatica, 23*(1), 149-160.

Coca, D. (2003). Review of results and perspectives of nonlinear process identification from experimental data. *Advances in Space Research, 32*(1), 337-345.

Coca, D., Balikhin, M. A., Billings, S. A., Alleyne, H. S. C. K., & Dunlop, M. (2001). Time domain analysis of plasma turbulence observed upstream of a quasi-parallel shock. *Journal of Geophysical Research: Space Physics, 106*(1), 25005-25021.

Coca, D., & Billings, S. A. (2002a). Identification of finite dimensional models of infinite dimensional dynamical systems. *Automatica, 38*(1), 1851-1865.

Coca, D., & Billings, S. A. (2002b). Identification of NARMAX and related models. *Control Systems, Robotics and Automation, 6*(1), 1-30.

Condrea, E. P. (2014). *Modelling, analysis and forecasting of deep sea oxygen isotape variations in response to orbital forcing.* (PhD), The University of Sheffield, Sheffield.

Curtain, R., & Morris, K. (2009). Transfer functions of distributed parameter systems: A tutorial. *Automatica, 45*(1), 1101-1116.

Davidson, P. A., Kaneda, Y., & Sreenivasan, K. R. (2013). *Ten chapters in turbulence*. Cambridge: Cambridge : Cambridge University Press, 2013.

De Brederode, V., & Bradshaw, P. (1978). Influence of the Side Walls on the Turbulent Center-Plane Boundary-Layer in a Square Duct. *Journal of Fluids Engineering, Transactions of the ASME, 100*(1), 91-96.

De Giorgi, M. G., De Luca, C. G., Ficarella, A., & Marra, F. (2015). Comparison between synthetic jets and continuous jets for active flow control: Application on a NACA 0015 and a compressor stator cascade. *Aerospace Science and Technology, 43*(1), 256-280.

De Gooijer, J. G., & Hyndman, R. J. (2006). 25 years of time series forecasting. *International Journal of Forecasting, 22*(1), 443-473.

Dean, B., & Bhushan, B. (2012). The effect of riblets in rectangular duct flow. *Applied Surface Science, 258*(1), 3936-3947.

Desta, T. Z., Brecht, A. V., Meyers, J., Baelmans, M., & Berckmans, D. (2004). Combining CFD and data-based mechanistic (DBM) modelling approaches. *Energy & Buildings, 36*(1), 535-542.

Driver, D. M., & Jovic, S. (1994). *Backward-facing step measurements at low Reynolds number, Re(sub h)=5000*. Retrieved from NASA, USA:

Fattorini, H. O., & Sritharan, S. S. (1992). Existence of Optimal Controls for Viscous Flow Problems. *Proceedings of the Royal Society: Mathematical and Physical Sciences (1990-1995), 439*(1), 81-102.

Fernández-Cara, E., Guerrero, S., Imanuvilov, O. Y., & Puel, J. P. (2004). Local exact controllability of the Navier–Stokes system. *Journal de mathématiques pures et appliquées, 83*(1), 1501-1542.

Frank, M. W. (2011). *Fluid mechanics*. New York: New York : McGraw-Hill, c2011.

Fransson, J. H. M. (2015). Transition to Turbulence Delay Using a Passive Flow Control Strategy. *Procedia IUTAM, 14*(1), 385-393.

Friederich, U. (2012). *Nonlinear system identification and analysis of adaptive neural information processing in the fly early visual system.* (MSc), The Universiy of Sheffield, Sheffield, UK.

Fu, Z., Iwaki, Y., Motozawa, M., Tsukahara, T., & Kawaguchi, Y. (2015). Characteristic turbulent structure of a modified drag-reduced surfactant solution flow via dosing water from channel wall. *International Journal of Heat and Fluid Flow, 53*(1), 135-145.

Fung, E. H. K., Wong, Y. K., Ho, H. F., & Mignolet, M. P. (2003). Modelling and prediction of machining errors using ARMAX and NARMAX structures. *Applied Mathematical Modelling, 27*(1), 611-627.

Fursikov, A. V. (2001). Stabilizability of Two-Dimensional Navier—Stokes Equations with Help of a Boundary Feedback Control. *Journal of Mathematical Fluid Mechanics, 3*(1), 259-301.

Gad-El-Hak, M. (1989). Flow Control. *Applied Mechanics Reviews, 42*(1), 261-293.

Gao, Y., & Er, M. J. (2005). NARMAX time series model prediction: feedforward and recurrent fuzzy neural network approaches. *Fuzzy Sets and Systems, 150*(1), 331-350.

García, C. E., Prett, D. M., & Morari, M. (1989). Model predictive control: Theory and practice—A survey. *Automatica, 25*(1), 335-348.

Gautier, N., & Aider, J. L. (2013). Control of the separated flow downstream of a backward-facing step using visual feedback. *Proceedings of the Royal Society A: Mathematical, Physical and Engineering Sciences, 469*(2160), 1-13.

Gautier, N., & Aider, J. L. (2014a). Feed-forward control of a perturbed backward-facing step flow. *Journal of Fluid Mechanics, 759*(1), 181-196.

Gautier, N., & Aider, J. L. (2014b). Upstream open loop control of the recirculation area downstream of a backward-facing step. *Comptes rendus - Mécanique, 342*(6), 382-388.

George, D. A. (1959). *Continuous nonlinear systems*. Retrieved from Cambridge, USA:

George, P. (2003). Turbulence: Suddenly it's chaos. *Nature, 424*(1), 1002.

Gibson, J. F. (2012). Channelflow: A spectral Navier-Stokes simulator in C++ (Version 1.5). U. New Hampshire: J. F. Gibson.

Gibson, J. F. (2014). *Channelflow's Users Manual*. U. New Hampshire: Gibson, J. F.

Gibson, J. F., Halcrow, J., & Cvitanović, P. (2008). Visualizing the geometry of state space in plane Couette flow. *J. Fluid Mech., 611*(1), 107-130.

Glynn, A. N. (2011). *Activity Summary.* Paper presented at the Distribution.

Grebenkin, I., Muradov, K., & Davies, D. (2015). A stochastic approach for evaluating where On/Off zonal production control is efficient. *Journal of Petroleum Science and Engineering, 132*(1), 28-38.

Gresho, P. M. (1991). Some current CFD issues relevant to the incompressible Navier-Stokes equations. *Computer Methods in Applied Mechanics and Engineering, 87*(1), 201-252.

Guo, L. Z., & Billings, S. A. (2007). Detection of fatigue cracks in a beam using a spatio-temporal dynamical system identification method. *Journal of Sound and Vibration, 299*(1), 22-35.

Guo, Y., Guo, L. Z., Billings, S. A., Coca, D., & Lang, Z. Q. (2012). Characterizing Nonlinear Spatio-Temporal Systems in the Frequency Domain. *International Journal of Bifurcation and Chaos, 22*(2), 9-15.

Guo, Y., Guo, L. Z., Billings, S. A., & Wei, H. L. (2015). Identification of continuous-time models for nonlinear dynamic systems from discrete data. *International Journal of Systems Science, 47*(12), 1-11.

Haritonidis, J. H. (1989). *The Measurement of Wall Shear Stress* (Vol. 45). Berlin, Heidelberg: Springer Berlin Heidelberg.

Havârneanu, T., Popa, C., & Sritharan, S. S. (2006). Exact internal controllability for the two-dimensional Navier–Stokes equations with the Navier slip boundary conditions. *Systems & Control Letters, 55*(1), 1022-1028.

Haynes, B. R., & Billings, S. A. (1994). Global analysis and model validation in nonlinear system identification. *Nonlinear Dynamics, 5*(1), 93-130.

He, F., Billings, S. A., Wei, H. L., Sarrigiannis, P. G., & Zhao, Y. (2013). Spectral Analysis for Nonstationary and Nonlinear Systems: A Discrete-Time-Model-Based Approach. *IEEE Transactions on Biomedical Engineering, 60*(1), 2233-2241.

He, F., Sarrigiannis, P. G., Billings, S. A., Wei, H. L., Rowe, J., Romanowski, C., . . . Yianni, J. (2016). Nonlinear interactions in the thalamocortical loop in essential tremor: A model-based frequency domain analysis. *Neuroscience, 324*(1), 377-389.

He, F., Wei, H. L., & Billings, S. A. (2013). Identification and frequency domain analysis of non-stationary and nonlinear systems using time-varying NARMAX models. *International Journal of Systems Science, 46*(1), 2087-2100.

Heenan, A. F., & Morrison, J. F. (1998). Passive control of backstep flow. *Experimental Thermal and Fluid Science, 16*(1), 122-132.

Heins, P. H. (2012). ChannelFlow Inhomogeneous Boundary Conditions (Version 1.0). The University of Sheffield: Department of Automatic Control & Systems Engineering.

Heins, P. H. (2015). *Modelling, Simulation and Control of Turbulent Flows.* (PhD), The University of Sheffield, Sheffield.

Heins, P. H., Jones, B. L., & Sharma, A. S. (2016). Passivity-based output-feedback control of turbulent channel flow. *Automatica, 69*(1), 348-355.

Henning, L., & King, R. (2007). Robust Multivariable Closed-Loop Control of a Turbulent Backward-Facing Step Flow. *Journal of Aircraft, 44*(1), 201-208.

Henson, M. A. (1998). Nonlinear model predictive control: current status and future directions. *Computers and Chemical Engineering, 23*(1), 187-202.

Hervé, A., Sipp, D., Schmid, P. J., & Samuelides, M. (2012). A physics-based approach to flow control using system identification. *Journal of Fluid Mechanics, 702*(1), 26-58.

Ho, C. M., & Tai, Y. C. (1998). Micro-electro-mechanical-systems (MEMS) and fluid flows. *Annual Review of Fluid Mechanics, 30*(1), 579-612.

Hong, X., Mitchell, R. J., Chen, S., Harris, C. J., Li, K., & Irwin, G. W. (2008). Model selection approaches for non-linear system identification: a review. *International Journal of Systems Science, 39*(1), 925-946.

Huang, L., Fan, B., & Dong, G. (2010). Turbulent drag reduction via a transverse wave traveling along streamwise direction induced by Lorentz force. *Physics of Fluids, 22*(1), 1503-1508.

Huang, S. C., & Kim, J. (2008). Control and system identification of a separated flow. *Physics of Fluids, 20*(1), 101509-101527.

Hyndman, R. J., & Koehler, A. B. (2006). Another look at measures of forecast accuracy. *International Journal of Forecasting, 22*(1), 679-688.

Ipcc. (2014). *Climate change 2013 : the physical science basis : working group I contribution to the fifth assessment report of the intergovernmental panel on climate change*. Retrieved from New York, USA

Jing, X. J., Lang, Z. Q., & Billings, S. A. (2008a). Mapping from parametric characteristics to generalized frequency response functions of non-linear systems. *International Journal of Control, 81*(1), 1071-1088.

Jing, X. J., Lang, Z. Q., & Billings, S. A. (2008b). Output frequency response function-based analysis for nonlinear Volterra systems. *Mechanical Systems and Signal Processing, 22*(1), 102-120.

Jing, X. J., Lang, Z. Q., & Billings, S. A. (2008c). *The properties of output frequencies of nonlinear volterra systems*. Retrieved from Sheffield:

Jing, X. J., Lang, Z. Q., & Billings, S. A. (2010). Output frequency properties of nonlinear systems. *International Journal of Non-Linear Mechanics, 45*(1), 681-690.

Jing, X. J., Lang, Z. Q., & Billings, S. A. (2011). Nonlinear influence in the frequency domain: Alternating series. *Systems & Control Letters, 60*(1), 295-309.

John, D. A. (1995). *Computational fluid dynamics : the basics with applications*. New York: McGraw-Hill.

Jones, B. L., Heins, P. H., Kerrigan, E. C., Morrison, J. F., & Sharma, A. S. (2015). Modelling for robust feedback control of fluid flows. *Journal of Fluid Mechanics, 769*(1), 687-722.

Jones, B. L., & Kerrigan, E. C. (2010). When is the discretization of a spatially distributed system good enough for control? *Automatica, 46*(1), 1462-1468.

Joshi, S. S., Speyer, J., & Kim, J. (1997). A systems theory approach to the feedback stabilization of infinitesimal and finite-amplitude disturbances in plane Poiseuille flow. *Journal of Fluid Mechanics, 332*(1), 157-184.

Jung, W. J., Mangiavacchi, N., & Akhavan, R. (1992). Suppression of turbulence in wall-bounded flows by high-frequency spanwise oscillations. *Physics of Fluids A, 4*(1), 1605-1607.

Kang, S. M., Speyer, J., & Kim, J. (2015). Controller Synthesis for Periodic, Linear-Distributed Parameter Systems: Channel Flow Application. *Journal of Guidance, Control, and Dynamics, 38*(1), 993-1000.

Kasagi, N., Suzuki, Y., & Fukagata, K. (2009). Microelectromechanical Systems-Based Feedback Control of Turbulence for Skin Friction Reduction. *Annual Review of Fluid Mechanics, 41*(11), 231-251.

Keerthi, S., & Gilbert, E. (1988). Optimal infinite-horizon feedback laws for a general class of constrained discrete-time systems: Stability and moving-horizon approximations. *Journal of Optimization Theory and Applications, 57*(1), 265-293.

Kerschen, G., Worden, K., Vakakis, A. F., & Golinval, J. C. (2006). Past, present and future of nonlinear system identification in structural dynamics. *Mechanical Systems and Signal Processing, 20*(1), 505-592.

Kim, J. (2003). Control of turbulent boundary layers. *Physics of Fluids, 15*(1), 1093-1105.

Kim, J., & Bewley, T. R. (2007). A Linear Systems Approach to Flow Control. *Annual Review of Fluid Mechanics, 39*(1), 383-417.

Kim, J., Moin, P., & Moser, R. (1987). Turbulence statistics in fully developed channel flow at low Reynolds number. *J. Fluid. Mech., 177*(1), 133-166.

Kim, K., Beskok, A., & Jayasuriya, S. (2005). *Nonlinear system identification for the interaction of synthetic jets with a boundary layer*. Paper presented at the 2005 American Control Conference, Portland, USA.

Kim, K., & Sung, H. J. (2006). Effects of unsteady blowing through a spanwise slot on a turbulent boundary layer. *Journal of Fluid Mechanics, 557*(1), 423-450.

Kim, K. I., & Powers, E. J. (1988). A digital method of modeling quadratically nonlinear systems with a general random input. *Acoustics, Speech and Signal Processing, IEEE Transactions on, 36*(1), 1758-1769.

Kittler, J., & Devijver, P. A. (1982). Statistical Properties of Error Estimators in Performance Assessment of Recognition Systems. *IEEE Transactions on Pattern Analysis and Machine Intelligence, 4*(2), 215-220.

Klumpp, S., Meinke, M., & Schröder, W. (2010). Drag reduction by spanwise transversal surface waves. *Journal of Turbulence, 11*(1), 1-13.

Koide, Y., Sasaki, R., Kameya, Y., & Motosuke, M. (2015). A burst wave-induced plasma actuator for controlling separated flow over a backward-facing step at low Reynolds numbers. *Experimental Thermal and Fluid Science, 66*(1), 72-78.

Korda, M., & Cigler, J. (2012). Nonquadratic stochastic model predictive control: A tractable approach. *Automatica, 48*(1), 2352-2358.

Kotta, Ü., Bartosiewicz, Z., Pawłuszewicz, E., & Wyrwas, M. (2009). Irreducibility, reduction and transfer equivalence of nonlinear input–output equations on homogeneous time scales. *Systems & Control Letters, 58*(1), 646-651.

Kotta, Ü., Zinober, A. S. I., & Liu, P. (2001). Transfer equivalence and realization of nonlinear higher order input–output difference equations. *Automatica, 37*(11), 1771-1778.

Kubo, Y., Modi, V. J., Kotsubo, C., Hayashida, K., & Kato, K. (1996). Suppression of wind-induced vibrations of tall structures through moving surface boundary-layer control. *Journal of Wind Engineering and Industrial Aerodynamics, 61*(1), 181-194.

Lang, Z. Q., & Billings, S. A. (1996). Output frequency characteristics of nonlinear systems. *International Journal of Control, 64*(1), 1049-1067.

Lang, Z. Q., & Billings, S. A. (1997). Output frequencies of nonlinear systems. *International Journal of Control, 67*(1), 713-730.

Lang, Z. Q., & Billings, S. A. (2000). Evaluation of output frequency responses of nonlinear systems under multiple inputs. *IEEE Transactions on Circuits and Systems II: Analog and Digital Signal Processing, 47*(1), 28-38.

Lang, Z. Q., & Billings, S. A. (2004). *Energy Transfer Properties of Nonlinear Systems in the Frequency Domain*. Retrieved from Sheffield:

Lang, Z. Q., Billings, S. A., Yue, R., & Li, J. (2007). Output frequency response function of nonlinear Volterra systems. *Automatica, 43*(1), 805-816.

Le, H., Moin, P., & Kim, J. (1997). Direct numerical simulation of turbulent flow over a backward-facing step. *J. Fluid Mech., 330*(1), 349-374.

Lee, C., Kim, J., Babcock, D., & Goodman, R. (1997). Application of neural networks to turbulence control for drag reduction. *Physics of Fluids, 9*(1), 1740-1747.

Lee, C., Kim, J., & Choi, H. (1998). Suboptimal control of turbulent channel flow for drag reduction. *Journal of Fluid Mechanics, 358*(1), 245-258.

Lee, J. H. (2011). Model predictive control: Review of the three decades of development. *International Journal of Control, Automation and Systems, 9*(1), 415-424.

Lee, K. H., Cortelezzi, L., Kim, J., & Speyer, J. (2001). Application of reduced-order controller to turbulent flows for drag reduction. *Physics of Fluids, 13*(1), 1321-1330.

Lee, M., & Moser, R. D. (2015). Direct numerical simulation of turbulent channel flow up to Re=5200. *Journal of Fluid Mechanics, 774*(1), 395-415.

Lee, S. J., & Lee, S. H. (2001). Flow field analysis of a turbulent boundary layer over a riblet surface. *Experiments in Fluids, 30*(1), 153-166.

Leontaritis, I. J., & Billings, S. A. (1985a). Input-output parametric models for non-linear systems Part I: deterministic non-linear systems. *International Journal of Control, 41*(2), 303-328.

Leontaritis, I. J., & Billings, S. A. (1985b). Input-output parametric models for non-linear systems Part II: stochastic non-linear systems. *International Journal of Control, 41*(1), 329-344.

Leontaritis, I. J., & Billings, S. A. (1987). Experimental design and identifiability for non-linear systems. *International Journal of Systems Science, 18*(1), 189-202.

Li, L. M., & Billings, S. A. (2001). Continuous time non-linear system identification in the frequency domain. *International Journal of Control, 74*(1), 1052-1061.

Li, L. M., & Billings, S. A. (2011). Estimation of generalized frequency response functions for quadratically and cubically nonlinear systems. *Journal of Sound and Vibration, 330*(1), 461-470.

Li, W., Jessen, W., Roggenkamp, D., Klaas, M., Silex, W., Schiek, M., & Schröder, W. (2015). Turbulent drag reduction by spanwise traveling ribbed surface waves. *European Journal of Mechanics - B/Fluids, 53*(1), 101-112.

Li, Y. C. (2013). Major open problems in chaos theory, turbulence and nonlinear dynamics. *Dynamics of Partial Differential Equations, 10*(1), 379-392.

Li, Y. C. (2014). The distinction of turbulence from chaos -- rough dependence on initial data. *Electron. J. Differ. Equ., 36*(6), 1305.2864.

Lin, J. C. (2002). Review of research on low-profile vortex generators to control boundary-layer separation. *Progress in Aerospace Sciences, 38*(1), 389-420.

Liu, J. J. (2002). A new GUI interpretation tool for the non-linear frequency response function. *Journal of the Franklin Institute, 339*(1), 431-454.

Liu, J. J., Cheng, S. J., Kung, I. C., Chang, H. C., & Billings, S. A. (2001). Non-linear system identification and fault diagnosis using a new GUI interpretation tool. *Mathematics and Computers in Simulation, 54*(1), 425-449.

Liu, J. J., Lee, Y. W., Wang, F. C., Uppala, R., & Chen, P. H. (2006). Time and frequency domain identification and analysis of a permanent magnet synchronous servo motor. *Journal of the Chinese Institute of Engineers, 29*(1), 683-695.

Ljung, L. (2004). *State of the art in linear system identification: Time and frequency domain methods*. Paper presented at the 2004 American Control Conference, Boston, USA.

Ljung, L. (2010). Perspectives on system identification. *Annual Reviews in Control, 34*(1), 1-12.

Lofdahl, L., & Gad-El-Hak, M. (1999a). MEMS-based pressure and shear stress sensors for turbulent flows. *Measurement Science and Technology, 10*(1), 665.

Lofdahl, L., & Gad-El-Hak, M. (1999b). MEMS applications in turbulence and flow control. *Progress in Aerospace Sciences, 35*(1), 101-203.

Loxton, R., Lin, Q., & Teo, K. L. (2013). Minimizing control variation in nonlinear optimal control. *Automatica, 49*(1), 2652-2664.

Lumley, J., & Blossey, P. (1998). Control of turbulence. *Annual Review of Fluid Mechanics, 30*(1), 311-327.

Luo, W., & Billings, S. A. (1995). Adaptive model selection and estimation for nonlinear systems using a sliding data window. *Signal Processing, 46*(1), 179-202.

Maeder, U., Borrelli, F., & Morari, M. (2009). Linear offset-free Model Predictive Control. *Automatica, 45*(1), 2214-2222.

Maeder, U., & Morari, M. (2010). Offset-free reference tracking with model predictive control. *Automatica, 46*(1), 1469-1476.

Mahmood, M., & Mhaskar, P. (2012). Lyapunov-based model predictive control of stochastic nonlinear systems. *Automatica, 48*(1), 2271-2276.

Mao, K. Z., & Billings, S. A. (2000). Multi-directional model validity tests for non-linear system identification. *International Journal of Control, 73*(1), 132-143.

Mayne, D. Q. (2014). Model predictive control: Recent developments and future promise. *Automatica, 50*(1), 2967-2986.

Mayne, D. Q., & Michalska, H. (1990). Receding horizon control of nonlinear systems. *IEEE Transactions on Automatic Control, 35*(1), 814-824.

Mayne, D. Q., & Rawlings, J. B. (2001). Correction to "Constrained model predictive control: stability and optimality". *Automatica, 37*(1), 483.

Mayne, D. Q., Rawlings, J. B., Rao, C. V., & Scokaert, P. O. M. (2000). Constrained model predictive control: Stability and optimality. *Automatica, 36*(1), 789-814.

Mendes, E. (1993). C/FORTRAN NARMAX implementation (Version 1.0). The University of Sheffield: Automatic Control & Systems Engineering.

Meng, Q., Guan, Y., & Xie, A. (2011). *A review of CFD-based system identification.* Paper presented at the 2011 Chinese Control and Decision Conference, Mianyang, China.

Mito, Y., & Kasagi, N. (1998). DNS study of turbulence modification with streamwise-uniform sinusoidal wall-oscillation. *International Journal of Heat and Fluid Flow, 19*(1), 470-481.

Moin, P., & Mahesh, K. (1998). Direct numerical simulation: A Tool in Turbulence Research. *Annual Review of Fluid Mechanics, 30*(1), 539-578.

Morari, M., & Lee, J. H. (1999). Model predictive control: past, present and future. *Computers & Chemical Engineering, 23*(1), 667-682.

Morari, M., & Maeder, U. (2012). Nonlinear offset-free model predictive control. *Automatica, 48*(1), 2059-2067.

Moser, R. D., Kim, J., & Mansour, N. N. (1999). Direct numerical simulation of turbulent channel flow up to Re-tau=590. *Physics of Fluids, 11*(1), 943-945.

Nakayama, Y. (1999). *Introduction to fluid mechanics*. London: Arnold.

Nam, S. W., & Powers, E. J. (1994). Application of higher order spectral analysis to cubically nonlinear system identification. *IEEE Transactions on Signal Processing, 42*(2), 1746-1765.

Neumann, J., & Wengle, H. (2003). DNS and LES of Passively Controlled Turbulent Backward-Facing Step Flow. *Flow, Turbulence and Combustion, 71*(1), 297-310.

Nguyen, P. A., & Raymond, J. P. (2015). Boundary Stabilization of the Navier--Stokes Equations in the Case of Mixed Boundary Conditions. *SIAM Journal on Control and Optimization, 53*(1), 3006-3039.

Nuij, P. W. J. M., Bosgra, O. H., & Steinbuch, M. (2006). Higher-order sinusoidal input describing functions for the analysis of non-linear systems with harmonic responses. *Mechanical Systems and Signal Processing, 20*(1), 1883-1904.

Obeid, S., Jha, R., & Ahmadi, G. (2012). *Closed-loop feedback control of flow over a flapped airfoil at high angles of attack using identified NARMAX model*. Paper presented at the 2001 Fluids Engineering Division Summer Meeting, New Orleans, USA.

Ogata, K. (2010). *Modern control engineering* (5th ed., I ed.). Boston, [Mass.] London: Boston, Mass. London : Pearson, c2010.

Okada, K., Miyaji, K., Fujii, K., Oyama, A., Nonomura, T., & Asada, K. (2010). *Computational study of the synthetic jet on separated flow over a backward-facing step*. Paper presented at the ASME 2010 International Mechanical Engineering Congress and Exposition, New Orleans, USA.

Osborne, R. (1995). On the Dynamical Theory of Incompressible Viscous Fluids and the Determination of the Criterion. *Proceedings: Mathematical and Physical Sciences, 451*(1), 5-47.

Park, H. J., Sun, G., & Kim, C. J. (2014). Superhydrophobic turbulent drag reduction as a function of surface grating parameters. *Journal of Fluid Mechanics, 747*(1), 722-734.

Park, H. J., Tasaka, Y., Oishi, Y., & Murai, Y. (2015). Drag reduction promoted by repetitive bubble injection in turbulent channel flows. *International Journal of Multiphase Flow, 75*(1), 12-25.

Pasquetti, R., & Peres, N. (2015). A penalty model of synthetic micro-jet actuator with application to the control of wake flows. *Computers & Fluids, 114*(1), 203-217.

Pearson, R. K., & Kotta, Ü. (2004). Nonlinear discrete-time models: state-space vs. I/O representations. *Journal of Process Control, 14*(1), 533-538.

Peng, Z. K., Lang, Z. Q., & Billings, S. A. (2007). Linear parameter estimation for multi-degree-of-freedom nonlinear systems using nonlinear output

frequency-response functions. *Mechanical Systems and Signal Processing, 21*(1), 3108-3122.

Peng, Z. K., Lang, Z. Q., Wolters, C., Billings, S. A., & Worden, K. (2011). Feasibility study of structural damage detection using NARMAX modelling and Nonlinear Output Frequency Response Function based analysis. *Mechanical Systems and Signal Processing, 25*(1), 1045-1061.

Perlin, M., Dowling, D. R., & Ceccio, S. L. (2016). Freeman Scholar Review: Passive and Active Skin-Friction Drag Reduction in Turbulent Boundary Layers. *Journal of Fluids Engineering, 138*(1), 91104-911034.

Peyton Jones, J. C. (2007). Simplified computation of the Volterra frequency response functions of non-linear systems. *Mechanical Systems and Signal Processing, 21*(1), 1452-1468.

Peyton Jones, J. C., & Billings, S. A. (1989). Recursive algorithm for computing the frequency response of a class of non-linear difference equation models. *International Journal of Control, 50*(1), 1925-1940.

Peyton Jones, J. C., & Billings, S. A. (1993). Mean levels in nonlinear analysis and identification. *International Journal of Control, 58*(1), 1033-1052.

Peyton Jones, J. C., & Choudhary, K. (2012a). Efficient computation of higher order frequency response functions for nonlinear systems with, and without, a constant term. *International Journal of Control, 85*(1), 578-593.

Peyton Jones, J. C., & Choudhary, K. (2012b). Output frequency response characteristics of nonlinear systems. Part I: general multi-tone inputs. *International Journal of Control, 85*(1), 1263-1278.

Peyton Jones, J. C., & Choudhary, K. (2012c). Output frequency response characteristics of nonlinear systems. Part II: overlapping effects and commensurate multi-tone excitations. *International Journal of Control, 85*(1), 1279-1292.

Poli, A. A., & Cirillo, M. C. (1993). On the use of the normalized mean square error in evaluating dispersion model performance. *Atmospheric Environment. Part A. General Topics, 27*(1), 2427-2434.

Pollard, A. (1998). Passive and active control of near-wall turbulence. *Progress in Aerospace Sciences, 33*(1), 689-708.

Pouryoussefi, S., Mirzaei, M., & Hajipour, M. (2015). Experimental study of separation bubble control behind a backward-facing step using plasma actuators. *Acta Mechanica, 226*(1), 1153-1165.

Prandtl, L. (1905). Uber Flussigkeitsbewegung Bei Sehr Kleiner Reibung. *III Internationalen Mathematiker-Kongresses, 5*(1), 484-491.

Qin, S. J., & Badgwell, T. A. (2003). A survey of industrial model predictive control technology. *Control Engineering Practice, 11*(1), 733-764.

Quadrio, M., & Ricco, P. (2004). Critical assessment of turbulent drag reduction through spanwise wall oscillations. *J. Fluid Mech., 521*(1), 251-271.

Quadrio, M., Ricco, P., & Viotti, C. (2009). Streamwise-travelling waves of spanwise wall velocity for turbulent drag reduction. *Journal of Fluid Mechanics, 627*(1), 161-178.

Rahrooh, A., & Shepard, S. (2009). Identification of nonlinear systems using NARMAX model. *Nonlinear Analysis: Theory, Methods & Applications, 71*(1), 1198-1202.

Rathnasingham, R., & Breuer, K. S. (2003). Active control of turbulent boundary layers. *Journal of Fluid Mechanics, 495*(1), 209-233.

Raymond, J. P. (2006). Feedback Boundary Stabilization of the Two-Dimensional Navier--Stokes Equations. *SIAM Journal on Control and Optimization, 45*(1), 790-828.

Raymond, J. P. (2007). Feedback boundary stabilization of the three-dimensional incompressible Navier–Stokes equations. *Journal de mathématiques pures et appliquées, 87*(1), 627-669.

Reynolds, O. (1894). On the Dynamical Theory of Incompressible Viscous Fluids and the Determination of the Criterion. *Proceedings of the Royal Society of London (1854-1905), 56*(1), 40-45.

Ricco, P., & Dilib, F. (2010). The influence of wall suction and blowing on boundary-layer laminar streaks generated by free-stream vortical disturbances. *Physics of Fluids, 22*(4), 044101-044121.

Ricco, P., Ottonelli, C., Hasegawa, Y., & Quadrio, M. (2012). Changes in turbulent dissipation in a channel flow with oscillating walls. *Journal of Fluid Mechanics, 700*(1), 77-104.

Ricco, P., & Quadrio, M. (2008). Wall-oscillation conditions for drag reduction in turbulent channel flow. *International Journal of Heat and Fluid Flow, 29*(1), 891-902.

Ricco, P., & Wu, S. (2004). On the effects of lateral wall oscillations on a turbulent boundary layer. *Experimental Thermal and Fluid Science, 29*(1), 41-52.

Ritz, C. P., & Powers, E. J. (1986). Estimation of nonlinear transfer functions for fully developed turbulence. *Physica D: Nonlinear Phenomena, 20*(1), 320-334.

Rossiter, J. A. (2003). *Model-based predictive control : a practical approach.* Boca Raton: CRC Press.

Rowley, C. W. (2005). Model reduction: proper orthogonal decomposition. *International Journal of Bifurcation and Chaos, 15*(1), 997-1013.

Rozhdestvensky, B. L., & Priymak, V. G. (1982). Numerical simulation of two-dimensional turbulence in a plane channel. *Computers and Fluids, 10*(1), 117-126.

Ruisi, R., Zare-Behtash, H., Kontis, K., & Erfani, R. (2016). Active flow control over a backward-facing step using plasma actuation. *Acta Astronautica, 126*(1), 354-363.

Sandberg, I. (1983). On Volterra expansions for time-varying nonlinear systems. *IEEE Transactions on Circuits and Systems, 30*(1), 61-67.

Santillo, M. A., Hoagg, J. B., Bernstein, D. S., & Powell, K. (2006). *CFD-Based Adaptive Flow Control for Steady Flow Field Modification.* Paper presented at the 45th IEEE Conference on Decision and Control, San Diego, USA.

Sattarzadeh, S. S., Fransson, J. H. M., Talamelli, A., & Fallenius, B. E. G. (2014). Consecutive turbulence transition delay with reinforced passive control. *Physical Review E, 89*(6), 61001-61021.

Savran, A. (2013). Discrete state space modeling and control of nonlinear unknown systems. *ISA Transactions, 52*(1), 795-806.

Savran, A., & Kahraman, G. (2014). A fuzzy model based adaptive PID controller design for nonlinear and uncertain processes. *ISA Transactions, 53*(1), 280-288.

Scott Collis, S., Joslin, R. D., Seifert, A., & Theofilis, V. (2004). Issues in active flow control: theory, control, simulation, and experiment. *Progress in Aerospace Sciences, 40*(1), 237-289.

Segawa, T., Kawaguchi, Y., Kikushima, Y., & Yoshida, H. (2002). Active control of streak structures in wall turbulence using an actuator array producing inclined wavy disturbances. *Journal of Turbulence, 3*(1), 1-25.

Sjöberg, J., Zhang, Q., Ljung, L., Benveniste, A., Delyon, B., Glorennec, P. Y., . . . Juditsky, A. (1995). Nonlinear black-box modeling in system identification: a unified overview. *Automatica, 31*(1), 1691-1724.

Smagorinsky, J. (1963). General Circulation Experiments with the Primitive Equations. *Monthly Weather Review, 91*(1), 99-164.

Spalart, P. R., Strelets, M., & Travin, A. (2006). Direct numerical simulation of large-eddy-break-up devices in a boundary layer. *International Journal of Heat and Fluid Flow, 27*(1), 902-910.

Sutardi, C. Y., & Ching, C. Y. (1999). Effect of a transverse square groove on a turbulent boundary layer. *Experimental Thermal and Fluid Science, 20*(1), 1-10.

Swain, A. K., & Billings, S. A. (1998). Weighted Complex Orthogonal Estimator for Identifying Linear and Nonlinear Continuous Time Models from Generalised Frequency Response Functions. *Mechanical Systems and Signal Processing, 12*(1), 269-292.

Temam, R. (1977). *Navier-Stokes equations : theory and numerical analysis*. Oxford: North-Holland Publishing Co.

Terekhov, V. I., Smul'skii, Y. I., & Sharov, K. A. (2012). Interference of separated flows behind backward-facing step in the presence of passive control. *Technical Physics Letters, 38*(1), 125-128.

Tsai, J. S. H., Wang, C. T., Kuang, C. C., Guo, S. M., Shieh, L. S., & Chen, C. W. (2010). A NARMAX model-based state-space self-tuning control for nonlinear stochastic hybrid systems. *Applied Mathematical Modelling, 34*(1), 3030-3054.

Tsai, Z. R. (2013). Robust digital design of continuous-time nonlinear control systems using adaptive prediction and random-local-optimal NARMAX model. *Applied Mathematics and Computation, 221*(1), 152-163.

Tsang, K. M., & Billings, S. A. (1992). Reconstruction of linear and non-linear continuous time models from discrete time sampled-data systems. *Mechanical Systems and Signal Processing, 6*(1), 69-84.

Tuttle, M. H., & Bushnell, D. M. (1979). *Survey and bibliography on attainment of laminar flow control in air using pressure gradient and suction*. Retrieved from NASA, USA:

Tuttle, M. H., & Maddalon, D. V. (1982). *Laminar flow control, 1976 - 1982: A selected annotated bibliography*. Retrieved from NASA, USA:

Uruba, V., Jonáš, P., & Mazur, O. (2007). Control of a channel-flow behind a backward-facing step by suction/blowing. *International Journal of Heat and Fluid Flow, 28*(1), 665-672.

Vaccaro, J. C., Elimelech, Y., Chen, Y., Sahni, O., Jansen, K. E., & Amitay, M. (2015). Experimental and numerical investigation on steady blowing flow control within a compact inlet duct. *International Journal of Heat and Fluid Flow, 54*(1), 143-152.

Varadan, V. K., & Varadan, V. V. (2000). Microsensors, microelectromechanical systems (MEMS), and electronics for smart structures and systems. *Smart Materials and Structures, 9*(1), 953.

Vazquez, R., & Krstic, M. (2007). A Closed-Form Feedback Controller for Stabilization of the Linearized 2-D Navier-Stokes Poiseuille System. *IEEE Transactions on Automatic Control, 52*(1), 2298-2312.

Viswanath, P. R. (2002). Aircraft viscous drag reduction using riblets. *Progress in Aerospace Sciences, 38*(1), 571-600.

Wahidi, R., Chakroun, W., & Al-Fahed, S. (2005). The behavior of the skin-friction coefficient of a turbulent boundary layer flow over a flat plate with differently configured transverse square grooves. *Experimental Thermal and Fluid Science, 30*(1), 141-152.

Wang, L., Luo, Z. B., Xia, Z. X., Liu, B., & Deng, X. (2012). Review of actuators for high speed active flow control. *Science China Technological Sciences, 55*(1), 2225-2240.

Wei, H. L., Lang, Z. Q., & Billings, S. A. (2007). An Algorithm for Determining the Output Frequency Range of Volterra Models With Multiple Inputs. *IEEE Transactions on Circuits and Systems II: Express Briefs, 54*(1), 532-536.

Wei, H. L., Liu, J., & Billings, S. A. (2003). *Term and Variable Selection for Nonlinear System Identification*. Retrieved from Sheffield:

Wu, C., & Kanai, T. (2016). Data-driven detailed hair animation for game characters. *Computer Animation and Virtual Worlds, 27*(1), 221-230.

Wu, G. C., Baleanu, D., Zeng, S. D., & Deng, Z. G. (2015). Discrete fractional diffusion equation. *Nonlinear Dynamics, 80*(1), 281-286.

Wu, X., Lang, Z. Q., & Billings, S. A. (2006). *Output Frequencies of A Class of Nonlinear Systems*. Paper presented at the 13th IEEE International Conference on Electronics, Circuits and Systems, Nice, France.

Wu, Z., Wong, C., Wang, L., Lu, Z., Zhu, Y., & Zhou, Y. (2015). A rapidly settled closed-loop control for airfoil aerodynamics based on plasma actuation. *Experimental Methods and their Applications to Fluid Flow, 56*(1), 1-15.

Xu, F., Gao, Z., Ming, X., Xia, L., Wang, Y., Sun, W., & Ma, R. (2015). The optimization for the backward-facing step flow control with synthetic jet based on experiment. *Experimental Thermal and Fluid Science, 64*(1), 94-107.

Yan, Y., Coca, D., & Barbu, V. (2008). Internal Optimal Controller Synthesis for Navier–Stokes Equations. *Numerical Functional Analysis and Optimization, 29*(1), 225-242.

Yan, Y., Coca, D., & Barbu, V. (2009). Finite-dimensional controller design for semilinear parabolic systems. *Nonlinear Analysis: Theory, Methods & Applications, 70*(1), 4451-4475.

Young, P. C. (2006). The data-based mechanistic approach to the modelling, forecasting and control of environmental systems. *Annual Reviews in Control, 30*(1), 169-182.

Yue, R., Billings, S. A., & Lang, Z. Q. (2005a). An investigation into the characteristics of non-linear frequency response functions. Part 1: Understanding the higher dimensional frequency spaces. *International Journal of Control, 78*(1), 1031-1044.

Yue, R., Billings, S. A., & Lang, Z. Q. (2005b). An investigation into the characteristics of non-linear frequency response functions. Part 2: New analysis methods based on symbolic expansions and graphical techniques. *International Journal of Control, 78*(1), 1130-1149.

Yue, R., Lang, Z. Q., & Billings, S. A. (2004). Non-linear System Frequency Response Analysis (NSFRA) Toolkit (Version 1.0). Sheffield, United Kingdom: Department of Automatic Control and Systems Engineering.

Zare, A., Lieu, B. K., & Jovanovic, M. R. (2012). *Turbulent drag reduction by streamwise traveling waves*. Paper presented at the IEEE 51st Annual Conference on Decision and Control Maui, USA.

Zhang, G., Eddy Patuwo, B., & Y. Hu, M. (1998). Forecasting with artificial neural networks:: The state of the art. *International Journal of Forecasting, 14*(1), 35-62.

Zhang, H., & Billings, S. A. (1993). Analysing non-linear systems in the frequency domain--I. The transfer function. *Mechanical Systems and Signal Processing, 7*(1), 531-550.

Zhao, H., Wu, J. Z., & Luo, J. S. (2004). Turbulent drag reduction by traveling wave of flexible wall. *Fluid Dynamics Research, 34*(1), 175-198.

Zheng, C. R., Zhang, Y. C., & Zhang, W. Y. (2011). Large eddy simulation of separation control over a backward-facing step flow by suction. *International Journal of Computational Fluid Dynamics, 25*(1), 59-74.

Zheng, G. L., & Billings, S. A. (1999). Qualitative validation and generalization in non-linear system identification. *International Journal of Control, 72*(1), 1592-1608.

Zhou, Y., & Bai, H. L. (2011). Recent advances in active control of turbulent boundary layers. *Science China-Physics Mechanics & Astronomy, 54*(1), 1289-1295.

Zhu, D., Billings, S. A., Balikhin, M. A., Wing, S., & Coca, D. (2006). Data derived continuous time model for the Dst dynamics. *Geophysical Research Letters, 33*(1), 4101-4105.

Zhu, Q. M., & Billings, S. A. (1997). *Properties of higher order correlation function tests for nonlinear model validation.* Paper presented at the 23rd International Conference on Industrial Electronics, Control and Instrumentation, New Orleans, USA.

Zhu, Q. M., Wang, Y., Zhao, D., Li, S., & Billings, S. A. (2013). Review of rational (total) nonlinear dynamic system modelling, identification, and control. *International Journal of Systems Science, 46*(1), 2122-2133.

Zwart, H. (2004). Transfer functions for infinite-dimensional systems. *Systems & Control Letters, 52*(1), 247-255.